LASP
LABORATORY FOR ATMOSPHERIC AND SPACE PHYSICS
UNIVERSITY OF COLORADO AT BOULDER

Laboratory For Atmospheric and Space Physics

LASP Engineering Division
University of Colorado
Boulder, Colorado

CLARREO Pathfinder
Algorithm Theoretical Basis Document
Document No. 151599

Approvers List

Prepared By	Paul Smith
Approved By	Peter Pilewskie
Configuration Management	

Rev	Change Description	By
-	Initial Document	Paul Smith
A	Added Uncertainty Budget	Paul Smith
B	Added Secondary On-orbit calibrations and Pen-ray Calibration with ILS considerations	Paul Smith
C	Added information on data products, added transmissive diffuser flat field sections	Paul Smith
D	Updated version. Added thorough theoretical treatment of instrument. Added more information on data products. Added responses to LaRC comments from previous version.	Paul Smith
E	Updated to include all of the algorithm development that will be used by the science data system flight code. This includes all the new information from the characterization and calibration test campaign. Removed all old information from pre-calibration. Re-organized to mimic the flow of the flight data pipeline.	Paul Smith, Michael Gerrity, Tony Barsic
F	Updated instrument equations to reflect newest understanding of measurement. Added solar zenith angle uncertainty section.	Paul Smith

0.1 Table of Contents

0.2 Table of Figures

0.3 Reference Documents

Document Ref	**Title**
1	Espejo, J., Belting, C., Drake, G., Heuerman, K., Kopp, G., Lieber, A., Smith, P., and Vermeer, B.: “A Hyperspectral Imager for High Radiometric Accuracy Earth Climate Studies,” SPIE Proc., 21-25 Aug. 2011
2	Agile #157567 Rev. A, CLARREO Preliminary Characterization and Calibration Plan
3	Kopp et al., Geosci. Instrum. Method. Data Syst., 2017, doi:10.5194/gi-6-169-2017
4	Changyong Dou, Xiaodong Zhang, Hojin Kim, Jaganathan Ranganathan, Doug Olsen, and Huadong Guo. “Geolocation Algorithm for Earth Observation Sensors Onboard the International Space Station.” Photogrammetric Engineering & Remote Sensing. Vol. 79, No. 7, July 2013, pp. 625–637.
5	TSIS SIM ATBD: https://docserver.gesdisc.eosdis.nasa.gov/public/project/TSIS/TSIS_Algorithm_Theoretical_Basis_Document_151430RevA.pdf
6	Janesick, J.R., Scientific Charge-Coupled Devices, SPIE, Bellingham, WA, 920 pp, 2001, ISBN: 9780819436986
7	Lukashin, C., Jin, Z., Kopp, G., MacDonnell, D.G., and Thome, K.: “CLARREO Reflected Solar Spectrometer: Restrictions for Instrument Sensitivity to Polarization," IEEE Transactions on Geoscience and Remote Sensing, 53, #12, 6703-6709, Dec. 2015, DOI 10.1109/TGRS.2015.2446197
8	Roithmayr, C.M., Lukashin, C., Speth, P.W., Kopp, G., Thome, K., Wielicki, B.A, and Young, D.F.: “CLARREO Approach for Reference Inter-Calibration of Reflected Solar Sensors: On-Orbit Data Matching and Sampling,” IEEE Transactions on Geoscience and Remote Sensing, 52 #10, Oct. 2014, pp. 6762-6774, doi:10.1109/TGRS.2014.2302397
9	Smith, P., Drake, G., Espejo, J., Heuerman, K., and Kopp, G.: “A Solar Irradiance Cross-Calibration Method Enabling Climate Studies Requiring 0.2% Radiometric Accuracies,” ESTF 2011, June 2011
10	Born and Wolf. “Principles of Optics.” Cambridge University Press. 7th ed. pp. 638. 1959. ISBN: 0 521 642221

Document Ref	**Title**
11	John W. Chapman, David R. Thompson , Mark C. Helmlinger, Brian D. Bue, Robert O. Green, Michael L. Eastwood, Sven Geier, Winston Olson-Duvall and Sarah R. Lundeen: “Spectral and Radiometric Calibration of the Next Generation Airborne Visible Infrared Spectrometer (AVIRIS-NG). Remote Sens. 2019, 11, 2129; doi:10.3390/rs11182129
12	Craig J. Sansonetti, Marc L. Salit, and Joseph Reader.: “Wavelengths of spectral lines in mercury pencil lamps.” 74 APPLIED OPTICS / Vol. 35, No. 1 / 1 January 1996
13	Bate, Mueller, White. “Fundamentals of Astrodynamics.” Dover Books on Astsronomy, Dover Publications, Inc. New York, 1971
14	David M. Harber, Karl F. Heuerman, Greg A. Kopp, George Lawrence, "Aperture edge scatter calibration of the cavity radiometers for the spaceflight Total Irradiance Monitor," Proc. SPIE 6296, Earth Observing Systems XI, 62961I (8 September 2006); doi: 10.1117/12.679615
15	Agile #157566, Payload Specification Document (SE-8)
16	A. Khadjavi, “Calculation of solid angle subtended by rectangular apertures.” J. Opt. Soc. Am. 58, 1417 (1968).
17	Corrosion in Space, A. de Rooij Head of Materials Technology Section Product Assurance and Safety Department Materials and Components Technology Division European Space Agency European Space Technology and Research Centre Noordwijk, The Netherlands
18	David A. Haner, Brendan T. McGuckin, Robert T. Menzies, Carol J. Bruegge, and Valerie Duval, “Directional–hemispherical reflectance for Spectralon by integration of its bidirectional reflectance,” Applied Optics, 1998
19	Agile #159759, CPRS, SDS Software Development and Management Plan (SDMP)
20	Agile #159736, CPRSP Payload Concept of Operations
21	Agile #181253, CPRS Geolocation Algorithm
22	Agile #181340, CLARREO Pathfinder, HySICS Characterization and Calibration Report

0.4 Acronyms/Abbreviations

Acronym	**Meaning**
LASP	Laboratory for Atmospheric and Space Physics
TBD	To be determined
TBW	To be written
4MA	Four mirror anastigmat (telescope)
ADC	Analog-to-digital converter
ATBD	Algorithm Theoretical Basis Document
BRDF	Bidirectional reflectance distribution function
CLARREO	Climate Absolute Radiance and Refractivity Observatory
CPRS	CLARREO Pathfinder Reflected Solar
DN	Data number
FPA	Focal plane array
FPN	Fixed pattern noise
FSS	Fine sun sensor
HPS	HySICS Pointing System
HySICS	HyperSpectral Imager for Climate Science
IR	Infrared
LASP	Laboratory for Atmospheric and Space Physics
LED	Light-emitting diode
NIST	National Institute of Standards and Technology
PTFE	Polytetrafluoroethylene (Teflon)
SIM	Spectral Irradiance Monitor (TSIS instrument)
SNR	Signal-to-noise ratio
SSI	Spectral solar irradiance
TBW	To be written
TE	Transverse-electric

Acronym	**Meaning**
TM	Transverse-magnetic
TSIS	Total and Spectral Solar Irradiance Sensor
UV	Ultraviolet
ILS	Instrument Line Shape
OSF	Order Sorting Filter
CTE	Coefficient of Thermal Expansion
ROIC	Read Out Integrated Circuit

1.0 Scope

This version of the ATBD contains the information for the measurement equation, data products, and result on-orbit calibrations, algorithms, and uncertainties. For details about the optical system and layout, see [1, 3, 15]. For details about the payload ground characterization and calibration, see [2].

2.0 Introduction

2.1 Purpose of this Document

This Algorithm Theoretical Basis Document (ATBD) describes the algorithms used to produce all data levels of solar and Earth-viewing irradiance for the Climate Absolute Radiance and Refractivity Observatory (CLARREO) Pathfinder mission Hyperspectral Instrument for Climate Science (HySICS) instrument. The ATBD is not meant to be the sole reference for the HySICS instruments, data and algorithms. Other documents will be generated to explain, in much greater detail than presented here, instrument design and operation [15], instrument calibration [2], and the ground data system [19]. These related documents should be consulted to complement the information contained here. This ATBD provides one step towards insuring proper data stewardship of measurements Earth-viewing irradiance since a well-documented calibration history will allow for the comparison and evaluation of the HySICS instrument to its future analogs.

2.2 Contributing Authors

Paul Smith, Calibration Scientist

3.0 Algorithm Description

3.1 Conversion from the Instrument Signal to SI-traceable Data Product

The intent of the HySICS instrument is to measure both the solar irradiance and the Earth reflected radiance with the same instrument, thereby eliminating instrument common-mode variations [9]. The ratio of the two measurements is purely relative, and, if measured at nearly the same time, can be used to represent the reflectivity of the Earth scene. When coupled with an external measurement of the solar spectral irradiance, the HySICS instrument can be used to determine the reflected radiance of the measured Earth scene.

Figure 1 shows a high level flowchart of the entire process for converting a HySICS measurement of an object, either the Earth or the Moon, into the final data product, radiance, or reflectance. Every portion of this chart will be discussed in sections 3.0, describing the measurement equation and the dark green fields in this chart, and section 5.1.3, describing all the image conditioning steps, the gain corrections, and the dark corrections.

There are multiple on-orbit calibrations, implicitly used throughout the reflectance and radiance pipeline. Figure 2 shows a similar high level flowchart of the SSI (solar spectral irradiance) measurement. Figure 3 is a flat field flowchart, Figure 4 is a blank aperture flowchart, and Figure 5 is a Pen-ray flowchart. Note that all of the flowcharts are identical through the image conditioning, gain, and partially through the dark correction steps.

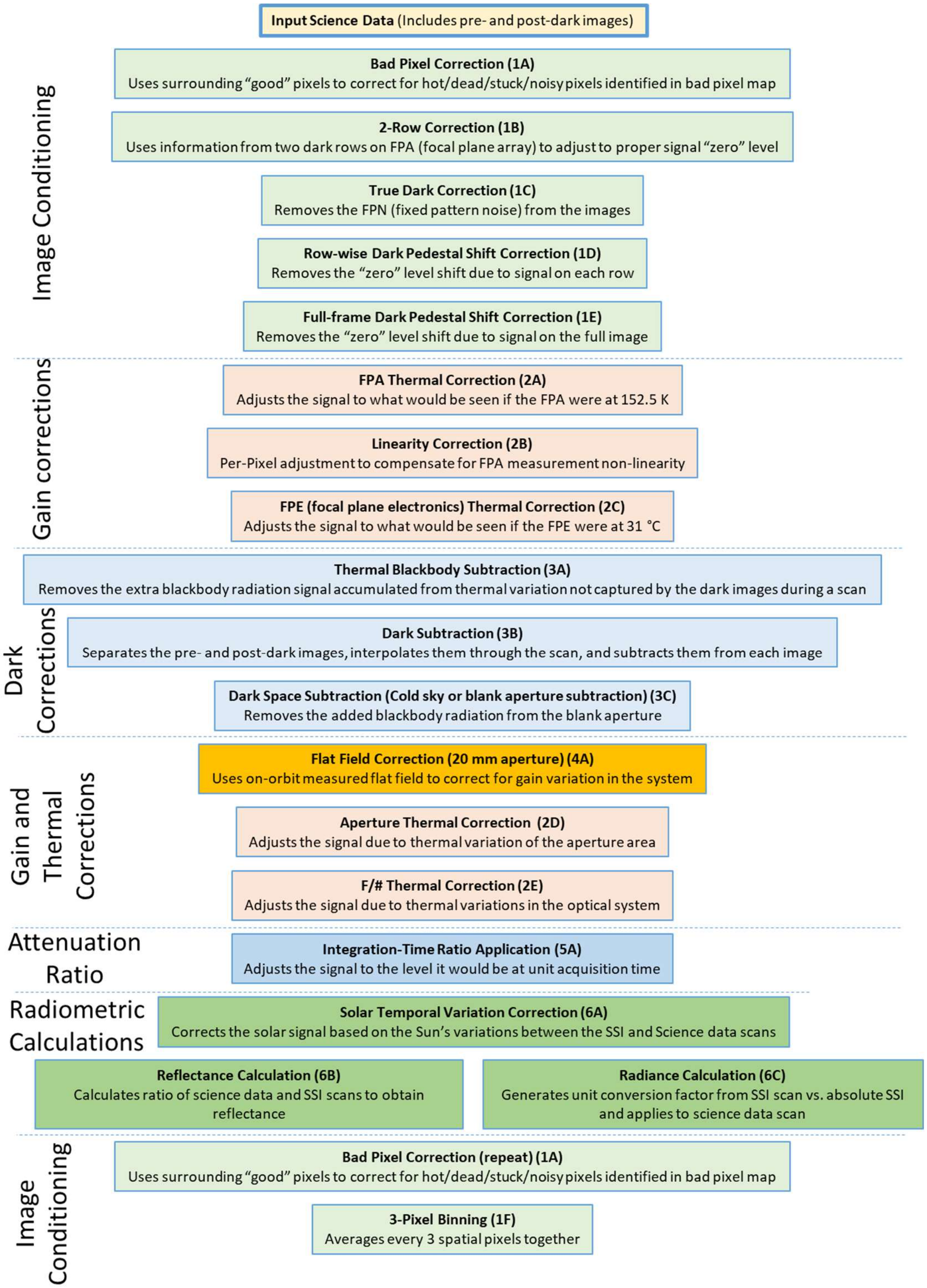

Figure 1. High level flowchart of the CPRS measurement to data product flow. Light green represents the image conditioning steps, used to turn the FPA's native output into a scientific product, red represents the gain steps, which also containing FPA corrections, but also thermal and flat field corrections, light blue represents the dark corrections, orange is the flat field, and dark green are the radiometric corrections and output.

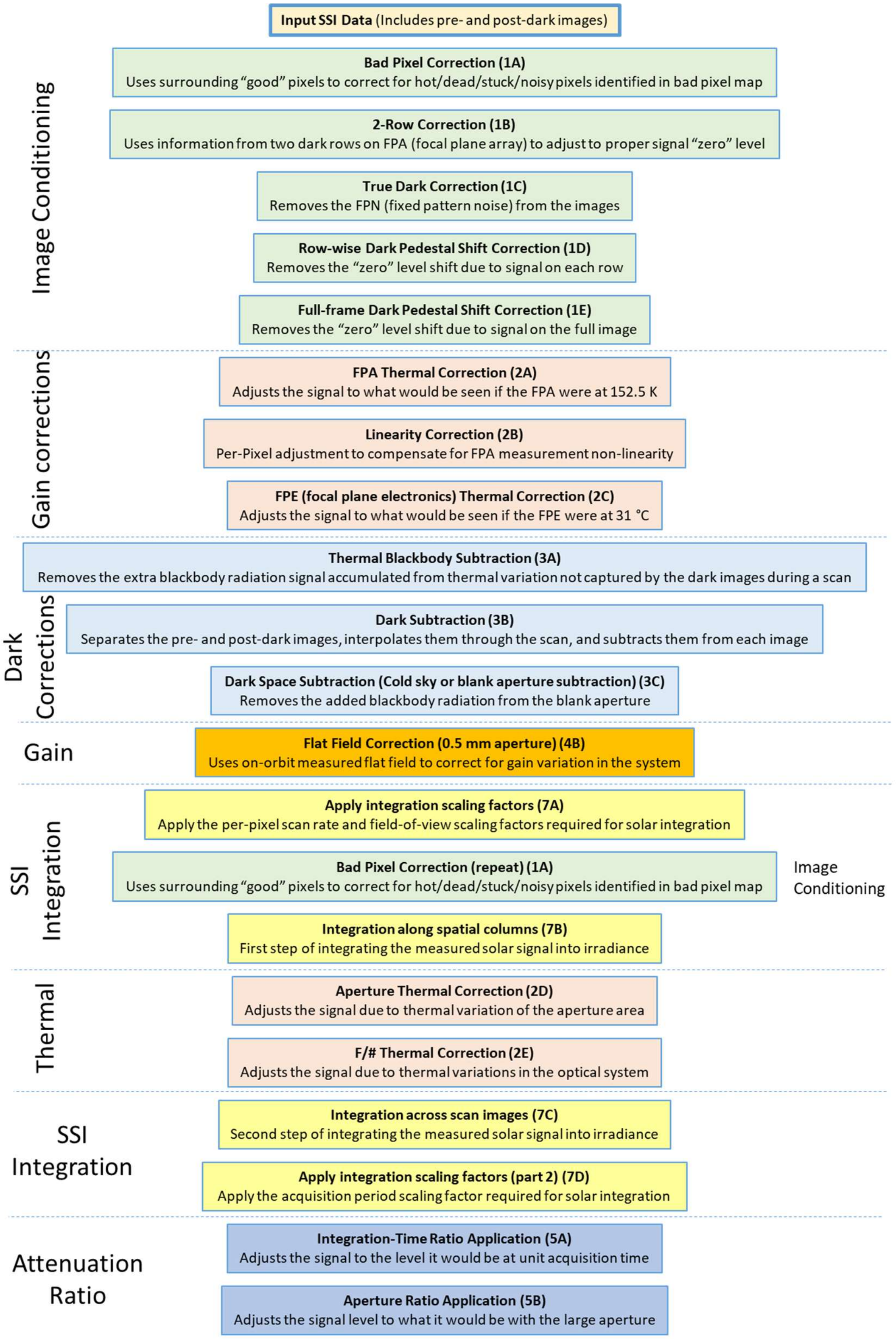

Figure 2. The SSI (solar spectral irradiance) data flow chart. This data product is used for both the reflectance and radiance SI-traceable products described in the previous flowchart. The SSI integration steps are in bright yellow.

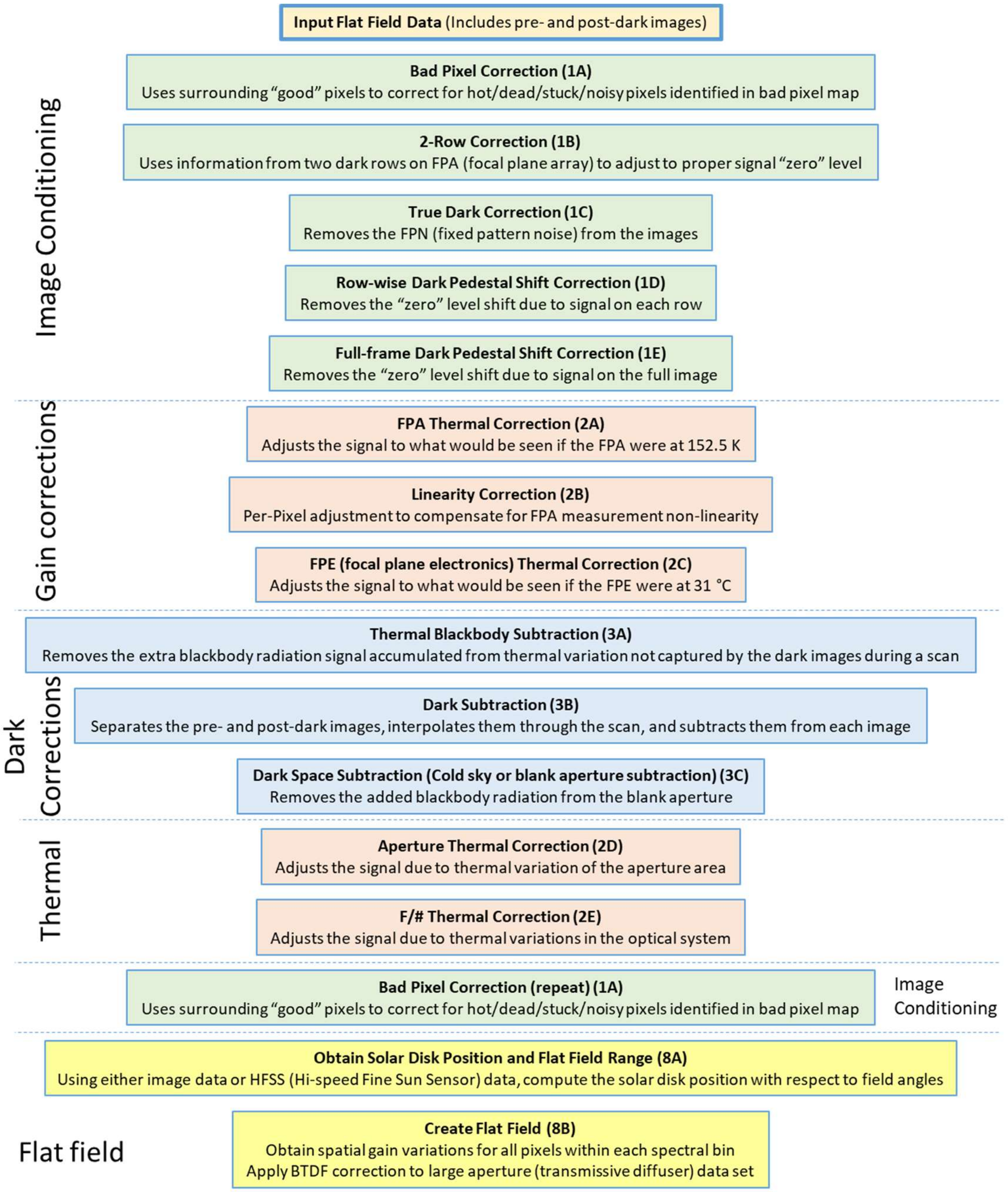

Figure 3. The flat field data flowchart. The data output from this path is used in the reflectance, radiance and SSI pipelines. The flat field creation steps are in bright yellow.

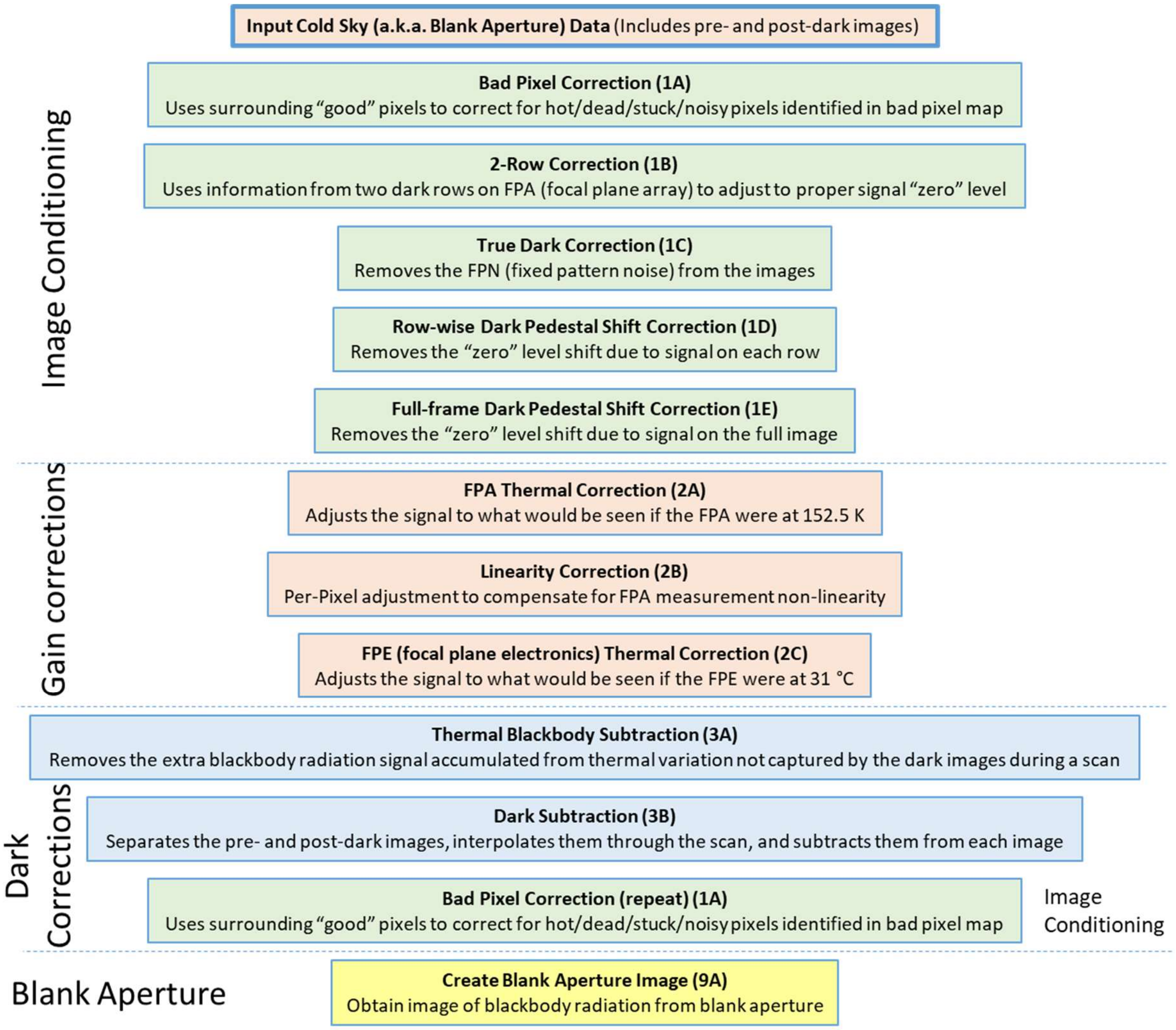

Figure 4. The cold sky (blank aperture) flowchart. This data is used in all of the above flowcharts to subtract off blackbody radiation generated by the blank aperture.

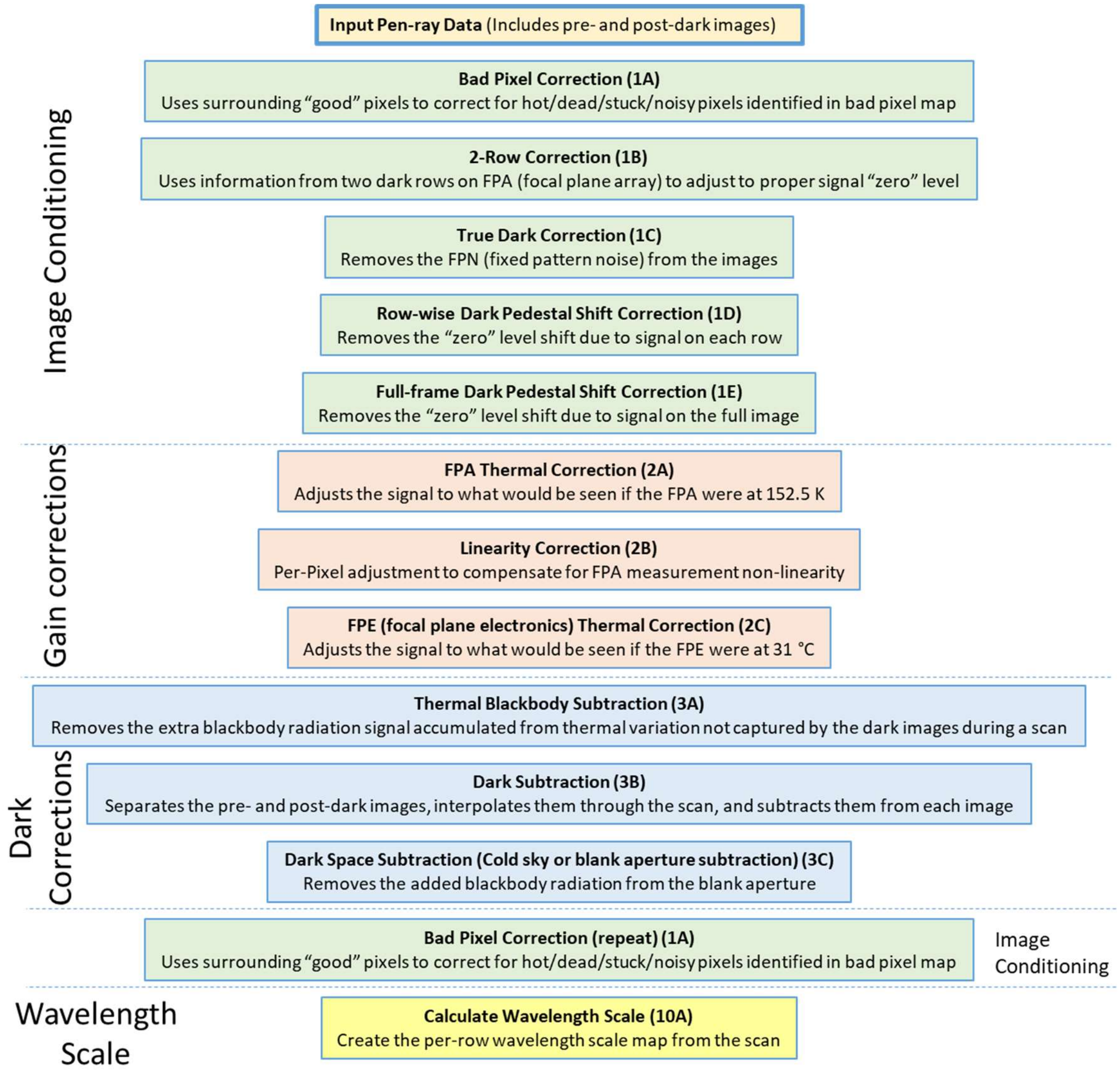

Figure 5. The Pen-ray wavelength scale calculation flow chart. The data from this process provides the knowledge of the spectral axis of all HySICS measurements.

The five primary flowcharts presented here detail every step in all the calibration data processing flows as well as every step in the level 1A data product with a reflectance or radiance output. The uncertainties associated with these processing steps will be addressed in section 6.0. Many of the processing steps in these pipelines are identical, and will only be discussed a single time in this document. To help the reader orient themselves with respect to the algorithms, the boxes have been labeled with an identifier number (1-10) and letter (A-F). The identifiers are identical on different pipelines if the algorithm does not change between each of the pipelines. These algorithm identifiers are interspersed throughout this document to identify where in the pipelines the text is referring to.

3.1.1 HySICS Measurement Overview

The next several sections will describe the HySICS measurements from an overview. At a high-level, the measurements are separated into a reflectance measurement and a radiance measurement. These sections are meant to provide a framework to orient the reader to the HySICS measurement. The full measurement mathematical model is described in detail in section 3.1.3. The primary measurement of the HySICS instrument is of surface reflectance and the uncertainty goals are defined for reflectance, although radiance values and uncertainties are provided as well.

The HySICS instrument measures the outgoing spectral radiance from an object, such as the Earth or Moon, and the incoming irradiance from the Sun. The spectral range is from 350 to 2300 nm, with approximately 3 nm sampling (6 nm resolution). The spatial field of view is 10 degrees, with 480 pixel measurements, or 75 arcsec per pixel. From the nominal 400 km altitude of the international space station (ISS) [13], each pixel covers 145 m on an Earth-viewing scene at nadir. Science measurements made by the instrument will average groups of every three pixels, making the coverage 435 m per super-pixel. In the cross-track direction, the ISS will sweep across 500 m during the acquisition period, making the spatial image pixels approximately 435 x 500 m on the ground.

The instrument takes pictures through a narrow slit, approximately 75 arcsec wide to match the pixel angular width. The slit is parallel to columns of the detector and therefore also the spatial dimension of each detector image. Light that enters through the slit is dispersed in the spectral direction, perpendicular to the along-slit (spatial) direction. Since the slit and the detector are matched in angular space, the slit can be thought of as being filled by a single pixel across (75 arcsec) and 480 pixels along (10 degrees) to create the full field of view. Images taken by the instrument appear as very narrow, but long patches of ground. However, every column in the detector represents a different wavelength of that same patch of ground. Each column is sometimes referred to as a wavelength bin. The images can be assembled into composite images of the ground, which will appear to be normal camera images at different wavelengths.

3.1.1.1 HySICS Measurement Equation

Being a relative measurement, the instrument measurement equation can be couched as a ratio between the SI-traceable reflected radiance and the measured scene:

$$L_{obj}(\lambda) \; = S'_{obj}(\lambda) \cdot C(\lambda) \cdot \alpha(\lambda) \qquad 1$$

where $L_{obj}(\lambda)$ is the SI-traceable reflected radiance (usually given in $W/(m^2 \cdot sr \cdot nm)$), and $S_{obj}(\lambda)$ is the instrument measured scene, given in instrument data numbers (DN) [3]. $C(\lambda)$ represents the unit conversion factor, given in $\frac{\left[\frac{W}{m^2 \cdot nm}\right]}{[DN]\cdot[sr]}$, measured on-orbit through the calibration scans described in section 5.2, and $\alpha(\lambda)$ represents the unitless instrument attenuation factor [algorithm 5A – 5B], measured in a laboratory before the CPRS flight, and described in more detail in section 5.1.2. The attenuation factor is dependent on the area of the input apertures and the integration times used while observing the Sun and the Earth, and on the full instrument optical path, which varies slightly for each pixel in an image. While not explicitly written in equation 1, the attenuation factor is different for each pixel in a measurement, which could be specified as $\alpha(\lambda, n)$ where n represents the pixel number. Note that the attenuation factors will be measured in a laboratory before flight, and that these measurements are described in detail in [2].

The unit conversion factor term is given by:

$$C(\lambda) = \frac{E_{Sun,t=t1}(\lambda)}{\mathcal{E}_{Sun,t=t1}(\lambda)} \qquad 2$$

where $E_{Sun,\, t=t1}(\lambda)$ is the solar spectral irradiance, given by the TSIS SIM measurement or a solar model, and generally in the units of W/(m^2 · nm). $\mathcal{E}_{Sun,t=t1}(\lambda)$ is the instrument measurement of the spectral solar irradiance, in DN · sr, and given by the full solar disk integration at all wavelengths, as described in section 5.2.1. The solid angle units, sr, are implicit in the integration of irradiance over the solar disk. Ideally, both the HySICS solar spectral irradiance measurement and the TSIS SIM solar spectral irradiance measurement should occur at, or close to, the same time, shown by the $t = t_1$ subscript.

In all the equation terms, wavelength, or λ, is the independent quantity, and can be given in any of the usual wavelength units, including nm. It is important to note that neither the dispersion scale, nor the instrument line shape of each instrument will be equivalent and a conversion between the two instruments is required, as outlined in Section 5.2.1.4.1.

3.1.1.2 Radiance

The scaling of the instrument measurement, natively in DN, to SI-traceable radiance units [algorithm 6C], equation 1 is directly followed. The unit conversion factor, C(λ), is dependent on the integration of the radiance of the Sun, and therefore on the instrument pixel solid angle, given in steradians. The pixel solid angle varies for each pixel and will be measured in the laboratory before flight, described in [2]. The detailed treatment of the pixel solid angle is described in 3.1.3.4, where it will be shown that the across-slit dimension of the pixel solid angle can be incorporated into the HySICS SSI measurement.

3.1.1.3 Reflectance

The HySICS instrument fundamentally makes a measurement of the reflected solar radiance from the surface of either the Moon or the Earth [algorithm 6B]. Using the common radiometric definition for reflectance as a ratio of radiance to irradiance, the HySICS instrument equation is:

$$R_{obj}(\lambda) = \pi \frac{L_{obj,t=t2}(\lambda)}{E_{Sun,t=t2}(\lambda)} \qquad 3$$

where $L_{obj,t=t2}(\lambda)$ is the spectral radiance of the measured object, as described in the previous section, and $E_{Sun,t=t2}(\lambda)$ is the solar spectral irradiance, as described in section 5.2.1. The factor of π is from the common reflectance definition, and is present to provide a uniform solid angle over which the radiance is taken, making the reflectance unitless. Ideally, the solar irradiance and object radiance should be measured simultaneously, as indicated by the $t = t_2$ subscript, although it does not need to happen at the same time as the previously mentioned $S_{Sun,t=t1}(\lambda)$, which is required for the instrument calibration.

Substituting the equations for $L_{obj,t=t2}(\lambda)$ and $C(\lambda)$, the reflectance becomes:

$$R_{obj}(\lambda) = \frac{S'_{obj,t=t2}(\lambda)}{\mathcal{E}_{Sun,t=t1}(\lambda)} \cdot \alpha(\lambda) \cdot \pi \cdot \frac{E_{Sun,t=t1}(\lambda)}{E_{Sun,t=t2}(\lambda)} \tag{4}$$

which has been rearranged to highlight the ratios involved. The first term is a pure ratio of the HySICS- measured object radiance, in DN, to the HySICS-measured solar spectral irradiance, in DN · sr. These two measurements cannot occur physically at the same time, since the same instrument is used to make both, as indicated by the t_1 and t_2 subscripts. The attenuation factor, $\alpha(\lambda)$ is still required, since the instrument changes its attenuation configuration between the two measurements. The final term, $E_{Sun,t=t1}(\lambda)/E_{Sun,t=t2}(\lambda)$, is a ratio of solar spectral irradiances, measured simultaneously with the instrument solar spectral irradiance measurement ($t = t_1$) and the instrument object measurement ($t = t_2$) [algorithm 6A]. The reflectance measurement has units of 1/sr.

The value of the reflectance terminology is that if the solar spectral irradiance has not changed between the HySICS SSI measurement and HySICS object measurement, the final term of the reflectance equation, and associated uncertainties, drop out. The reflectance becomes a ratio between the HySICS object and HySICS SSI measurements, with some additional proportionality constants. This is a particularly powerful observation in the visible and IR portions of the spectrum, where the solar spectral irradiance is likely quite stable for long periods of time. Because of the lack of uncertainties associated with the solar spectral irradiance (from the TSIS SIM measurement, and the spectral matching between the two instruments), the reflectance formulation of the HySICS output has a lower uncertainty than the radiance formulation.

3.1.2 Dependence on Solar Zenith Angle

In the above equations, the solar spectral irradiance is measured by the instrument on-orbit. The light used in the reflectance ratio must be reduced due to the geometry of the land surface where the reflected signal is being measured. The oblique solar incidence angle is given by the solar zenith angle, θ_{SZA}, and the signal is reduced by $\cos\theta_{SZA}$. With this update, the full reflectance equation becomes:

$$R_{obj}(\lambda) = \frac{S'_{obj,t=t2}(\lambda)}{\mathcal{E}_{Sun,t=t1}(\lambda) \cdot \cos\theta_{SZA}} \cdot \alpha(\lambda) \cdot \pi \cdot \frac{E_{Sun,t=t1}(\lambda)}{E_{Sun,t=t2}(\lambda)} \tag{5}$$

The dependence on the solar zenith angle is applied to the reflectance in [algorithm 6B]. Further equations in this document will assume the solar zenith angle without explicitly including the term to highlight the ratios involved.

3.1.3 HySICS Measurement: Detailed Equations

The following section is meant to elaborate on the high-level overview of section 3.1.1. It begins with the detector equation and radiometry equations for the instrument to show that the fundamental value measured by the HySICS instrument is radiance. It also investigates the on-orbit calibration approach and describes the flat fielding techniques and the solar irradiance measurement and the attenuation factor from a radiometric perspective. Ultimately, it shows how to apply the solar irradiance measurement to the Earth- or lunar-measurement to create the reflectance ratio and a radiance value. The steps detailed in this section are expanded to the expected measurement techniques described in section 5.0. When applicable throughout this section, the uncertainties associated with each step are noted, which informs the full uncertainty description in section 6.0.

3.1.3.1 Detector Equation

The HySICS instrument uses a two-dimensional HgCdTe pixel array. Each pixel has the physical description of a common detector pixel, given by equation 6 [6].

$$S = P_{\#} \cdot QE_i \cdot \eta_{FPA} \cdot \sigma_v \cdot A_{FPA} \cdot A_{FPE} \cdot A_{ADC} \qquad 6$$

Where S is the measured value, chosen to use the same notation as equation 1, and is in the raw camera units, DN (digital number) sometimes known as “counts”. $P_{\#}$ represents the number of photons incident on the pixel. The classic detector quantum efficiency (in electrons/photon) is the combination of the next two terms, $QE_i \cdot \eta_{FPA}$, which represent the interacting photons, and the quantum yield, in photons/photon, and electrons/photon respectively. The next four terms are all measurements of the detector gain, the sensitivity, σ_v, in volts/electron, the FPA and FPE gain terms, $A_{FPA} \cdot A_{FPE}$, both in volts/volt, and the analog-to-digital conversion, A_{ADC}, in DN/volt. The unit equation is:

$$[DN] = [Photons] \cdot \left[\frac{Photons}{Photon}\right] \cdot \left[\frac{e^-}{Photon}\right] \cdot \left[\frac{V}{e^-}\right] \cdot \left[\frac{V}{V}\right] \cdot \left[\frac{V}{V}\right] \cdot \left[\frac{DN}{V}\right] \qquad 7$$

The detector outputs a digital value that is proportional to the number of photons that are incident on it. The proportionality constant, also called the pixel gain, is different for every pixel, depending on microscopic differences in the pixel, which can affect the quantum efficiency, and variations in the electronic chain that amplifies and produces a digital signal. The pixel gain is shown in equation 7:

$$G_n = QE \cdot \eta_{FPA} \cdot \sigma_v \cdot A_{FPA} \cdot A_{FPE} \cdot A_{ADC} \qquad 8$$

And the output value of a single pixel is given by:

$$S_n = G_n \cdot P_\# \tag{9}$$

Several of the most important uncertainty contributions are manifested in the detector equation. The incoming number of photons is inherently a noisy process, since the photons do not arrive at even time intervals. The noise, commonly known as shot noise, becomes an equivalent noise when converted to electrons. It can be inferred either directly from the number of photons, if that quantity is known, but is usually calculated based on the number of electrons, as described in section 6.5.2.2. In addition, all the gain terms add electronic noise, together known as read noise. The read noise is the noise present in a measurement with no incoming photons, at an infinitely short exposure time, to also eliminate the dark current and dark current shot noise (section 6.5.1.2). It can be estimated for each pixel by removing all sources of light and using the shortest exposure possible with a very cold detector to reduce the dark current. The dark current itself is not a noise source, as it does not change from image to image, and can be subtracted via dark image subtraction (section 5.1.3.10), but it adds a second contribution of shot noise, called dark current shot noise. Finally, because the signal is digitized, there is a quantization noise contribution. For a high-resolution detector, this noise source tends to be a small total contribution, and is described in section 6.5.3.

All these noise sources are purely random, independent noise sources. They can always be summed in quadrature to determine the total amount of random noise present on each pixel in an image. In addition to the random noise sources, there are systematic uncertainties that can be present in a detector measurement. These sources include sensor non-linearity, either in the camera integration time, the gain, or electronic digital conversion of the signal (addressed in sections 5.1.3.7, and 6.7.11), dark pedestal shift (described in section 5.1.3.5).

3.1.3.2 Radiometric Equation

Given that the output of the detector is dependent on the number of incident photons, it is necessary to determine the number of photons that travel through the optical system to a single pixel on the detector. This value can be found using equation 10, the radiometric equation for a pixel-based spectrometer.

$$P_\# = L \cdot (A_0 cos\theta) \cdot \Omega_n \cdot \Lambda \cdot \eta \cdot \frac{\lambda}{hc} \cdot t \tag{10}$$

Where $P\#$ is again the number of photons incident on a single pixel, L is the object radiance, A_0 is the input aperture area, θ is the tilt of the input aperture, Ω_n is the pixel solid angle (changed from the previous Ω_{pixel} to indicate that the solid angle is potentially different for every pixel), Λ is the spectral line width, η is the instrument efficiency, $\frac{\lambda}{hc}$ is the inverse of photon energy, and t is the integration time. All of the units for each of these terms are shown in equation 11, written in the same order as the radiometric equation:

$$[Photons] = \left[\frac{W}{m^2 \cdot sr \cdot nm}\right] \cdot [m^2] \cdot [sr] \cdot [nm] \cdot \left[\frac{Photons}{Photon}\right] \cdot \left[\frac{Photon}{W \cdot s}\right] \cdot [s] \tag{11}$$

The object being measured is assumed to have a spectral radiance of L, given in SI units. This object can be the Earth, the Sun, or the Moon for the HySICS instrument. Although the Sun is generally discussed as an irradiance source, each small point on the surface of the solar disk outputs a radiance. The total irradiance is the integral of all the radiance point sources across the disk, and will be discussed in section 3.1.3.4.

The amount of light that enters the instrument is determined by the total area of the input aperture, scaled by the reduction in area due to aperture tilt, $A_0 cos\theta$. For solar observations, the input aperture is 0.5 mm in diameter, and for Earth and lunar views, the input aperture is 20 mm in diameter. If the instrument is pointed directly at a target, the center pixel in the slit will have 0 degrees of tilt in the aperture, while the two edge pixels will have -5 and +5 degrees of aperture tilt respectively.

The pixel solid angle, Ω_n, is a description of how much radiance each pixel sees on the source object. It is approximately 75 x 75 arcsec square, although each pixel projection is convolved by the instrument point spread function. This term is expected to be different, and not perfectly square, for every pixel. It is measured for each pixel over the full operating temperature range, as discussed in [2].

The light that enters into the instrument is reflected off 7 different aluminum mirrors, an aluminum-coated grating, and transmitted through an order sorting filter before being incident on the detector. All of these reflections and transmissions reduce the instrument efficiency, η. This term is a description of the fraction of light that reaches the detector for each pixel. Like the solid angle and the aperture tilt, it is expected to be different for each pixel.

The light that reaches the detector has been spectrally dispersed in the across-slit direction by the grating. Each pixel column only sees the amount of light that is spectrally available at the column location, with a spectral width defined by Λ. From a unit-analysis perspective, this term is used to cancel the "per-nm" present in the input radiance term. It represents an integral due to convolving the pixel spectral width with the instrument line shape (ILS), in a similar way as the pixel solid angle is convolved with the instrument point spread function. Like the previous terms, it can also be different for each pixel, simply due to slight variations in the optical system and grating efficiency for each pixel.

The $\frac{\lambda}{hc}$ term is the number of photons per joule, or the inverse of the energy per photon. It is used to transform the power in the input radiance to number of photons at the detector.

The final term in transforming power to number of photons is the integration time, t, which must be present to define the amount of time that photons are collected by the detector.

It is now possible, through a combination of equations 9 and 10, to describe the pixel response based on the input radiance, integration time, and aperture area, as shown in equations 12.

$$S_n = G_n \cdot \left(\frac{L\lambda}{hc} \cdot t \cdot A_0\right) \cdot \Omega_n \cdot \Lambda_n \cdot \eta_n \cdot cos\theta_n \tag{12}$$

Where the dependent terms, L, t, and A_0, have been grouped for clarity. All the other terms are assumed to be different for every pixel, and have been assigned the subscript n to indicate this variability. In addition, the pixel solid angle and the spectral line width terms could be replaced by their integrals to indicate that they are spatially and spectrally varying terms respectively.

The uncertainties in the radiometric equation are all as expected: uncertainty in the aperture area and tilt, uncertainty in the pixel solid angle, spectral line width, instrument efficiency, center wavelength of each pixel, and integration time. Many of these uncertainty quantities drop out of the analysis because of the common-mode measurement made by the HySICS instrument, or are directly measured as part of the instrument attenuation factor, as will be described in the next several sections.

3.1.3.3 Flat Field Measurement Equations

The expected variation in all the pixels, shown by all the terms with the n subscript in equation 12, will be measured and calibrated out of the science measurements. The on-orbit calibrations used to achieve this measurement is called the flat field, and consists of putting the same amount of light on each pixel within the slit [algorithms 8A - 8B]. This concept implies that a constant source is scanned along the slit. The technique and algorithm are described in section 5.2.2. The idea is that if the same amount of light (radiance) is put on each pixel, then variations in response from pixel to pixel are due to variations in the gain, solid angle, spectral line width, instrument efficiency and input tilt.

The amount of light on each pixel is given by a variation of equation 12:

$$S_n = G_n \cdot \left(\frac{L_0 \lambda}{hc} \cdot t \cdot A_0\right) \cdot \Omega_n \cdot \Lambda_n \cdot \eta_n \cdot cos\theta_n \qquad 13$$

Where the input radiance has been replaced by a constant radiance, L_0. All the terms in parenthesis are expected to be constant for every pixel in the slit during a flat field scan.

The object of the flat field scan is to determine the variations in each pixel response compared to an average pixel response for the whole column of pixels, in each column on the detector. The flat field correction to pixel n is given by equation 14:

$$ff_n = \frac{\overline{S_n}}{S_n} = \frac{\frac{1}{N}\sum_n S_n}{S_n} \qquad 14$$

Where ff_n is the nth pixel correction factor, and the bar notation indicates an average response over all N pixels in a column. This correction factor will be used to scale the measurement value on the pixel in question. If the pixel has a lower response than average, the correction factor is larger than unity. If the pixel has a higher response than average, the correction factor is less than unity. The average flat field correction factor for every column will, by definition, be unity.

The expanded form of the flat field correction factor is given by equation 15:

$$ff_n = \frac{\frac{1}{N}\sum_n \left(G_n \cdot \left(\frac{L_0\lambda}{hc} \cdot t \cdot A_0\right) \cdot \Omega_n \cdot \Lambda_n \cdot \eta_n \cdot cos\theta_n\right)}{G_n \cdot \left(\frac{L_0\lambda}{hc} \cdot t \cdot A_0\right) \cdot \Omega_n \cdot \Lambda_n \cdot \eta_n \cdot cos\theta_n} = \frac{\overline{G_{col}}}{G_n \cdot \Omega_n \cdot \Lambda_n \cdot \eta_n \cdot cos\theta_n} \qquad 15$$

Where $\overline{G_{col}}$ is the average “gain” of a column:

$$\overline{G_{col}} = \frac{1}{N}\sum_n (G_n \cdot \Omega_n \cdot \Lambda_n \cdot \eta_n \cdot cos\theta_n) \qquad 16$$

The units of $\overline{G_{col}}$ are $\left[\frac{DN}{Photon}\right] \cdot sr \cdot nm$. Note that $\overline{G_{col}}$ is a constant for each column of the detector. In addition, note that this term is constant even if the pixel solid angle and spectral line width are replaced by their integrals.

To apply the flat field to a single pixel, equation 17 is used:

$$ff_n \cdot S_n = \frac{\overline{G_{col}} \cdot G_n \cdot \left(\frac{L\lambda}{hc} \cdot t \cdot A_0\right) \cdot \Omega_n \cdot \Lambda_n \cdot \eta_n \cdot cos\theta_n}{G_n \cdot \Omega_n \cdot \Lambda_n \cdot \eta_n \cdot cos\theta_n} = \overline{G_{col}} \cdot \left(\frac{L\lambda}{hc} \cdot t \cdot A_0\right) \qquad 17$$

The unit analysis is shown in equation 18:

$$[DN] = \left[\frac{DN}{Photon} \cdot sr \cdot nm\right] \cdot \left(\left[\frac{W}{m^2 \cdot sr \cdot nm} \cdot \frac{Photons}{W \cdot s}\right] \cdot [s] \cdot [m^2]\right) \qquad 18$$

After combining constants $\overline{G_{col}}$ and $\frac{\lambda}{hc}$ into a single constant, $\overline{G'_{col}}$=$\overline{G_{col}}\frac{\lambda}{hc}$, Equation 17 can be re-written as equation 19:

$$ff_n \cdot S_n = \overline{G'_{col}} \cdot L \cdot A_0 \cdot t \qquad 19$$

This is a convenient notation, since it codifies an output level for each pixel based on an average gain value for the whole column, an input radiance, aperture area, and integration time. As described in section 5.2.2, the instrument is designed to perform two flat field measurements: one for the larger, Earth-viewing aperture, and one for the smaller, solar-viewing aperture. The two flat fields will produce different flat field corrections, depending on the aperture used. They are mathematically identical, although the constants are different for both, as shown in equation 20 and 21:

$$S'_{obj} = ff^{20} \cdot S_{obj} = \overline{G'_{col}} \cdot L_{obj} \cdot A_{20} \cdot t_{20} \qquad 20$$

$$S'_{Sun} = ff^{05} \cdot S_{Sun} = \overline{H'_{col}} \cdot L_{Sun} \cdot A_{05} \cdot t_{05} \qquad 21$$

The two gain terms, $\overline{G'_{col}}$ and $\overline{H'_{col}}$, are for the Earth-viewing aperture and solar viewing aperture respectively, and the following terms indicate the radiance source, the aperture area, and the integration time.

The flat field measurement contains all the uncertainties from the radiometric equation combined in the gain terms, as can be seen in equation 16. There is a hidden uncertainty in the flat field measurement, though, in the L_0 term in equation 15. This is the term that indicates the same radiance is incident on each pixel. If, however, there is not the same radiance, any variation will be mistaken as gain variation in the pixel response. Many of the uncertainties contributors pertaining to the flat field measurement are an attempt to quantify this variation, including pointing errors during the scan, aligning the scan data peaks on each pixel, as described in section 6.7.21, and spectral distortions in the optical system. In addition, all the uncertainties associated with acquiring FPA images are present in the flat field measurement.

3.1.3.4 Solar Spectral Irradiance Measurement Equations

Since both the radiance and reflectance observations are dependent on the incoming solar irradiance, described in equations 2 and 4, it is necessary to also determine the HySICS measurement of solar spectral irradiance [algorithms 7A - 7D]. To obtain the irradiance of an object is obtained by integrating the radiance measurement over all solid angles, shown in equation 22:

$$E_{Sun}(\lambda) = \int_{\Omega_{Sun}} L_{Sun}(\lambda, \Omega)\partial\Omega \tag{22}$$

Where $E_{Sun}(\lambda)$ is the solar spectral irradiance, and Ω_{Sun} is the full solid angle subtended by the solar disk. For a digitized version of the integral, equation 23 is used:

$$E_{Sun,Imager} = \sum_{n}\sum_{i} L_{Sun,n,i} \cdot \Omega_{n,i} \tag{23}$$

Where the $E_{Sun,Imager}$ indicates the irradiance measured by an imaging instrument, shown schematically in Figure 6:

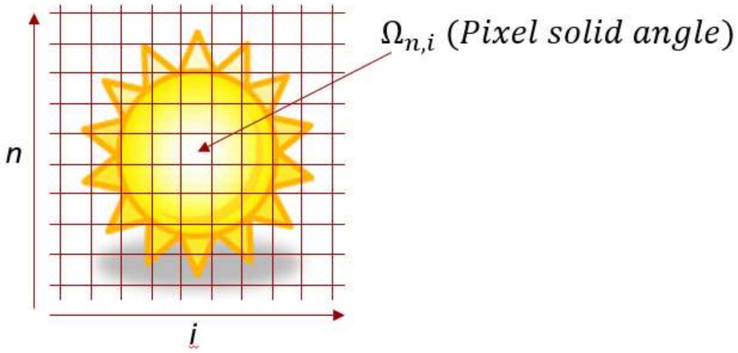

Figure 6. Schematic representation of digitized integral over solid angle of the Sun.

The HySICS imager spatial direction is parallel to the slit, and represented by n, the pixel number within a column. The orthogonal direction, composed of images taken while the slit is scanned across the Sun, is indexed by i, indicating an image number. Each pixel in the image covers a solid angle denoted by $\Omega_{n,i}$.

The HySICS instrument grid spacing is nearly regular in the n direction, but consists of quite a bit of overlap and irregularity in the i direction due to the acquisition cadence and 2-axis pointing system (see section 5.2.1). Instead, the images are acquired as shown in Figure 7:

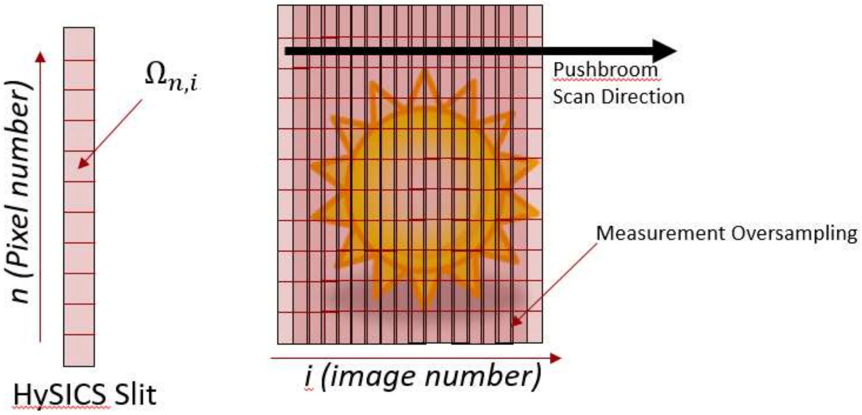

Figure 7. HySICS instrument solar scan with pixel overlap in the across-slit direction due to acquisition cadence and scan rate.

The amount of overlap between neighboring images is given by equation 24:

$$\gamma = \frac{\Omega_{\perp}}{r \cdot T} = \frac{\Omega_{\perp}}{\Omega_M} \qquad 24$$

Where γ is called the overlap, or oversampling, factor, $\Omega_{\perp}$is the across-slit field-of-view for each pixel in radians, r is the scan rate, given in radians per second, T is the acquisition cadence, set to 1/15th of a second for CLARREO HySICS, and Ω_M is the across-slit angular motion of the slit. For the general case of arcing scans the oversampling factor varies for each pixel along the slit, and must be considered separately for each pixel.

For the HySICS instrument, the total digitized integral of the solar irradiance is scaled by this overlap factor, as shown in equation 25:

$$\mathcal{E}_{Sun} = \frac{\mathcal{E}_{Tot}}{\gamma} = \sum_n \sum_i \frac{S'_{Sun,n,i}}{\gamma_n} \cdot \Omega_{n,i} = \sum_n \sum_i S'_{Sun,n,i} \cdot \Omega_{M,n,i} \cdot \Omega_{\parallel,n,i} \qquad 25$$

Where $S'_{Sun,HySICS}$ indicates the HySICS-based pixel measurement of the ideal Sun measurement, S'_{Sun}, and γ_n is the nth pixel overlap factor. In words, if all the pixels from all the images of a solar scan were summed, the total irradiance would be larger than the real irradiance by the overlap factor, and would need to be reduced by that factor.

The pixel solid angle is separated into its perpendicular component in equation 24 to enable a combination with the oversampling factor. The small-angle approximation of the pixel oversampling factor is shown in equation 25:

$$\Omega \approx \Omega_{\perp} \cdot \Omega_{\parallel} \tag{26}$$

Where $\Omega_{\perp}$ and $\Omega_{\parallel}$ are the perpendicular and parallel field-of-views, in radians. For small angles of 75 arcsec, the pixel angular width and height, the error in the approximation is 0.077 ppm, calculated using the exact square solid angle from [16]. This amount of error is ignored in the uncertainty budget.

When combined with the oversampling factor, the pixel solid angle can be written:

$$\Omega \approx \gamma \cdot r \cdot T \cdot \Omega_{\parallel} = \gamma \cdot \Omega_{M} \cdot \Omega_{\parallel} \tag{27}$$

This becomes a convenient representation for the HySICS instrument because it directly ties the measurement to the observation values of the scan rate and acquisition cadence. This is also the final component to describing the full HySICS solar spectral irradiance (SSI), with the steps shown in equations 28 to 31.

$$E_{Sun} = \sum_{n}\sum_{i} L_{Sun,n,i} \cdot \Omega_{n,i} \tag{28}$$

$$E_{Sun} = \sum_{n}\sum_{i} \frac{S'_{Sun,n,i}}{\overline{H'_{col}} \cdot A_{05} \cdot t_{05}} \cdot \Omega_{n,i} \tag{29}$$

$$E_{Sun} = \frac{1}{\overline{H'_{col}} \cdot A_{05} \cdot t_{05}} \cdot \sum_{n}\sum_{i} S'_{Sun,n,i} \cdot \gamma \cdot r_{n} \cdot T \cdot \Omega_{\parallel,n,i} \tag{30}$$

$$E_{Sun} = \frac{1}{\overline{H'_{col}} \cdot A_{05} \cdot t_{05}} \cdot \sum_{n}\sum_{i} S'_{Sun,n,i} \cdot \Omega_{M,n,i} \cdot \Omega_{\parallel,n,i} \tag{31}$$

Where equation 28 begins with the definition shown in equation 23. Equation 29 adds the measured value based on flat-field corrected radiance from equation 21 [algorithm 4B]. Equation 30 converts the solid angle into measurable components from equation 27 [algorithms 7A, 7D] . And equation 31 indicates that the HySICS measurement is being used, from equation 25.

In words, this equation indicates that the solar irradiance is dependent on the gain of each column, the aperture area and the integration time. It also consists of the sum of all pixels in the solar irradiance scan, both in the along-slit direction and for every image in the scan. The measured pixel values are scaled by the scan rate and acquisition cadence and the along-slit component of the pixel solid angle. The scan rate and the along-slit scan angle can vary for every pixel. It should be noted that the average gain of the columns, $\overline{H'_{col}}$, is still an unknown quantity, and this equation does not give an SI-traceable solar spectral irradiance. The precise scan rate per pixel will be very well known, however, from the pointing platform.

The uncertainties present in the solar spectral irradiance measurement are still the same radiometric quantities hidden in the gain term, and the FPA image uncertainties. The newly present uncertainties include errors in the measurement of the scan rate, determined by the fine sun sensor, described in section 6.7.13, the acquisition cadence, which is dependent on a highly stable electronic oscillator, and uncertainty in the along-slit pixel field-of-view, which is measured in the lab, and described in the characterization and calibration plan [2].

3.1.3.5 Attenuation Ratio Measurement Equations

As shown in equation 1, the attenuation ratio is of equal importance as the solar spectral irradiance for both the reflectance and radiance measurements. The attenuation ratio will be measured in the lab over the full operating temperature range, as described in the characterization and calibration plan, [2]. That measurement consists of placing a bright, uniform radiance source with high spectral and temporal stability in front of the instrument and measuring the instrument response with the large aperture and small apertures. With the formalism introduced here, this measurement can be described with the following equations:

$$ff^{05} \cdot S_{05} = \overline{H'_{col}} \cdot L_0 \cdot A_{05} \cdot t_{05} \tag{32}$$

$$ff^{20} \cdot S_{20} = \overline{G'_{col}} \cdot L_0 \cdot A_{20} \cdot t_{20} \tag{33}$$

Where the radiance term is L_0, the laboratory radiance source. The attenuation is a ratio of these two quantities:

$$\alpha = \frac{\overline{H'_{col}} \cdot L_0 \cdot A_{05} \cdot t_{05}}{\overline{G'_{col}} \cdot L_0 \cdot A_{20} \cdot t_{20}} = \frac{\overline{H'_{col}} \cdot A_{05} \cdot t_{05}}{\overline{G'_{col}} \cdot A_{20} \cdot t_{20}} \tag{34}$$

By using the ratio of the two measurements, the intricacies of the average column gain terms are folded into a single measurement. This attenuation factor represents the ratio between the average gain of the columns with the 20 mm aperture and the average gain of the columns with the 0.5 mm aperture. When combined with the two flat field measurements, the attenuation ratio describes how the response of each pixel changes for the two configurations of the HySICS instrument [algorithms 5A – 5B].

The attenuation factor uncertainties include the common contributors from the FPA image uncertainties. The complicated radiometric uncertainties are converted into a single measurable, unitless quantity: the ratio of the instrument response for the two apertures. This indicates that uncertainties in the measurement, such as temporal uncertainty in the light source radiance, L_0, and spatial non-uniformity in the radiance between the large aperture and small aperture measurements must be included.

3.1.3.6 Reflectance Measurement Equations

Starting with the definition of reflectance:

$$R_{obj} = \pi \frac{L_{obj}}{E_{Sun}} \tag{35}$$

This formalism can now describe the HySICS measurement of each part of this equation. The object radiance is generated from equation 20:

$$L_{obj} = \frac{S'_{obj}}{\overline{G'_{col}} \cdot A_{20} \cdot t_{20}} \tag{36}$$

And the solar irradiance is re-written here, although the HySICS measurement subscript is assumed:

$$E_{Sun} = \frac{1}{\overline{H'_{col}} \cdot A_{05} \cdot t_{05}} \cdot \sum_{n} \sum_{i} S'_{Sun,n,i} \cdot r \cdot T \cdot \Omega_{\parallel,n,i} \tag{37}$$

The reflectance is then the ratio of these quantities:

$$R_{obj} = \pi \cdot \frac{S'_{obj}}{\sum_n \sum_i S'_{Sun,n,i} \cdot \Omega_{M,n,i} \cdot \Omega_{\parallel,n,i}} \cdot \frac{\overline{H'_{col}} \cdot A_{05} \cdot t_{05}}{\overline{G'_{col}} \cdot A_{20} \cdot t_{20}} \tag{38}$$

Where the attenuation factor can be directly substituted:

$$R_{obj} = \pi \cdot \frac{S'_{obj}}{\sum_n \sum_i S'_{Sun,n,i} \cdot \Omega_{M,n,i} \cdot \Omega_{\parallel,n,i}} \cdot \alpha \tag{39}$$

This is a per-pixel calculation of the reflectance of an object, either the Sun or Moon, based on the HySICS measurement, S'_{obj} [algorithm 6B]. The appropriate flat field correction has been applied to each measurement: either the object radiance or the solar irradiance. The attenuation factor, α, is dependent on the wavelength, as indicated by the col subscripts in the gain terms. The scan rate and along-slit solid angle are both functions of the pixel location within the slit, and the image cadence, T, is constant for all pixels. Equation 39 is a completely defined equation, with all terms known, and provides the reflectance in SI units of sr^{-1}. It is important to note that the across-slit solid angle component drops out of this equation. The reason it does not need to be included is that the HySICS measurement of the solar irradiance is physically scaled by the across-slit solid angle term.

The uncertainties of each of the components of equation 39 have been addressed in earlier sections.

3.1.3.7 Radiance Measurement Equations

In order to convert reflectance to radiance in SI-units, the known solar irradiance term is must be applied. Rather than deriving the radiance equation, it is easier to use a ratio technique that builds off the definition for reflectance equation 35, and the HySICS-measured quantity in equation 39. This yields the equation 40;

$$\pi \frac{L_{obj}}{E_{Sun}} = \pi \cdot \frac{S'_{obj}}{\sum_n \sum_i S'_{Sun,n,i} \cdot \Omega_{M,n,i} \cdot \Omega_{\parallel,n,i}} \cdot \alpha \tag{40}$$

Where the left-hand side is a ratio of quantities in SI-units, and the right-hand side is the previously derived reflectance, a ratio in native instrument DNs. In this case, E_{Sun} is the same irradiance used in equation 2, and can be taken from another instrument, such as TSIS SIM. Rearranging terms gives the radiance in SI-units, equation 41 [algorithm 6C]:

$$L_{obj} = \frac{S'_{obj}}{\sum_n \sum_i S'_{Sun,n,i} \cdot \Omega_{M,n,i} \cdot \Omega_{\parallel,n,i}} \cdot \alpha \cdot E_{Sun} \qquad 41$$

The methodology for using another instrument's irradiance data is described in section 5.2.1.5. Note that all the terms from equation 1 are now present in this formulation. The unit conversion factor is given by:

$$C = \frac{E_{Sun}}{\mathcal{E}_{Sun}} = \frac{E_{Sun}}{\sum_n \sum_i S'_{Sun,n,i} \cdot \Omega_{M,n,i} \cdot \Omega_{\parallel,n,i}} \qquad 42$$

And the HySICS-measurement of the object, S'_{obj}, and the attenuation factor, α, are in the expected locations. This derivation is for each pixel, n, which each have a known, fixed wavelength, so the wavelength dependence of equation 1 is omitted from this equation.

The uncertainty in the radiance measurement must include the uncertainty in the solar spectral irradiance measurement in SI-units. This is dependent on the uncertainty of another instrument, such as TSIS SIM, and can have a large increase in the overall uncertainty value when compared to the reflectance measurement. This contribution is not addressed in this document but can be found at [5]. In addition, matching uncertainty to ensure that the two solar spectra are directly comparable is necessary.

4.0 Data Products

The data products generated by the HySICS instrument will be stored as described in [19] with the goal of providing enough information for the inter-calibration of other on-orbit instruments [8]. There are three levels of data products to be generated by HySICS. Level 0 contains the unprocessed instrument, telemetry, and ancillary data. Level 1A contains the ground and lunar scan data converted to radiance and reflectance units and associated calibration data products. Level 1B contains the ground and lunar scan data converted to the radiometrically-calibrated data cubes gridded on desired spatial and spectral scales.

4.1 Data Product Terminology

To facilitate discussions of the data products, the terminology laid out here will be used in this document.

4.1.1 FPA Image

An *FPA image* is used to represent the spatial/spectral image generated by the FPA (focal plane array). An example FPA image is shown in Figure 8. In general, if the ambiguous term "image" is used, it will be referencing an FPA image. All data values in an FPA image are in DNs.

The FPA image in the data product will consist of 160 rows of data in the spatial dimension. The detector outputs 480 rows, but every 3 rows are averaged into a single pixel for an FPA image. The spectral dimension consists of 638 columns of data. The detector itself outputs 640 columns of data, but the first two columns of data are dark image information, will not contain any signal from the object or calibration scene.

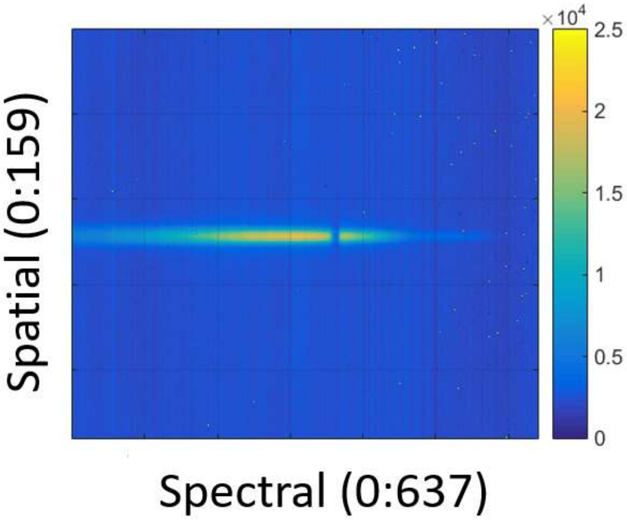

Figure 8. An FPA image.

4.1.2 Composite Image

A *composite image* is used to represent a spatial/spatial (or spatial/temporal) image. This is an image that is generated by taking a slice from multiple images of an across-slit scan (most likely an Earth or lunar scene) and combining them into an image. The image can be a single wavelength, at any available wavelength bin, or an RGB (red, green, blue) image where any wavelength can be used for each of the three colors. An example composite image is shown in Figure 9.

A composite image uses the spatial scale from the FPA image, and so still has 160 pixels in one dimension. The other spatial dimension depends on the number of images used in the composite. For example, if all images in a 2000 image scan are used, there will be 2000 pixels in the second dimension.

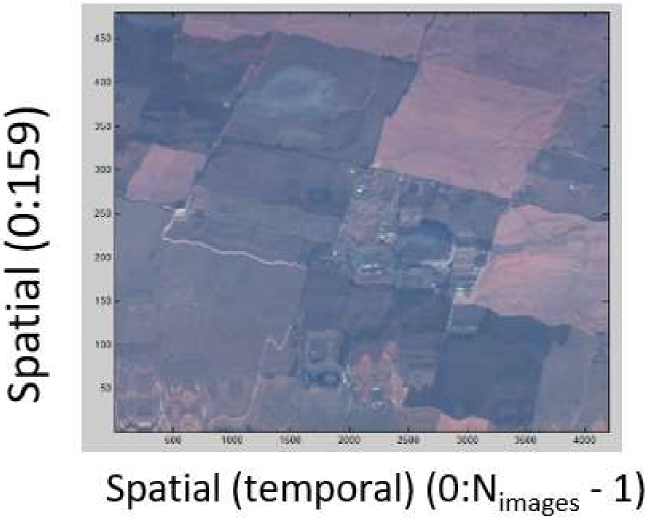

Figure 9. A composite image.

4.1.3 Scan

A *scan* is a sequence of FPA images. The number of images can be as small as 1 to as large as thousands.

4.1.4 Datacube

A *datacube* is a spatial/spatial/spectral data set. It could also be defined as spatial/temporal/spectral data set. In data-space, it represents FPA images that are stacked vertically like slices of bread in a loaf. It also represents composite images that are placed on top of each other. An example datacube is shown in Figure 10. In this representation, the vertical dimension is spectral, with 638 pixels, the narrow dimension is spatial, with 160 pixels, and the wide dimension is spatial (or temporal) with the same number of pixels as images in a scan. The image on the top face of the datacube is an RGB composite image used to visually identify the contents of the datacube, and would not be present in the data set itself.

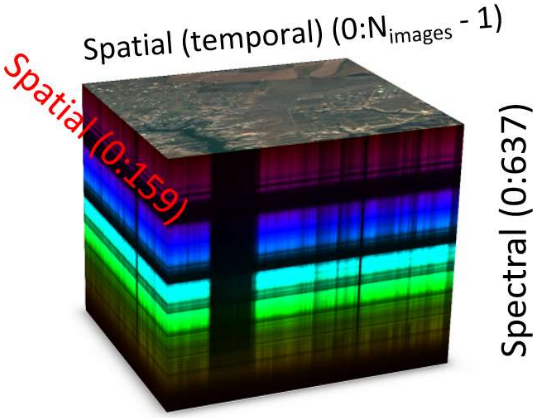

Figure 10. A datacube representation.

4.2 Level 0 Data Product

The level 0 data product is meant to contain all of the science and telemetered data in the most unprocessed form available, the raw images, represented in DN, taken by the sensor, and the telemetry data associated with them. The data transmitted to the ground has already undergone a minor amount of post-processing, however, in order to reduce the data size and enable more efficient data collection. The raw flight data must be compressed using a lossless JPEG compression engine and transmitted to the ground in its compressed form. To achieve adequate compression, the data must also have the constant sensor variation, or FPN (fixed pattern noise), subtracted from the images, and to ensure that the resulting FPN subtracted images do not have any negative values, since all sensor data is represented by a 16-bit positive value, a known offset is added to each image. The flight processing data processing flow chart is shown in Figure 11.

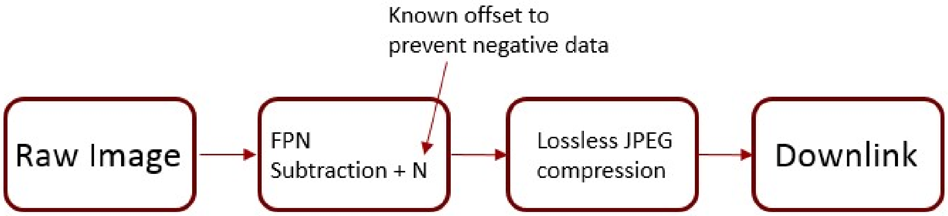

Figure 11. On-orbit processing flow chart for the image data.

Once on the ground, the data will be reconfigured to its original form. It will be uncompressed using the complimentary JPEG uncompression algorithm, the offset will be removed, and FPN will be added back into the images. This series of processing steps is shown in Figure 12. The resulting image data is exactly the same image data that was acquired by the instrument. In addition, the original, compressed images will not be saved to minimize storage capacity.

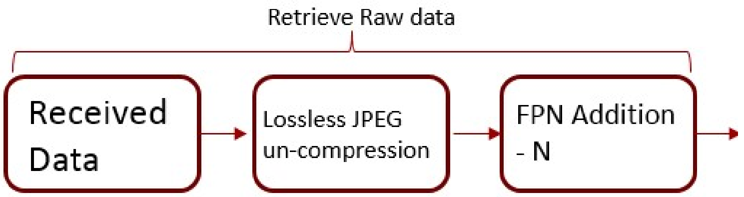

Figure 12. Processing steps to convert image data back to unprocessed values. The resulting images are in the level 0 data format.

The primary level 0 data set contains a series of these individual FPA (focal plane array) images. It will contain all science scans of the Sun, the Moon, and the ground, which will be interspersed with calibration scans of the Sun and the Moon, and internal calibration scans, including the Pen-ray and dark images. Additionally, every image will be time-tagged so that it can be put in sequence with telemetry data and location information from the ISS. The telemetry data will consist of all instrument temperatures, pointing information from the HPS (HySICS pointing system), and pointing and location information from the ISS, and also have associated timing information.

4.3 Level 1A Data Product

The level 1A data product consists of all the ground and lunar scan data converted to calibrated reflectance and radiance units, sr^{-1} and $W/_{(m^2 \cdot sr \cdot nm)}$ respectively. Both these products are available and stored separately. At this level, all the calibration data has been applied to the image data, and is stored in an accessible form as well. The image data consists of sets of all contiguous ground scans, which may be part of a nadir scan, an inter-calibration scan, or a vicarious calibration site, and lunar cross-slit scans. The calibration data will be stored and processed separately. In addition, the corresponding uncertainties, separated into systematic and random, are available for both reflectance and radiance data products. The uncertainties contain a single value for each pixel of every image, representing the fractional uncertainty present in that pixel's measurement data. A schematic representation of the level 1A data product is shown in Figure 13. In this figure, the two dimensional data is shown as a sheet, and one dimensional data is shown as arrows. The sizes of each are intended to show a representation of the amount of data stored for different parts of the data product.

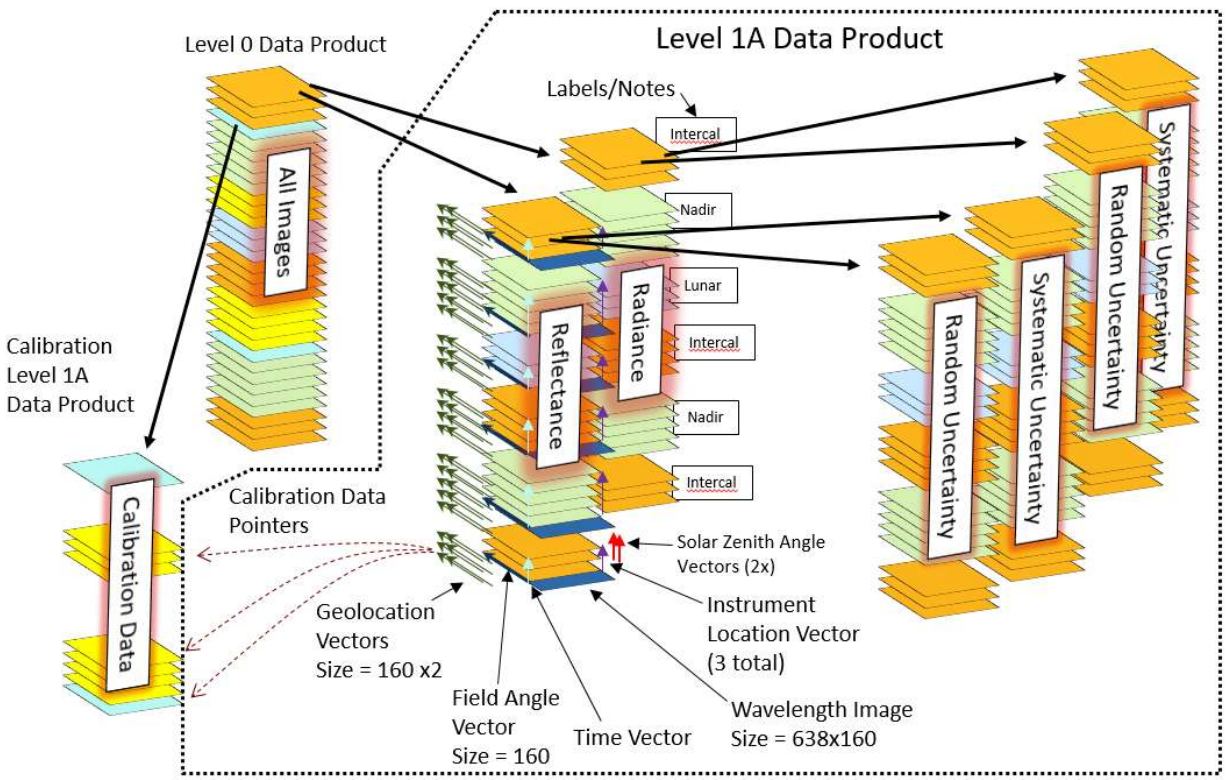

Figure 13. Schematic representation of the level 1A data product

The images in each scan are grouped together in the level 1A data, and labeled with scan type and notes which may include data quality or imaged features. Scan type can include nadir, intercal, or lunar, and may include a “preliminary” tag if they are produced before the data product release date.

All the image data in this product is again time-tagged so it can be sequenced with other events, such as pointing and temperature telemetry. This effectively creates a vector with one element per image of the scan. The time value will likely be in UTC (Coordinated Universal Time).

Each pixel within the slit will be geolocated, producing a pair of geolocation vectors for each image. The vectors will have 160 elements, the same as the number of pixels in an FPA image column. The vectors will contain latitude and longitude coordinates for Earth scenes, and RA (Right Ascension and Declination) for lunar scenes.

In order to compute the geolocation data for each pixel in the level 1B data product, all geolocation data will also need to be computed in the level 1A data product. This information will be available in the level 1A for users to grid data on a different grid spacing than the level 1B data if they desire. There is a small uncertainty associated with gridding the data, and doing it twice (re-gridding after the level 1B data has already been gridded) will likely increase the measurement uncertainty. If the user intends to re-grid the data, it may have slightly lower uncertainty if they start directly from the level 1A data set. The geolocation algorithm is discussed in section 4.4.1.

Two field angle vectors will be provided with each image. The field angle vectors represents the angular position, in inclination and azimuth (TBR), of the center of each pixel in the slit.

Two solar zenith angle vectors will be provided for each scan as well, with one element per image within the scan. They represent the solar direction during the image acquisition.

In addition, three instrument location vectors, using GPS coordinates, will be provided with each scan, again with one element per image. The combination of GPS coordinates, geolocation, and field angles is redundant, since the third value can be found if the other two are known. The three are provided for convenience.

Each scan also contains a wavelength image, a two-dimensional map of the center wavelength of each pixel on the detector, provided in nm. The wavelength scale may shift due to thermal variations while on orbit. This shift will be measured via a Pen-ray measurement (see section 5.2.3). Additionally, optical distortions will cause the wavelength to shift slightly for different pixels within the slit, which will also be apparent in the Pen-ray measurement. The wavelength scale will be measured periodically to monitor the thermal shifts and optical distortion, and determine the wavelength of each pixel in an FPA image.

Lastly, a vector containing the solar spectral irradiance, in SI-units, at the time of the scan, or the closest available one, will be provided. Every reflectance and radiance value must be corrected for any temporal changes that occur in the solar spectrum between the HySICS SSI measurement and the science measurement. This correction relies on knowledge of the SSI at the time of the scan, as indicated in equation 4. The full version of the SSI data is stored with each scan rather than a single pointer to ensure that the relevant SSI data set, which would otherwise not be part of the CLARREO data product, is not lost or changed.

Pointers to the HySICS-measured calibration data sets will be provided to enable re-computation of each scan. These pointers will specify the flat field, dark images, SSI scan, thermal corrections, Pen-ray measurement, and lab data associated with each scan. It is important to note that each of these calibration data sets will also point to the calibrations used with them, creating a dependency tree shown in Figure 14.

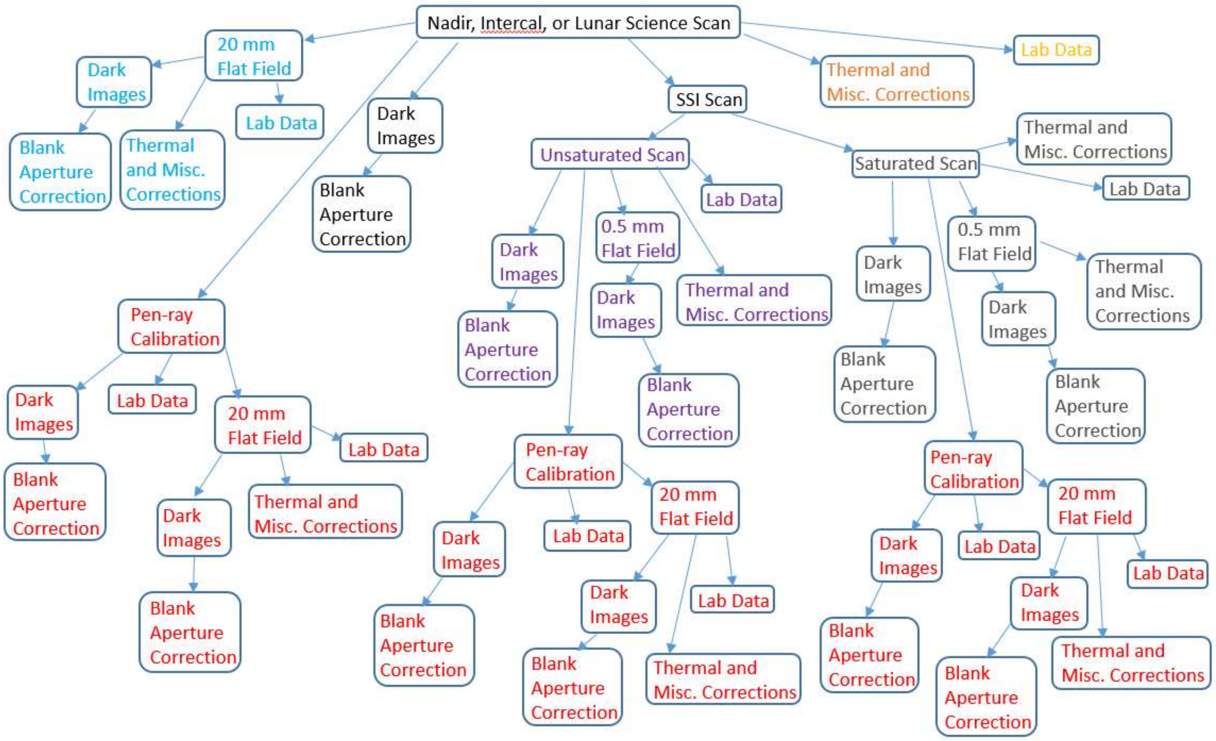

Figure 14. Level 1A data product dependency tree. Primary branches are color-coated to assist in visualization of tree.

Both radiometric products will also have an associated uncertainty for every pixel. The uncertainty value will be given as a fractional uncertainty of the total signal measured by that pixel. It will also be separated into two independent terms: the random and the systematic uncertainty for each pixel, σ_{random} and $\sigma_{systematic}$. The random uncertainty will be reducible through averaging multiple pixels together, and will reduce as the square root of the number of pixels used. The systematic uncertainty will never reduce through averaging. The total uncertainty of a pixel is found by summing the two terms in quadrature: $\sigma_{total} = \sqrt{\sigma_{systematic}^2 + \sigma_{random}^2}$. This total uncertainty is not stored with each image, but left for the data consumer to calculate, and adjust based on the number of averaged pixels, if desired.

4.3.1 Level 1A Data Processing Steps: Science Data

The level 0 data product must undergo multiple steps before conversion to reflectance or radiance values. The data type is either calibration data (solar scans, flat fields, or Pen-ray sets) or science data (ground or lunar scans), and must be processed accordingly, although many of the steps required by both data types are similar. A representative flow chart of the level 1A data processing for science data is shown in Figure 15 (the full version is shown in Figure 1).

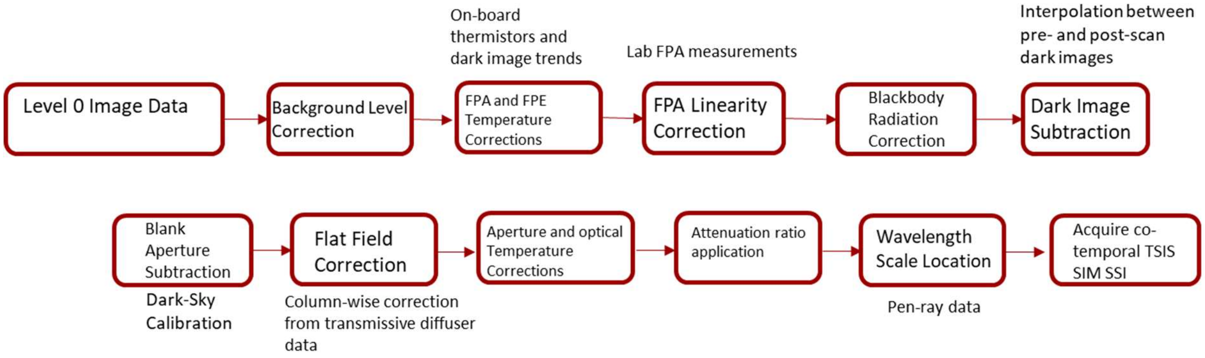

Figure 15. Level 1A abridged science data processing flow chart.

The zero-level of the FPA has been observed to have a slight variation, called the dark-pedestal shift, which occurs in two ways: on each row, and dependent on the total signal within that row, and for the full sensor, and dependent on the total signal on the sensor itself. The full-sensor correction, also called the background level correction (section 5.1.3.5corrects for the change in background level based on total power on the sensor. The correction is an adjustment of the zero DN level which may have a small decrease that is proportional to total detected power. Algorithms 1B, 1D, and 1E all address this shift. In addition, a convenient correction, the true-dark correction [algorithm 1C], is also applied in this step. It represents a subtraction of the fixed pattern noise, the expected signal at an integration time of zero. This subtraction enables many of the following corrections and uncertainty estimations to naturally reduce to zero at a zero signal, instead of an arbitrary offset. Note that the true-dark signal is also present in the dark images, and gets properly re-introduced in the dark subtraction step.

Electronic temperature corrections, including both the FPA and FPE thermal corrections, are due to electronic components that slightly change their response due to temperature changes [algorithms 2A, 2C]. For example, the FPE's temperature sensitive components include the analog to digital converters and amplifiers. The FPA's temperature sensitive components are the line-driver amplifiers on each pixel column output. As a result, the signal offset and gain can vary a small amount due to FPA and FPE thermal variation. This variation is quantified and used to correct the signals during these steps of the processing.

The FPA linearity will be measured on the ground [2], and a correction will be applied to the data if necessary (section 5.1.3.7) [algorithm 2B]. This correction is primarily dependent on the signal level of each pixel on the sensor, and serves to linearize the sensor dynamic range. It will be a pixel-by-pixel correction, but will be applied in the same way for every image in a scan, and likely for every image during the entire mission.

If the temperature of the instrument changes during the course of the scan, however, there is an additional signal contribution due to blackbody radiation (section 5.1.3.9). The baseline level of blackbody radiation is captured by dark images, and removed during the dark image subtraction step, but this cannot account for changes in the blackbody background signal. This signal is studied at different temperatures whenever a dark image is acquired, and the amount of blackbody background will be correlated with instrument temperatures in order to predict its contribution for every image of a scan [algorithm 3A].

Every image will have an associated dark image (section 5.1.3.10), which represents the zero DN reference level with the instrument in the same configuration as for the science data scan. Ideally, when the dark image is subtracted from the image data, a zero DN signal represents no light on a pixel [algorithm 3B].

The blank aperture correction (section 5.1.3.11) to the dark image is a measurement of how much extra light the blank aperture itself is adding to the dark image. The dark images must be corrected for this additional light, which is measured during a dark-space observation [algorithm 3C].

The 20 mm flat field correction (section 5.2.2) is applied at this point. The flat field itself is measured on-orbit, and must be generated prior to this application. The flat field is a measurement of the variation in the pixel gain for each pixel, and is used as a pixel-by-pixel multiplier on the image data. Every image in a data set will use the same flat field correction [algorithm 4A].

The instrument also has additional physical changes due to thermal variations, including the aperture area changing size, and the f/# of the input telescope (the 4MA), changing slightly [algorithm 2D, 2E]. Both the physical area of the input aperture, and the radius of curvature and position of the telescope mirrors, changes based on the CTE of aluminum. Both corrections are full-image corrections on all pixels of the FPA.

The data must be properly scaled by the attenuation ratio in order to compare solar measurements and nadir science measurements. There are two attenuation factors that HySICS uses to be able to observe the Sun: a shorter integration time, and a smaller aperture. Both, or either of these factors can be applied to the reflectance data or to the SSI data. To reduce passing of telemetry between different pipelines, the integration time attenuation is applied to both the reflectance data and the SSI data sets. They are both scaled to the signal expected at an integration time of 1 RT (row time) [algorithm 5A]. This scaling effectively divides the measured signal by its integration time, changing it to a measurement of total flux. The aperture ratio is only applied to the SSI scan, effectively changing it to the signal that would have been measured had the large aperture been used.

Although not a correction, it is important to determine the wavelength scale of each image based on Pen-ray data (section 5.2.3). The wavelength scale is expected to make small movements due to thermal variations during the flight. Both the reflectance and radiance are dependent on wavelength, and require an accurate wavelength scale to be converted from DN to SI units [algorithm 10A].

It is also important to collect the co-temporal TSIS SIM SSI data set while the pipeline is being processed [algorithm 6A]. This data is necessary to calculate the temporal variation described in equation 5.1.3.16.

4.3.1.1 Conversion to Reflectance Data Product

After the steps outlined in section 4.3.1 are completed, the data must be converted to the final data product output, the reflectance and the radiance [algorithm 6A, 6B]. The reflectance data product flow is shown in Figure 16.

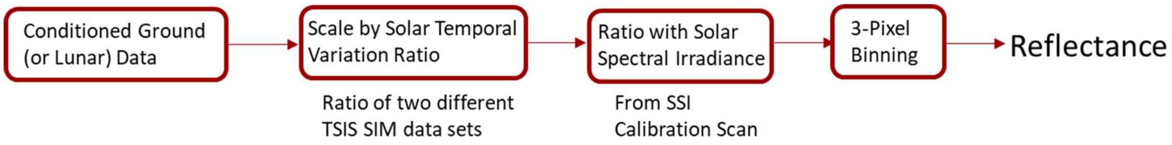

Figure 16. The reflectance data product flow.

The input to this stage is assumed to already have been conditioned via the steps outlined in Figure 15. At this point, the steps indicated in equations 4 and 39 are followed. The attenuation ratio was already applied to the data in the form of the integration time scaling to a unit value. The aperture ratio is applied to the SSI data set. Both of these quantities are measured in the laboratory before launch [2]. The application of the attenuation factor allows the solar measurement data to be directly compared to the science object measurement data. The solar temporal ratio scales the reflectance data by the ratio of the TSIS SIM SSI taken simultaneously with the reflectance data and the TSIS SIM SSI taken simultaneously with the HySICS SSI scan [algorithm 6A].

The ratio with solar irradiance occurs next [algorithm 6B], and must be scaled by the solid angle, which occurs implicitly in the SSI data product. As described in equation 39, the solid angle scaling reduces to the along-slit field-of-view for each pixel, the acquisition cadence, and the scan rate, or per image motion of the instrument [algorithms 7A, 7C]. The result is scaled by the temporal solar variation, to account for solar spectral changes between the time when the SSI was measured and the time of the science object measurement (equation 4).

Binning (averaging) every three pixels in the spatial direction (section 5.1.3.19) occurs after the final calculation of reflectivity. This step changes the image size from a 480x640 pixel image to a 160x640 pixel image. The binned spatial pixels will be close to the desired 500 m width from the ISS when pointing nadir. One of the primary benefits of this step is the data volume reduction, but it also helps reduce the some of the random image uncertainties by a bit [algorithm 1F].

4.3.1.2 Conversion to Radiance Data Product

The radiance data product flow is shown in Figure 17, based on equation 41.

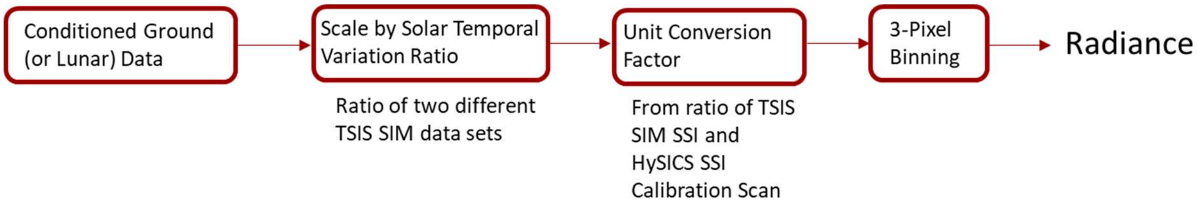

Figure 17. The radiance data production flow.

It also assumes that the input data has been conditioned as described in Figure 15, and contains the same steps as the reflectance data product, including the application of the attenuation ratio in the form of the integration time, which occurs in the previous Level-1A flowchart, and aperture ratios, which occurs in the SSI data product. The ratio of the TSIS SIM solar spectral irradiance with the HySICS solar spectral irradiance, again with the solid angle applied, determines the unit conversion factor from equation 42. The unit conversion factor is a calibration of the instrument, and represents a conversion from the native DNs to irradiance units. As such, the solar spectral irradiance variation between SSI and science object measurements is not needed for the radiance data product, unlike for the reflectance data product.

4.3.2 Level 1A Data Processing Steps: Calibration Data

The calibration data required to convert the ground and lunar scans into reflectance and radiance values will also be available in the level 1A data product. This calibration data consists of solar irradiance scans (section 5.2.1), both types of flat field scans (sections 5.2.2.4 and 5.2.2.6), dark field measurements (section 5.1.3.11), and Pen-ray acquisitions (section 5.2.3). There will also be some infrequent calibration or verification activities that may fall into this category, including linearity measurements (section 5.3.3), aperture ratio measurements (section 5.3.4), lunar or solar limb scans (section 5.3.1), and degradation measurements (section 5.3.2).

The SSI scans require all of the same steps as the nominal science data, and also include the integration steps detailed in section 5.2.1.1. In addition, the aperture ratio attenuation factor is applied to the SSI data [algorithm 5B], which transforms the SSI data to what it would be if it had been taken with the large aperture. The integration time is similarly scaled to a value of one [algorithm 5A]. The flat field scans follow the same steps up to the application of the flat field, where they deviate and the data is used to generate the flat field correction. Similarly, the Pen-ray measurements contain all of the corrections, including the flat field correction, but not the application of the attenuation factors. The dark sky calibration sets do not include the flat field application, since it is a correction used on images that have light. In addition, the SSI and flat field scans can be generated using two sets of acquisitions: a nominal unsaturated scan of the Sun, and a saturated scan of the Sun, where spectral regions that did not contain as much power are stronger. These flat fields are merged, creating a single, completely unsaturated scan that has higher signal strength across the full spectrum (section 5.2.1.4).

4.3.2.1 Dark Image Calibration Data Product

Dark image subtraction is an important component to all science data processing and calibration data processing (section 5.1.3.10). All dark images will undergo the same processing steps, and incur the same types of uncertainty contributions as the science acquisition images. 250 dark images will be acquired both pre-and post- scan for every scan run by the instrument. By obtaining this number of dark images, the independent noise sources, including read noise, thermal shot noise, dark current shot noise, and quantization noise can all be reduced through averaging. In order to apply the dark image subtraction to a data set, the dark image will be interpolated temporally over the full acquisition time. Ideally, there are no trends to the dark image, which would mean that the dark image associated with every FPA image is identical, and equivalent to the average of all 500 dark images acquired. If there is a trend, the dark image interpolation will estimate the true dark image value for each image within a data set, but still contain some amount of averaging depending on the fit function.

In addition to the 500 dark images, every image will also contain two rows of dark data, which have purposefully been blacked out to observe dark trends during the scan acquisition period.

The correction that uses these two rows is called the two-row correction [algorithm 1B], see section 5.1.3.2. Most electronic trends or noise will be present on these rows, and provide a way to make a correction for electronic variations. In particular, the sensor, being on an independent clock, can have a timing jitter associated with the start acquisition signal arrival time. The dark row value addresses this source of noise.

The schematic of the dark images is shown in Figure 18. The level 0 data product, represented by the stack of images on the left, contains all the measurement scans, color-coded to represent different types of scans. For every one of these scans, there are 500 dark images, represented by the gray images before and after the expanded scan (green). The dark rows are represented by the two black lines on the side of each image in the scan. The center cartoon indicates that the dark images are interpolated through the scan set temporally, generating a dark image associated with every FPA image of the scan.

Also shown in Figure 18 is a blank aperture correction data set (section 5.1.3.11). The blank aperture correction is a small correction to each dark image based on the temperature of the blank aperture and measured amount of light that the blank aperture adds to the instrument. The creation of the blank aperture image occurs in algorithm 9A, and the steps are described in section 5.1.3.11. The blank aperture correction will be a single image, possibly scaled based on temperature trends and flight data from the dark sky (also known as dark field, cold sky or blank aperture) scan that is subtracted from each dark image.

The level 1A data set for the dark image calibration associated with each scan will contain the interpolation equations for each pixel and the timing of each image of the scan. It will also contain a pointer to the dark sky scan used for the blank aperture correction. There will be enough data to reconstruct the dark images used for each data set at each FPA acquisition.

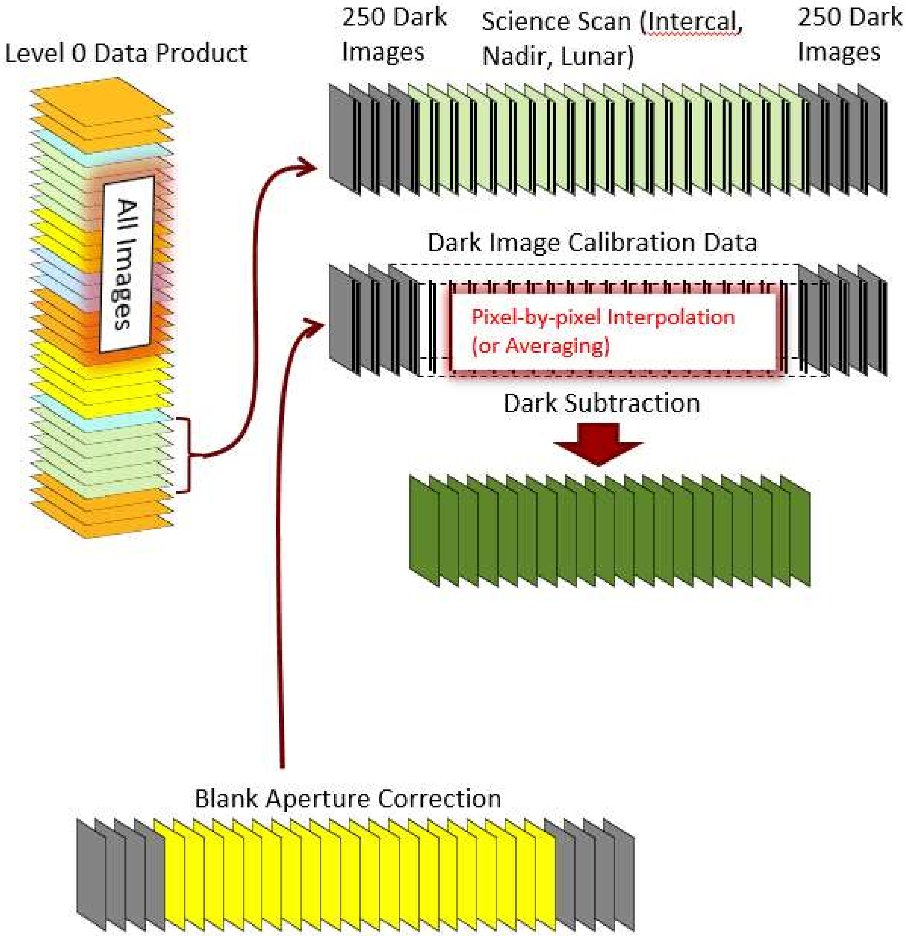

Figure 18. Dark image subtraction calibration data product.

4.3.2.2 Flat Field Scan Calibration Data Product

The flat field scans consist of images that show the response of each row of pixels to the same radiance input, described in section 5.2.2.3. The goal of the data processing it to determine the response, or gain, of each pixel compared to the average response of all pixels within its column. The complete flat field processing steps are shown in Figure 3. There are two types of flat field scans, the 0.5 mm aperture flat field, and the 20 mm flat field. For the 20 mm flat field, there is an additional step of applying a correction for the transmissive diffuser BTDF (section 5.2.2.2). The BTDF is measured in the lab and is represented by a single correction value for each pixel row of a raw FPA image, before the 3-pixel binning. It will contain 480 values that will be used to directly scale the amount of light on each pixel row.

The result of each flat field scan is a single image that represents the flat field scaling for each pixel in an image. It will have 480 x 638 values, and each pixel in an FPA image will be multiplied by the corresponding flat field correction value [algorithm 8A, 8B]. The flat field map will be stored in the level 1A calibration data set. The flat field data products will also have calibration data sets associated with them, including dark images and their associated blank aperture correction, thermal corrections, and will use lab data, such as the FPA non-linearity correction, and the corrections for the aperture and FPE.

4.3.2.3 Pen-ray Measurement Calibration Data Product

The Pen-ray calibration (section 5.2.3) is the primary method for determining the HySICS dispersion. It uses the known atomic spectrum from a Pen-ray lamp and compares it to the measured spectrum from the scan. The scan will consist of 500 dark images, and 1 minute of Pen-ray images. The Pen-ray images will be dark image corrected and corrected for blackbody radiation trends, but do not need to go through many of the other corrections since a precision power level is not required for the Pen-ray analysis.

The atomic spectrum of the Pen-ray slowly changes from argon lines, when it is cold, to mercury lines, when it is hot, and it transitions over the course of approximately 45 seconds. The required lines come from both species, which means that images will be used from different acquisition times during the measurement. Several images will be averaged together for each portion of the acquisition used.

Ideally, the wavelength of each column is equal, but in a real optical system, there is usually a small amount of distortion that changes the wavelength scale on different rows. As a result, a wavelength map is necessary to determine the wavelength at each pixel. This map will be a 160 x 638 pixel image, and will be stored with each of the level 1A science data scans [algorithm 10A]. While many scans may use the same Pen-ray dispersion map, it is integral to every science image that HySICS acquires, making the storage redundancy worthwhile. It must be used by every consumer of the HySICS data, while all the other calibration data sets do not need to be used unless one is re-calculating or confirming the radiance or reflectance data.

4.3.2.4 Solar Spectral Irradiance Scan Calibration Data Product

The solar spectral irradiance (section 5.2.1) is a fundamental part of both the reflectance and radiance data products (equations 39 and 41). Its data processing is very similar to the science data processing steps, and is shown in Figure 19. One difference, however, is the combination of a saturated and unsaturated scan (sections 5.2.1.4) into a single scan. The combination occurs on a per-column basis. For example, from one scan columns 3 through 200 may be used, and from the other scan, columns 201 through 638 may be used. The partial images will be stitched into a single image with 638 columns. (The actual columns will be determined by observing their saturated content, and choosing the scan that has the highest signal level without saturation.) There will be a different integration time ratio depending on which part of the combined image is being used. The equations 39 and 41 are for each pixel on the detector considered separately, so the spectral variation in integration time does not affect the resulting data product.

The schematic for the calibration data product is shown in Figure 20. There are three integration steps added compared to the reflectance data pipeline: the integration scaling factors [algorithm 7A, 7D], the column-wise integration [algorithm 7B], and the across-image integration [algorithm 7C]. The integration is split into two steps to make the uncertainty calculation through integration process easier. Both unsaturated and saturated corrected scans will be stored in the level 1A calibration data product for future reference. The integrated, HySICS-measured solar spectral irradiance will also be stored, along with the corresponding TSIS SIM solar spectral irradiance. For the reflectance science data product, the HySICS SSI will be used as the reflectance denominator, and the TSIS SIM SSI will be used for temporal corrections to SSI, and for the radiance data product, the HySICS SSI and the TSIS SIM SSI will both be used for the unit conversion factor ratio.

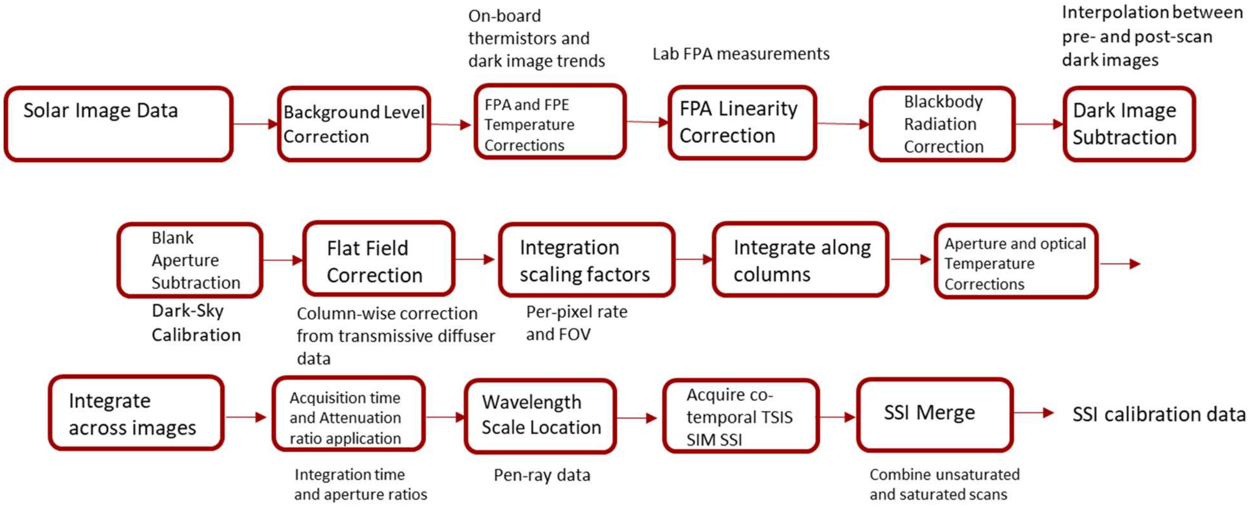

Figure 19. Flow chart for HySICS SSI calibration data.

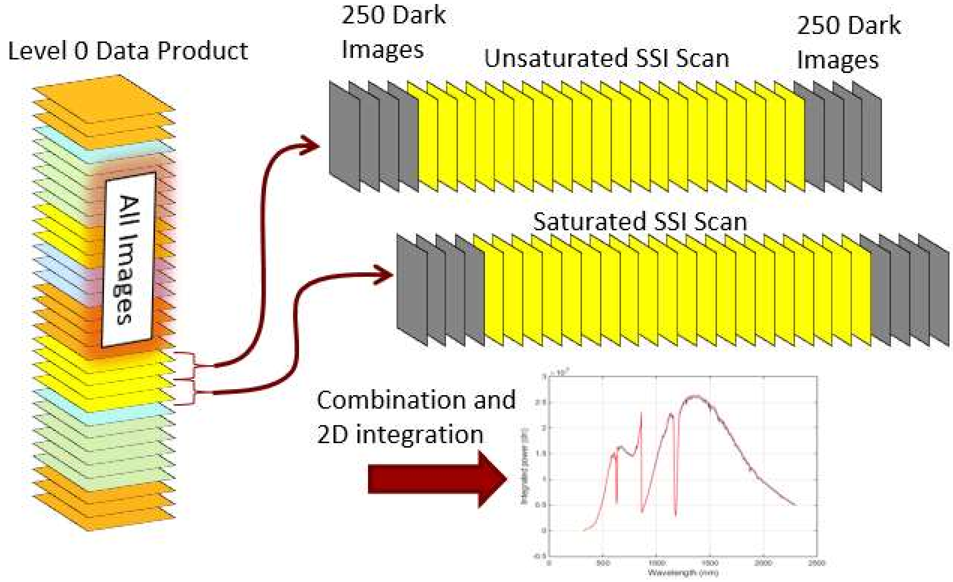

Figure 20. SSI calibration data product schematic.

4.4 Level 1B Data Product

The level 1B data product contains the radiometrically calibrated data cubes for ground and lunar scans on known spatial and spectral scales. The primary differences between level 1A and level 1B are that the data is now gridded to the desired spatial and spectral scales, the ground scene data is still associated with geolocation information (section 4.4.1). Only the nadir scans will be transformed into level 1B data. The inter-calibration and lunar scans will only exist in the level 1A data. The axes of the data cubes will have a regular spacing, in latitude and longitude (or RA and dec) on the two spatial axes, and in nm on the spectral axis. To achieve the regular spacing, the data will be interpolated in both in the spatial and spectral dimensions. This requirement implies interpolation both in the acquisition time and in the pointing direction of every pixel. The interpolation will add a small additional amount of uncertainty to each pixel on top of the level 1A uncertainties. The added uncertainty is likely dependent on a statistical analysis of the data set, to be addressed in future versions of this document. A representation of the level 1B data product is shown in Figure 21.

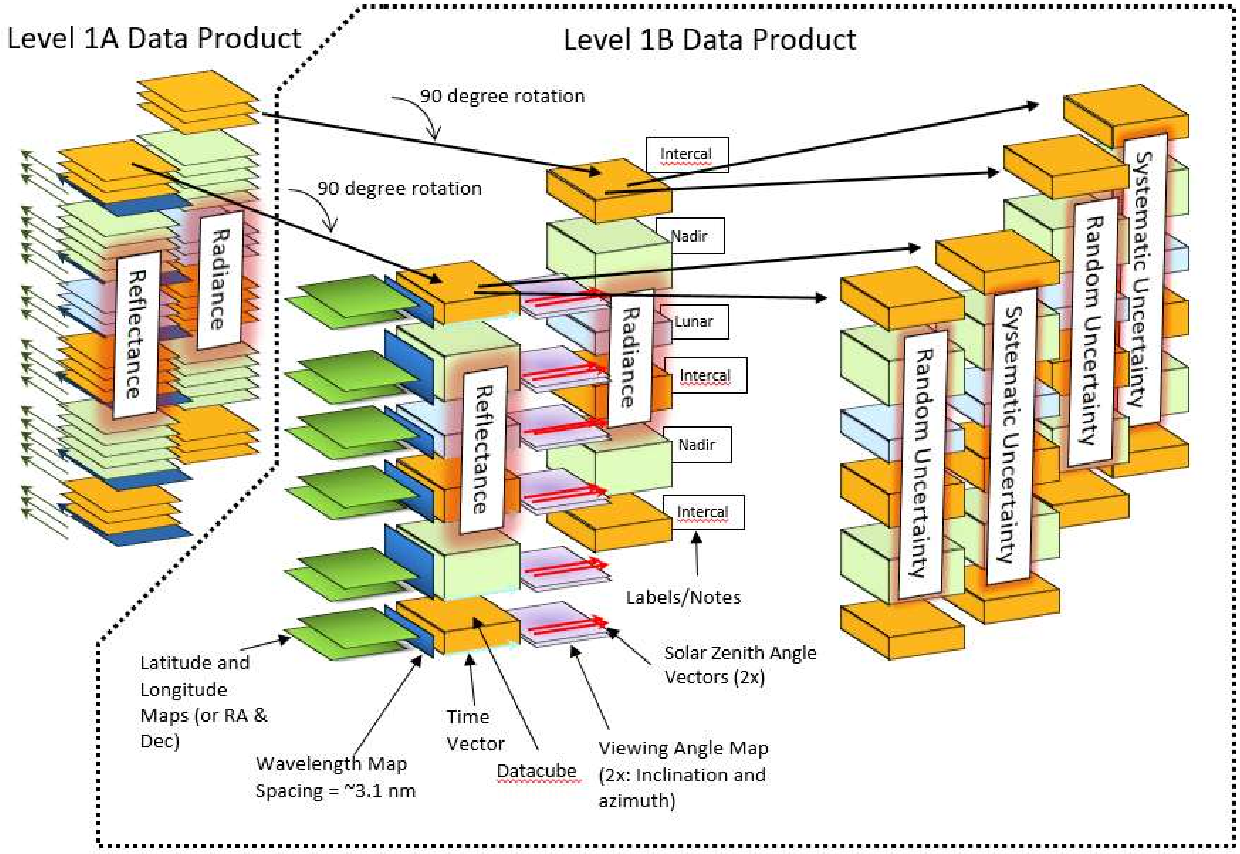

Figure 21. Level 1B data product schematic representation.

There are many similarities to the level 1A data product, such as including both reflectivity and radiance data cubes, and per-pixel random and systematic uncertainties for each. Again, it will be the data consumer's responsibility to combine the uncertainties into a total uncertainty depending on the number of pixels averaged.

The level 1B data cube now has spatial images along the horizontal axes, and the spectral information along the vertical axis, like a stack of pictures all taken at a different wavelength, similar to the data cube shown in section 4.1.4. This orientation means that the data has been rotated 90 degrees from that shown in level 1A, where the horizontal axes are spatial and spectral, the same as an FPA image. The two horizontal axes represent latitude and longitude (or RA and dec for lunar data cubes) and have a grid spacing of 500 m. The vertical axis is the same for all level 1B data cubes, and contains 638 wavelength values, in nm and spaced by approximately 3.1 nm from around 350 nm to around 2300 nm. The ideal spectral grid will be determined after instrument alignment. Because the spectrum is expected to shift over the course of the mission, the two dimensional map of the pixel center wavelengths will be interpolated along each row to the ideal spectral grid. An example of the flight geometry, the spatial gridding, and a data cube representation is shown in Figure 22.

The acquisition time of each pixel will be available as a map with the same number of pixels as a spatial slice of the data cube. The acquisition time will pertain to each pixel, and will be interpolated to match the spatial gridding. As in the level 1A case, the times will be given in UTC. An example of the acquisition time map is shown in Figure 22, where the color scale represents a time. All portions of the map with the same color were acquired simultaneously.

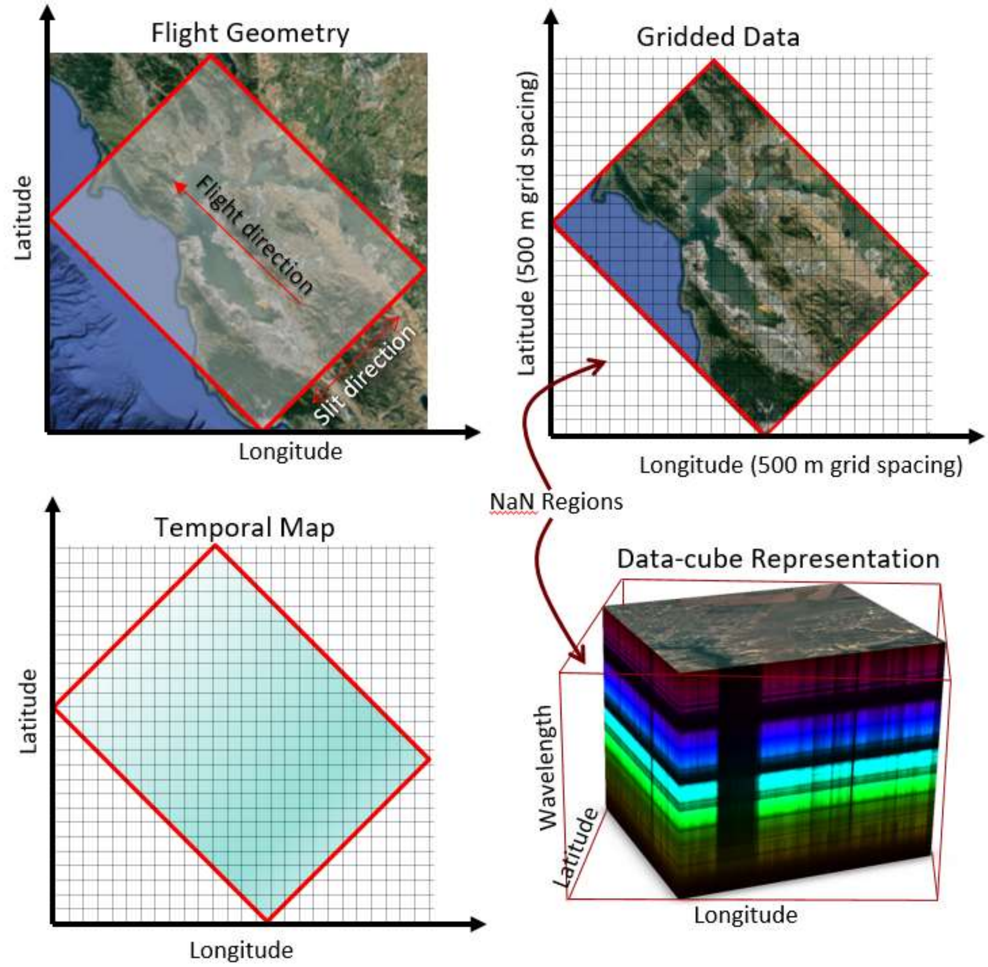

Figure 22. Level 1B spatial gridding representation. The upper left plot shows the flight geometry, with the slit perpendicular to the scan direction. The upper right plot shows the gridding onto latitude and longitude

coordinates. The lower left plot shows the temporal map, where all pixels within the slit at any single instant have the same acquisition time. The lower right image shows the resulting data cube, with rectilinear coordinates in the spatial directions.

As seen in Figure 22, the composite scan image will usually not lie on rectilinear coordinates, and there will be gaps in the data set if it is placed on a normal coordinate system. Although the composite scan image is represented by a rectangle in this example, it is likely to not be rectangular as well, especially when the instrument is slewing during an intercal scan. The data gaps will likely need to be filled with something that indicates there is no data present, such as a -9999 (invalid number).

The interpolated viewing angle of each pixel is also provided as two maps: an azimuth map and an inclination map. These maps are the same size as the acquisition time map, determined by the spatial slice of the data cube.

As in the level 1A case, there will be metadata to aid in searching, which will include the scene type (ground scan, lunar scan, vicarious calibration site, or inter-calibration observation), notes on data quality and look directions. Unlike the level 1A data product, there will be no calibration data sets stored in the level 1B product.

4.4.1 Geolocation Algorithm

Geolocation from the ISS is a problem that has been addressed in previous papers [4]. For a more complete description of the algorithm, see Agile #181253 [21]. For CPRSP, the geolocated position on the WGS84 ellipsoid of each HySICS pixel will be calculated as described in the algorithm below:

1. Calculate HySICS boresight vector in CTRS (WGS84) coordinate frame
    a. HySICS boresight vector in the instrument frame is: [0 0 1]
        i. Note that the camera function will map all of the pixels as individual vectors based on their angle about the X-axis in the instrument frame, so the same geolocation algorithm can be applied to each individual camera pixel vector as will be shown for the primary boresight vector of [0 0 1].
    b. Boresight vector can be expressed in the CPRS baseplate frame through a series of transformations that are dictated by static misalignments and the gimbal angles.
        i. The static misalignments will be measured several times during the I&T phase of the program.
        ii. The gimbal angles will be reported in telemetry.
    c. Boresight vector can be expressed in the ECI (J2000) frame by application of the baseplate to ECI coordinate transformation that is reported by the star tracker
    d. Boresight vector can be expressed in the CTRS (WGS84) coordinate frame by application of the ECI to CTRS coordinate transformation that is provided in the BAD packet: [CDT_PS_PDCTRSAttQ0 CDT_PS_PDCTRSAttQ1 CDT_PS_PDCTRSAttQ2 CDT_PS_PDCTRSAttQ3]

2. Calculate CPRS position in CTRS (WGS84) coordinate frame
    a. CPRS nominal position in ISS body frame is known as: [10.8" -999.9" 267.6"]
    b. CPRS position can be expressed in the CTRS frame by application of two coordinate transformations:
        i. ISS body to ECI (J2000) transform; provided in BAD packet: [CDT_PS_PDInertAttQ0 CDT_PS_PDInertAttQ1 CDT_PS_PDInertAttQ2 CDT_PS_PDInertAttQ3]
        ii. ECI (J2000) to CTRS (WGS84) transform; provided in BAD packet: [CDT_PS_PDCTRSAttQ0 CDT_PS_PDCTRSAttQ1 CDT_PS_PDCTRSAttQ2 CDT_PS_PDCTRSAttQ3]
    c. Absolute position of CPRS in CTRS frame can be obtained by adding it to the ISS position in CTRS frame; provided in BAD packet: [CDT_PS_PDCTRSPosX CDT_PS_PDCTRSPosY CDT_PS_PDCTRSPosZ]
3. Calculate intersection of HySICS boresight vector with WGS84 ellipsoid
    a. Given the CPRS position and unit vector in the CTRS frame, the intersection (XYZ position) with the WGS84 ellipsoid is easily calculated as the closed-form solution to a quadratic equation.
4. Calculate lat/lon based on XYZ position, which is a closed-form solution when altitude = 0.

This algorithm follows the flow chart shown in Figure 23.

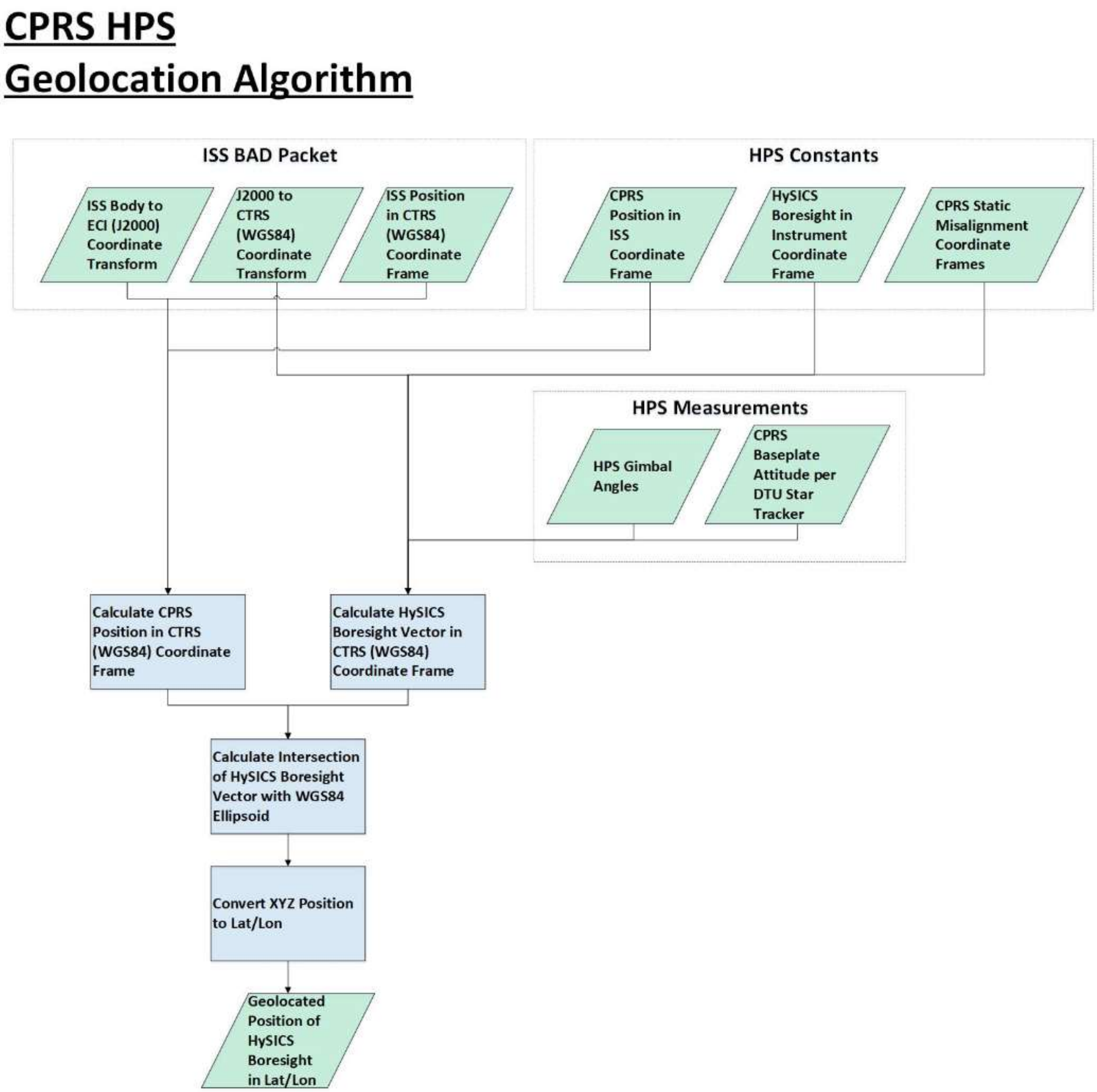

Figure 23. CLARREO Pathfinder geolocation algorithm flow chart.

5.0 On-orbit Reflectance and Radiance Acquisition and Processing

The fundamental measurement that the HySICS instrument makes is a radiance per pixel, in un-calibrated units of DN, and across the full 350 – 2300 nm spectral range. As described in the instrument equations of section 3.1.1.2, it is necessary to either ratio the radiance measurement with a comparable spectral irradiance measurement of the Sun, in order to compute reflectance of each pixel, or scale the measured, un-calibrated values by an instrument calibration, called the unit conversion factor, to compute an SI-traceable radiance.

This section is meant to describe the possible on-orbit measurements, and give more thorough descriptions of the algorithms used to convert the raw data into reflectance and radiance. It also describes the on-orbit calibration measurements that are used in the reflectance and radiance calculations. The section will still refer back to Figure 1 – Figure 5, to provide the reader with a sense of where in each pipeline the algorithms are used.

5.1 On-orbit Science Measurement Description

The primary goal of the CPRS instrument is to make hyperspectral measurements of the Earth surface. These measurements will be used for benchmarking data, inter-calibrations with other on-orbit instruments, and calibrations of vicarious sites, including desert scenes and water scenes. A secondary goal is to measure the lunar irradiance. Many on-orbit instruments are capable of viewing the Moon, and may be able to cross-calibrate off the lunar surface. This measurement is similar to the solar irradiance scan, but uses the large aperture and the longest exposure time.

5.1.1 Earth Scenes

The nominal Earth scene collection scenario is to merely point the instrument at nadir and begin taking data with the 20 mm aperture in place, at the maximum exposure time. Two representative, un-calibrated ground images of a desert scene and a cloud scene from the HySICS balloon flight are shown in Figure 24. The SI-traceable, calibrated irradiance of the cloud scene is shown in Figure 25, with all the calibrations discussed in previous sections and following the irradiance measurement equation from section 3.1.1. Note that while irradiance is shown (because it was available at the time of writing) this image would normally be converted to reflectance or radiance. The ideal field-of-view for the instrument is 10 degrees, although it was measured at 10.147 degrees for the HySICS-balloon instrument. It will be similar for the CPRSP instrument. The per-pixel angular size is therefore 0.021 degrees, or 76.1 arcsec. The along-slit angular size of each pixel will be carefully measured in the laboratory, as per [2].

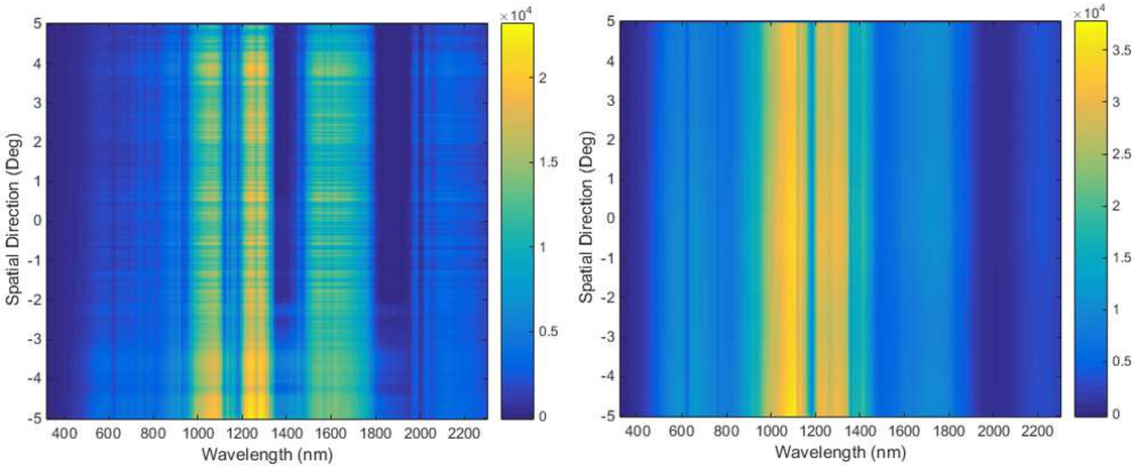

Figure 24. Uncalibrated ground scenes from the HySICS balloon flight. The image on the left is of a desert scene with a few clouds near the bottom of the field of view, and the image on the right is of a thick ice cloud scene. The color scale is in DN.

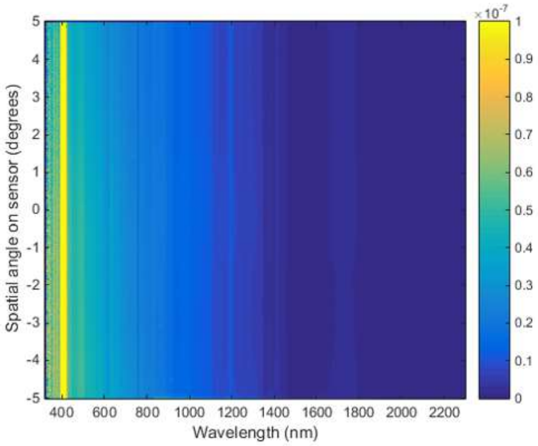

Figure 25. Calibrated ice cloud scene irradiance from HySICS balloon flight. The color scale is in W/(m^2 x nm).

5.1.1.1 Earth Scene Data-Cubes

As the instrument takes nadir data at 15 Hz, assuming that the ISS direction of travel is perpendicular to the slit, the images can be used to assemble a radiance or reflectance data-cube, which will be the final result of the level 1B data product (section 4.4). The data-cubes are made by stacking all the images figuratively together like slices of bread in a loaf. A representative data-cube is shown in Figure 26. There are two spatial axes in the cube, the two horizontal axes in the figure, and one spectral axis, the vertical axis in the figure. Every vertical slice in the data-cube represents an image of the ground scene that was over-flown at a different wavelength. The UV slice is at the top of the data-cube in the figure, although it could be on either side. The image on the top is a RGB image assembled from three compiled images at approximately 570, 540, and 440 nm. The data-cube is made from 4200 images. The left-side horizontal axis is 480 pixels (will be 160 pixels for CPRSP), the vertical axis is 640 pixels, and the second horizontal axis is 4200 pixels.

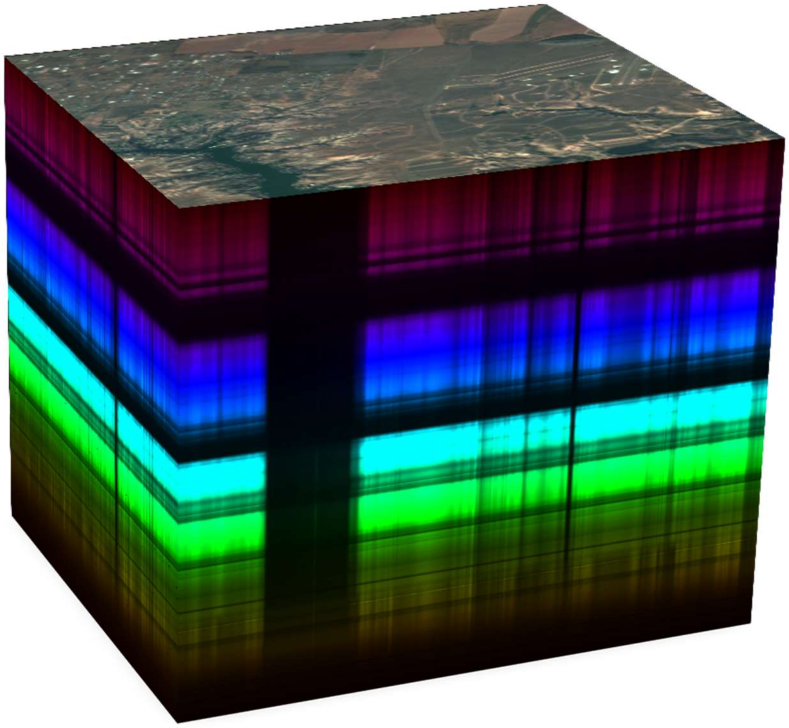

Figure 26. HySICS-balloon flight data-cube assembled from 4200 images. Top face is an RGB image taken from red, green, and blue slices.

5.1.1.2 CPRS Throughput Calculations

The total system efficiency of the CPRS instrument is determined using the reflectivity of the aluminum mirrors, incorporating the seven bounces in the optical path and the incident and reflection angles of each, and the simulated grating efficiency, provided by Zeiss. The resulting system efficiency is shown in Figure 27.

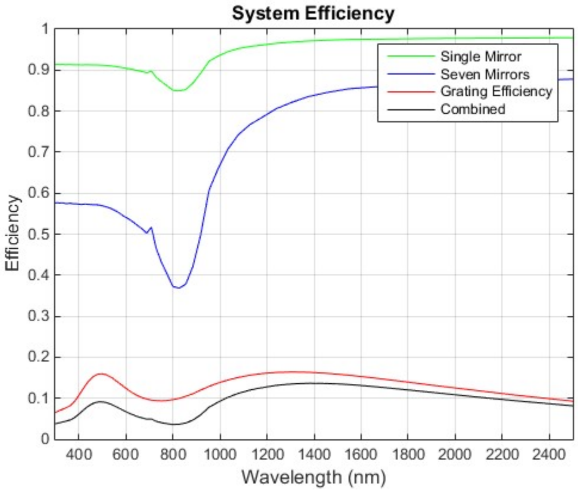

Figure 27. Full CPRS system efficiency. This plot shows the efficiency for a single aluminum mirror, seven aluminum mirrors with the expected reflection angles, the grating, and the total efficiency.

Given the simulated radiance levels shown in Figure 28, and the full system efficiency, it is possible to estimate the radiance and signal at the FPA, as shown in Figure 29 and Figure 30. At the highest integration time, and with the 20 mm aperture, the highest signal level, in photoelectrons, is expected to be just below the full well of the FPA pixels. This operating point is convenient because it provides the highest signal, and therefore best signal-to-noise ratio, but still allows for a reduced integration time it is found that the signals start to saturate.

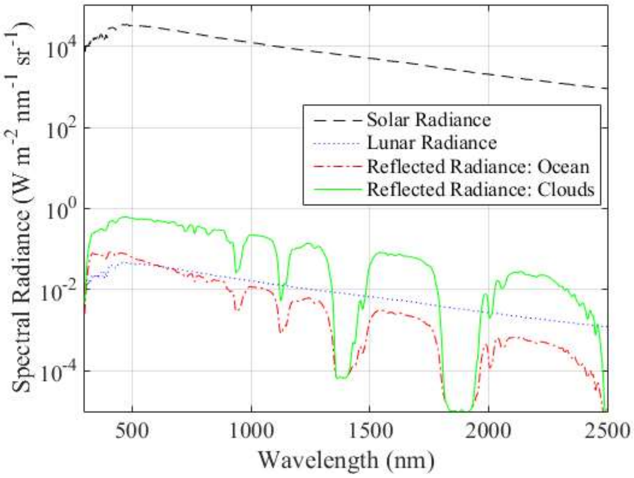

Figure 28. Expected radiance levels from Sun, Moon, bright clouds, and a dark ocean scene.

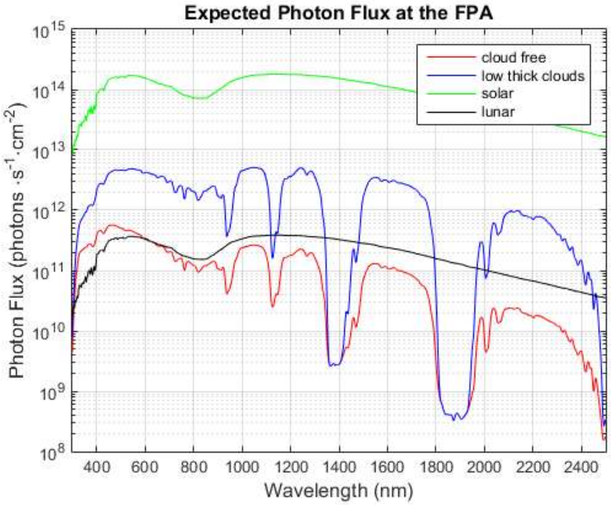

Figure 29. Expected signal at the FPA. This plot includes the photon flux for a solar scene, with the 0.5 mm aperture, and lunar, and two types of cloud scenes.

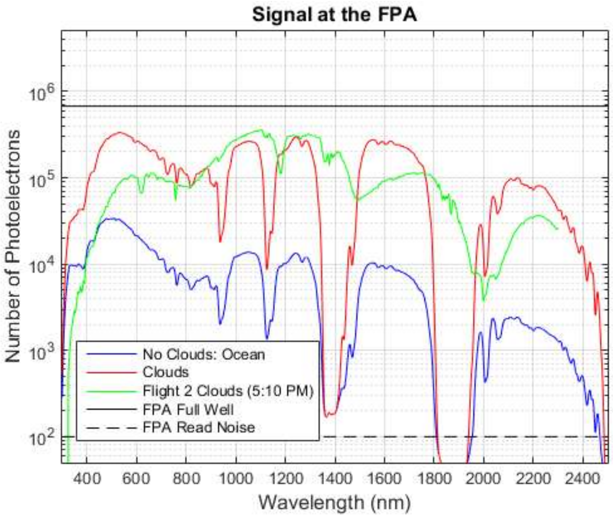

Figure 30. Number of photoelectrons at the FPA. This plot also includes a cloud scene from the HySICS balloon flight for comparison.

5.1.1.3 Random Noise in Ground Measurements

All camera measurements have several well-understood noise sources (also described in section 3.1.3.1) that reduce the signal-to-noise ratio in an image. The most common of these are sensor read noise, photon shot noise, and dark current shot noise. In addition, for an instrument that measures into the IR, blackbody shot noise must be included.

Read noise is the random noise generated by the camera electronics. For the HySICS balloon instrument, this noise level was measured for every pixel, with an average of just over 8 DN. This noise is the same regardless of signal level, so the fractional noise due to read noise is reduced for higher signal. Shot noise is the noise due to the quantization of photons in a measurement. This noise increases as the square root of the total number of photons (or electrons, but the two are related by FPA quantum efficiency). Therefore, for a higher number of photons, the fractional noise due to shot noise is reduced.

Dark current shot noise is the noise generated by the electron shot noise from dark current. The actual dark current signal is removed from the measurement by dark subtraction, but the shot noise associated with it is not. For the HySICS balloon sensor, the dark current was less than the ADC quantization limit, and therefore unmeasurable unless the sensor temperature was increased. The shot noise is also extremely small.

The blackbody radiation background from the instrument is also mostly removed from the image during the dark image subtraction, with the exception of the blackbody radiation from the blank aperture. Since this signal also has associated shot noise, it is important to characterize this subtracted signal and include its shot noise into the measurement uncertainty.

If all these noise sources are included in the measurement, the expected signal-to-noise ratio, given the signals in the previous section, is shown in Figure 31, with the associated uncertainty shown in Figure 32. This figure also assumes a 3-pixel averaging, which gives a 0.5 km ground size. It should be noted that these uncertainties can only be determined, and validated, from real ground measurements. Therefore, in addition to being the primary science data, ground measurements are also important to validate the measurement itself.

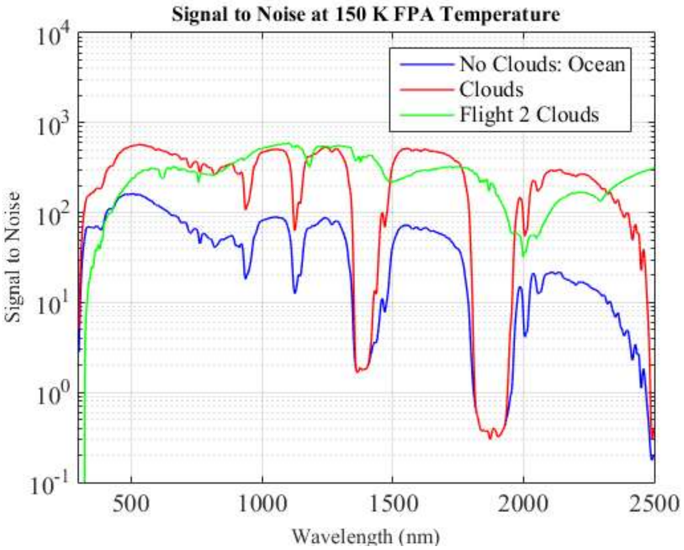

Figure 31. Expected signal-to-noise ratio. This figure shows the SNRs for bright cloud scenes, dark ocean scenes, and a comparison SNR from the HySICS balloon flight. It includes all common random noise sources, read noise, shot noise, dark current shot noise, and blackbody shot noise.

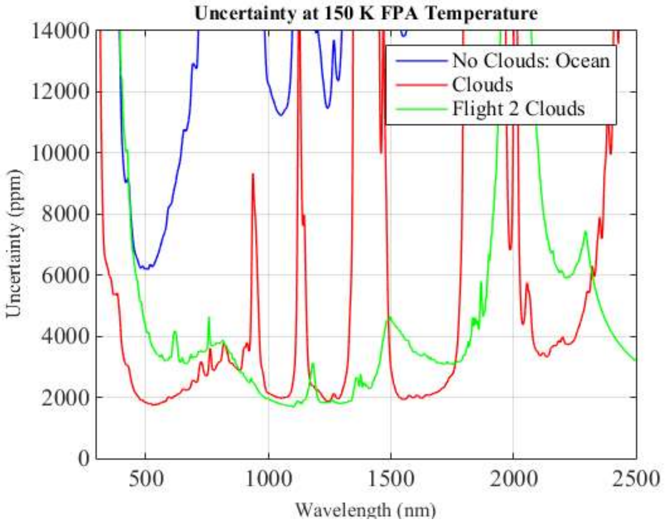

Figure 32. Expected uncertainty. This figure shows the associated uncertainty given the previous SNRs, and accounting for read noise, shot noise, dark current shot noise, and blackbody shot noise.

5.1.1.4 Ground Measurement Wavelength Scale

As described in section 5.2.3, a Pen-Ray lamp is used to set the wavelength scale of the instrument. The amount of uncertainty due to uncertainty in this scale is determined by the gradient of the measured ground spectrum. In regions with high gradient, a small amount of wavelength uncertainty translates into high measurement uncertainty. For the simulated cloud spectrum in Figure 30, given the wavelength scale uncertainty described in section 5.2.3.2 the resulting measurement uncertainty is shown in Figure 33. Similar to the read noise and all types of shot noise, the verification of the wavelength uncertainty relies on having a measured ground spectrum.

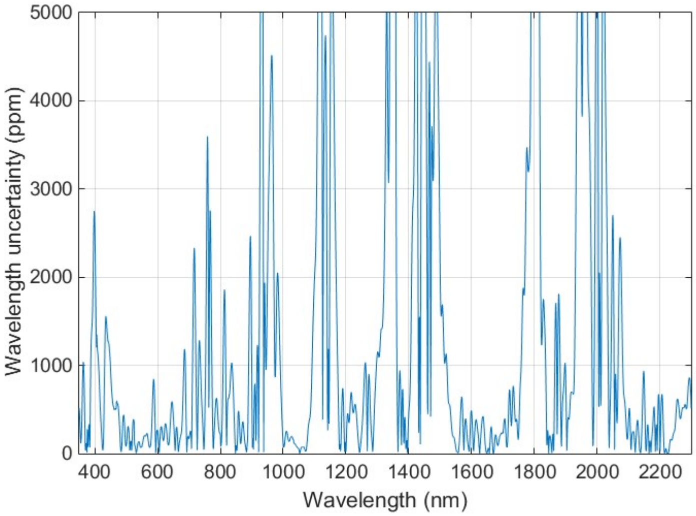

Figure 33. Estimated wavelength uncertainty. This plot shows the wavelength uncertainty given the best estimate of wavelength scale from the HySICS balloon flights, and a simulated cloud spectrum. Note that the

uncertainty is less than 1000 ppm for most of the spectrum, but can be above 5000 ppm where there is a high gradient, such as at the edges of the water absorption bands.

5.1.1.5 CPRS Polarization Sensitivity

It has been shown that inter-calibrations with other on-orbit instruments is sensitive to polarization uncertainty [7]. For an instrument that is insensitive to polarization, a highly polarized scene will be measured the same regardless of instrument orientation. For an instrument that is sensitive to polarization, however, different signal levels will be measured for 90 degree rotations around boresight of the instrument.

Given the desire to reduce polarization sensitivity, the instrument is designed compensate for polarization sensitivity introduced from reflections off the aluminum mirrors. The compensation is accomplished through including four bounces off the 4MA mirrors in the vertical plane, where the TE polarization is less sensitive, and four bounces off the Offner mirrors, where the TM polarization is less sensitive. The final instrument efficiency ultimately becomes the same for both polarizations, as shown in Figure 34.

The seventh bounce in the system, is off the grating, not an aluminum mirror, and causes the system to pick up the polarization sensitivity of the grating, shown in Figure 35. If this efficiency is used instead of the aluminum mirror for the seventh bounce, the full instrument efficiency is shown in Figure 36.

The common measurement for grating sensitivity is diattenuation, a measurement of contrast between the two polarizations:

$$Diattenuation = \frac{P_1 - P_2}{P_1 + P_2} \qquad 43$$

where P_1 and P_2 are the efficiencies of the TE and TM polarizations respectively. The diattenuation of the grating and the full system are shown in Figure 37. The full system diattenuation is less than 0.5% from 350 nm to 1600 nm, and less than 2% over the full wavelength range.

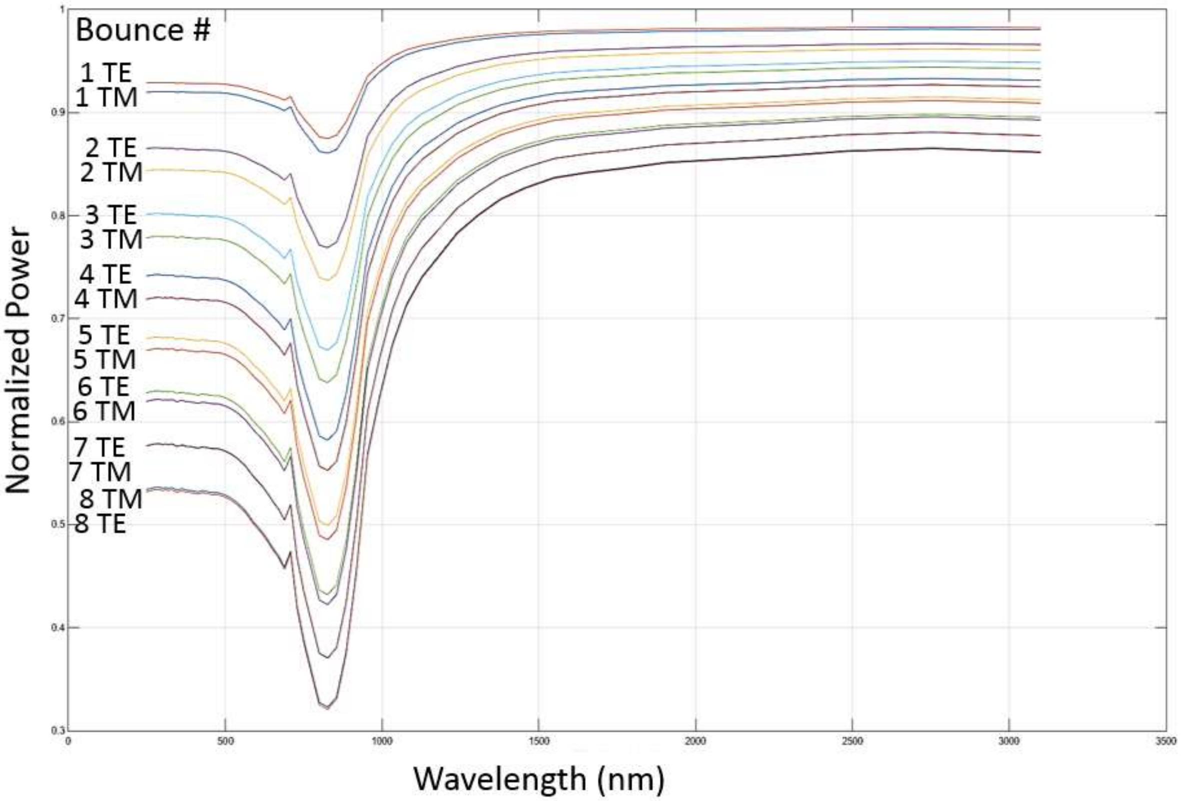

Figure 34. TE and TM polarization reflection efficiency for full system of aluminum mirrors.

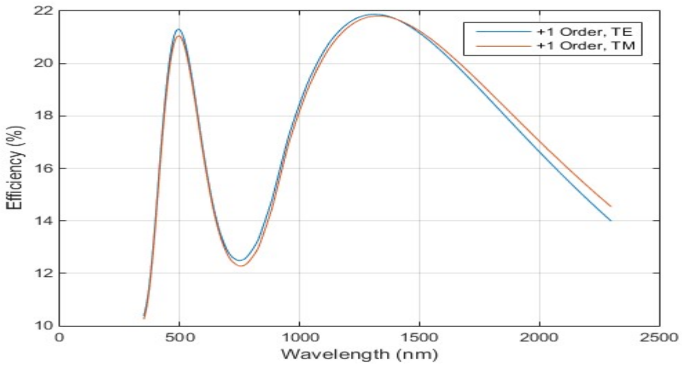

Figure 35. TE and TM efficiencies of the grating.

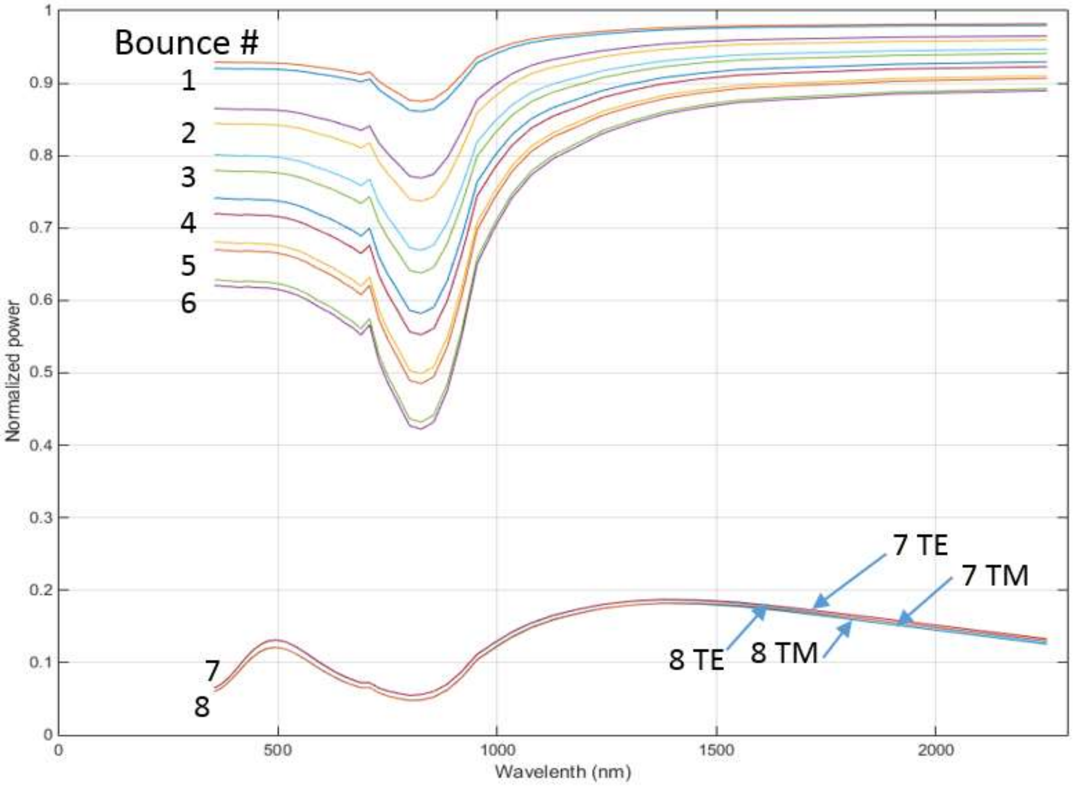

Figure 36. Full system efficiency including Zeiss grating. The polarization sensitivity is slightly increased in the IR region of the eighth bounce.

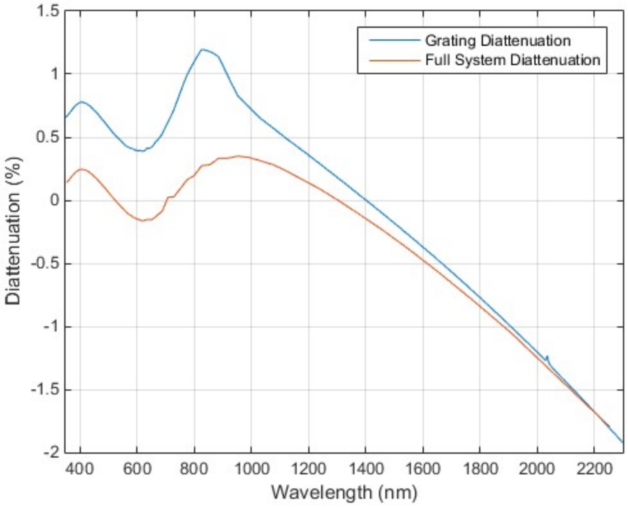

Figure 37. Grating and full system diattenuation. The full system diattenuation is less than 0.5% from 350 nm to 1600 nm.

5.1.2 Lunar Reflectance Scan

The second type of on-orbit science measurement is the lunar reflectance scan, which is similar to the solar irradiance scan (section 5.2.1), except it uses the 20 mm aperture and the longest integration time. The goal of the scan is to both measure the reflectance of different parts of the lunar surface and also integrate all the light coming from the Moon for different phases and libration positions. The lunar irradiance, a measurement of the total integrated power, can be used for other on-orbit instruments to cross-calibrate themselves. The lunar phase will be measured at least from -90 degrees to +90 degrees (waxing half-moon to waning half-moon), and possibly using even smaller crescents, although the full range will depend on the lunar availability at the time of flight.

The scan will go from -0.5 degrees to +0.5 degrees around the center of the lunar disk, with an imaging frame rate of 15 Hz, and a nominal scan rate of 0.156 deg/sec, with a scan time of 13.6 seconds. The most general lunar reflectance scan motion is shown in Figure 38. As in the solar scan case, the two-axis gimbal will usually scan the lunar disk along an arc (Figure 38a). In addition, the Moon will appear to be rotating due to the motion of the ISS around the Earth (Figure 38b). The projection of the slit (not to scale) is shown as the series of green rectangles across the lunar crescent, and will overlap other images based on the motion of the slit, the frame rate, and the location along the slit. The integrated irradiance summation will take into account the oversampling factor to properly integrate all the lunar light.

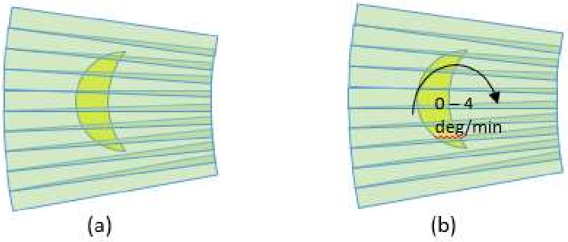

Figure 38. A) Lunar reflectance scan motion, B) with apparent lunar motion. Projected slit is shown as green rectangles that move across lunar disk.

Like the ground images measured at nadir, the lunar irradiance scan can be combined into an image data-cube, with spatial scales along two axes, and the spectral scale along the third. One wavelength, 1233 nm, of a lunar data-cube from the HySICS-balloon flight is shown in Figure 39. The color-scale in the image is the corrected irradiance value, in W/(m^2 nm). The phase of the Moon during the flight was slightly less than -90 degrees.

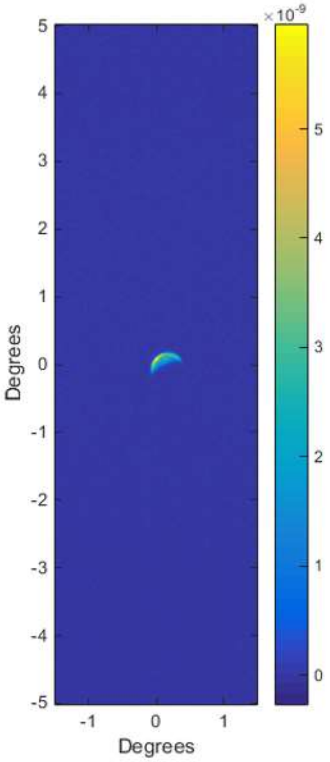

Figure 39. HySICS-balloon flight lunar irradiance at 1233 nm.

The lunar irradiance data will be treated similarly to the ground measurements, and will be stored as raw data in the level 0 data product, as un-gridded, but corrected, data in the level 1A data product, and as gridded and corrected data in the level 1B data product (see Section 4.0 for more information). The level 1A data product will also contain uncertainty estimations for every pixel in the scan. Coordinates of each pixel on the Moon will be given in right ascension and declination coordinates, rather than as geolocated coordinates. Since the Moon is moving throughout the scan, the coordinates will be temporally dependent. The handling of the lunar movement is left for future discussion.

The per-pixel lunar irradiance values are determined through the exact same series of calibrations used on the Earth scenes. In section 3.0, the *obj* subscript in equations 1 – 4 is left ambiguous because it can be used for either Earth or lunar images.

In order to integrate the lunar spectral irradiance into a single value, a similar procedure as the solar irradiance is used. This procedure is outlined in the following table.

Step	Description
1	For Nth image: Determine oversampling factor based on scan geometry and FSS pointing

Step	Description
2	Expand oversampling factor into matrix that can be directly multiplied pixel-by-pixel with image
3	Multiply each pixel by required oversampling factor
4	Add resulting image to cumulative summation image
5	Repeat from step 1 on next image
6	Sum cumulative image in spatial dimension. This creates a lunar spectral irradiance vector, 640 elements long.
7	To use spectral irradiance vector for inter-calibration, integrate over desired bandwidth. Some ILS manipulation may be required, depending on the inter-calibration instrument.

5.1.3 Reflectance Algorithm Description

This section details all the algorithms that are used for the L1A reflectance data pipeline. Many of these algorithms are also used in calibration data pipelines.

5.1.3.1 Bad Pixel Correction

The first correction that is performed on every image is the hot/dead/noisy pixel correction, called the bad pixel correction [algorithm 1A]. Every FPA has a small percentage of pixels that do not function properly. These pixels fall into one of three types: hot pixels, which are always stuck at the same level, although not necessarily the maximum level, dead pixels, which never turned on, or extremely noisy pixels. All three of these types of pixels can be identified from a pixel by pixel standard deviation of the dark images. If a pixel is either hot or dead, it has a standard deviation of 0, and if it is noisy, it has a very high standard deviation. On HySICS, noisy pixels are identified as those with a standard deviation greater than 5σ over the average standard deviation of all pixels. Once the hot/dead/noisy pixels are identified, they are mapped and replaced by the average of all normal surrounding pixels. The replacement algorithm looks for a minimum number of "good" pixels (initially set at 8, but can be increased if necessary at a later date) in the surrounding pixels. If the nearest ring of pixels does not contain enough to achieve the minimum number, the next ring of pixels is examined. The sequence continues until the minimum number have been identified. A HySICS balloon flight bad pixel map is shown in Figure 40.

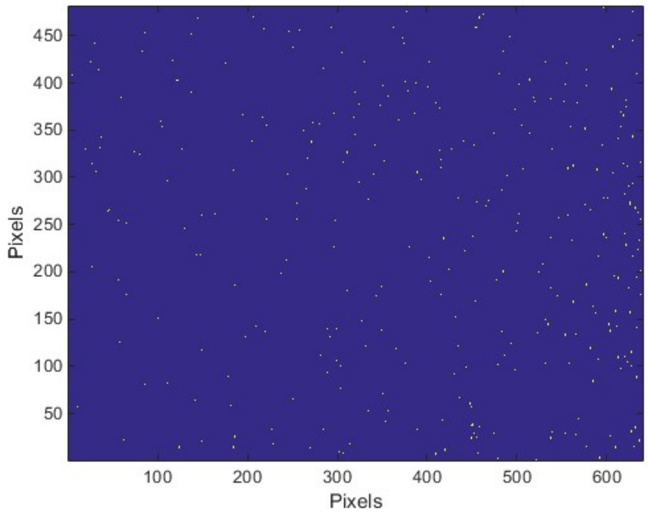

Figure 40. Bad pixel image from HySICS balloon flight. This image includes all pixels that had a variation larger than five standard deviations above the average variation during a dark image acquisition.

The bad pixel correction algorithm is performed twice during all pipelines, as the first algorithm and the last algorithm prior to a final computation with the data. The first time removes bad pixels so that they will not adversely affect summations and averages that will be performed later on the images. However, the rest of the algorithm is run on pixels that are the mean of the raw values surrounding them, and may end up being slightly different than the values that would be found from the second application of the algorithm, after all the corrections have been performed on the neighboring pixels.

5.1.3.1.1 Bad Pixel Correction Implementation

Step	Description
1	Run through all bad pixels in previously computed map
2	On first pixel, identify list of all surrounding pixels in nearest ring of pixels
3	Ignore all pixels in list that are also on the bad pixel map
4	Count number of remaining pixels on list
5	If number of pixels on list is fewer than the minimum number threshold, expand search to next wider ring of pixels, and repeat from step 3
6	Once enough pixels have been identified, average all pixels in list and assign that value to the bad pixel
7	Repeat on next bad pixel

5.1.3.2 Two-row correction

Calibration testing revealed several undesired FPA behaviors that must be accounted for in the image processing. The first effect is a periodic frame-to-frame jitter in the measured signal level which develops at high integration times, which is ultimately caused by the interplay of the two clock on the FPE which runs the FPA and the clock on the HISIE which generates the trigger signal for the FPA. These clocks run independently, and both models and lab measurements show that this leads to an inconsistent time interval between frames which will jump between two values in a periodic manner. At the highest integration times, there is insufficient time for the FPA to fully reset following a frame before the next integration period starts, and this leads to the FPA developing a frame-to-frame memory, which ultimately manifests as jitter in the measured signal level, the magnitude of which can approach ~3,000 DN at the highest integration times, as seen in Figure 41.

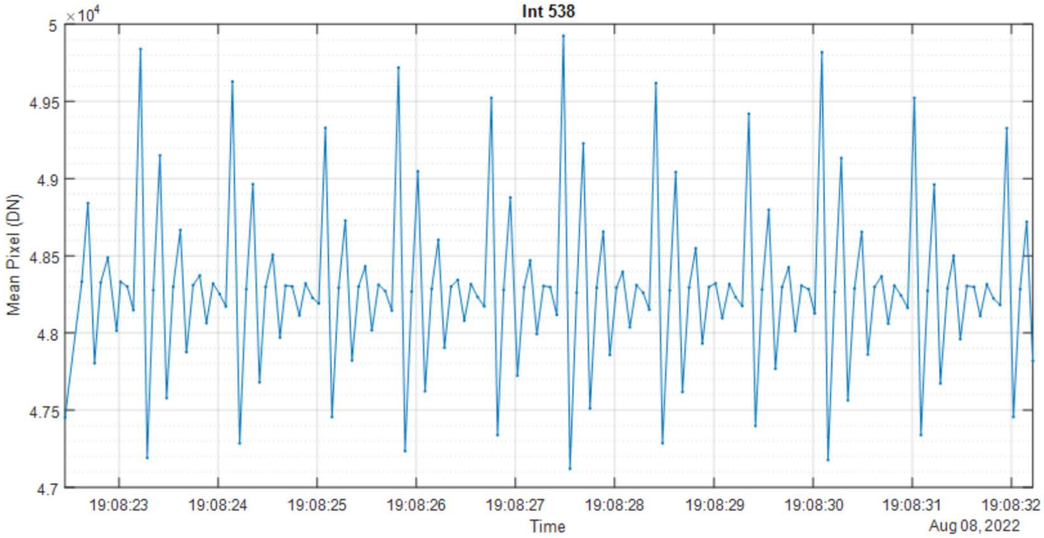

Figure 41. The frame-to-frame jitter due do to the inconsistent time interval between frames. The mean pixel value of the full FPA is plotted by frame timestamp for ~150 frames looking at a temperature stabilized target. The peak-valley noise approaches 3,000 DN.

The second and third effect are related, and both referred to as ‘dark pedestal shifts’. Generally, this is an observed depression in the detector baseline level in response to light hitting the detector. The first of these is a full frame effect, where light hitting any part of the detector depresses the baseline level for the entire detector. Additionally, there is a further effect which occur on a row by row basis, where light hitting one part of a row depresses the baseline level for all of the pixels in that row.

These three effects are dealt with via a series of corrections. The first correction in the chain is the ‘two-row correction’, which takes advantage of two ‘extra’ rows on the FPA. While these rows are not exactly dark rows – i.e. rows which simply do not see light but are otherwise identical to the rest of the FPA – they are close enough that we can make use of them with some limitations. Importantly testing showed these rows can be used to almost entirely correct for the frame-to-frame jitter, and to address most of the full frame dark pedestal shift as well.

The general strategy is that, while these extra rows are not identical to the rest of the FPA, because they also see the timing jitter and full frame dark pedestal shift, but are not sensitive to light, they can be used a proxy to measure the sum of these undesired effects on a frame by frame basis and thus be used to correct for these effects. A simple version of this would be to simply take the mean of all the pixels in the two extra rows, and subtract this value from each pixel in the FPA, and this is observed to work pretty well. However, we found we can do better by taking advantage of the fact that the pixels in the extra rows are not all identical to one another, but are rather grouped into regions with different capacitances, ranging between 0 and 70 fF. These regions all have slightly different sensitivities to the timing jitter and full frame dark pedestal shifts, and therefore rather than using the simple mean, we can instead see how well each different capacitance region individually corrects for these effects. This can be further extended to arbitrary capacitance levels via a linear least squares fit of signal vs capacitance on a frame by a frame basis. Ground testing and analysis found that the frame-to-frame timing jitter is minimized when we correct it using an effective capacitance of 54.2 fF.

5.1.3.2.1 Two-row correction Implementation

Step	Description
1	Loop through every image
2	Average the extra rows, grouped by capacitance
3	Do a linear OLS fit of signal vs capacitance
4	Use the fit to calculate the expected signal from a 54.2 fF capacitance region
5	Subtract the expected signal from the image

5.1.3.3 True Dark Correction

Following the two row correction we do a true dark subtraction. The true dark images are images taken in ground calibration during the cold target test, and are ideally images where absolutely no light is hitting the FPA. We have separate true dark image for each integration time, and the two row correction has been applied to them as well. By subtracting off a true dark image the output image represents an image measured relative to what the detector would measure with absolutely no light. This is done because two of the corrections – the row dark pedestal and linearity – depend on the absolute signal level, and it is convenient to have these the signal level scale, and thus the corrections, go to zero for a true dark image.

5.1.3.3.1 True Dark Correction Implementation

Step	Description
1	Load the appropriate two-row corrected dark image for the integration times
2	Subtract the dark image from each image in the scan

5.1.3.4 Row-wise Dark Pedestal Shift Correction

Next is a correction for the row level dark pedestal shift. Testing showed that for this effect the baseline level depression is linearly proportional to the total signal in a row, up to a saturation point, at which point there is no further depression (see Figure 42). This correction works by summing each row, thresholding that value at the saturation point, and multiplying it by the measured effect slope in DN/DN to get the predicted depression for each row, and adding these values to the image on a row-wise basis.

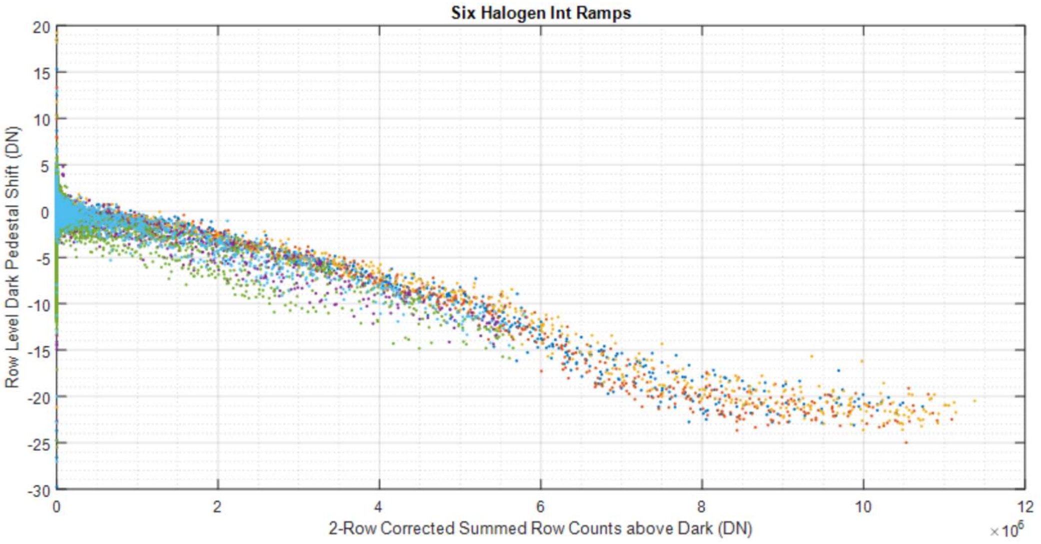

Figure 42. The measured row level dark pedestal shift, with the summed row counts on the x-axis, and the measured dark pedestal shift on the y-axis, for six data sets, each in a different color. The effect is linear up until a saturation point, after which there is no further depression.

5.1.3.4.1 Row-wise Dark Pedestal Shift Correction Implementation

Step	Description
1	Loop through every image
2	Take the sum of each row in the scan from columns 3 - 640
3	Threshold each row sum at the saturation point

Step	Description
4	Multiply each row sum by the row dark pedestal slope
5	For each row, subtract the result from each pixel

5.1.3.5 Full-frame Dark Pedestal Shift Correction

After dealing with the row level dark pedestal shift is a correction address what is left of the full frame dark pedestal shift after the two row correction. The calibration testing showed the residual depression after the two row correction depends linearly on the total signal on the detector. However, the proportionality constant is observed to vary both with integration time, and with pixel, and is determined in a two-step process making use of many different data sets.

The first step combines several data sets where light illuminated one region of the detector, along with dark images without light taken under identical conditions. The depression can be observed in a non-illuminated region of the detector, and correlated with the total signal at a variety of integration times. Importantly, because we cannot measure the effect over the full detector, but only in a region which is not illuminated, this does not allow for a pixel by pixel measurement of the slope, but only of the total slope for a large region of the detector. This gives us an initial estimate of the dark pedestal slope vs integration time.

The second step allows us to finely measure the slope of the dark pedestal shift vs integration time, but only at high integration times. To do this, we use a series of four data sets taken in the warm target tests, where the detector looked a constant scene while images were taken over the whole range of integration times. In each data set, the detector looked at a temperature stabilized blackbody source, which was held at different temperatures in each data set.

This process begins by applying a preliminary dark pedestal correction based on the one generated in the first step. For each data point, in each data set, we sum the total counts in the detector, multiply the slope estimate for that particular integration time, and add that much signal to every pixel in the detector.

If we consider a single pixel, for each data set we can make a plot of signal vs integration time. These are very nearly linear, with the slope depending on the temperature of the blackbody source. If we take each data point in a data set, and divide by the integration time it was taken at, we can generate a second plot of DN/sec vs DN, again getting a curve for each data set. If the detector were perfectly linear in response these would be flat lines. Each curve can then be normalized by the maximum value it attains, so the four curves overlap. This produces a set of curves like those shown in Figure 43.

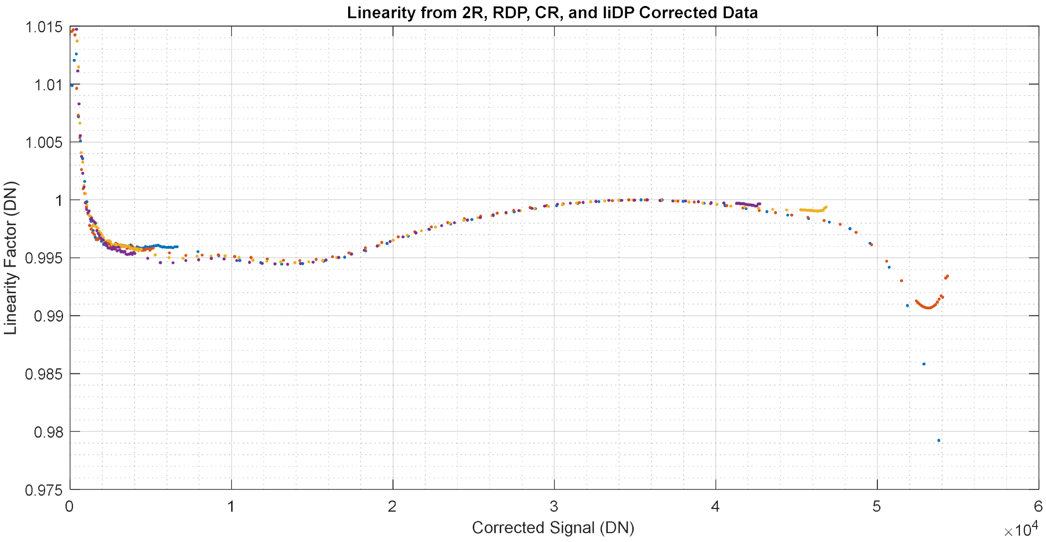

Figure 43. The linearity profiles for the full detector from the four warm target data sets.

Here we see four individual measurements of the detector nonlinearity, plotted against measured signal. This is a plot of the mean signal for the full FPA, but in the actual analysis this is done for every pixel. The important thing in this plot are the deviations seen in the purple, yellow, and red curves at high signal levels away from the other curves. These deviations are caused by the changing dark pedestal slope with integration time. Because the four data sets had four different temperature blackbody scenes, they each reached a given signal level at a different integration time. At the highest integration times (those above 500 row times) the slopes of the full frame dark pedestal shift increases rapidly, and this rapid change in the slope causes an integration time dependent signal change away from the overall linearity trend, resulting in these deviation.

By characterizing the magnitude of these deviations from the main trend, we can see, for each pixel and integration time, how additional signal is missing because of the full frame dark pedestal shift, which tells us how much the actual full frame dark pedestal shift slope deviates from our initial estimate.

We characterize this deviation by first generating a smoothed linearity curve for each pixel, using only the data acquired with an integration time below 500 row times. Then, we loop through each data point in each data set. For each data point, we determine how much additional signal needs to be added to make that data point to fall on the general trend. This gives us a measurement of the magnitude of the residual full frame dark pedestal shift, for each pixel, at each integration time. By dividing these by the total signal in the frame, we build a map of residual full frame dark pedestal slope for each pixel and each integration time, and this is what we use for the correction.

To apply the full frame dark pedestal correction, we start with the map of slope vs pixel for each every integration time. For low integration times the value is the same for all pixels, but above 500 row times we have different values for each pixel. The total counts in the detector are summed, and by multiplying this sum by the slope map for the appropriate integration time we determine how much additional signal must be added to each pixel to correct for the residual full frame dark pedestal shift.

5.1.3.5.1 Full-frame Dark Pedestal Shift Correction Implementation

Step	Description
1	Load the appropriate map of full frame dark pedestal slopes for the integration time
2	Loop through each image
3	Sum the full FPA, from rows 1 – 478 and columns 3 - 640
4	Multiply the slope map by the total summed counts
5	Subtract the resulting image from the input image

5.1.3.6 FPA Thermal Correction

The FPA output varies slightly depending on the temperature of the FPA and on the signal level, and must be corrected to a center temperature, chosen to be 152.5 K [algorithm 2A]. This effect was measured during the cold target test [2] where the blackbody target was held at a very constant temperature while the FPA was warmed from its nominal low temperature of 147.5 K. During the warmup, the signal level was varied by changing the integration time, and data was acquired at 21 different signal levels, from almost no signal to nearly saturated. The resulting data set is shown in Figure 44.

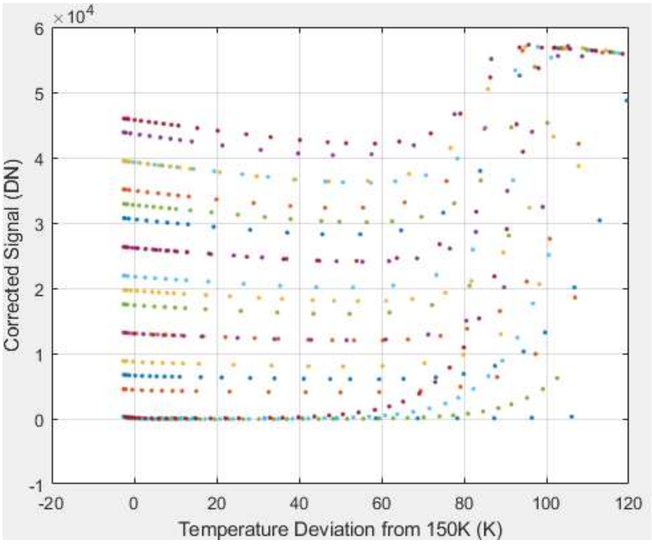

Figure 44. FPA behavior versus temperature for various signal levels. The signal level is grouped by color.

For all of the signals, the measured value decreases slightly as the temperature is increased until the temperature deviation is 40 – 60 degrees above the nominal operating temperature. At this point, the signal level sharply increases.

The physics of the temperature behavior is not well understood. The sharp increase in signal level for higher temperatures is believed to be the expected exponential increase in dark current, which eventually dominates the signal. The decrease in signal level is quite gradual, and may be due to thermal stresses on the FPA or internal electronic circuitry changing operation slightly.

The gradual decrease is consistent, and can be modeled around the FPE operational temperature range, from 150 K to 155 K. Several models, dependent on both FPA temperature and signal level, have been studied. The one that models the behavior best is has the form:

$$Out(T,S) = A(S) \cdot ln\left(T - T_{ref}\right) + B(S) \cdot \left(T - T_{ref}\right) + C(S) \qquad 44$$

Where

$$A(S) = A_0 \cdot exp(A_1 \cdot S) + A_2 \qquad 45$$

$$B(S) = B_2 \cdot S^2 + B_1 \cdot S + B_0 \qquad 46$$

$$C(S) = C_1 \cdot S + C_0 \qquad 47$$

And the A, B, and C coefficients are constants given by:

A_0 = -421.066, A_1 = -8.4165e-5, A_2 = -73.132, B_2 = 2.89e-8, B_1 = -0.0037, B_0 = 35.14, C_1 = 1.00, C_0 = 703.67, and T_{ref} = 143.5. There has been some work to make these coefficients also dependent on the column, but they do not vary much from the values shown.

It is important to note that the variation in FPA temperature over the course of a scan is extremely small. It has been measured at better than 0.014 °C over 12 hours. This indicates that the correction is also small, and sometimes negligible.

5.1.3.6.1 FPA Thermal Correction Algorithm Implementation

Step	Description
1	Repeat for all images in scan
2	On the image, for every pixel, compute the expected signal given the measured signal and FPA temperature
3	On the image, for every pixel, compute the expected signal given the measured signal and the nominal FPA temperature (152.5 K)
4	Compute the delta between the two calculations
5	Subtract delta from the measured signal

5.1.3.7 Linearity Correction

The linearity correction is used to correct for observed nonlinearity in the detector response that depend only on the measured signal level. The linearity correction is generated from a number of data sets taken in the cold target test campaign. In each data set, the FPA was temperature stabilized, and then ramped through its range of integration times, each time taking ~150 images of a stabilized, constant scene. In some of the tests the scene was provided by a temperature stabilized blackbody source. In these tests by adjusting the blackbody temperature we could adjust the light flux. In other tests it was provided by an LED, and the flux could be adjusted by adjusting the LED drive current. Additionally, a test were done where the FPA looked at a blackbody source cryogenically cooled to 135K to provide ‘true dark’ images – that is, images as close as possible to what the FPA sees with no light upon it. Several of the linearity data sets are shown in Figure 45.

For each test, we apply the initial bad pixel correction, two row correction, true dark subtraction, and row dark pedestal shift correction, the full frame dark pedestal shift correction, as well as a quasi-correction for the cursed row phenomena (see Appendix B). With this, we generate a linearity profile for each data set. This is done by dividing the measured signal at each point by the true integration time. The true integration time is the integration time register setting, plus an offset determined to be equal to 0.965 row times. In a perfect detector, this would be a constant quantity through the entirety of each data set, giving you a measure of total flux in units of DN / (row time). Nonlinearities in the response cause this quantity to vary over the acquisition. This quantity is normalized by the maximum value for each individual data set, and this can then be plotted against the signal level to generate a plot of nonlinearity vs. signal level (see Figure 46).

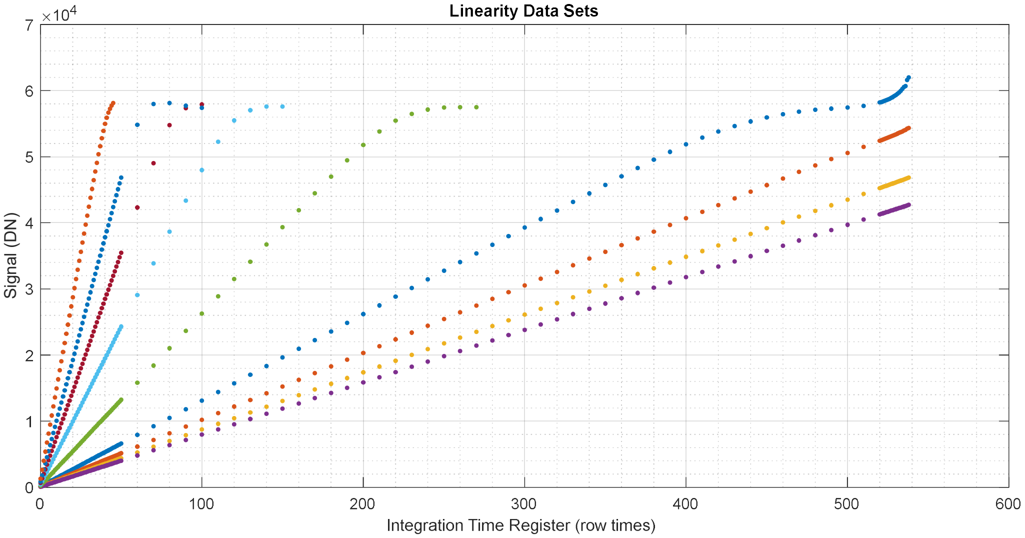

Figure 45. The signal vs integration time for a variety of data sets used for the linearity correction, following all of the initial corrections.

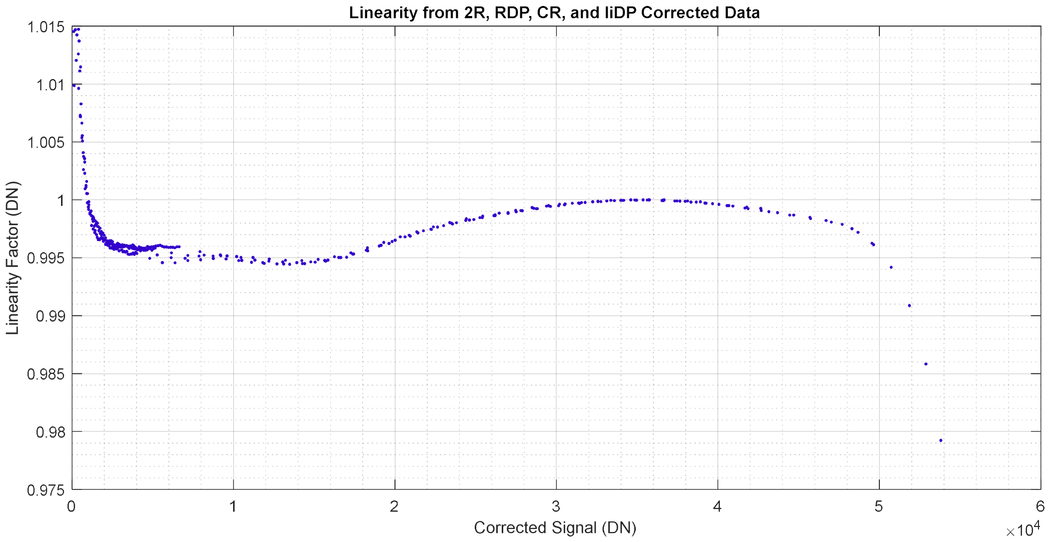

Figure 46. The general linearity profile plotted against the corrected signal level for the warm target data sets.

Such a profile is generated for each pixel on the detector. Then, a full linearity curve is fit by dividing the signal range into a number of bins, and for each bin finding the mean of all the data points within that bin. This gives us images of the linearity factor vs signal level for the entire FPA. The correction is applied on a per pixel basis. The pixel's signal level is used to determine a linearity correction factor by interpolating that signal level onto the curve of linearity factor vs signal level for that specific pixel. Then, the pixel's signal is divided by this linearity factor

$$sig_{corr} = \frac{sig}{l_f} \quad 48$$

The uncertainty in the linearity correction can be calculated with standard error propagation.

$$\sigma_{sig_{corr}} = \sqrt{\left(\frac{\partial sig_{corr}}{\partial sig}\right)^2 \sigma_{sig}^2 + \left(\frac{\partial sig_{corr}}{\partial l_f}\right)^2 \sigma_{l_f}^2} \quad 49$$

$$\sigma_{sig_{corr}} = \sqrt{\left(\frac{1}{l_f}\right)^2 \sigma_{sig}^2 + \left(\frac{sig}{l_f}\right)^2 \sigma_{l_f}^2}$$

Here, sig is the measured signal after all the preceding corrections, and σ_{sig} is the associated uncertainty. This is driven by read noise and shot noise, as well as any uncertainty from the previous corrections. The uncertainty in the linearity factor, l_f, comes from the residuals from generating the curve of linearity factor vs signal level, which are used calculate the uncertainty in the mean of the correction factor at that signal level.

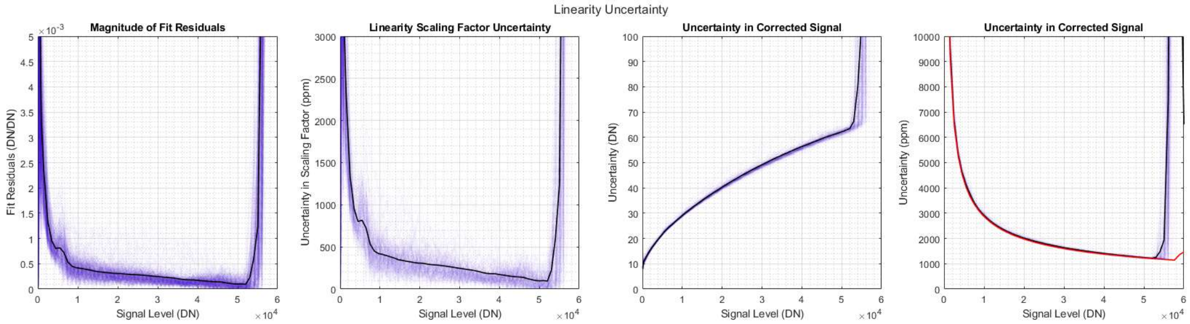

Figure 47. The uncertainty in the linearity correction. The left two plots show the magnitude of the linearity factor fit residuals as a function of signal level in both units of the linearity factor (DN/DN) and in ppm. A selection of pixels are shown in purple, and the mean of the whole FPA in black. The right two plots show the uncertainty in the corrected signal as a function of signal level, using only read noise and shot noise for the uncertainty in the signal. Again individual pixels are shown in purple, and the mean of the whole FPA in black. On the far right, the red line indicates the noise floor from read noise and shot noise.

The uncertainty is calculated for each pixel, and this is shown in the left two plots in Figure 47, in units of the linearity scaling factor on the far left (DN/DN), and ppm next to it. Each purple line shows the uncertainty for an individual pixel (~600 total pixels are plotted), and the black line shows the FPA mean. The right two plots calculate the total uncertainty in the corrected signal as a function of signal level, using only read noise and shot for the uncertainty in the signal, which are calculated from the read noise and gain values on a per pixel basis from the photon transfer curves found in the cold target test campaign. This is shown in both DN (center right plot) and ppm (right most plot). In the right most plot, the red line shows the noise floor from the read noise and shot noise.

This can be extended to calculate the noise as a function of wavelength, using a simulated 30% Lambertian scene, shown in Figure 48. The simulated scene gives a per pixel signal estimate, from which the per pixel total noise can be calculated, allowing for the calculation of the total uncertainty following the linearity correction.

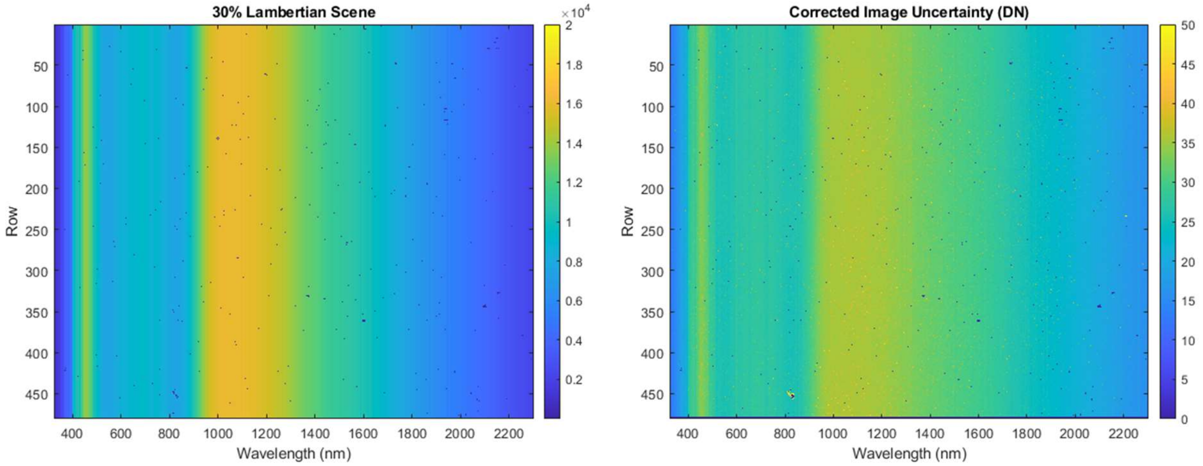

Figure 48. A simulated 30% Lambertian scene (left), and the associated total uncertainty (right) after the linearity correction.

By averaging along columns of the uncertainty image, we can arrive at the total uncertainty as a function of wavelength, shown in Figure 49. The purple curve shows the net total uncertainty for this scene as a function of wavelength (again, using only read and shot noise for the uncertainty in the signal), while the red shows an 'effective linearity correction uncertainty', found by subtracting the signal uncertainty from the total uncertainty in quadrature, which gives a measure of how much uncertainty the linearity correction can be expected to add in isolation for this type of scene.

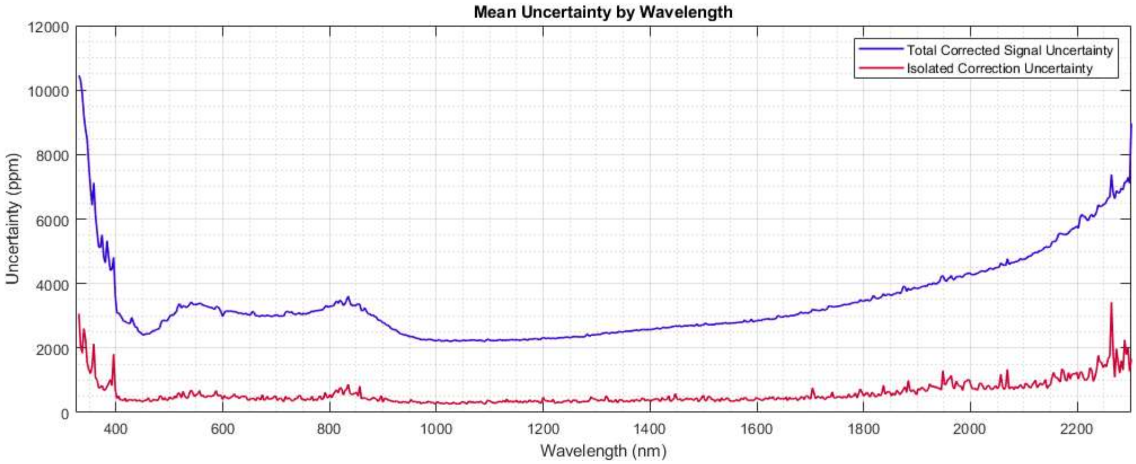

Figure 49. The total uncertainty as a function of wavelength for a 30% Lambertian scene following the linearity correction, and an 'effective linearity correction uncertainty' for the linearity correction in red.

5.1.3.7.1 Linearity Correction Implementation

Step	Description
1	Load the linearity factor vs signal level data file
2	Loop through each image
3	Loop through each pixel
4	Interpolate the linearity factor vs signal level curve for that pixel for the actual signal level
5	Divide the signal level by the interpolated linearity factor.

5.1.3.8 FPE Thermal Correction

Like the FPA, the FPE also experiences small changes based on the temperature of the electronic components, and must be corrected to an ideal temperature, chosen to be 31 °C [algorithm 2C]. The FPE is thermally stabilized during flight to minimize the temperature variations. The components that vary output based on their temperature are expected to be the eight ADCs, and their input amplifiers. During the testing, the output of each of the ADC channels was carefully measured over a very wide temperature range of nearly 50 °C given a known input voltage. The eight resulting curves are shown in Figure 50.

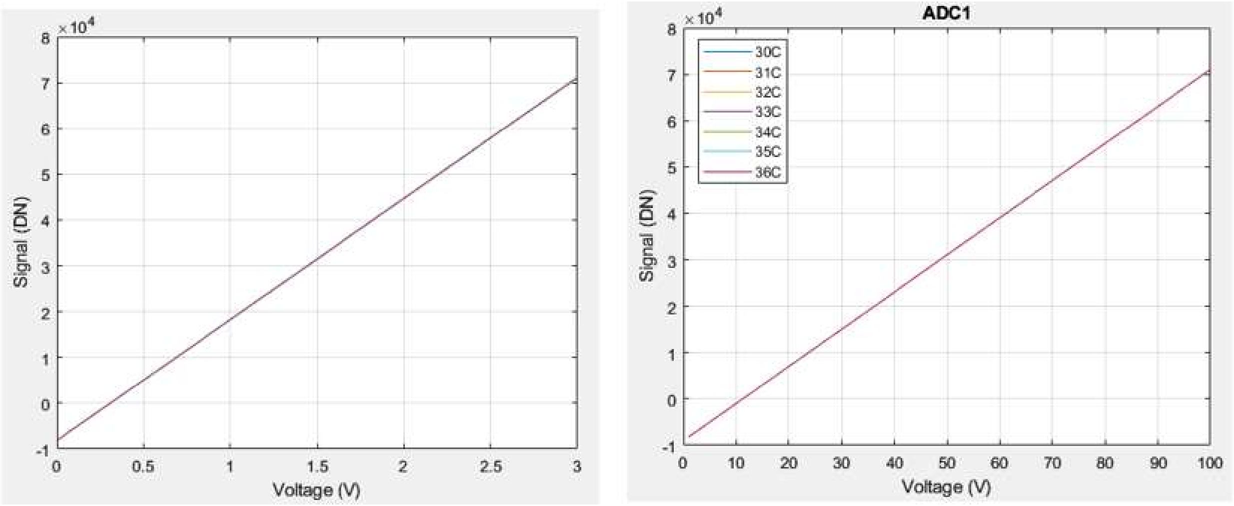

Figure 50. The eight transfer curves of the FPE ADCs at a single temperature (left) and the transfer curve of ADC 1 over several temperatures from 30 °C to 36 °C (right). The shown plots are linear fits of the measured values.

The ADCs are so similar that it is difficult to discern the differences from this figure, however, the linear fit offset and gain over temperature show the differences in Figure 51.

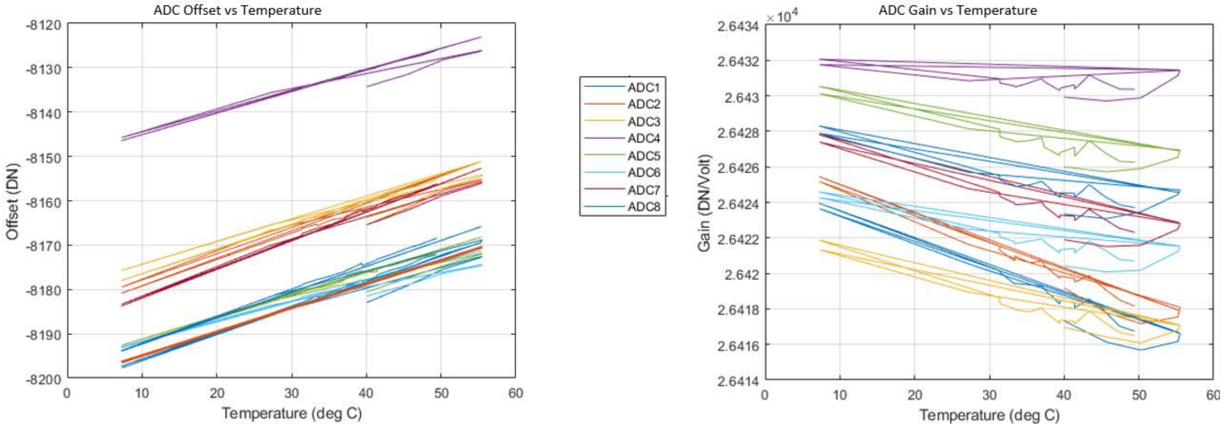

Figure 51. ADC offset and gain values versus temperature for all 8 ADCs.

The ADC fits themselves are quite linear over the 50 °C measurement range, and can themselves be fit to generate 32 coefficients (the offset-slope, offset-intercept, gain-slope, and gain-intercept) for each ADC.

Given a measured value for each ADC, at a known temperature, it is possible to calculate the ADC input voltage. With the voltage, it is then possible to estimate what the response would have been at a different temperature, such as the ideal 31 °C temperature. Like for the FPA, the thermal swings are extremely small for the FPA, measured at better than 0.004 °C, making this correction very small.

5.1.3.8.1 FPE Thermal Correction Implementation

Step	Description
1	Repeat for all images in scan
2	On the image, for every pixel on each ADC, compute the ADC voltage given the measured signal and measured temperature.
3	Compute the expected output for each ADC given the voltage.
4	Calculate the delta between the two measurements.
5	Subtract the delta from the measured signal.

5.1.3.9 Blackbody Radiation Correction

Any error in the zero reference level (measured by a dark image) of every pixel becomes a systematic error in the measurement, which is the reason that so much effort is put into making an accurate dark image subtraction. Much of the system variability in the dark image acquisition will be quantified by the pre- and post-scan dark images. This technique, however, only captures the linear variation in the dark images. If the instrument temperature varies non-linearly during a scan, its blackbody radiation contribution will not be observed in the dark images, and will therefore cause an error in the scan data.

It is unlikely that the instrument temperatures will change very rapidly, or in a particularly non-linear fashion. However, if they do, they will be tracked by a host of thermistors continuously monitoring the instrument temperatures at multiple locations. During the commissioning period, the temperatures during dark image acquisitions will be monitored. If the dark images change appreciably with a temperature variation, it will be measured, and used to build up a correlation table of dark image values versus temperature. This correlation data will be used to correct for non-linear temperature variation, and therefore non-linear blackbody radiation variation, during the science and calibration scans.

This algorithm has been studied and created for the temperatures and gradients present in a laboratory environment [algorithm 3A]. The measurement is a relatively simple one: take images of the blank aperture while slowly varying the temperature of the instrument enclosure and monitor all thermistors. It was found that the signal in the dark images was directly proportional to the temperature of the order sorting filter thermistor. This thermistor is quite close to the FPA, on the mount holding the OSF within 1 mm of the FPA. The proportionality slope is slightly different for each pixel, and shown in Figure 52, where the color represents the added blackbody signal due to temperature change, in DN/°C at the second longest integration time (537 RT).

Like the other temperature corrections discussed earlier, the blackbody correction is used to estimate what the signal would have been at a nominal temperature, set to 12.15 °C for the order sorting filter thermistor. The temperature difference is calculated, corresponding to a variation in the signal, given by the blackbody slope map, and that variation is subtracted from the measured signal.

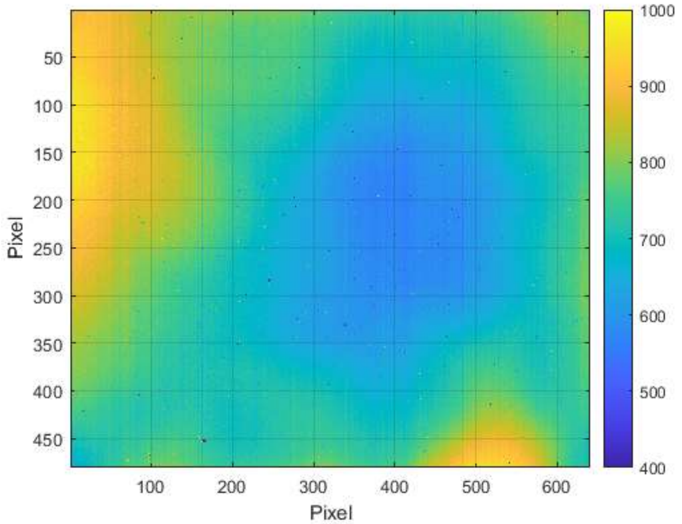

Figure 52. Blackbody radiation proportionality slope for each pixel. The colors are in DN/°C.

5.1.3.9.1 Blackbody Correction Implementation

Step	Description
1	Loop through every image
2	Estimate the temperature change from the order sorting filter thermistor
3	Multiply the blackbody radiation correction slope map by the temperature difference
4	Subtract the result from the measured signal

5.1.3.10 Dark Image Correction

Every image taken with the instrument will contain artifacts from the sensor array, electronics, and optical system. These artifacts include sensor fixed pattern noise (FPN), dark current, and blackbody radiation from the optical bench. To measure their contribution, 250 dark images are taken before and after every instrument measurement scan. A blank aperture, coated with a low reflectivity surface on the instrument-facing side, is used to block all incoming light from the scene. The resulting image, a dark image, contains only the unwanted, background sources, and can be subtracted from all images in the measurement [algorithm 3B]. A dark image from the HySICS balloon flight, with the optical bench temperature at around 3 degrees C, is shown in Figure 53. Optical bench blackbody radiation, although wavelength dependent, and higher at the longer wavelengths, will be present over the full image because it is not dispersed by the grating. The dark image is always taken in close temporal proximity to the actual measurement to minimize the possibility of background variation, and taken at the same exposure level. To help eliminate any dark signal trends from the data, the 250 pre-scan and 250 post-scan dark images are interpolated, on a pixel-by-pixel basis, across the full scan range. It should also be noted that the dark images undergo all the same corrections as the nadir science images until the application of the dark image correction. This ensures that the nadir images and dark images are on equivalent scales.

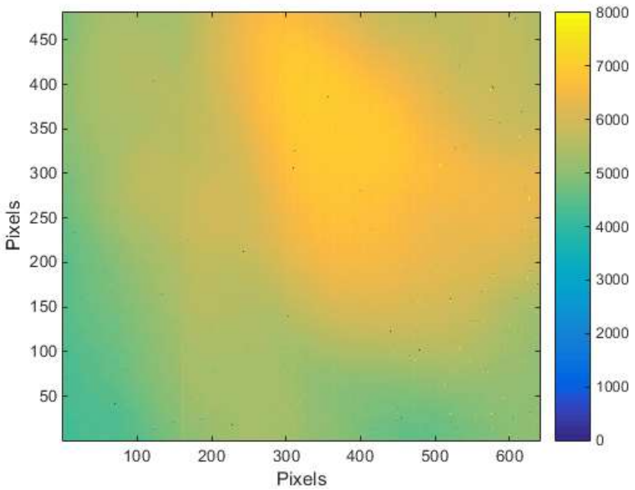

Figure 53. Nominal dark image from the HySICS balloon flight, taken with optical bench at 3 degrees C. This dark image consists of blackbody radiation from the instrument, including the blank aperture, and dark current and fixed pattern noise from the FPA.

5.1.3.10.1 Dark Image Correction Implementation

The dark image algorithm primarily consists of interpolating the images across the same time period as the scan. The interpolation will happen on a pixel-by-pixel basis, and fit the pre-scan and post-scan data with a line. The dark image will be chosen depending on the time of the scan image it is associated with. A table outlining the algorithm steps is shown below.

Step	Description
1	Compute the average pre-scan dark image, and assign to the average acquisition time.
2	Compute the average post-scan dark image, and assign to the average acquisition time.
3	Linearly interpolate from the pre-scan dark image to the post-scan dark image, creating a new dark image at each of the nadir image acquisition times.
4	Subtract dark image from associated scan image

5.1.3.11 Dark Field (or Blank Aperture or Cold Sky) Measurement

When the blank aperture is in place, it can introduce a small amount of blackbody radiation into the dark image that is not present during a measurement scan. This radiation will only be observed at longer wavelengths, approximately 1900 nm and higher, because it will be imaged on the slit and dispersed by the grating. To measure this added signal, the instrument will occasionally take images of a dark portion of space, without the aperture in place. The difference between a normal dark image, with the black aperture in place, and the dark field should be entirely due to added blackbody radiation from the blank aperture [algorithm 3C]. The temperature of the aperture wheel will be continuously monitored, and used to make the blank aperture blackbody radiation correction during normal operations.

5.1.3.11.1 Dark Field Measurement Implementation

The blank aperture radiation contribution must be added back into the measurements after being subtracted off in the dark image subtraction, which may have over-estimated the dark signal by the amount of light produced by the blank aperture. The algorithm steps are shown in the following table.

Step	Description
1	Calculate added blank aperture light
1a	Average all blank aperture images from one measurement (normally called the dark images)
1b	Average all dark field images from one measurement (images of a dark section of space)
1c	Subtract dark field measurement from blank aperture measurement = Blank aperture contribution
2	Subtract blank aperture contribution from all dark images (Equivalent of adding blank aperture contribution to all dark subtracted images)

5.1.3.12 Flat Field Algorithm

To correct for optical and FPA gain variations in the spatial dimension, a multiplicative correction is applied to every pixel, called the flat field correction [algorithm 4A]. The creation of the flat field is covered in section 5.2.2. The flat field is specified to be a multiplication, which is easier to implement in the on-board FPGA rather than a more common division. A new flat field for both the solar viewing and Earth viewing apertures will be created periodically throughout the mission. The application is as simple as multiplying each image pixel by the flat field correction.

5.1.3.12.1 Flat Field Implementation

Step	Description
1	Loop through every image
2	Multiply the image pixel-by-pixel by the corresponding flat field (large or small aperture, closest in time to nadir data acquisition)

5.1.3.13 Aperture Temperature Correction

If the temperature of the apertures change, they will expand or contract based on the CTE of aluminum, approximately 23.6 ppm/degree C. The aperture temperature correction scales all images to their signal at that temperature [algorithm 2D]. In principle, this expansion can change the aperture ratio if the solar SSI and ground measurements are made at different temperatures, although this tends to be a very small effect for the temperature changes likely to be observed during the mission. If, for example, the temperature of the large aperture is 23 degrees during a nadir measurement, and the temperature of the small aperture is 33 degrees during the corresponding solar calibration measurement, then the effective aperture ratio is 1599.23, rather than the ideal 1600 if there were no thermal change. This amounts to a 480 ppm change in the signal, which is small, but still a sizable fraction of the required mission uncertainty. The aperture ratio variation versus a higher temperature on the small aperture is shown in Figure 54.

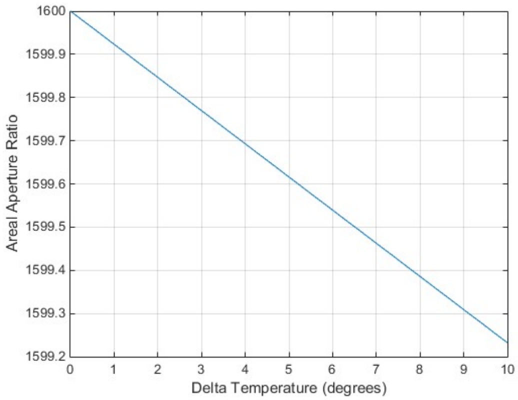

Figure 54. Aperture areal ratio versus increase in temperature on solar-viewing aperture.

5.1.3.13.1 Aperture Temperature Correction Implementation

Step	Description
1	Calculate temperature from on board thermistors (there are 3 on the aperture wheel)
2	Calculate the change in temperature from the ideal aperture temperature (24 °C)
3	Calculate the change in aperture area from the aluminum CTE (23.6 ppm/°C)
4	Scale every pixel value by the change in aperture area

5.1.3.14 F-Number Thermal Correction

Like the apertures, the mirrors of the entrance telescope (4MA) are made from diamond-turned aluminum. If there are temperature changes, there is a very small change in the telescope behavior, slightly changing the focal length, and modeled as an F-number change assuming the pupil size is constant. This thermal change, linearly dependent on the temperature of the telescope, effectively changes the scene brightness by a very small amount, as shown in Figure 55.

The ideal temperature of the 4MA is 24.3 °C, and the F-number thermal correction scales all images to what they would have been at that temperature [algorithm 2E]. Like the other thermal corrections, the delta between the measured and ideal temperatures is used with the F-number correction slope, or 366 ppm/°C. Also like the other thermal variation corrections, the 4MA temperature is not expected to change rapidly during the flight, since it is thermally controlled with the rest of the enclosure. In vacuum, its thermal variation is measured at 0.04 °C.

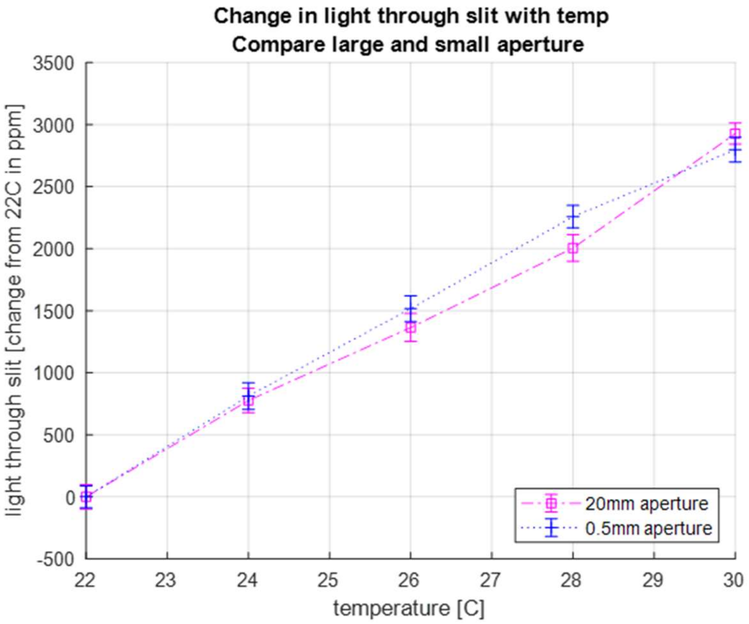

Figure 55. Light variation due to thermal changes in the 4MA, shown in ppm.

5.1.3.14.1 F-Number Thermal Correction Implementation

Step	Description
1	Measure temperature from on board 4MA thermistor
2	Calculate the change in temperature from the ideal aperture temperature (24.3 °C)
3	Calculate the change in signal level from F-number variation
4	Scale every pixel value by the change in signal level

5.1.3.15 Integration Time Correction

After all the image conditioning algorithms have been applied, the attenuation factors are applied to the data. There are two attenuation factors: the integration time ratio and the aperture ratio. The aperture ratio is only applied to the SSI scan data, and will be addressed in section 5.2.1.2. The integration time ratio is intended to be a ratio of the integration time used with the solar scans versus the nadir scans. To facilitate application of the ratio, given the disperse acquisition of the two data sets, they are both scaled to their values had they been acquired at 1 RT (or 122.85 µs) [algorithm 5A]. During the reflectance or radiance calculation, when the nadir data is divided by the HySICS SSI, the integration time ratio automatically becomes part of the scaling.

Superficially, the scaling is as simple as dividing the data by the integration time, in row times. However, laboratory measurements have shown that the FPA has a small zero-offset, of 0.965 RT. In other words, if the FPA integration time is set to 0 RT, it actually acquires for 0.965 RT, or 118.55 µs. To actually scale the image data to an integration time of 1 RT, this zero-offset must be added to their integration time.

5.1.3.15.1 Integration Time Correction Implementation

Step	Description
1	Scale all images by 1/(integration time + zero offset)

5.1.3.16 Solar Temporal Variation Correction

As discussed in section 3.1.3.6, a change in the solar spectral irradiance between the SSI measurement and the nadir science scan, must be properly accounted for in the reflectance measurement [algorithm 6A]. The solar spectral irradiance is measured twice a day by TSIS SIM, and in general will have a temporally close enough measurement to be used for the solar temporal variation.

Similarly to the calculation of the unit conversion factor, discussed in section 5.2.1.5, the required SSI variation should be the SSI as measured by the HySICS instrument. Since TSIS SIM cannot directly make a HySICS SSI measurement, the HySICS ILS is convolved with the TSIS SIM SSI. This convolution is done for both the SIM measurement taken during the nadir science scan and during the HySICS SSI scan. The ratio of the two SIM measurements, called the solar temporal SSI ratio, is a slightly smoother version of the ratio than it would be with the un-convolved SIM measurements. The ratio can be sampled at each spectral bin of HySICS, and then used to directly scale all spectral components of the nadir data.

5.1.3.16.1 Solar Temporal Variation Correction Implementation

Step	Description
1	Obtain TSIS SIM SSI taken nearly simultaneously as HySICS SSI measurement
2	Convolve TSIS SIM SSI with HySICS ILS (called SSI 1)
3	Obtain TSIS SIM SSI taken nearly simultaneously as HySICS nadir science measurement
4	Convolve TSIS SIM SSI with HySICS ILS (called SSI 2)
5	Calculate temporal SSI ratio: SSI 1 / SSI 2
6	Scale nadir data by temporal SSI ratio

5.1.3.17 Reflectance Calculation

The reflectance calculation, as seen in (eq. 3) is straightforward. The nadir science data is divided by the HySICS SSI and multiplied by a factor of pi [algorithm 6B].

As discussed in section 5.2.1, however, the SSI scan is performed twice: once with a completely unsaturated detector, and once that purposefully saturates the brighter spectral portions of the solar signal in order to increase the signal level of the dimmer parts of the spectrum. These two scans must be properly merged before being used to calculate the reflectance. Only the brightest, unsaturated data from either scan is used. Note that these scans have already been scaled to their respective values at a unit integration time, making them comparable with each other. In addition, it is possible that these two scans have a small wavelength shift associated with them. Their respective wavelength maps must also be merged in the same way as the signal data. In other words, if one column of the merged data comes from the unsaturated SSI, then the merged wavelength map must also contain that column from the unsaturated SSI wavelength map.

5.1.3.17.1 Reflectance Calculation Implementation

Step	Description
1	Obtain the TSIS SSI scans taken at same time as HySICS unsaturated SSI scan
2	Convolve above TSIS SSI with HySICS ILS
3	Obtain the TSIS SSI scans taken at same time as HySICS saturated SSI scan
4	Convolve above TSIS SSI with HySICS ILS
5	Make a list of the columns with saturated data from the saturated SSI scan
6	Merge those columns from the unsaturated SSI scan with the other columns from the saturated SSI scan
7	Merge those columns from the unsaturated SSI scan wavelength map with the other columns from the saturated SSI scan wavelength map
8	Calculate ratio of nadir science data and merged SSI scan

5.1.3.18 Radiance Calculation

The heart of the radiance calculation is generating the unit conversion factor (eq. 1) from the HySICS measured SSI and the SIM measured SSI [algorithm 6C]. The ratio of these two values is a measurement of the instrument behavior, and provides a calibration value, in $(W/(m^2 \cdot sr \cdot nm))/DN$. It provides a conversion from the native DN units to SI-traceable radiance units. Since it is a measurement of the instrument behavior, the measured signal does not need to be scaled by the solar temporal variation, although, if it is found that it is changing appreciably on orbit, it may be interpolated between SSI measurements to provide a more accurate conversion factor.

Like the reflectance calculation, the radiance calculation, and the unit conversion factor in particular, uses both the unsaturated and saturated SSI scans, merged in the same way as described in the reflectance section. In addition, to make the SSI scans comparable, they must be convolved with the ILS from the other instrument, as described in section 5.2.1.5. That convolution also smooths out the unit conversion factor across the spectral dimension, as might be expected, since the SIM ILS is over 20 nm wide in the IR. However, since the unit conversion factor is already a smooth, slowly varying function over wavelength, the smoothing does not decrease the instrument spectral bandwidth.

The final step in creating the unit conversion factor is merely finding the ratio of the TSIS SIM SSI and the HySICS SSI. Note that the conversion factor should be the same for all spatial rows (or field angles) and any measurement spatial variation is accounted for by the flat field. However, there is a slight shift in the wavelength scale for different spatial rows, due to the optical distortions in the system. To account for this, the unit conversion factor is interpolated to the wavelength scale of the row that it is applied on.

After finding the ratio and interpolating to the proper spectral scale, the radiance is merely the multiplication of the measured nadir science data and the unit conversion factor on each row.

5.1.3.18.1 Radiance Calculation Implementation

Step	Description
1	Obtain the TSIS SSI scans taken at same time as HySICS unsaturated SSI scan
2	Convolve above TSIS SSI with HySICS ILS
3	Obtain the TSIS SSI scans taken at same time as HySICS saturated SSI scan
4	Convolve above TSIS SSI with HySICS ILS
5	Make a list of the columns with saturated data from the saturated SSI scan
6	Merge those columns from the unsaturated SSI scan with the other columns from the saturated SSI scan
7	Merge those columns from the unsaturated SSI scan wavelength map with the other columns from the saturated SSI scan wavelength map
8	Convolve HySICS SSI with TSIS SIM ILS
9	Generate unit conversion factor: divide SIM SSI by HySICS SSI
10	Interpolate unit conversion factor to nadir science scan wavelength map

Step	Description
11	Multiply nadir science scan data by unit conversion factor

5.1.3.19 3-Pixel Averaging

Following the creation of the reflectance and radiance data products for every pixel in a full image, the measurement on every three pixels is averaged in the spatial dimension, reducing the size of the data from 480 x 640 pixels to 159 x 640 pixels [algorithm 1F]. This step has the benefit of not only reducing the size of the images, but also reduces the random noise uncertainty contributors by the square root of three. The geolocated super-pixel will be specified at the center of the central pixel in the average. It should be noted that this step must come after all pixel-level corrections, including the flat field correction (section 5.2.2) and the linearity correction (section 5.1.3.7).

This step is particularly straightforward for the radiance data product, where the pixels can be directly averaged since radiance is a primary unit of measurement. For the reflectance case, however, the proper method is to average the radiance value in the numerator, and the irradiance value in the denominator, as shown in equations 50and 51.

$$R_1 = \pi \frac{L_{1,\,obj}}{E_{1,Sun}}, \quad R_2 = \pi \frac{L_{2,\,obj}}{E_{2,Sun}}, \quad R_3 = \pi \frac{L_{3,\,obj}}{E_{3,Sun}} \tag{50}$$

$$\bar{R} = \pi \frac{\overline{L_{obj}}}{\overline{E_{Sun}}} = \pi \frac{\frac{1}{3} \cdot (L_1 + L_2 + L_3)}{\frac{1}{3} \cdot \left(E_{1,\,Sun} + E_{2,\,Sun} + E_{3,\,Sun}\right)} \tag{51}$$

Where the 1, 2, and 3 in the subscripts indicate the three pixels that are being averaged. The HySICS measured solar spectral irradiance is a single vector of 640 values that is nearly the same for every row, or pixel, in this set of equations: $E_{1,\,Sun} = E_{2,\,Sun} = E_{3,\,Sun}$. In this case, the average reflectance reduces to:

$$\bar{R} = \pi \frac{\frac{1}{3} \cdot (L_1 + L_2 + L_3)}{E_{Sun}} = \frac{\pi}{3}(R_1 + R_2 + R_3) \tag{52}$$

Which is equivalent to the average of the three reflectance pixels. Therefore, to create the 3-pixel averaged reflectance image, the average of every three pixels will also be used.

It should be noted that the solar irradiance term actually does change very slightly between the three pixels due to the spectral distortion, which shifts the spectrum on different rows. However, this shift amounts to 0.006 nm, or 1/510th of a pixel of shift over the three pixels, and is ignored.

At 350 nm, this shift is half the step size of the Chkur high-resolution solar spectrum pictured in Figure 70.

Note that the final row, number 478, is not averaged with the two extra dark rows, which makes the total number of rows 159 rather than 160.

5.1.3.19.1 3-Pixel Averaging Implementation

Step	Description
1	Loop through every column
2	Average pixels 1, 2, 3 within the column for both radiance and reflectance images, and place result as pixel 1 in new image
3	Repeat on next set of three pixels, and continue through pixels 475, 476, 477

5.2 In-flight Calibration

In order to calibrate the CPRS instrument, both $C(\lambda)$ and $\alpha(\lambda)$ must be determined [3]. $C(\lambda)$ is completely measured during flight through a series of calibration measurements, consisting of the solar irradiance scan (section 5.2.1), the 0.5 mm aperture flat field, and the 20 mm aperture flat field (section 5.2.2). The solar irradiance scan is the previously described measurement of the total spectral irradiance of the Sun, $S_{Sun,t=1}$, and, with some manipulation, can be comparable to the solar spectral irradiance from a secondary instrument. All images taken with the instrument must also be corrected for gain variations in each pixel, which due to variations in the optical surfaces, are different for the 0.5 mm aperture and the 20 mm aperture. As a result, a measurement of the instrument flat field measurement must be made twice.

The instrument also contains an on-board HgAr Pen-Ray lamp, used during the flight to match the wavelength scale of across all measurements. The lamp emits fixed atomic spectral lines that can be used to determine the wavelength scale of the instrument, as described in section 5.2.3. In addition, the CPRS will have the capability to measure a dark portion of space to determine the amount of residual blackbody radiation from the blank aperture used for dark images, described in section 5.2.4. These on-orbit calibrations are described by the flowchart algorithms in Figure 1 - Figure 5.

The instrument attenuation factor, $\alpha(\lambda)$, is measured on the ground. There are two primary components to the attenuation: the sensor integration time, and the 0.5 mm to 20 mm aperture ratio. Since measurements at various exposure times will be made during the mission, the linearity of the sensor must be well understood and characterized, as described in [2]. The aperture ratio, which serves the double purpose of attenuating the measured Sun irradiance and reducing the UV exposure in the instrument, is also measured in a laboratory over all wavelengths, also described in [2].

5.2.1 Solar Irradiance Scan

The solar irradiance scan is a cross-slit scan of the disk of the sun meant to measure the spectral solar irradiance in native instrument units, DN, described in section 3.1.3.4. When measured by the HySICS instrument, it represents the $S_{Sun,t=1}(\lambda)$ term within the unit conversion factor, $C(\lambda)$. The scan begins -1.5 degrees from the center of the solar disk (which is approximately 0.5 degrees in diameter in the HySICS spectral range), scans the instrument slit perpendicularly across the disk at 0.079 degrees per second with an acquisition frequency of 15 Hz, and ends at +1.5 degrees from the center of the solar disk, as shown in Figure 56. At the beginning of the scan, the solar disk will not be within the instrument field of view, but a small amount of diffracted light from the edge of the entrance aperture will be visible. As the scan progresses, and the Sun gets closer to boresight, the amount of visible diffracted light will slowly increase. When the solar disk comes into view, the amount of light will rapidly increase, reaching a maximum at the center of the disk, as shown in Figure 57, a solar irradiance scan from the HySICS balloon flight.

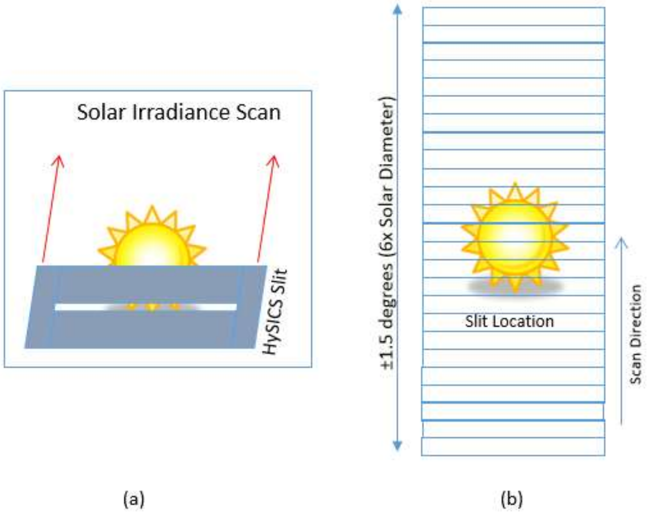

Figure 56. Conceptual diagram of solar irradiance scan. Slit width and height are not to scale in either image. 2a. shows conceptually how the slit moves across the solar disk. Since the 4MA telescope images the sun directly onto the slit plane, the instrument takes a picture of the sliver of Sun that makes it through the slit. 2b. shows the full range of the scan compared to the size of the solar disk. The scan will start 3 solar diameters (1.5 degrees) from the center of the disk, and end 3 solar diameters on the other side. The range of the scan is chosen to collect as much diffracted light as possible at the edges of the scan.

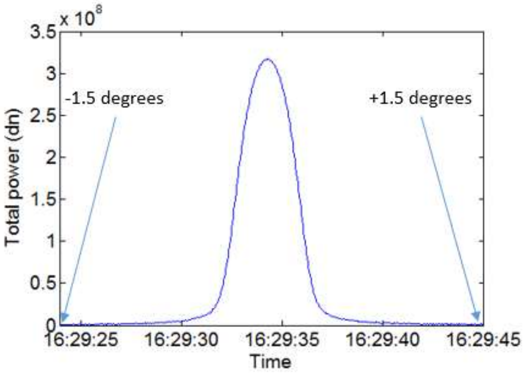

Figure 57. Total measured power (DN) in a solar irradiance scan from HySICS balloon flight. At the left and right sides of the scan, only light diffracted off the edges of the input aperture can be seen. In the middle of the scan, the solar disk comes into the instrument field of view, and the measured power rapidly increases.

Since the HySICS Pointing System (HPS) is an azimuth-elevation gimbal, it is only possible to scan perpendicularly to the Sun if it is located on the plane perpendicular to the Q1 gimbal axis, shown in Figure 58. In this specific case, due to the expected mismatch between the acquisition frequency, the slit angular width, and the scan rate, parts of the sun will be measured multiple times. If both the scan rate and the acquisition frequency are constant, the oversampling of the solar disk is also constant. However, in the more general case, the Sun will not be located on the plane perpendicular to the Q1 gimbal axis, and the scan will arc across the center of the solar disk, as shown in Figure 59a. When this occurs, the scan geometry is further complicated by the apparent rotation of the solar disk due to the motion of the ISS around the Earth, shown in Figure 59b. In the general case, the per-pixel scan rate, which is a scaling factor in the SSI integration, is calculated in ECI (Earth Centered Inertial) coordinates, which removes this disk rotation.

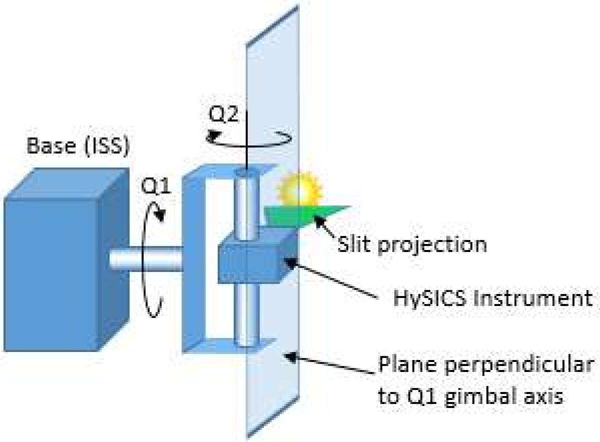

Figure 58. CPRS gimbal orientation and solar disk location for rectilinear scanning. This figure highlights the specific case when the Sun is located directly on the plane perpendicular to the Q1 gimbal axis. In this orientation, the Q1 axis will move the slit linearly across the solar disk.

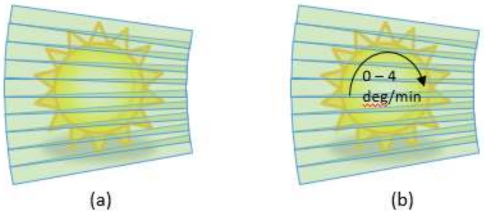

Figure 59. Generalized slit motion across solar disk. 5a. represents the motion of the slit across the face of the disk when the Sun is off the plane perpendicular to the Q1 gimbal axis. The arc will have higher curvature the farther the Sun gets from the plane. In the real case, in 5b, the Sun will also have an apparent roll due to motion of the ISS around the earth. All of these motions will need to be accounted for to calculate the oversampling of each point on the Sun.

Knowledge of the instrument pointing and acquisition cadence during the scan acquisition times is necessary to determine the oversampling factor of each pixel in each image (see equation 24). Although not used in the SSI calculation, the geometric slit width will also be measured by a non-contact optical measurement at NIST, Gaithersburg. A similar measurement of the HySICS balloon flight slit is shown in Figure 60. The HySICS balloon slit width was 28.297 um. Throughout the scan, HPS and resolver data will provide enough information to convert the pixel lines of sight into ECI coordinates. This set of angular coordinates is inertial, and includes both ISS motion in addition to scan motion. The apparent angular scan rate is calculated in ECI coordinates. On the balloon flight, the HySICS Fine Sun Sensor (FSS) was used to determine the scan rate. Note that for the CLARREO HySICS gimbal system, the HFSS does not provide enough information to completely decouple the two pointing axes. However, as an example, Figure 61a shows the FSS yaw position during a solar irradiance scan. In the simple case of a linear scan, rather than the more general arc scan, the oversampling of each measurement can be determined from the slope of the FSS yaw position, shown in Figure 61b as degrees per image. In post processing, each image is inversely scaled by its oversampling factor in the specific case of a linear scan, and each pixel is inversely scaled by its oversampling factor in the general case (equation 31).

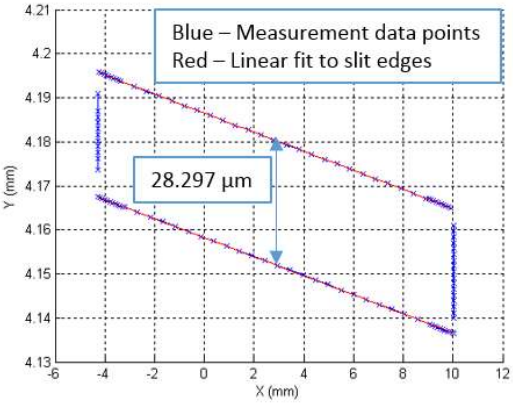

Figure 60. NIST measurement of HySICS balloon slit. An optical, non-contact measurement of the HySICS balloon slit, which is skewed by the high aspect ratio of the plot (80 µm high by 18 mm wide), shows that the slit is 28.297 µm wide, corresponding to a 70.7425 arcsec field of view in the across-slit dimension.

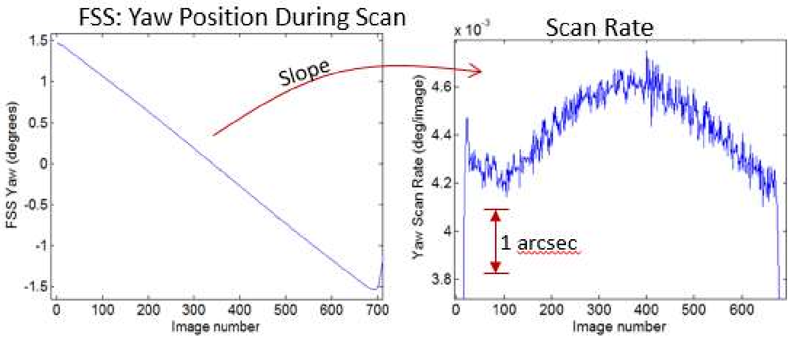

(a) (b)

Figure 61. Fine sun sensor yaw position during HySICS balloon flight solar irradiance scan. Figure 61a shows the position of every image during the scan, and Figure 61b shows the numerical derrivative of the position, which indicates the instantaneous scan rate at each image. The scan rate is one component of the oversampling factor for each image in the scan.

After the integration scaling factors (the per-pixel scan rate, per-pixel along-slit FOV, and acquisition period) have been applied [algorithms 7A and 7D], columns of each image can be summed, producing a 638 point vector for each image [algorithm 7B]. Only a small range of the FPA image is used in the along-column integration step, of 1-1.5 degrees, to capture the diffracted light where it is visible, but not further, which increases the noise in the summation, since read noise is summed in quadrature for each pixel in the integration (section 6.5.2.2 and 6.5.1.2). The final range of the summation will be determined by on-orbit solar data. Integration in the other dimension, across images, is accomplished by summing the vectors [algorithm 7C]. This summation produces a plot similar to that shown in Figure 62. This plot represents the total power detected in the scan for every wavelength bin, and is comparable to plots of the total solar spectral irradiance from other instruments or models. There are a couple of key features in the HySICS-measured solar spectral irradiance from the balloon instrument, including the two dips at 650 nm and 1190 nm, caused by the boundary of the order sorting filter located just in front of the camera, and the very low efficiency in the UV and visible regions, from 350 – 800 nm, due to the low relative efficiency of the HySICS grating. A similar dip is expected around 615 nm on the HySICS instrument, due to an edge in the order sorting filter.

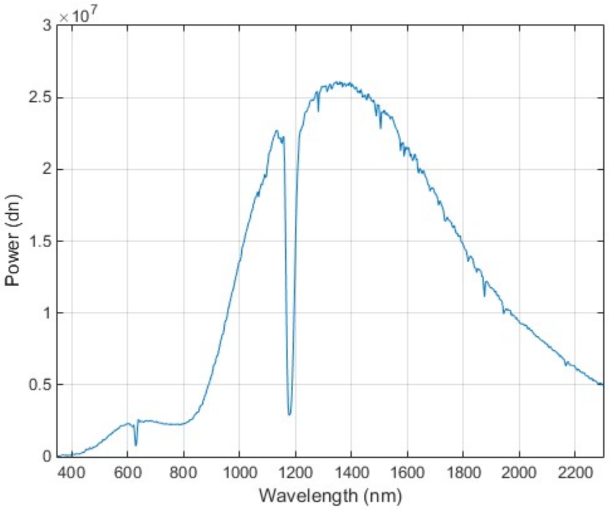

Figure 62. HySICS-measured solar spectral irradiance (un-calibrated). This plot represents all the light collected by the HySICS balloon instrument during a solar spectral irradiance scan, in DN. It has been integrated in both spatial dimensions, and the integration factors for every pixel have been applied.

5.2.1.1 Solar Irradiance Scan Integration Algorithm Implementation

The algorithmic implementation of the solar irradiance scan described thus far includes applying three integration scaling factors (from equation 31) and an integration of multiple images [algorithms 7A – 7D]. The multiplication factors are the per-pixel angular scan rate, the per-pixel along-slit field of view, and the image acquisition period. The angular scan rate and the acquisition period can also be multiplied together to equivalently give an angular scan distance, rather than rate. In the most general case both the per-pixel integration factors are applied to each image as a multiplication factor associated with each row. The multiplication can be implemented either as each element of a matrix multiplied by another matrix which has constant rows, as is shown in Figure 63, or as a for-loop where each row is multiplied by the oversampling factor at the field location of the row. The resulting image is then added to the cumulative sum of all images in the irradiance scan.

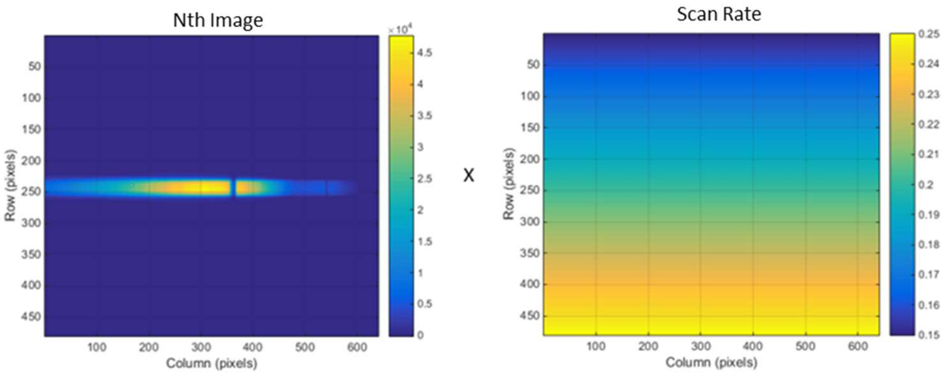

Figure 63. Solar image scaling by oversampling factor. This multiplication step is performed on every image in the irradiance scan. The resulting images are summed together.

In addition, the image acquisition must be synchronized with the gimbal motion. If this is not the case, then only the images taken while the gimbal is sweeping across the solar disk should be used, requiring another step in the processing algorithm. The following sections detail each step of the solar integration algorithms.

5.2.1.1.1 Integration Scaling Factors (Part 1) Implementation

Step	Description
1	Loop through all images
2	For Nth image: Determine per-pixel scan rate based on scan geometry and HPS pointing
3	Obtain per-pixel along-slit FOV (from laboratory measurements)
4	Expand scan rate and per-pixel along-slit FOV into matrix with constant rows. (Also may multiply each row individually, depending on how the for-loop is implemented.)
5	Multiply each pixel by scaling factors

5.2.1.1.2 Integration along Spatial Columns Implementation

Step	Description
1	Loop through all images
2	Sum pixels of each column surrounding the solar spectrum, rows 183 – 279 (only use pixels near the spectrum to avoid adding noise)

5.2.1.1.3 Integration across Scan Images Implementation

Step	Description
1	Loop through all vectors created from previous column-wise summation
2	Sum vectors in the image dimension

5.2.1.1.4 Integration Scaling Factors (Part 2) Implementation

Step	Description
1	Multiply SSI vector by acquisition period (1/15th of a second)

5.2.1.2 Aperture Attenuation

As noted earlier, the instrument contains a large aperture, 20 mm diameter, for Earth viewing, and a small aperture, 0.5 mm in diameter, for solar viewing, and the ratio of the two must be applied in order to be able to properly find the ratio of the two scans [algorithm 5B]. The aperture is located at the instrument pupil plane, which means that the size of the aperture limits the amount of light entering the system, rather than causing a vignette, as would occur in any other plane. Ideally, if the optical path were exactly the same for both apertures, the amount of light entering the system would be proportional to the area of the aperture. However, there are components that behave slightly different depending on the size of the light interaction area, namely the grating, and to a lesser extent, the order sorting filter. To compound the problem, the grating efficiency changes not only with light interaction area, but also with the wavelength of light being used. To account for all these optical variations, the instrument aperture attenuation ratio is measured over the full spectral range [2]. The aperture attenuation ratio from the HySICS balloon flight is shown in Figure 64.

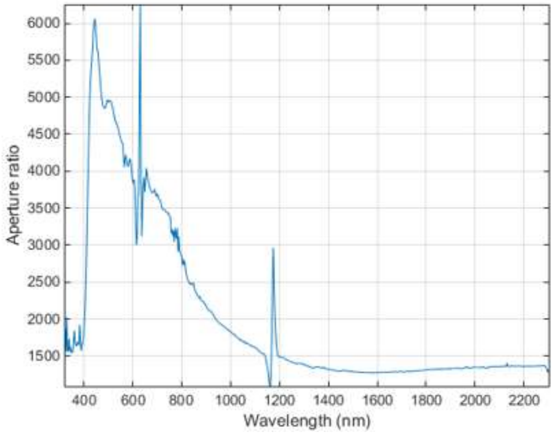

Figure 64. HySICS-balloon aperture attenuation ratio versus wavelength.

The ratio shown here is the ratio of the amount of detected light at each wavelength from the large aperture divided by the amount of detected light at each wavelength from the small aperture. The areal ratio should be around 1600. The large peak between 400 and 1100 nm is due to the reduced grating efficiency for the small aperture, which has fewer grating lines of interaction with the light. Although likely not present in the CPRSP aperture attenuation ratio, the spikes were caused by the edges of the HySICS balloon instrument order sorting filter.

The aperture ratio needs to only be applied to either the nadir science data or the SSI scan. If applied to the nadir science data, the resulting values are reduced by the ratio, as if the nadir data had been collected with the small aperture instead of the large aperture. If applied to the SSI scan, the values are increased, as if the SSI scan used the large aperture. These two options are ultimately equivalent following the reflectance ratio calculation. The aperture ratio is chosen to be applied to the SSI scan to facilitate internal data transfer between functions of the flight data pipelines.

5.2.1.2.1 Aperture Attenuation Algorithm Implementation

Step	Description
1	Interpolate aperture attenuation ratio to the pixel wavelength bins in nadir science data set
2	Divide SSI scan pixel-by-pixel by the aperture attenuation ratio

5.2.1.3 Diffraction Effects

During the solar irradiance scan, the incoming light from the sun will be diffracted by the sharp edges of the input aperture, shown conceptually in Figure 65. The 0.5 mm aperture, when coupled with the 4MA imaging telescope, has a resolvable spot diameter of 461 μm at a wavelength of 2300 nm, significantly larger than the width of the slit. Most of the diffracted light is collected during the course of the scan, as shown in Figure 66, but not all of it. The light that is diffracted at a higher angle than the scan (> ±1.5 degrees) in the plane of the scan, and the light that is diffracted outside of the slit field of view (> ±5 degrees) perpendicular to the scan will fall outside of the collection window.

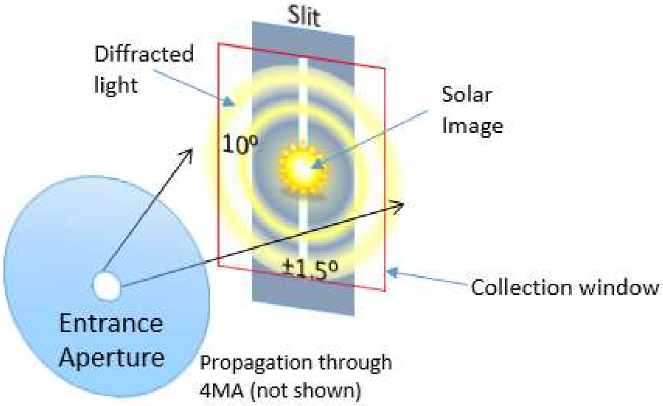

Figure 65. Conceptualization of diffraction from entrance aperture. The collection window is as tall as the slit, and as wide as the scan, centered on the image of the Sun. Although not shown, if the solar irradiance scan is arced due to the gimbal pointing, the collection window will also be arced (as shown in Figure 59).

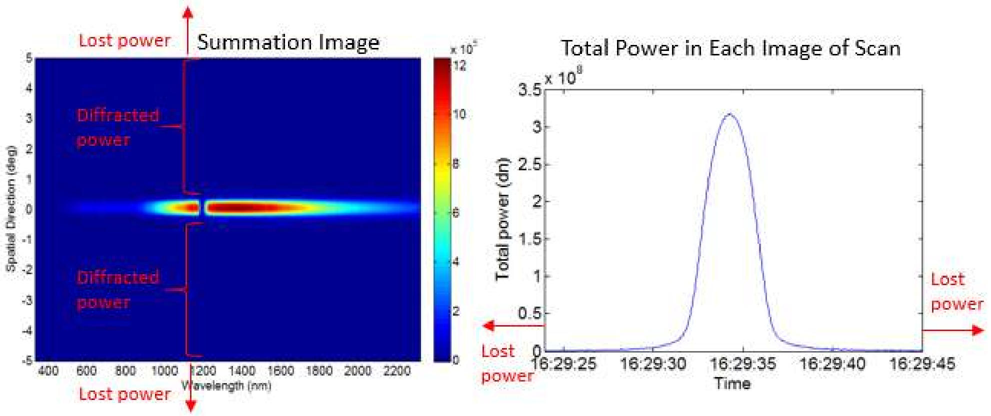

Figure 66. Total diffracted light collected. The left image is the image resulting from a spatial integration in the across-slit direction. The streak through the middle represents the spectrum of the integrated solar disk. Light in the image that falls above and below the center streak represents light that is still collected by the slit, while light that falls above and below the slit, off the image, is lost. Similarly, the plot on the right represents the total power collected by each image during the scan. Light that falls outside of the scan range, off the plot, is lost.

Diffraction effects can be calculated, as described in appendix A. However, during the HySICS instrument measurement campaign, diffraction was directly measured, as described in [2]. In addition, the aperture ratio measurement, also described in [2] was set up to represent the solar field angles as closely as possible, and characterizes all losses through the system, including diffraction. Therefore, the aperture ratio attenuation factor already includes the effect of diffraction on the SSI measurement. The ratio will be adjusted to account for small differences between the solar measurement and the aperture ratio measurement, but these variations are expected to be small compared to the total light diffracted.

5.2.1.3.1 Diffraction Algorithm Implementation

The effects of diffraction are completely captured by the application of the aperture ratio attenuation factor in the SSI data pipeline. A second implementation is not necessary.

5.2.1.4 Saturated Scans

The HySICS instrument will measure less light near both edges of its spectral range, at 350 nm and 2300 nm, due to the combination of solar spectrum, the grating efficiency, and aluminum mirror reflectance. The reduced light contributes to a higher uncertainty in the measurement because of the lower signal-to-noise ratio, and is the primary factor driving increased measurement uncertainty for the solar irradiance scan. By acquiring a second solar irradiance scan with a higher integration time, the signal-to-noise ratio can be increased in the inefficient spectral regions. In the second scan, weak spectral regions will have a higher signal level, and the previously strong regions will be saturated, making them unusable. However, during post processing, the two scans are stitched together into a single integrated image, using the inefficient spectral regions from the second scan and the efficient spectral regions from the first scan. It should be noted that the detector manufacturer, Teledyne, believes that saturation of some portion of the detector will not affect the response of the unsaturated pixels. This problem has been observed in other detector structures, but will not be present in the CHROMA HgCdTe. An experimental verification of the detector will be used to validate the saturated scan methodology.

As an example, during the HySICS balloon flight, two spectral irradiance scans were used. The first one had the entire solar spectrum non-saturated, taken at a 0.67 ms integration time, and the second one that was saturated from approximately 800 nm and above, taken at 4.28 ms. In post processing, to determine the system efficiency, the saturated scan was used for the 350 nm to 800 nm range, and the non-saturated scan was used for the 800 nm to 2300 nm range, as shown in Figure 67. Note that for the balloon flight data, the integration time used on each portion of the spectrum was tracked, and eventually used as part of the system attenuation factor, $\alpha(\lambda)$. For CLARREO HySICS, the data from both these scans will be scaled to 1 RT immediately, which will eliminate the stair-step in the middle of this plot.

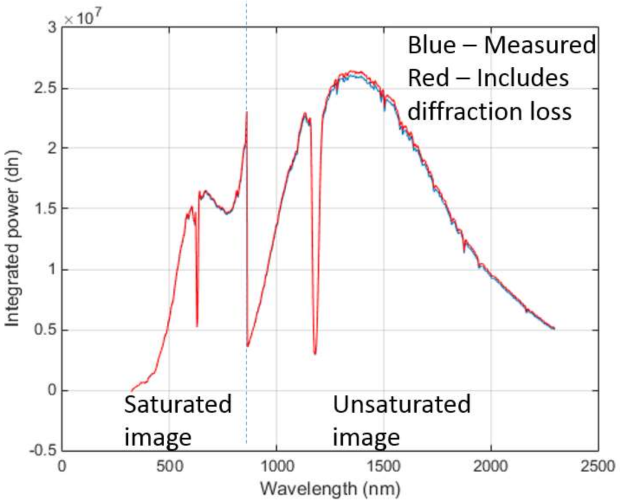

Figure 67. Total integrated light from two stitched solar irradiance scans, a saturated one, and a normal, unsaturated one. The benefit to using the saturated scan technique is the increased signal in inefficient regions of the measured spectrum, which can greatly reduce the uncertainty in the measurement.

5.2.1.4.1 Saturated Scan Algorithm Implementation

The steps outlined in the solar irradiance scan integration, section 5.2.1.1, must be executed for both solar scans, resulting in two solar irradiance vectors, both 640 elements long. The acceptable wavelength regions for each scan are based on where the spectra is unsaturated and the signal is maximized. Only wavelength bins that are unsaturated throughout all images of the scan can be used in the solar irradiance calculation. The expected wavelength region from the initial scan (unsaturated scan) is from 400-1500 nm, and the expected wavelength region from the second scan (saturated scan) is from 350-400 nm and again from1500-2300 nm.

5.2.1.5 Unit Conversion Factor

After correcting for lost light due to diffraction, and integrating the total solar irradiance scans, the final step to generating the unit conversion factor, $C(\lambda)$ is to determine the ratio of the TSIS SIM solar spectral irradiance (W/(m^2 · nm)) to the measured irradiance (DN). An example solar spectral irradiance used for the comparison is shown in Figure 70. Ideally, the unit conversion ratio is the SSI measured by an absolute instrument (TSIS SIM) divided by the SSI measured by HySICS, although it is slightly more complicated when using real instruments. It should be noted that the inverse of the unit conversion factor is a measurement of the full system efficiency. As previously mentioned, the solar spectral irradiance is given by either an instrument flying at the same time as CPRS, such as TSIS SIM [5], or a solar model, as was used for the HySICS balloon flight [3].

In order to calculate the unit conversion factor, the exact solar spectral irradiance, as it would be observed by the HySICS instrument, which is different from the TSIS SIM instrument measurement, must be known. Because these instruments are fundamentally different, the SIM SSI must be transformed into the HySICS SSI.

From a signal processing viewpoint, the SIM SSI is generated by convolving the real solar spectral irradiance with the SIM instrument line shape, and then sampled across the spectrum, as shown graphically in Figure 68. The SIM instrument line shape changes across the spectrum due to the wavelength dependent dispersion of the glass used in its dispersion element, a prism. It is narrowest in the UV, and widest in the IR. The sampling periodicity also changes across the spectrum to match the ILS, with 6-8 measurements per line shape [5]. This amount of sampling is expected to keep interpolation errors low enough to be inconsequential, and the actual required sampling versus interpolation error level will be studied by the TSIS SIM team.

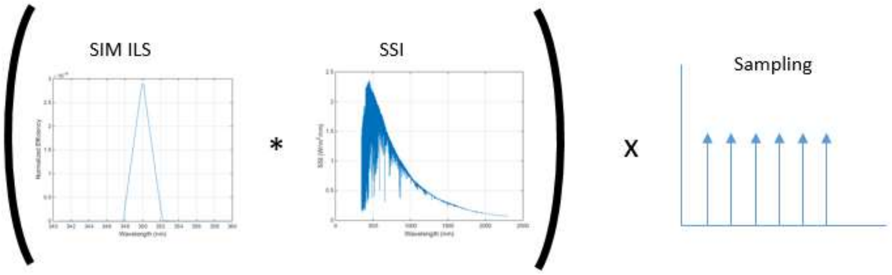

Figure 68. TSIS SIM solar irradiance spectrum from a signal processing viewpoint. The SSI is convolved with the SIM instrument line shape, and sampled periodically over the spectral range. Although not represented here, both the ILS and sampling periodicity vary across the spectrum.

Similarly, the HySICS SSI is generated by convolving the solar spectral irradiance with the HySICS instrument line shape, and then sampling it at each pixel. Pixel sampling is the equivalent of convolving the spectrum incident on the detector by a rect function set at the spectral width of a pixel, and then multiplying by a sampling comb function. The full procedure is shown graphically in Figure 69. The actual ILS measurements from the characterization campaign [2] already have the pixel rect function convolved with the ILS.

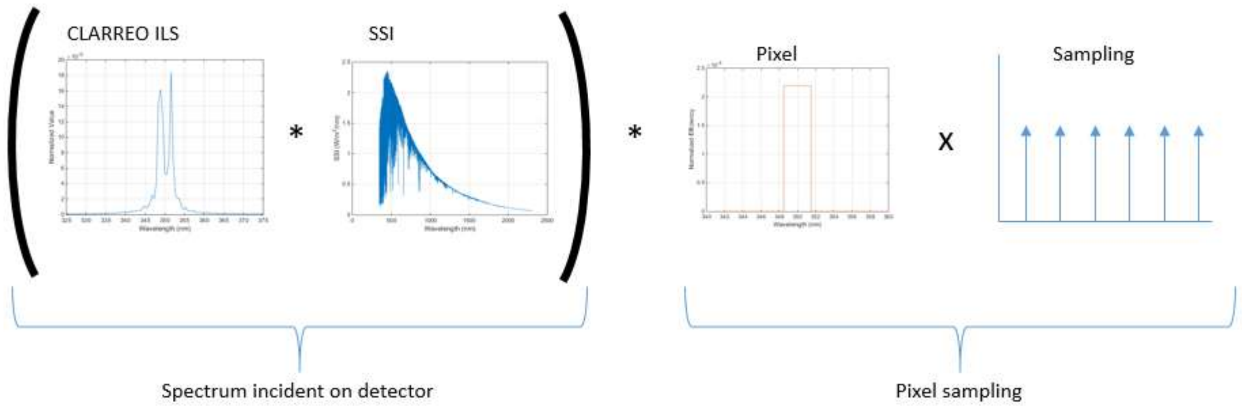

Figure 69. HySICS solar irradiance spectrum from a signal processing viewpoint. The SSI is convolved with the HySICS ILS, and incident on the detector. This signal is pixel-sampled via convolution with a pixel rectangle function and multiplied with a comb sampling function.

In order to match these two solar irradiance spectra, a few mathematical manipulations must be applied. To generate the same SSI measured by both instruments, the SIM SSI needs to be convolved with the HySICS ILS, and the HySICS SSI needs to be convolved by the SIM ILS. If the two instruments both had very high spectral resolution data compared to the spectral width of the ILS, the result of these two convolutions is identical, and they can be compared without adding uncertainty.

However, the HySICS spectral sampling frequency is wider than the SIM ILS from 350 nm to approximately 450 nm. The resulting convolution of the HySICS SSI with the SIM ILS generates a significant amount of error in this spectral region. To reduce the error, the HySICS spectrum is interpolated to a high spectral resolution, matching the SIM resolution, using a cubic piecewise spline. This high resolution HySICS measurement can then be convolved with the SIM ILS.

A simulation of the SSI comparison process is shown in Figure 70 through Figure 73. To simulate the measurement of the SIM SSI, a high resolution solar spectrum (the Chkur hires) is convolved with the SIM ILS, shown in Figure 70. Similarly, to simulate the measurement of the HySICS SSI, the Chkur hires spectrum is convolved with the measured HySICS ILS. It is also resampled at the HySICS spectral bins, Figure 71. These two spectra are assumed to be the measurements from the two instruments. To generate a high resolution version of the HySICS spectrum, it is interpolated up to the spectral resolution of the SIM spectrum, using a spline interpolation. Similarly, the SIM spectrum is interpolated to have a constant spectral resolution, using the step size of the SIM spectrum at around 350 nm. The high resolution HySICS spectrum is convolved with the SIM ILS, and the SIM spectrum is convolved with the HySICS ILS in Figure 73. Ideally, these two spectra should be identical. The ratio between the two spectra is shown in Figure 74. As can be seen, they are within 0.04% of being identical from around 450 nm and above. Below 450 nm, there is a difference between the two spectra due to errors in the spline interpolation compared to the true SSI. This difference spikes at high solar gradient wavelengths, and is as high as 1.5% at approximately 390 nm.

The ramifications of doing this “cross convolution” is that the high-frequency spectral features of both spectra are smoothed out. Where the spectra were already smooth, there is nearly no additional error. The ratio of these two smoothed spectra is the unit conversion factor, which now also has been smoothed by convolution with the ILSes of both instruments. The unit conversion factor (also the inverse of the system efficiency) is dependent on the components of the instrument, specifically the grating spectral efficiency, the aluminum mirror reflectivity, the order sorting filter transmission, and the detector quantum efficiency. None of the inputs to the unit conversion factor have high spectral frequency features, which means that the ratio is expected to be a smooth, slowly varying function, which will be largely unaffected by the convolution smoothing.

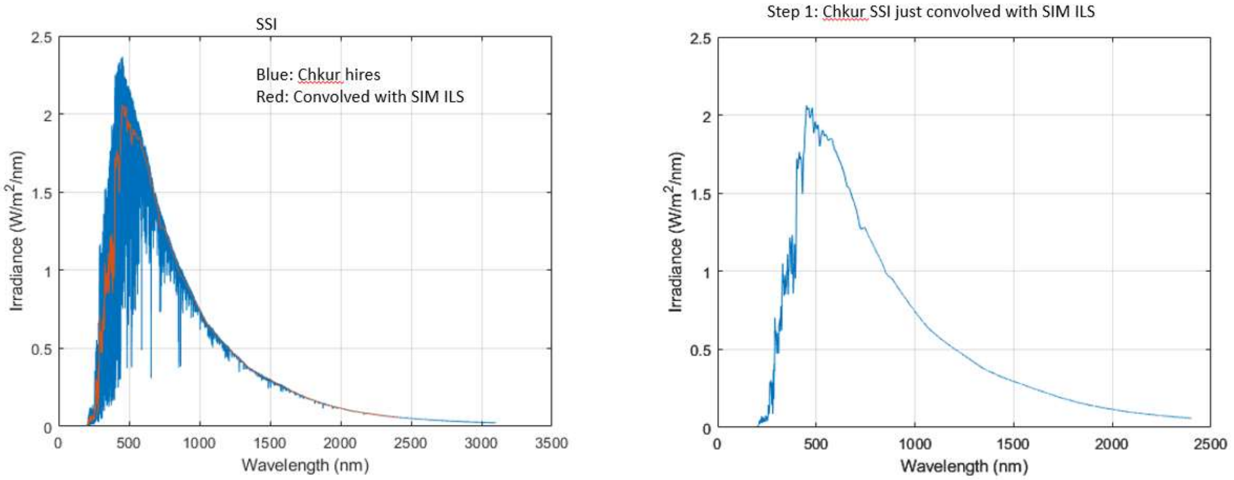

Figure 70. A high resolution SSI (Chkur hires) convolved with the SIM ILS.

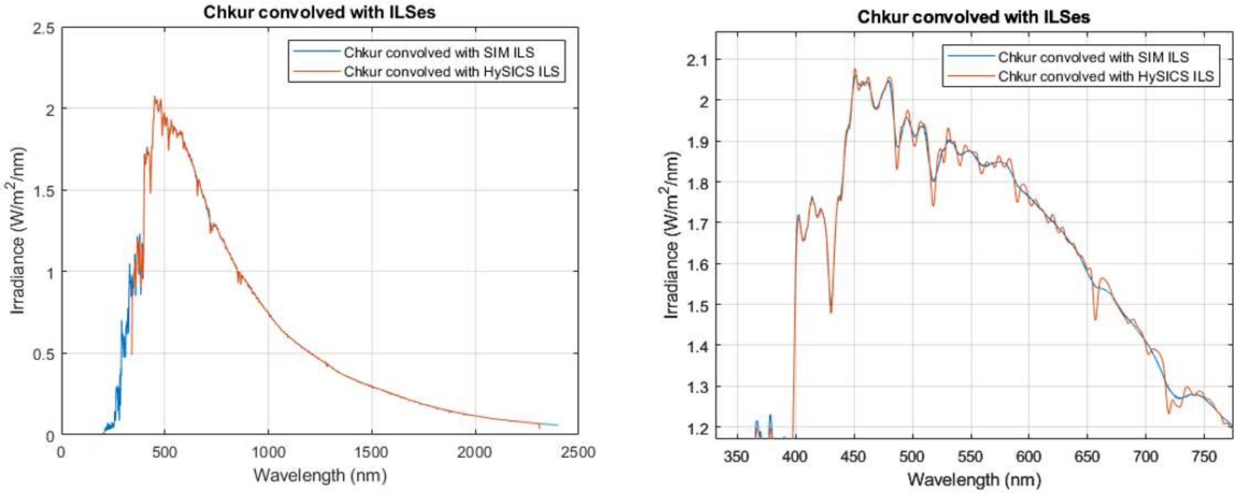

Figure 71. Chkur hires SSI convolved with SIM ILS and with HySICS ILS.

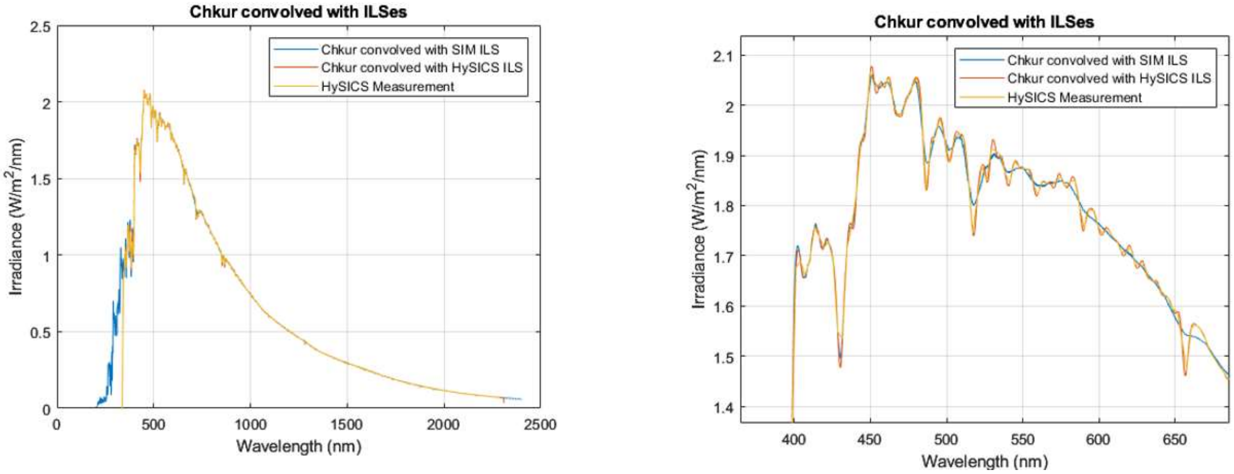

Figure 72. HySICS SSI resampled at wavelength bin locations. The yellow line linearly steps between the sampling locations, causing it to cut off high frequency and curved features.

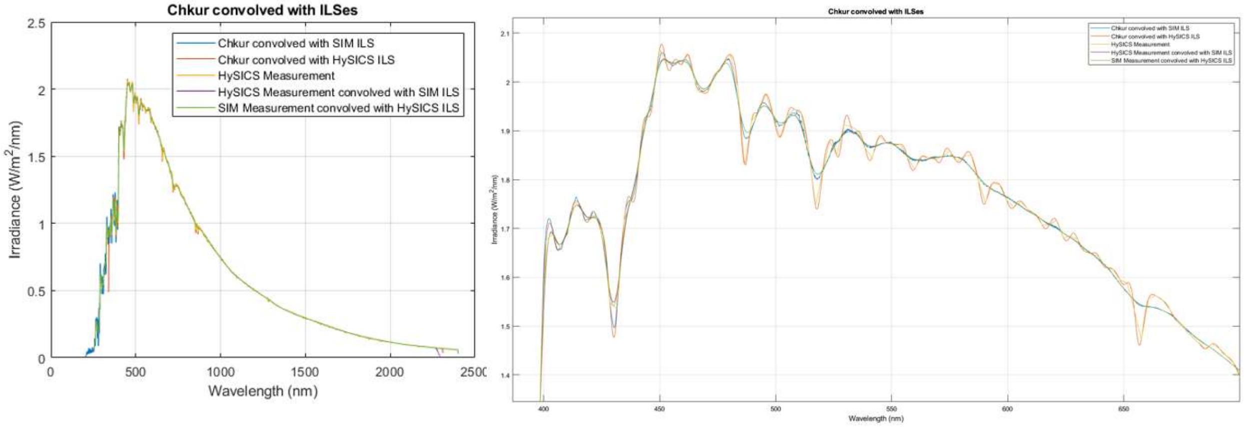

Figure 73. Interpolated HySICS SSI convolved with SIM ILS (purple) and SIM SSI convolved with HySICS ILS (green).

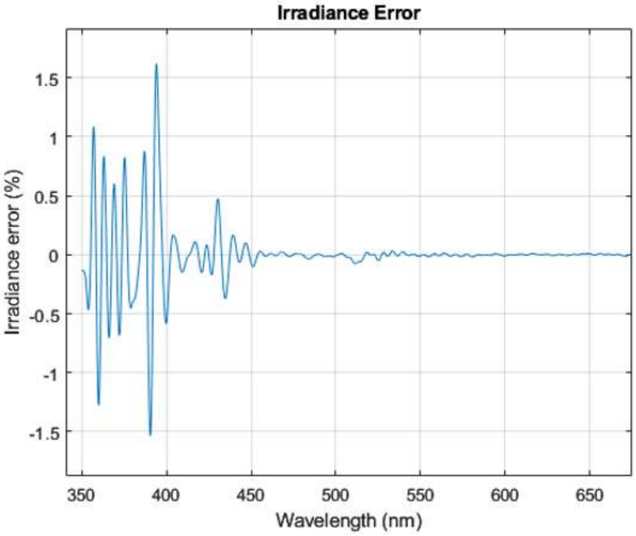

Figure 74. Percentage error between the two cross-convolved spectra. The errors above 700 nm are less than 0.01% ppm.

5.2.1.5.1 Unit Conversion Factor Algorithm Implementation

The unit conversion factor requires manipulation of both the TSIS SIM and HySICS data sets. The TSIS SIM data is convolved with the HySICS ILS, and the HySICS data is approximately convolved with the TSIS SIM ILS. Note that both instrument line shapes must be normalized to have unity area, but that they are known from ground testing. The steps of the algorithm are shown in the following table.

Step	Description
1	Convolve TSIS SIM SSI with HySICS ILS
1a	Linearly interpolate TSIS SIM SSI to the highest spectral resolution in the SSI
1b	Interpolate HySICS ILS to same spectral resolution, normalize to unit area, and center ILS
1c	Zero-pad shifted-ILS to fill out full spectral region
1d	Multiply interpolated-SIM SSI by ILS from 1c
1e	Sum all values and multiply result by wavelength sampling (Digital integral)
1f	Generate new vector with result placed at first wavelength element
1g	Repeat 1b-1f for all wavelengths in SIM SSI from 1a
2	Interpolate HySICS SSI using cubic spline to SIM SSI wavelength scale

Step	Description
3	Convolve HySICS SSI with SIM ILS (repeat convolution steps from step 1)
4	Divide Converted TSIS SIM SSI (1g) by converted HySICS SSI (3) = Unit conversion factor
5	Resample unit conversion factor to HySICS spectral grid

5.2.1.6 High-speed Fine Sun Sensor (HFSS)

During any scan used to observe the sun, the solar spectral irradiance scan and the 0.5 mm flat field, a High-speed Fine Sun Sensor (HFSS, or sometimes just FSS) will be used to determine the pointing location with respect to the center of the solar disk. The HFSS consists of a quad diode placed behind a square aperture and an ND filter stack. If the instrument is pointing directly at the center of Sun, the amount of power on each quadrant of the diode is the same. If it is not centered on the Sun, some of the quadrants will measure a higher level than the others. The relative difference of the HFSS diode can be used to partially determine the pointing, and will be used to actively stabilize the pointing platform in a solar centric coordinate system. During the HySICS flight, the stability of the HFSS pointing measurement was better than 0.7 arcsec.

5.2.2 Instrument Flat Field

Although the primary in-flight calibration for determining the unit conversion factor is the solar spectral irradiance scan, the images in the scan still contain pixel-to-pixel efficiency variations. Unless corrected, these variations can cause the exact same scan to measure different amounts of power if a different part of the sensor is used. The flat field scan concept is to place the exact same amount of light on each pixel in a wavelength bin, and measure the relative efficiency difference between pixels. Fundamentally, the efficiency variation is due to small changes in the full-system optical path from one pixel to the next as well as the gain variation in the camera pixels themselves. Since it is a measurement through the full optical system, the flat field scan must be performed twice; once with the solar viewing 0.5 mm aperture, and once with the Earth and lunar viewing 20 mm aperture, described mathematically in section 3.1.3.3. After the pixel-to-pixel variations are measured, a correction, called the flat field correction, can be applied to each image. The 0.5 mm flat field correction is applied to every image taken with the 0.5 mm aperture, while the 20 mm flat field correction is applied to every image taken with the 20 mm aperture.

5.2.2.1 Small Aperture Flat Field Scan Description (Solar Flat Field)

Flat-fielding the HySICS instrument is a full-system scan, and therefore needs to occur twice: once using the smaller solar-viewing aperture, and once using the larger Earth-viewing aperture.

Light passing through the two apertures interacts with different parts of the optical elements in the instrument, which can have different absorptivity, reflectivity, or efficiency. All of these variations in the optical train are measured during the flat field calibration scans and compensated during the post-processing application of the flat field correction.

Although different apertures are used for the two scans, the concept for both is to use a stable light source that can be swept across every pixel on the sensor, enabling a measurement of the relative response, or gain, of each. In orbit, the most stable light source is the Sun, which is used directly for the small aperture and indirectly for the large aperture flat field scans. An equivalent large aperture will be covered with a transmissive diffuser for the large aperture flat field scan. In both cases, the solar disk is scanned in the slit direction from the top of the imager, 5 degrees above bore sight, to the bottom of the imager, 5 degrees below bore sight, while images are continuously captured at a 15 Hz cadence. In practice, the scan is extended by at least 0.25 degrees on both sides to ensure the full instrument field of view is covered. (The scan is currently set at -6 degrees to +6 degrees around the center of the Sun in the CONOPS document [20].) The small aperture scan rate is 285 arcsec/second, and the full scan takes approximately 151 seconds to complete, during which time the light is considered to be stable. The large aperture scan rate is 1141 arcsec/second, and the full scan takes approximately 38 seconds to complete. For the small aperture scan, the resulting data is a series of images containing the solar spectrum stretched across the full sensor in the spectral direction, and moving down the sensor for each successive image in the spatial direction, as shown in Figure 75.

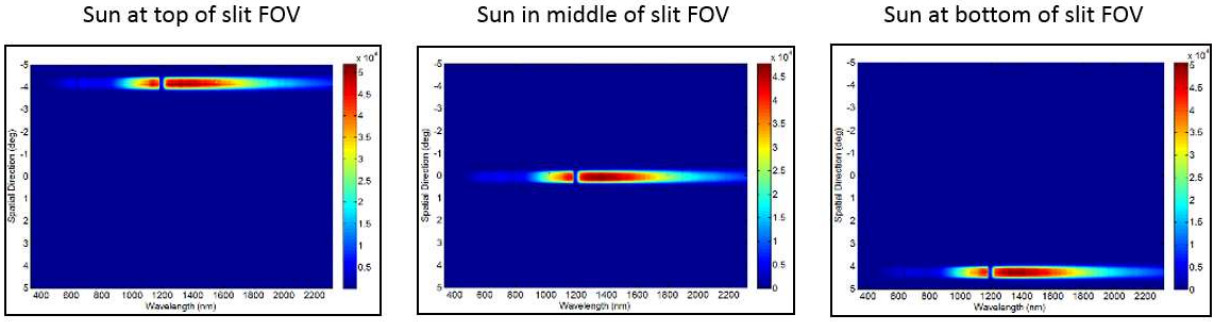
Sun at top of slit FOV

Sun in middle of slit FOV

Sun at bottom of slit FOV

Figure 75. Successive images during a solar flat field scan. The left image show the solar spectrum when the Sun is at one edge of the slit, the center image shows the Sun in the middle of the slit, and the right image shows the Sun at the other edge. Since the amount of light from the solar disk does not change during the scan, the gains of each illuminated regions of the camera can be compared to each other. A full-sensor flat field calibration is generated by illuminating all pixels of each wavelength with the same source.

Similarly to the solar spectral irradiance scan, the motion of the slit field of view due to the CPRS gimbal system is only on an orthogonal, non-coupled coordinate system only if the solar disk is in the plane perpendicular to the Q1 axis (Figure 58). In this case, motion of the Q2 axis moves the instrument bore sight parallel with the slit, and the Q1 axis will track the motion of the solar disk due to the movement of the ISS. In the general case when the solar disk is off the plane, the solar disk will rotate due to the motion of the ISS, and both gimbals will be required to track the sun. It should be noted that in the orthogonal gimbal movement case, every point along the sun within the slit field of view is scanned along every pixel in the instrument. As a result, there is more viable flat field data which can be used to reduce noise through averaging and to estimate measurement uncertainty. The more the solar disk rotates during the scan, the fewer points can be used in the data analysis, with the least amount of solar disk data occurring when only a single point on the sun is scanned along every pixel in the slit. The one notable exception to this rule occurs when the solar disk is deemed rotationally symmetric in its uniformity, meaning that there are no spatial features such as Sun spots, and the flat field scan is directly through the center of the solar disk.

5.2.2.2 Large Aperture Flat Field Scan Description (Transmissive Diffuser Flat Field)

It is more difficult to find a stable, uniform light source on orbit for use with the 20 mm aperture. Although the Moon can be used in a similar manner as the Sun described in Section 5.2.2.1, it is not a spatially uniform source, which drives the pointing requirements during the scan to an unachievable level. Instead, a transmissive diffuser will be placed in front of a duplicate 20 mm aperture, and the scan will be repeated on the Sun. The transmissive diffuser, shown in Figure 76, is a 100 µm thick piece of PTFE (Teflon). This diffuser acts as a nearly Lambertian source placed at the pupil plane of the 4MA telescope. If it had a perfectly Lambertian BTDF (Bi-directional Transmissive Distribution Function), the same amount of light would be diffused into each pixel angle, and no scan would be necessary. However, to account for the non-Lambertian nature of the BTDF, the Sun will again be scanned, ensuring that every field angle (for each pixel) has the same incident angle, shown for two field angles in Figure 77. There is also a very small thickness change in the PTFE, also shown in Figure 77, due to the non-normal incident and output angles for increasing field angles. In the range of ±5 degrees, the equivalent PTFE thickness changes by 0.4%. The resulting BTDF is expected to also change by a small amount, causing a variation in the amount of light incident on each pixel. This variation is expected to be very small, and will be measured during ground testing (see Characterization and Calibration Plan, Agile #157567 [2]).

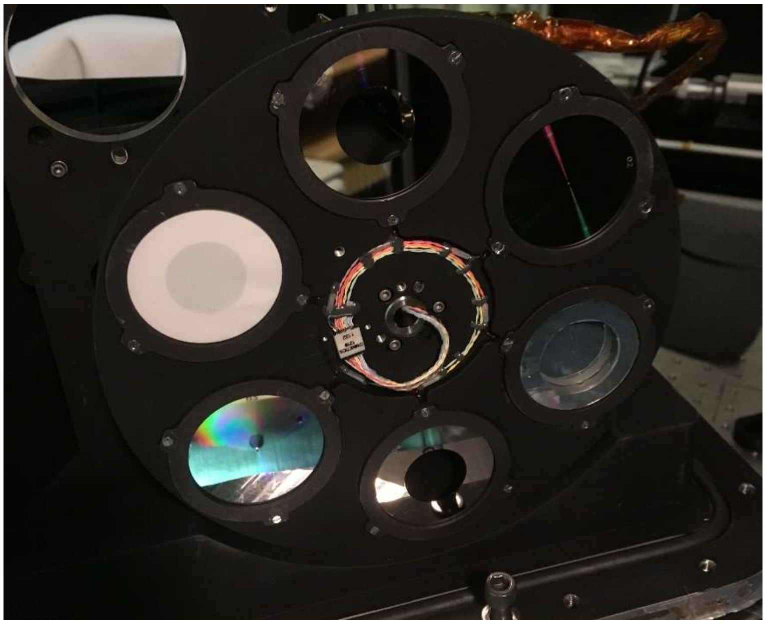

Figure 76. Transmissive diffuser mounted on the HySICS balloon instrument aperture wheel. The diffuser is a white piece of PTFE placed on top of an equivalent 20 mm aperture.

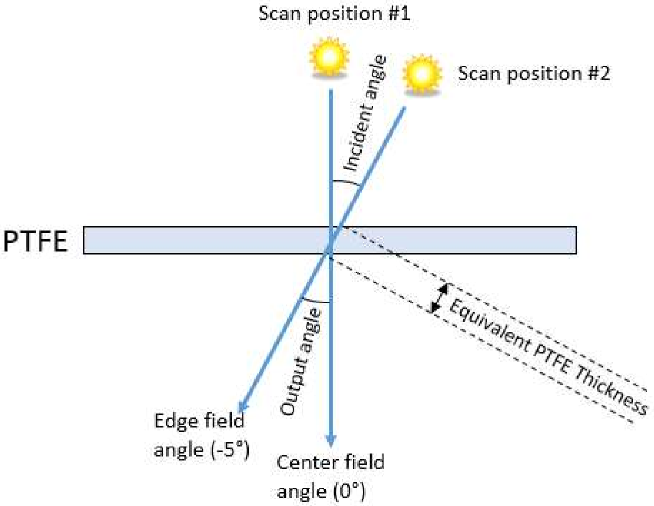

Figure 77. Simplified transmissive diffuser scan geometry. The incident and output angles are identical throughout the scan, which minimizes the amount of BTDF variation, although there is still a small change due to the equivalent thickness of the PTFE increasing at higher field angles.

The transmissive diffuser is nearly immune to on-orbit degradation by virtue of being placed at the pupil plane, directly on the aperture. As a result of this placement, all pixels use the exact same portion of the transmissive diffuser. If there is a mark, or non-uniform degradation on the diffuser, all pixels see the same mark, and the relative pixel-to-pixel light level is unchanged.

The light level of the Sun propagating through the diffuser is similar to that of reflected Sun off thick clouds. The scattering of the incident light nearly evenly into the full output hemisphere reduces the amount of light traveling along each field angle, and does not saturate the sensor despite looking at the Sun with the 20 mm aperture.

5.2.2.3 Flat Field Scan Analysis

Along each pixel column on the sensor, which corresponds to a single wavelength bin, variation in the detected power of the light source is considered to be variation in the response of the system at each pixel. Each wavelength bin is analyzed separately, since there is unknown spectral power structure in the light source (the Sun). In an ideal measurement, the system response would be measured at the peak of the light source as it passes each pixel during the scan. In practice, the imaging cadence will not be perfectly synchronized with the scan motion, and therefore the pixel responses cannot be directly compared, but instead must be compared with an average, super-sampled peak, built up using all pixels in a column. The central image of the light source as it travels across each pixel is determined from a curve fit and provides sub-integer accuracy in the location of the peak within the images. The peak from each pixel is interpolated and lined up with all the other peaks based on its sub-integer location, and used to generate the average peak. The average peak is defined as the unity gain peak, and all other peaks, as seen by each pixel, are compared to it, shown in Figure 78. Once the average peak has been determined, it can be used to more accurately locate the peak center of the light source on each pixel, iterating on the process and generating a new average peak until it stays constant from iteration to iteration.

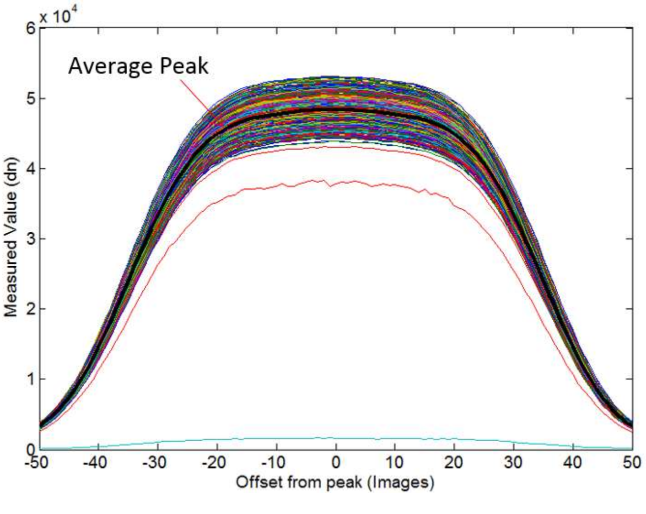

Figure 78. Measurement across solar disk for all pixels in wavelength bin at 1376 nm. This plot shows 480 separate measurements, one for each pixel in column 300 (1376 nm), and the average of all the measurements, in a thick, black line superimposed on the other plots. The variation in each pixel measurement is due to optical variations in the instrument, and gain variations in the camera pixels and electronics.

The usable width of the average peak to compare pixel gains is determined by the number of points along the Sun that cross every pixel in the column. For a linear scan, with no rotational motion of the solar disk, all points along the disk will cross every pixel. At the scan rate used for the HySICS balloon flight, 31 points across the solar disk were used. Any rotation of the solar disk or arcing of the scan around a fixed slit location due to gimbal geometry reduces the number of points that can be used.

Another way to look at the flat field scans is to compare each pixel value with all the other pixels in the wavelength bin. This comparison can be done as many times as there are points along the solar or lunar disk that pass through every pixel, or 31 times in the HySICS balloon flight solar case. Each of these 31 points creates a separate flat field. The average of these 31 flat fields is defined as the nominal flat field. The standard deviation of these 31 measurements can be taken as the random component of the uncertainty, and includes read noise and shot noise, since they are present in every image. The accuracy of both the average and the standard deviation of the comparisons increases with the number of points that can be used along the solar disk.

The transmissive diffuser flat field scan has the benefit of having a very flat peak moving across each pixel, and therefore a large number of measurements can be easily used. It is likely that the number of measurements in this case may be significantly more than for the small aperture (to be determined during commissioning), rather than just 31 in the solar flat field case. It is also immune to apparent solar rotation from the movement of the ISS, since all points on the solar disk are scrambled together via the diffuser.

Once the relative response of every pixel in every column has been determined, a flat field image can be built up, as shown in Figure 79, for both apertures for the HySICS balloon instrument. By definition, the average value of these images is unity, since the relative gain of all pixels is compared to the average gain. It should be noted that the flat field image is actually only a comparison of the pixel response in the spatial dimension, along each column of the image; there is no information to compare a pixel response in the spectral dimension, along rows of the sensor. The flat field image is used to inversely scale every image acquired by the HySICS instrument. If a pixel has a higher than average response, its measured value is reduced, and the opposite occurs for a pixel with a lower than average response.

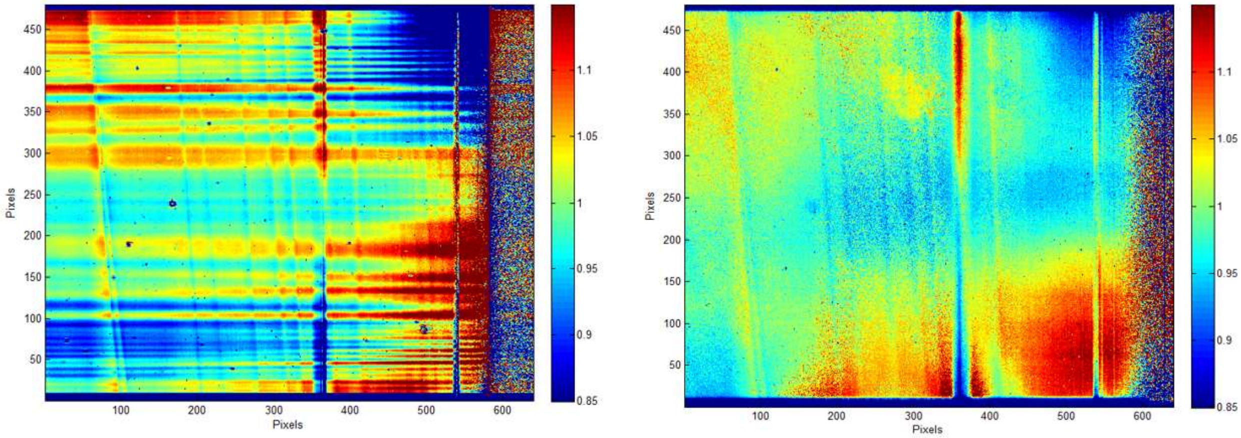

Figure 79. The HySICS balloon flight flat fields. The left image is the flat field for the 0.5 mm aperture, and the right image is the flat field for the 20 mm aperture. The colors on these plots represent the relative gain of each pixel compared to the average of all pixels in the same column. The noisy area on the right edge of both plots is the most UV portion of the sensor, which is inefficient, and has a very low signal to noise ratio.

5.2.2.4 Spectral Distortion Correction

Even the most perfectly aligned system will contain slight spectral distortions, such as keystone, over the full spatial range. The Pen-ray wavelength algorithm (section 5.2.3) identifies the wavelength for every pixel on the detector, including the distortion. During the flat field calibration scans, however, distortions mean that there is a slightly different part of the spectrum used for each row, even if the exact same portion of the solar disk is used in the flat fielding algorithm.

To correct for the spectral distortion, the spectrum on each row of the detector is interpolated, using a cubic spline to try to pick up curves in the spectral features, to the wavelength that should have been seen at each column with no distortion. One version of a measured distortion map, used to identify the amount of interpolation at each pixel, is shown in Figure 80.

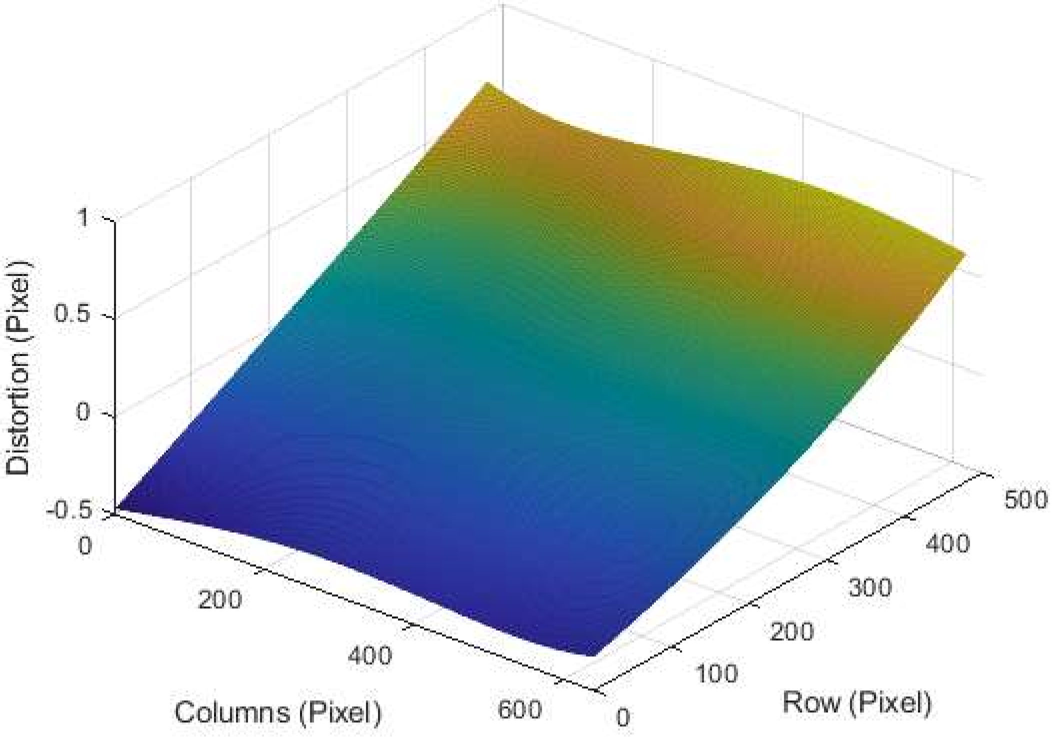

Figure 80. Measured distortion map, showing distortion, in spectral pixels, relative to the spectrum on the center row of the detector.

Note that the distortion map may change slightly with temperature, but can be re-analyzed with each Pen-ray measurement. If it is found to change too much during on-orbit operations, the re-analysis will be automated.

As might be expected, the distortion causes more error where there are high-gradient spectral features, and very low error where the spectrum is smooth and flat. The spline interpolation is more accurate where the spectrum is smooth as well. For the solar spectrum, the majority of the spectral distortion error will occur below 450 nm, where there are higher gradient features.

5.2.2.5 0.5 mm Flat Field Algorithm

The flat field is a relative measurement which is fundamentally just a comparison of how each pixel responds to the same amount of light. The difficulty in the scan algorithm is in choosing the right image for each pixel [algorithm 8A]. The image choice manifests itself in understanding exactly when the solar peak passes across each pixel during the scan. It can be done in two ways: either during post processing using a peak-finding technique, or with the fine sun sensor or HPS resolver data, if it is shown to be stable enough. For reference, the FSS data in the HySICS balloon flight was stable to better than 1 arcsec during solar pointing periods. If properly ascribed to the image data, this would provide better than 1/75th of a pixel of location accuracy. The first part of the flat field algorithm [algorithm 8A], which choses the proper scan images to be used for each row, assuming the FSS data will not be used, is outlined in the following table.

Step	Description
1	Step 1: Locate solar peak
1a	Assemble vector from all images of scan of one pixel (at a high-signal wavelength). Number of elements in vector is same as number of images in scan = pixel peak vector
1b	Curve fit vector with Gaussian to find initial peak location.
1c	Repeat 1a – 1b for all pixels in the column
2	Step 2: Generate average solar peak
2a	Resample and interpolate pixel peak vectors to ensure at least 1 arcsec resolution (~20x higher sampling if the scan rate was ~280 arcsec/sec)
2b	Line up all pixel peak vectors in a matrix, centered on the peak location for each vector (Matrix will contain 480 rows, one for each pixel.)
2c	Find mean of matrix along second dimension (not the peak vector dimension) = Average solar peak
3	If necessary, repeat steps 1a – 1b with average solar peak curve fit instead of Gaussian
4	If necessary, repeat steps 2a – 2c to generate more accurate average solar peak
5	Step 3: Determine usable portion of the solar disk based on scan rotation due to gimbal motion and number of positions that can be used to make a flat field
6	Step 4: Generate vector identifying image corresponding to solar peak crossing each row

This algorithm identifies the image number within a scan that corresponds with the solar peak landing on a particular row. Once the images have been chosen, the flat fields are created [algorithm 8B]. To do this, the algorithm uses the location of each position within the images that correspond to one particular flat field. The image number can be fractional, and is interpolated between neighboring images. In the example above, there are 31 such locations. Each of the locations is interpolated at each row, resulting in the signal that each pixel would have seen had the image been taken at exactly the instant that the portion of the solar disk crossed it. This signal is distortion corrected as described in section 5.2.2.4. The relative signal level of each pixel is compared to the average signal within that column at each wavelength. The average of the resulting values along every column is therefore forced to be unitary. In other words, the signal on a particular pixel may be slightly higher or slightly lower than the average of the full column of pixels, indicating its relative gain.

The process is repeated for every wavelength, which generates the full image flat field that also has a mean value of one. It is also repeated for every one of the identified positions on the solar disk, or 31 locations in the above example, generating 31 separate full image flat fields. These fields can be weighted, and ultimately averaged together, based on the expected goodness of their values. For example, flat fields that are generated from positions closer to the edge of the solar disk, where the signal is lower, and there is a higher power gradient, will have higher uncertainty associated with them.

This portion of the flat field algorithm [algorithm 8B] is outlined in the following table.

Step	Description
1	Loop through all identified positions on the solar disk
2	Loop through all columns
3	Loop through all pixels in a column
4	Using the vector of image locations for the solar peak crossing each pixel, interpolate signal to fractional image, and add that value to a 480 x 640 map of signal levels
5	Using distortion map, interpolate across spectral dimension to correct for optical spectral distortion
6	Normalize flat field: divide all pixels by the mean of their column
7	Create final flat field by taking average of flat fields for all identified positions on the solar disk (weight positions if desired).

5.2.2.6 20 mm Flat Field Algorithm Implementation

The implementation of the 20 mm flat field is similar to that of the 0.5 mm flat field. It is possible, however, that the transmissive diffuser is so Lambertian that a solar peak cannot be located. It would instead just look like a constant value over all pixels in a wavelength bin. In this case, it is necessary to use the FSS data to determine the peak location, or to assume that the scan was constant and crossed all expected field angles given gimbal resolver telemetry. However, because of the flatness of the source, the algorithm is also less sensitive to misalignments of the peaks, and does not require a resampling step. The required steps in the 20 mm flat field solar disk position algorithm [algorithm 8A] are shown in the following table.

Step	Description
1	Obtain gimbal scan range
2	Linearly distribute all images of scan within the gimbal scan range
3	Identify number of images that extend past the slit full field of view. This value will be the number of measurements that can be used to generate a flat field.
4	Create a vector of image locations that the solar peak should be crossing each row of the detector

Like the image identification step in the small aperture case, the peak image location for the 20 mm aperture can have fractional values, and will be interpolated between images. After this step, the processing of the large aperture flat field is identical to the small aperture flat field, with the exception of requiring a correction for the variation in signal transmitted through the diffuser, or BTDF correction. The relative signal transmission through the diffuser at all field angles was studied in the laboratory, and is used to adjust the measured signal on each pixel. The correction is shown in Figure 81. Note that this correction was studied on multiple pieces of transmissive diffuser, and before and after irradiation with an extreme UV source, with very little deviation from the plots shown here. It indicates that the signal drops by nearly 0.6% at the edges of the field angle range.

The outline of the 20 mm flat field creation steps [algorithm 8B] are shown in the following table.

Step	Description
1	Loop through all identified positions on the solar disk
2	Loop through all columns
3	Loop through all pixels in a column

Step	Description
4	Using the vector of image locations for the solar peak crossing each pixel, interpolate signal to fractional image, and add that value to a 480 x 640 map of signal levels
5	Using distortion map, interpolate across spectral dimension to correct for optical spectral distortion
6	Correct for transmissive diffuser BTDF
7	Normalize flat field: divide all pixels by the mean of their column
8	Create final flat field by taking average of flat fields for all identified positions on the solar disk (weight positions if desired).

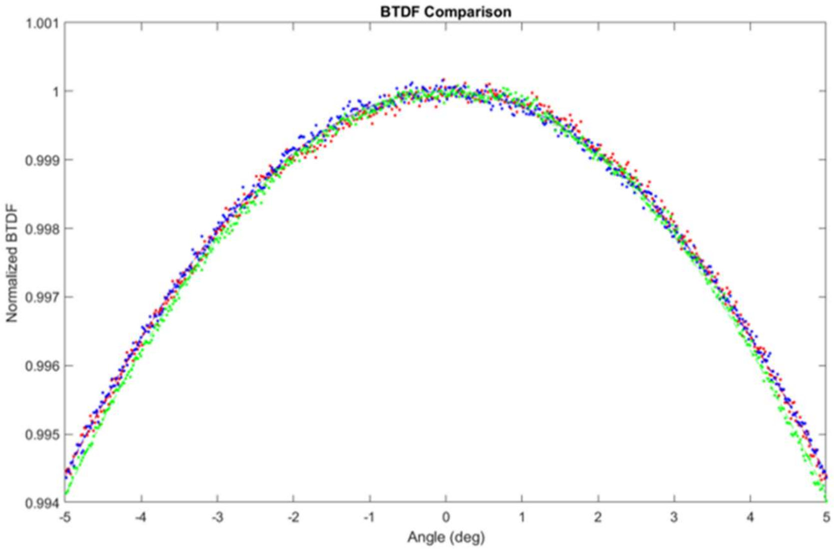

Figure 81. BTDF correction of the transmissive diffuser used in the large aperture flat field creation. The various colors represent different measurements taken over several years, and with different pieces of the transmissive diffuser. This BTDF is extremely similar to an ideal Lambertian diffuser, which follows a cosine^2 function.

5.2.2.7 0.5 mm Flat Field Pointing Requirements (Solar Flat Field)

The pointing requirement for the 0.5 mm flat field is derived directly from HySICS balloon data, which has the same field of view, spectral bin width, diffraction, and similar response as the CPRS HySICS instrument. Since the flat field goal is to get the same amount of light to fall on every pixel, it is instructive to see how quickly the light level on that pixel changes if the pointing were to drift in the cross-slit direction. This analysis can be accomplished by observing the rate of change in cross-slit solar scan data. Shown in Figure 82 are two HySICS balloon composite images of the sun, at different wavelengths, taken during an irradiance scan.

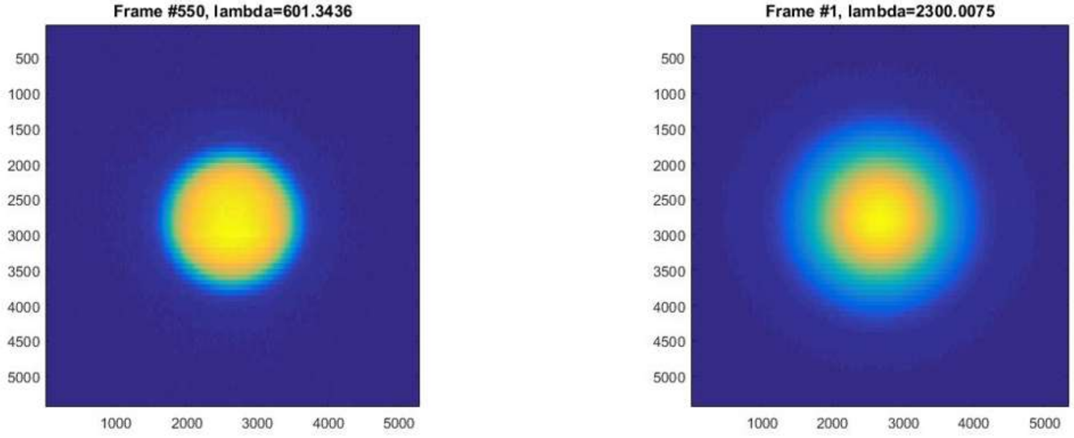

Figure 82. Two composite images of the sun from HySICS balloon flight, at 601 nm, and 2300 nm. The spatial coordinates are in arcsec. These composite images are built up from the data of a solar spectral irradiance scan, and are used to determine the pointing requirements of an along-slit scan. The solar disk at 2300 nm is spread out more than the 601 nm disk because of the higher diffraction at longer wavelengths.

A slice through the center of the solar disk, in DN, and derivative, in percent error/arcsec, are shown in Figure 83. If the point on the Sun is near the center of the solar disk, there is higher uniformity, and the scan can therefore tolerate a higher pointing error. If the flat field point is within ±70 arcsec from the center of the Sun, the power level will change by less than 0.1% if there is up to 15 arcsec of pointing error. With HySICS Pointing System (HPS) in closed-loop operation with the fine sun sensor, we would expect to be able to point within ±46 arcsec of the center of the sun, implying less than 0.05% error with 15 arcsec pointing jitter error.

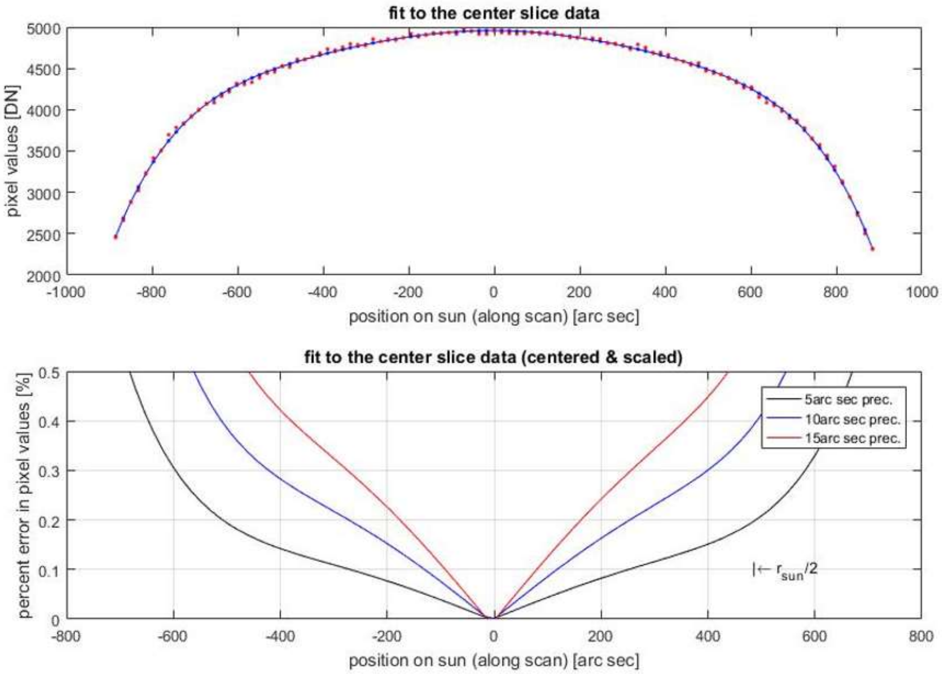

Figure 83. Slice through center of Sun and error in along-slit scan at different scan positions, and with different levels of pointing error. The top plot is a single slice through the center of the Sun, used to determine error in flat field scan. The bottom plot shows the error for different pointing error levels, 5, 10, and 15 arcsec. Since the Sun is particularly uniform directly in the middle of the solar disk, even a high pointing error of 15 arcsec causes almost no change in the solar power used in the flat field scans. If the scan is performed closer and closer to the edge of the solar disk, the amount of power change caused by all pointing errors shown can become quite high, on the order of 0.5% – 1%.

5.2.2.8 20 mm Flat Field Pointing Requirements (Transmissive Diffuser Flat Field)

Unlike in the solar flat field scan, the transmissive diffuser uniformizes the solar disk, making it nearly unsusceptible to pointing errors. Rather than observing an image of the Sun, as shown in Figure 82, the entire field will be constant, except for small variations due to the BTDF. Using estimations of the BTDF, the required pointing accuracy for this scan is around 1.3 degrees.

5.2.2.9 Miscellaneous Transmissive Diffuser Notes

This section is meant to address other concerns or issues regarding the usage of PTFE for an in-flight 20 mm flat field measurement. The PTFE is a very good depolarizer, and has been shown to depolarize a 100% polarized source to less than 1% after a single 45 degree bounce [18]. A similar polarization insensitivity can be expected for the flat field measurement.

If the PTFE diffuser were to heat up enough that the blackbody radiation output changed appreciably during a scan, it could throw off the flat field measurement in the IR, from 2000 – 2300 nm. A single, 480 image scan at 15 Hz acquisition frequency should take 32 seconds to complete. During this time period, the Spectralon should heat up less than 3 degrees, but if it did heat up more than 51 degrees, there would be a 0.1% error at 2300 nm.

In addition, PTFE has been shown to be nearly impervious to oxygen ion degradation [17], even at levels approximately five orders of magnitude higher than expected at ISS altitude. Similarly, static charge build-up is not expected to be a problem with the less than 4 square inches of exposed surface area required for a flat field scan. It will slowly be discharged through the metal of the aperture wheel and through the chassis ground.

5.2.3 Pen-Ray Calibration

All terms in the instrument equation are dependent on wavelength, implying that precise knowledge of the instrument wavelength scale is important. All terms will be interpolated to the instrument wavelength scale, including the solar spectral irradiance from another instrument, and the aperture ratio, which has a wavelength dependency as well. During the flight, temperature changes are expected to cause small shifts to the instrument optical alignment. The primary effect of the shifting is to cause the wavelength scale to move slightly. If there is an error in the knowledge of the wavelength scale, it can cause a large error in the vicinity of high spectral gradient features, such as at the edges of water absorption lines, or in the UV structure when observing the sun.

The HySICS instrument carries an on-board Hg-Ar Pen-Ray lamp that can be used for an absolute calibration of the instrument wavelength scale. The Hg-Ar lamp outputs spectral, atomic transition lines from 400 nm to around 2100 nm, shown in Figure 84. The atomic linewidths are on the order of 0.0025 nm [12] and considered to be delta functions in this analysis. The Pen-ray calibration has been partially experimentally validated on HySICS-balloon data, and has been examined carefully with added error sources in simulation. Pen-ray data has been collected with the CPRS flight hardware hundreds of times throughout the calibration campaign under a variety of conditions, and the wavelength scale algorithm has been applied to many of these datasets. As for all uncertainty items, they have been experimentally validated with the flight hardware.

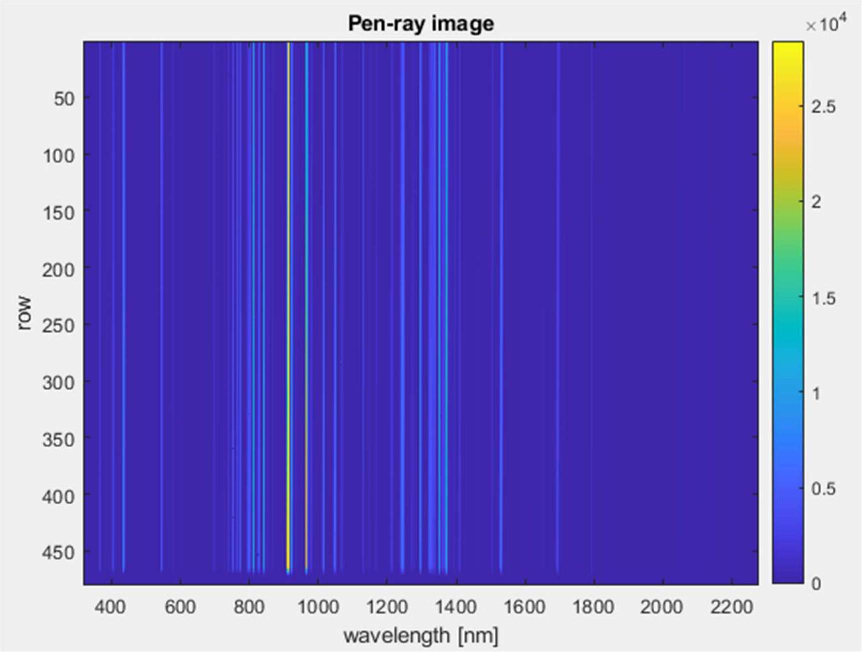

Figure 84: Example pen-ray image from CPRS.

5.2.3.1 Selection of Atomic Lines for Analysis

There are many theoretical atomic lines to choose from. With reasonable thresholds, one could identify 60+ lines in our pen-ray images. However, many of those lines are quite dim, or are clustered very close to many other lines. Tight clustering makes fitting less reliable. Therefore, this analysis uses 12 lines which were manually selected due to their high intensity and isolation from neighbors. Those lines are:

- Argon:
    - 912.2967 nm, 922.4498 nm,
    - 965.7786 nm, 978.4502 nm,
    - 1047.0053 nm, 1067.3566 nm,
    - 1694.0584 nm.
- Mercury
    - 404.65643 nm,
    - 435.83363 nm,
    - 546.07498 nm,
    - 1013.9787 nm,
    - 1529.4592 nm.

Even with the requirement of reasonable isolation from neighbors, many of the Argon lines are within 10-20 nm of a nearest neighbor. Although those are well-resolved, they are treated as pairs when it comes to fitting them to Gaussians as part of the wavelength scale estimation algorithm. The atomic lines that are treated as pairs are listed together on a single line in the list above.

5.2.3.2 Algorithm Summary

The sequence below describes the step-by-step algorithm for determining the wavelength scale for the full detector. These steps are described in detail in the following sections.

1. The only input is a video of pen-ray data (typically 800-900 frames collected over <1 minute).
2. Load the 4 datafiles that must be used to perform the calculations (mainly the atomic lines).
3. Determine which frames to use for the Argon lines (brightest at the start) and the Mercury lines (brightest at the end).
4. Average those frames to calculate 3 images. These are the images that will be analyzed row-by-row to calculate the wavelength scale.
5. Now we enter the sequence of steps that operate on a per-row basis. The subsequent steps (6-12) all occur on a single row at a time.
6. Calculate 3 spectra for the per-row analysis.
7. Determine an approximate wavelength scale to aid in peak matching.
8. Find peaks in the spectra.
9. Match NIST peaks to the data peaks found in the previous step.
10. Cycle through each peak (or pair of peaks) and individually fit it to a Gaussian (or Double Gaussian).
11. Analyze the set of Gaussian fit results to estimate a linear wavelength scale (linear fit).
12. Return to step 5 and repeat on each row.
13. Interpolate/extrapolate the m and b across the full detector.
14. Calculate the linear wavelength scale per pixel.
15. Calculate and apply the non-linear adjustment.
16. Calculate the linear uncertainty.
17. Incorporate the non-linear uncertainty.
18. Store the significant outputs for exporting from the function.

5.2.3.3 Algorithm Details

This section includes details for the steps outlined in the sequence above.

All tunable parameters of the wavelength scale have been thoroughly tested and fixed. Hence, there are no parameters to pass to the wavelength scale calculation function other than the corrected pen-ray dataset (“corrected” means background subtraction, flat fielding, etc.). This is possible because the pen-ray datasets are always collected under the same conditions and with the same integration time. The wavelength scale is influenced by temperature, but the algorithm does not need to know the temperature in order to properly perform the calculation. Therefore, the only input is the pen-ray dataset (typically 800-900 frames collected 1 minute).

Step 2 is to load the 4 required datasets. The main one is the list of 12 atomic lines. Additional required data includes a scalar adjustment to the linear scale, a set of 6 coefficients to generate a non-linear per-pixel adjustment, and the uncertainty information relating to the non-linear adjustment. These will be explained in more detail in subsequent sections.

Step 3 is to examine the pen-ray video and determine which frames to use to generate spectra on which to perform the fits. We need to grab frames from different times of the pen-ray acquisition because the Argon lines are brightest at turn-on, but Mercury lines are brightest at the end. In order to select the ideal frames, first calculate the mean signal per frame. The "turn-on" frame is when the mean signal makes the largest jump - use this time region for all Argon lines except the 912/922 nm pair.

912nm is typically saturated with 200-row times (pen-ray integration time), but decreases in intensity over time during the 1-minute acquisition of a pen-ray dataset. We can determine when the 912nm line is no longer saturating by looking at the maximum value in the center row (#240). The highest value at the turn-on frame is saturated; pick the 912nm unsaturated frame to be when the max value of the center row has dropped below 80% of this saturation value.

Next, determine the "turn-off" frame. Look for the biggest drop in the mean signal per frame. Make sure this drop is bigger than 100DN. If the biggest drop is less than 100DN, the pen-ray data probably doesn't include the turn-off event. In this case, use the final frame. This ought to never happen, but it is an important check to make sure the algorithm is robust to potential peculiarities in the datasets.

Based on these 3 frames, the next step is to pick the frames to average in order to make the spectra to analyze. All argon lines except the 912/922 nm pair use the 20 frames that begin at [turn-on frame + 10]. The 912nm line uses the 20 frames after the unsaturated frame. The mercury lines use the 20 frames just before [turn-off frame - 10]. See Figure 85 for an example of the indicated frames in a typical dataset.

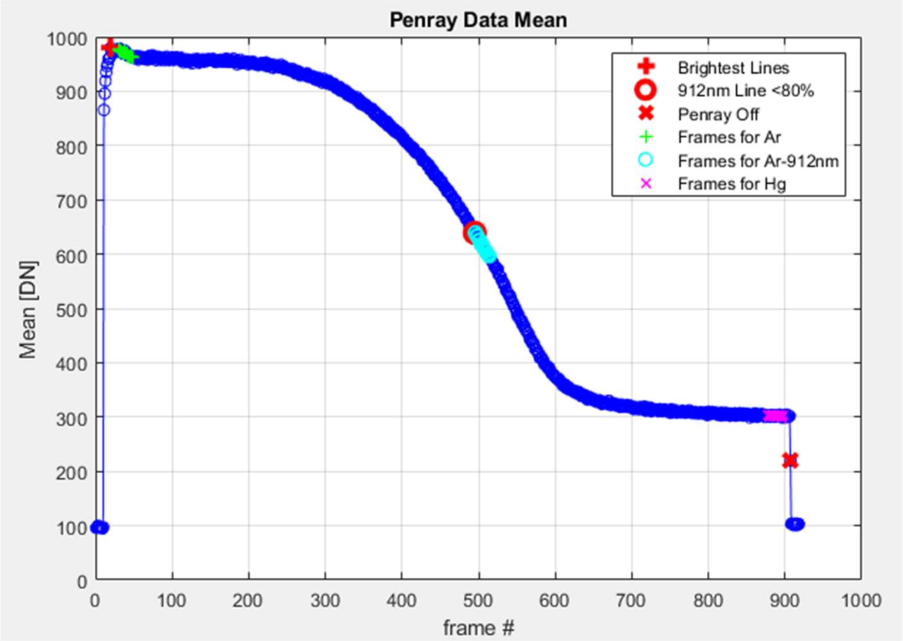

Figure 85: Determining which pen-ray frames to average to generate spectra for fitting.

Step 4 is to average these 3 separate 20-frame sets into 3 individual images. The ~900-frame pen-ray dataset is now condensed to just 3 images. This is the final step before we enter the main section of the algorithm. Steps 5-12 are contained in a loop that operates on each row of the detector (steps 5 and 12 are simply to demarcate the beginning and end of the loop).

Step 5 is the beginning of the loop. The loop only operates on rows 10:453. Starting at row 10 is necessary because of the 20-row averaging described in step 6. Similarly, the end of the loop is at row 453 because the data stops at row 463 due to slit/detector alignment.

Step 6 is to extract the row-of-interest from the 3 images calculated in step 4. Rather than extracting a single row, we average across 20 rows centered on the row-of-interest. This result is a set of 3 spectra (one for Argon lines, one for the 912/922 nm Argon line pair, and one for Mercury lines). See Figure 86 for an example of the 3 spectra.

Step 7 is to determine an approximate wavelength scale to aid in matching peaks in the data to the peak wavelengths of the theoretical atomic lines. First, find the highest peak in the Argon spectrum. This is the 912nm line. Next, assume the pixel spacing is 3.062 nm/pixel. This is very consistent across all test conditions and rows. In fact, during this parameter varied by only 163 ppm throughout the TVAC temperature ramp. These two pieces of information are enough to compute an approximate wavelength scale for this row. This approximate spectrum is correct to approximately half a pixel (~1.5nm). Check that it is reasonable by looking at the wavelength of the first bin. If it is less than 250nm or greater than 350nm, raise a warning. See Figure 86 for an example of the consistent high intensity of the 912 nm line.

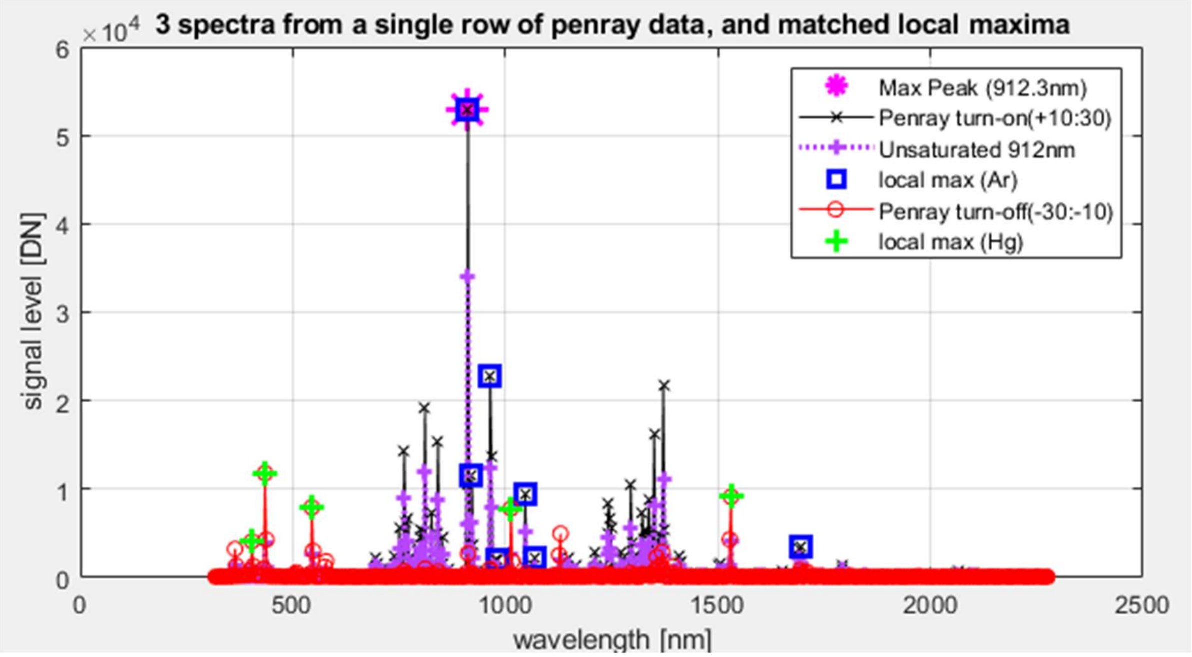

Figure 86: Example pen-ray spectra and local maxima.

Step 8 is to find the peaks in the spectra. A simple thresholded local maximum finder is sufficient; the 20-frame and 20-row averaging produces high-quality (low noise) spectra. The local maximum finder looks for points that are higher than the 2 points to either side, and greater than 250 DN. Although this threshold may seem low given that the smallest relevant peak is generally over 2000 DN (the 979 nm Argon line), the problem of matching local maxima to theoretical peaks (in step 9) is very easy given the selection of well-isolated peaks and the reasonably accurate approximate wavelength scale from the previous step. Hence, a low threshold makes the algorithm robust to changes in the data.

Step 9 is to match the theoretical NIST peaks to the local maxima found in the previous step. Simply pick the local maximum that is closest to the known NIST peak location. This assumes the appx wavelength scale calculated in step 7 is reasonably accurate. This peak matching is made easier by the fact that the 12 NIST peaks we are analyzing were selected because they are strongly present in our data and also well-isolated from nearby peaks. Figure 86 shows the 12 matched lines.

Step 10 is to cycle through each peak (or pair of peaks) and individually fit it to a Gaussian (or Double Gaussian). Slice out an 11-pixel region of data around the peak(s) (typically -5 : +5 pixels around the local max). In the case of the peak pairs, the region of data includes 5 pixels to either side of both peaks. Perform the Gaussian fit, and retrieve the center of the Gaussian from the fit output (this is a value in pixel number, with sub-pixel precision). See Figure 87 for an example of the results from this Gaussian fit of the 12 atomic lines.

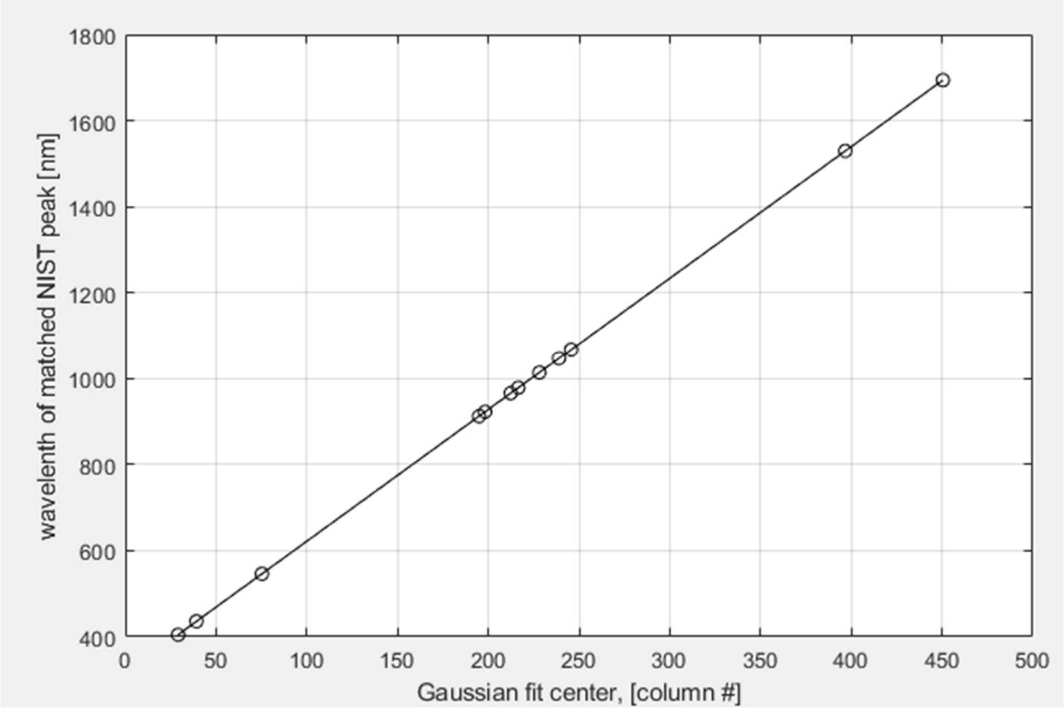

Figure 87: Results of the Gaussian fits to the 12 atomic lines in the pen-ray data.

Step 11 is to analyze the Gaussian fit results to estimate a linear wavelength scale. Shift the fit's x axis (detector column number) to be the "shifted column values." The shift is 210 pixels, which puts the horizontal axis origin in the center of the cluster of lines between 912 nm and 1067 nm. The choice of 210 pixels was selected to improve the uncertainty of the linear fit. Now, rather than the column number going from 1:640, the range is -209:430. With this shifted horizontal axis, we are ready to perform the linear fit. The linear fit provides 4 important values: the slope and intercept (m and b), and their associated 1-sigma uncertainties σ_m and σ_b.

Before storing these values and moving on to the next row, some slight adjustments are made. First, we return b back to the coordinate system prior to the 210-pixel shift described above. The shift follows directly from the basic algebra:

$$b_{shifted\ back} = b_{fit} - 210 * m \qquad 53$$

Furthermore, this intercept term is shifted by +0.22nm, as in the following equation:

$$b_{final} = b_{shifted\ back} + 0.224573nm \qquad 54$$

This shift is necessary to correct an difference between the optical paths of the pen-ray and science images. This shift is described in the following section of this document, "Section 5.2.3.4 Calculation of Linear Adjustments." Finally, we are finished with this row. Store the necessary values (m, b, σ_m and σ_b).

Step 12 is the end of the loop. Return to step 5 and repeat on all rows 10:453.

Step 13 is to extrapolate the m and b values to all rows 1:480. Fit the m-vs-row relationship to a 3rd-order polynomial and extrapolate. Replace the per-row values with the fit outputs. This smooths any row-wise variations that are likely due to noise and are not physical. Repeat the fit and extrapolation for the intercept term as well.

Step 14 is to use the slope and intercept values to calculate the linear wavelength scale for the full detector. We now have a wavelength bin for each pixel on the detector. An example is shown in Figure 88.

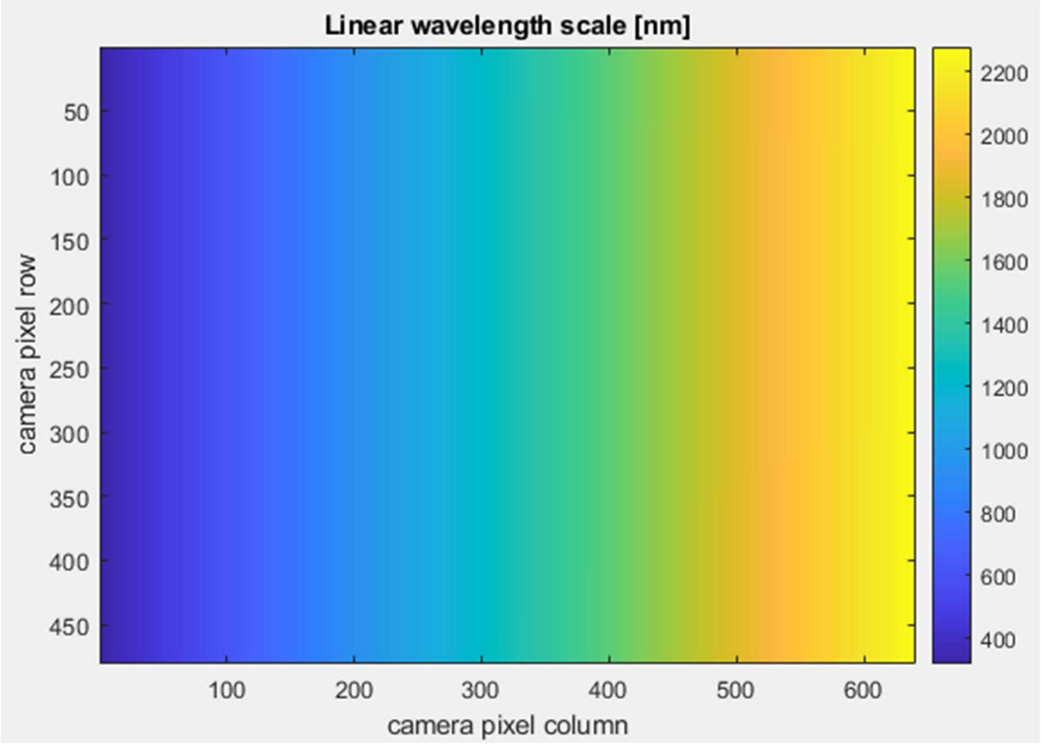

Figure 88: Linear wavelength scale, full detector.

Step 15 is to calculate and apply the non-linear adjustment. This adjustment involves 6 coefficients that depend on row, wavelength, row*wavelength, wavelength^2, and wavelength^2*row (plus an offset term). Load the 6 coefficients and calculate the non-linear adjustment matrix. Subtract the matrix from the per-pixel linear wavelength scale. The justification and calculation of the non-linear adjustment is described in "Section 5.2.3.5 Calculation of Non-Linear Adjustments."

This per-pixel wavelength map is the most significant result of the algorithm, and is the main output of the function.

Step 16 is to calculate the linear uncertainty. This calculation is based on the 1-sigma confidence intervals from the linear fit, σ_m and σ_b. First, these values must be extended to cover the rows beyond 10:453. Average the 10 rows at the top and bottom, and assign the extra rows this flat value. Calculate the per-pixel linear uncertainty using basic error propagation principles. For a single row, the calculation is:

$$\sigma_{linear} = \sqrt{\sigma_m^2 * col^2 + \sigma_b^2} \tag{55}$$

Where "*col*" is the shifted column number ranging from -209:430. Repeat this calculation for each row. The result is a 480x640 matrix containing the uncertainty associated with each wavelength bin in the detector. A representative linear uncertainty for the central row is shown in Figure 89.

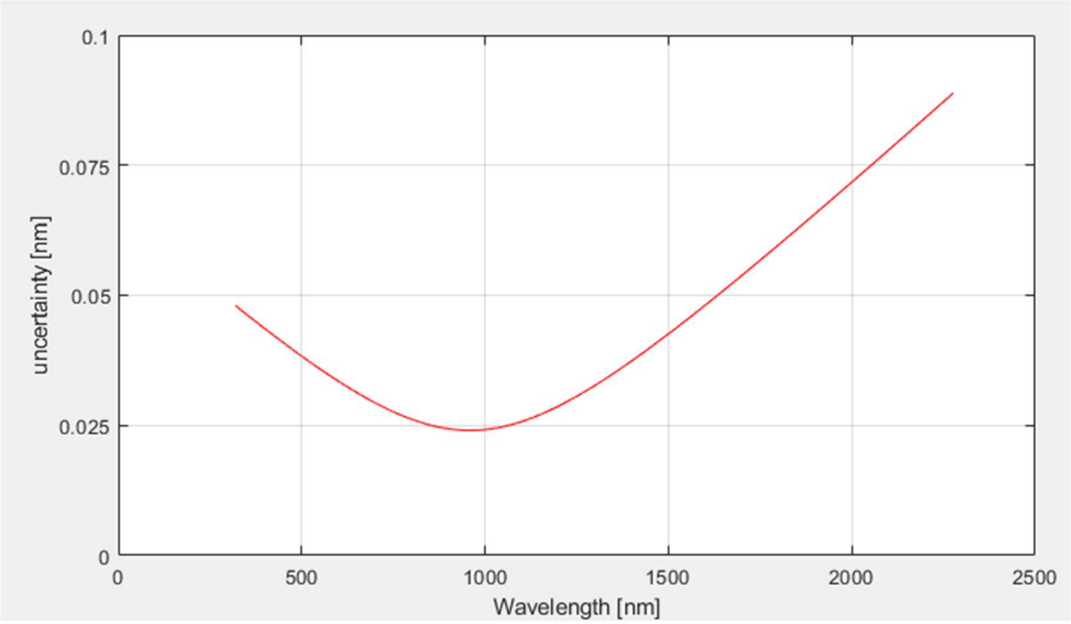

Figure 89: Linear wavelength scale uncertainty, row 240.

Step 17 is to incorporate the non-linear uncertainty. This is based on the covariance matrix of the non-linear coefficients, which were calculated by solving a system of linear equations using matrix algebra. Unlike the linear uncertainty values, these values do not change with each calculation of wavelength scale. Instead, they were calculated once along with the non-linear coefficients and stored in Required Data. The maximum value is 14 x 10^-3 nanometers. It has a value at each pixel on the detector. The Linear and non-linear uncertainties are combined as a sum of squares. It has a value at each pixel on the detector. This is a significant result and is included in the function outputs alongside the wavelength scale.

Step 18 is to assemble the important outputs and pass them. These outputs are:

a) The final wavelength scale (including non-linear correction) [640x480 matrix]
b) The linear wavelength scale [640x480 matrix]
c) The non-linear correction [640x480 matrix]
d) The combined (linear and non-linear) uncertainty [640x480 matrix]
e) The linear slope (m) per row [480x1 column vector]
f) The linear intercept (b) per row [480x1 column vector]

g) The wavelength scale function version (currently set to 'v0')
h) The date and time of the calculation

This concludes the wavelength scale algorithm.

5.2.3.4 Calculation of Linear Adjustments

The previous sections describe the method for analyzing a pen-ray dataset and calculating the wavelength scale for every pixel on the detector. As a verification, we compared the calculated wavelength scale to a set of lasers during CPRS's instrument-level TVAC test. The test involved 5 diode lasers: 660 nm, 785 nm, 852 nm, 1064 nm, and 1550 nm. During a cold-to-hot ramp, we collected a series of pen-ray datasets and then immediately switched to illuminating the diffuser with one of the diode lasers while simultaneously measuring the laser wavelength and stability with a high-resolution Fourier Transform Spectrum Analyzer (FTSA). This Spectrometer has an on-board self-calibration source. We repeated this process for all 5 laser wavelengths. The entire sequence of 5 pen-rays and 5 lasers was repeated 5 times, for a total of 25 laser measurements and 25 interspersed pen-rays.

These 25 measurements were then analyzed individually. An example of a single measurement analysis is shown in Figure 90. The laser spectrum as measured by the FTSA is shown in red. The mean of the 20 central rows of the detector are averaged to create a snapshot of the laser line on the CPRS detector. The wavelengths of the detector pixels were estimated using the pen-ray dataset from minutes before and the algorithm described above. We now have a direct comparison between the high-resolution FTSA and the CPRS wavelength scale estimation scheme. We fit the CPRS laser line to a Gaussian and compare the center of that fit to the FTSA peak. The difference (CPRS peak) – (FTSA peak) is referred to as the "CPRS wavelength error." In the example in Figure 90, the error is -0.19 nm. A negative error means the CPRS wavelength bins are "too low" when comparing to the spectrometer.

For some of the datasets (particularly the 660 nm laser), the laser sometimes exhibited a dual peak that was visible on the FTSA but was not visible in the CPRS data. The separation between the dual laser peaks was ~0.2 nm. Therefore, the peak of the FTSA data is not simply the highest measurement. Instead, we convolved the laser spectrum with the CPRS ILS, fit that to a Gaussian, and recorded the fit center. This is not shown in the analysis plots.

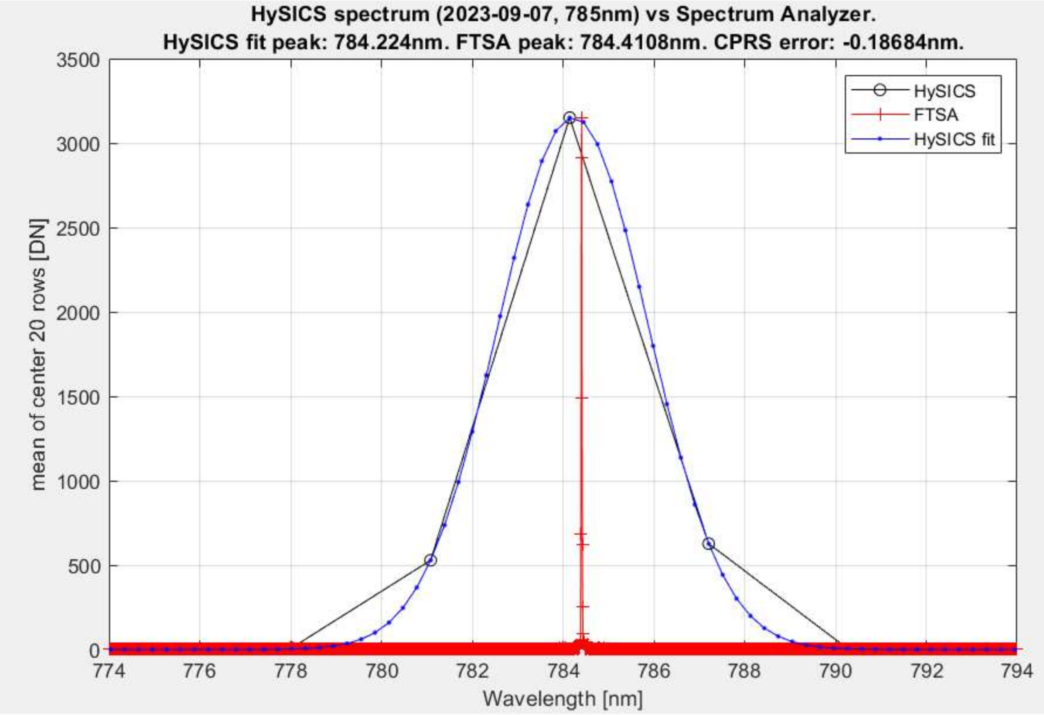

Figure 90: Wavelength scale TVAC verification experiment (single measurement).

The 25 measurements were all analyzed in this way, and the combined results are shown in Figure 91. Clearly there is a systematic shift between the FTSA and the CPRS data on the order of ~0.22 nm. No justification for this shift could be found in the wavelength estimate algorithm or FTSA.

We turned to optical raytrace simulations to investigate the possibility that the pen-ray and pen-ray mirror generate a slightly different distribution of light (spatially and angularly) than the diffuser, which ought to represent a near-perfect Lambertian or a natural scene. Complete mechanical components were included in the non-sequential simulations, as shown in Figure 92. That figure only shows a few hundred rays (and thus none are passing the slit). Billions of rays are required in order to get reasonably coverage of the detector. These simulations were compared to a similar simulation in which a Lambertian source was placed at the aperture to represent the diffuser. Both sources are assigned a wavelength of 700 nm, and both make a stripe on the simulated detector. The stripe cross-sections are shown in Figure 93. Indeed, there is a ~0.2 nm discrepancy between the two lines. The direction of the shift is consistent with the TVAC experimental observations; in the simulations, the pen-ray stripe is “higher” (to the right) of the diffuser’s stripe, although they are the same wavelength. This would result in a slight underestimate of the laser wavelength, as seen in the experiment in Figure 90. The simulations were repeated at more wavelengths across the spectrum, and the shift of 0.2 nm appeared to be consistent across wavelength.

The resolution of this discrepancy is to manually add 0.2 nm to the wavelength scale (the exact value after averaging all TVAC measurements is +0.22457321562888 nm). This is the shift described in Step 11 of the algorithm. This scalar value is one of the required pieces of information loaded at the beginning of the wavelength scale algorithm.

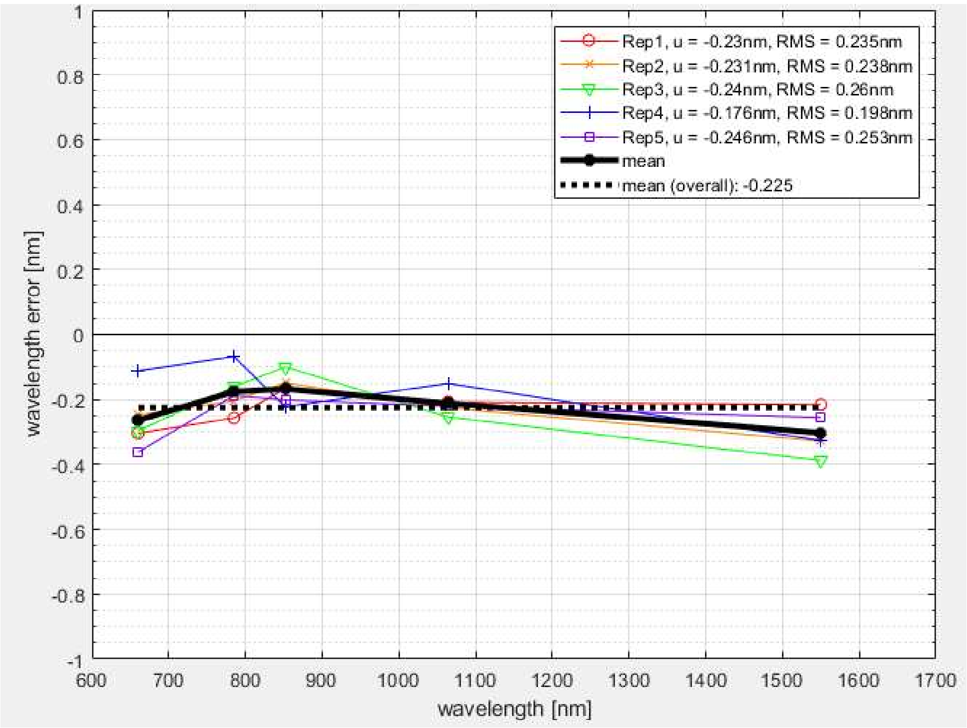

Figure 91: Wavelength scale TVAC verification experiment (conglomerate results).

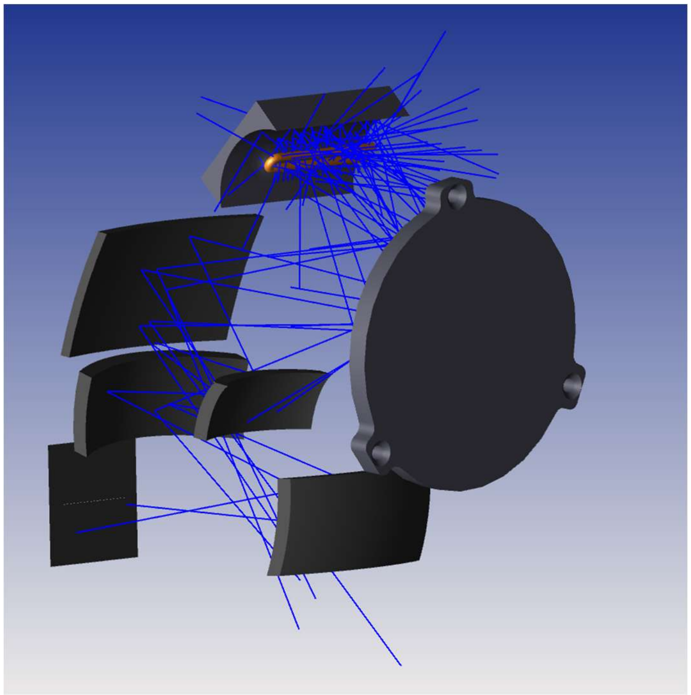

Figure 92: Optical raytracing simulations of the pen-ray hardware. The components shown here include the pen-ray bulb, the pen-ray collector mirror, the pen-ray aperture mirror, the 4 mirrors of the telescope, and the slit plane. The Offner spectrometer portion of the system (including the detector) are not shown in this figure, but are included in the raytrace.

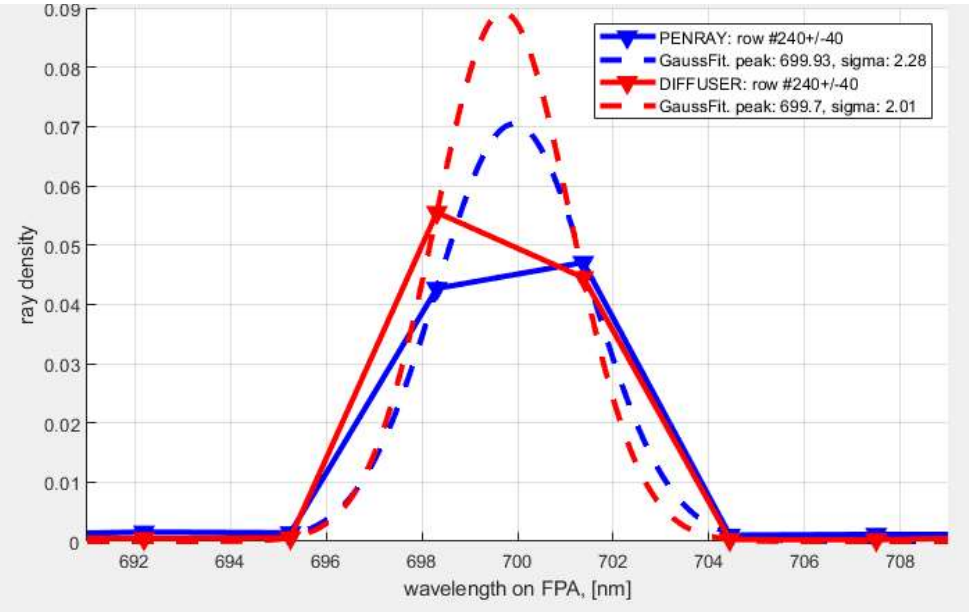

Figure 93: Optical raytrace results comparing the pen-ray and the diffuser.

5.2.3.5 Calculation of Non-Linear Adjustments

The final aspect of the wavelength scale algorithm is the non-linear adjustment. The linear adjustment described in the previous section brings the CPRS wavelength error to be centered around zero, and the remaining magnitude is less than 0.1 nm. However, when looking at rows towards the edges of the detector, the wavelength error increases and also exhibits more wavelength dependence, as can be seen in Figure 94.

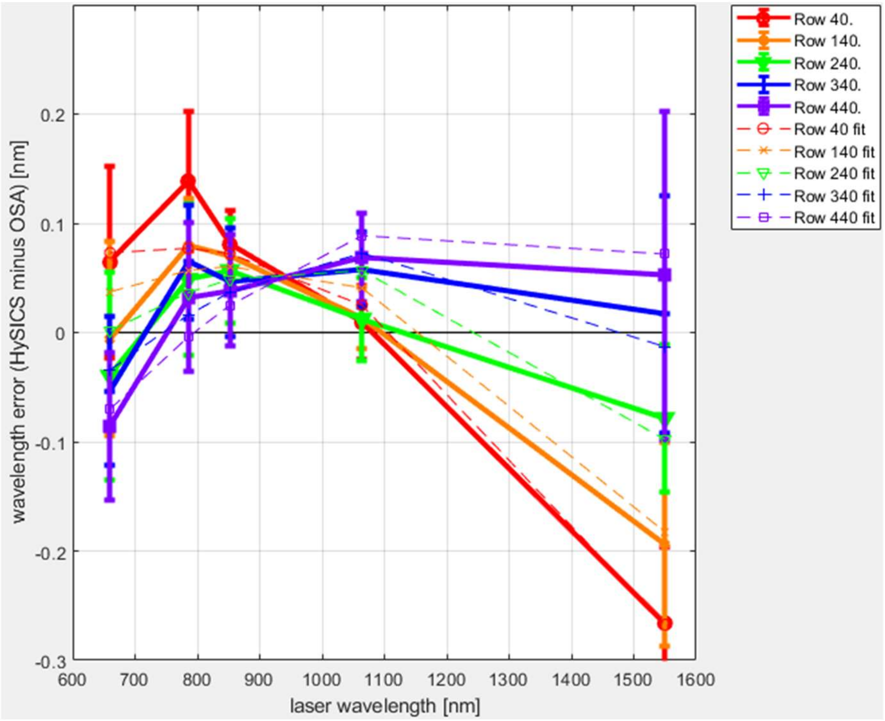

Figure 94: Wavelength error from TVAC data across different rows of the detector.

In order to correct for these row- and wavelength-dependent errors, we investigated the possibility of applying a correction that also depends on row and wavelength. We evaluated various fits that included linear, quadratic, and 3rd-order terms across both row and wavelength. The best result that also avoided over-fitting was a version that included linear row terms and 2nd-order wavelength terms. This is also visually apparent from the curves of the wavelength error in Figure 94. The 6 terms in the non-linear correction are:

- p21 * λ^2 * R
- p20 * λ^2
- p11 * λ * R
- p10 * λ
- p01 * R
- p00 * 1

Where pXX are the 6 coefficients, R is the row number (1:480), and λ is the wavelength in nm (from the linear wavelength scale). The 6 coefficients were calculated by looking at the set of results shown in Figure 94 and solving the linear algebra using matrix left divide. Since the matrices are not square, the solution is a least-squares type. After incorporating this non-linear correction into the wavelength scale algorithm and repeating the analysis of the TVAC data, the resulting wavelength error is shown in Figure 95. The means of all errors are less than |0.05 nm|, or 1/60th of a pixel.

The complete per-pixel non-linear correction is shown in Figure 96. This matrix is calculated once at the end of the wavelength scale algorithm from the 6 coefficients calculated here and subtracted from the linear wavelength scale. These 6 coefficients are one of the required pieces of information loaded at the beginning of the wavelength scale algorithm.

The uncertainty on these coefficients is calculated by looking at the diagonal terms in the covariance matrix. The non-linear uncertainty is much smaller than the linear uncertainties. The linear and non-linear uncertainties are combined in a root-squared sense. The non-linear uncertainty, like the non-linear coefficients, are one of the pieces of required data loaded at the beginning of the wavelength scale algorithm.

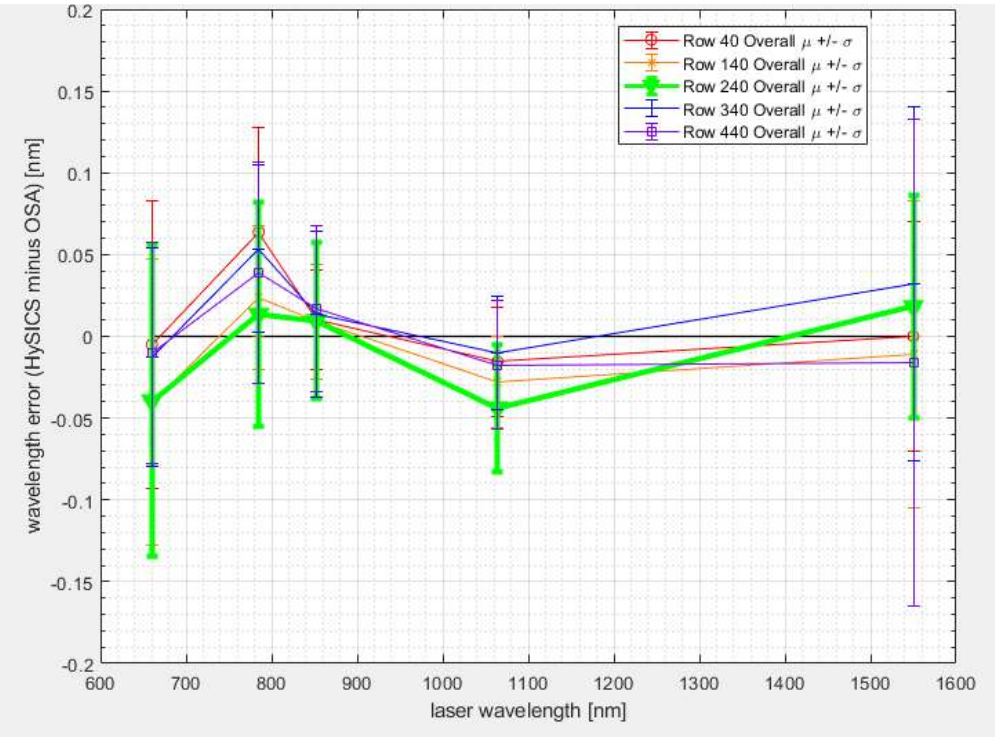

Figure 95: Wavelength error after non-linear correction.

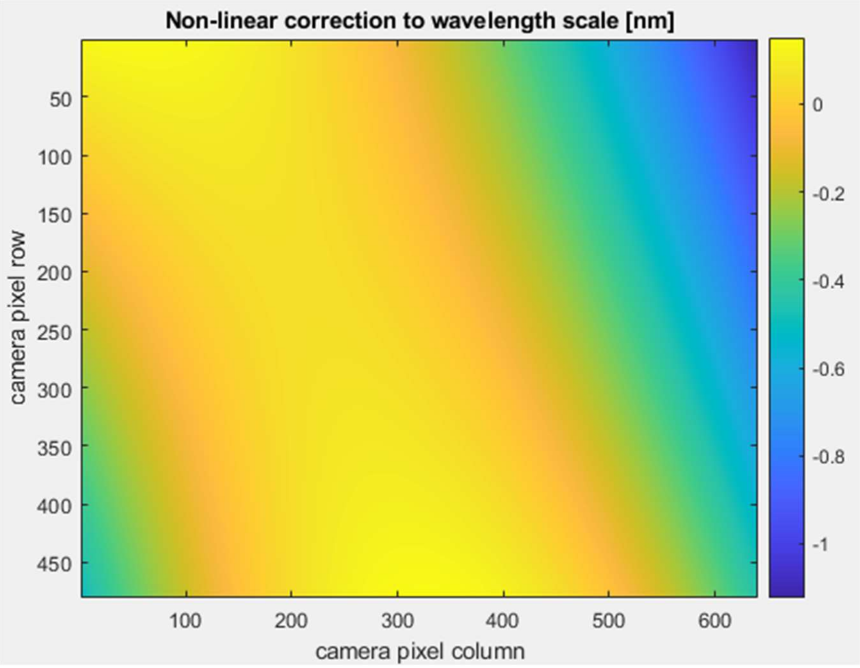

Figure 96: The per-pixel non-linear correction to the wavelength scale. For most rows and wavelengths, the non-linear correction is less than 0.1 nm (yellow).

5.2.4 Cold Sky (or Blank Aperture Correction or Dark Field Correction)

The majority of the dark images acquired during the CLARREO mission will use a blanked-off aperture slot on the aperture wheel, called the “blank aperture.” The blank aperture is coated with a black paint, which helps limit stray light and reflections, but generates blackbody radiation that can be detected by the system. The dark image will therefore have a slightly different amount of light than the expected background level of nadir science images. The correction for this extraneous light has several names, but amount to a blank aperture correction. The data generated from this correction follow the algorithm steps shown in Figure 4.

To generate the blank aperture correction, the instrument is turned to stare into dark space, where there is no source that can generate blackbody radiation, hence the “cold sky” name. At this position, a nominal scan with 250 dark images (with blank aperture), 250 cold sky images (without blank aperture), and 250 more dark images (with blank aperture) is acquired. This sequence gives a direct comparison between the signal with and without the blank aperture in place.

Several of the previously discussed correction steps can be ignored in this particular data step, including the aperture thermal correction and the f-number thermal correction, since there is no light coming through the aperture in this measurement.

The calculation of the blank aperture blackbody radiation is merely the difference between the interpolated dark images and the cold sky image, which occurs in the same way as the dark subtraction algorithm previously discussed (section 5.1.3.10). The dark subtracted cold sky images are averaged together to create the blank aperture correction [algorithm 9A].

5.2.4.1 Cold Sky Correction Implementation

Step	Description
1	Calculate average image from cold sky data set (assumes all image conditioning and correction steps have already been done)

5.3 Secondary On-Orbit Calibrations

Besides the primary calibrations already discussed, there are several secondary calibrations that may only be performed one or two times over the full mission. These calibrations consist of the lunar or solar limb scan, the degradation measurement, the sensor linearity measurement, and the aperture ratio measurement. These calibration activities will be described in this section.

5.3.1 Lunar or Solar Limb Scan

The solar flat field measurement requires that the instrument slews along the solar disk such that a single point on the Sun is passed over every pixel within the slit (described in section 5.2.2.1). There is a partial verification that this occurs properly simply be observing the data. As an imager, a narrow, rectangular slice of the Sun is visible, and if the instrument scans in the wrong direction, this will be evident by the width of the disk changing through the scan. A very small misalignment during the scan may not be observed in the scan data, however, and the power variation would instead be assigned to flat field variation.

To verify that the scan motion is indeed parallel to the slit, as necessary for the correct alignment, the limb of the Moon or Sun can be scanned. The power gradient at the edge of both sources is quite high, as shown in Figure 97, the lunar across-slit irradiance measurement from the HySICS balloon flight. At the limb of the Moon, for the phase that was available during the balloon flight, the power gradient is approximately 9e4 DN/arcsec, equivalent to 0.7% of the peak integrated power of any image of the scan, and well above the instrument uncertainty. Note that one image of scan motion is around 17 arcsec. The types of alignment errors that can occur in an along-slit scan are shown schematically in Figure 98. With the power gradient described, single arcsec errors either in the slew direction or in the slit clocking will be clearly visible. The solar limb does not have quite as high a gradient as the lunar limb, but it will still be able to identify most alignment errors in an along-slit scan, and has the benefit of having fine sun sensor feedback during the scan.

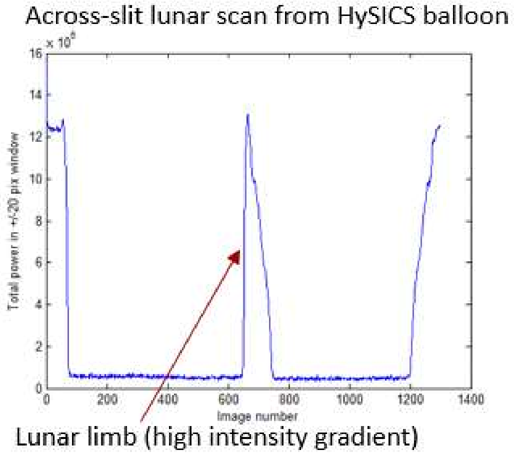

Figure 97. Across-slit scan of Moon. This scan demonstrates how high the power gradient is at the lunar limb. If an along-slit scan is performed at this location, small errors in the alignment are observable.

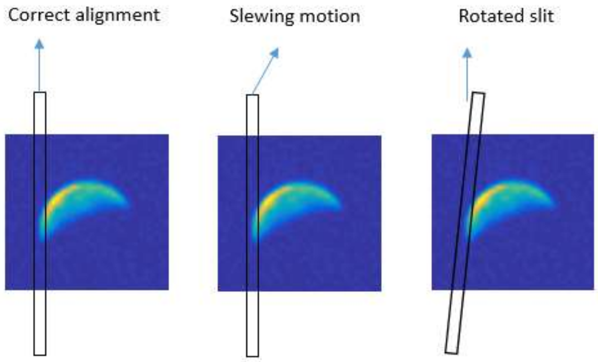

Figure 98. Types of misalignment errors in an along-slit scan.

5.3.2 Degradation Measurement

After multiple solar observations during the course of the mission, it may be desirable to show that there is no degradation in the optical path. The surface most likely to experience degradation is the first surface that light encounters in the optical path, the first 4MA mirror. When the small solar-viewing aperture is in place, the light mainly hits the first 4MA mirror in a small circular patch, with an area defined by the solar angle, the propagation length to the first mirror, and to a lesser extent, diffraction.

To detect if this portion of the mirror has experienced any degradation, it is possible to move the aperture slightly to an unexposed portion of the mirror, as shown in Figure 99. The total motion is around 2 degrees. The aperture wheel is able to move the aperture as shown. This test is only performed with the 0.5 mm aperture while looking at the Sun. Ideally, the instrument should measure the same power regardless of the input aperture position. In reality, there is likely to be slight changes in the measured power based on the uniformity of the optical components. However, this test can be run during the commissioning phase to obtain a baseline measurement of the relative power versus input aperture position. Then, later in the mission, if there has been any degradation in the solar scan, it will be detected by repeating this test.

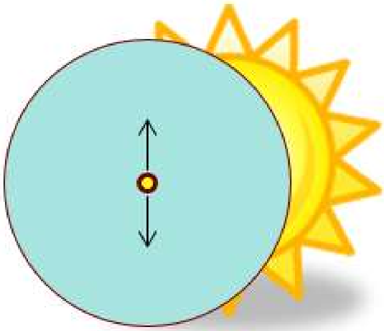

Figure 99. Schematic of the degradation measurement.

5.3.3 Linearity Measurement

The camera linearity is not expected to change during the course of the mission, which is desired since it is one of the two attenuation mechanisms that allow the solar-to-Earth comparison. If there were a stable on-orbit light source that had a light level observable over the full exposure time range without saturation, the camera linearity could be verified during the mission. Unfortunately, the required light source does not exist, but it may be possible to cover the integration range in two steps. With the small aperture, the exposure time can range from 16.8 μs (the minimum value) to 1.176 ms without saturation. With the large aperture and transmissive diffuser, the exposure time can range from 1.176 ms to 66.7 ms. Given a series of steps spaced across the full exposure time range, as shown in Figure 100, the camera linearity can be measured. At the shortest integration time for the transmissive diffuser measurement, 1.176 ms, the signal on the camera is expected to peak at around 450 DN, which is a particularly dim signal. In order to drive the read noise and shot noise down to 500 ppm uncertainty, 53 seconds of averaging would be required for this measurement. The amount of time required on all the other measurements is extremely short, on the order of 10 seconds or less.

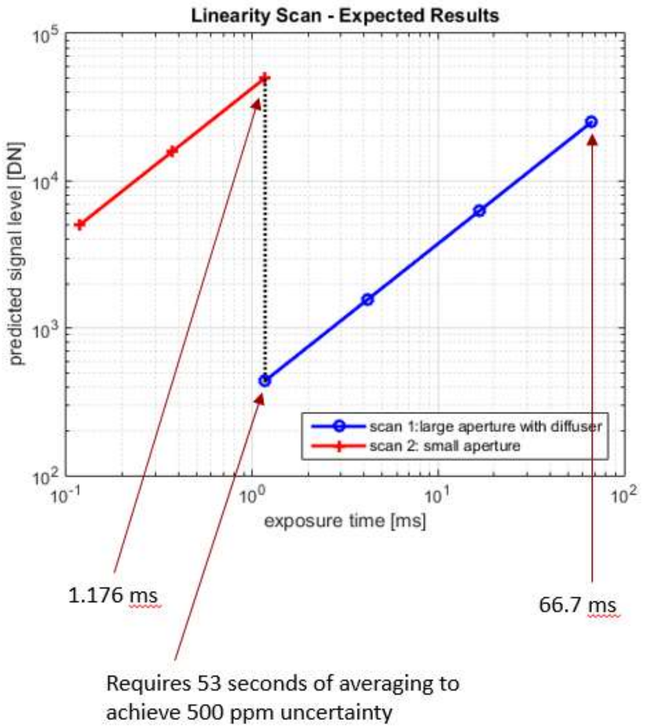

1.176 ms

66.7 ms

Requires 53 seconds of averaging to achieve 500 ppm uncertainty

Figure 100. Linearity scan using two signal ranges, generated by observing the Sun with the 0.5 mm aperture, and observing the Sun with the transmissive diffuser.

5.3.4 Aperture Ratio Measurement – Diagnostic Scan

Like the linearity measurement, it would be convenient to have an on-orbit measurement of the aperture ratio to show that it has not changed during the course of the mission. Again, if there were a stable on-orbit light source that could be viewed by both the 0.5 and 20 mm apertures, the aperture ratio could be directly measured. Unfortunately, no source exists because of the required 3 orders of magnitude area difference between the apertures. It may be possible to perform the measurement in two steps, however, by adding an aperture with an intermediate area. This aperture must be able to view the Sun at one of the shortest exposure times without saturation, but still be large enough to view the Moon at the longest exposure time. An aperture with a diameter of 2.09 mm would require a solar-viewing exposure of 67.2 µs. The aperture ratio can then be calculated between the small aperture and the intermediate aperture, and is tied to the camera integration time linearity. Then, both the intermediate aperture and large aperture are used to observe the moon, and an aperture ratio between them can also be calculated, and is tied to the camera signal level. Together, these aperture ratios should be equivalent to the aperture ratio between the large and small apertures. The required exposure times and signal levels are shown in Figure 101. The difficulty in this measurement will be that the moon is already particularly dim, and the maximum signal level with the intermediate aperture and a full Moon is expected to be around 270 DN. At this level, a significant amount of averaging, on the order of a couple of minutes of measurement, is likely to achieve the desired uncertainties. Unfortunately, the lunar signal level will be changing during this measurement, and will require a power level correction over the course of the measurement. It may be that the correction is evident in the data, as a slope in the total power. It also might be necessary to make the lunar measurement with the large aperture twice, before and after the intermediate aperture measurement, to be allow for interpolation in the lunar power during intermediate aperture measurement.

The aperture ratio measurement is severely limited by the low signal levels available while viewing the Moon with the intermediate aperture, and the high signal levels imposed while viewing the Sun with the intermediate aperture. Given these challenges, the measurement is considered a diagnostic observation more than an instrument self-calibration.

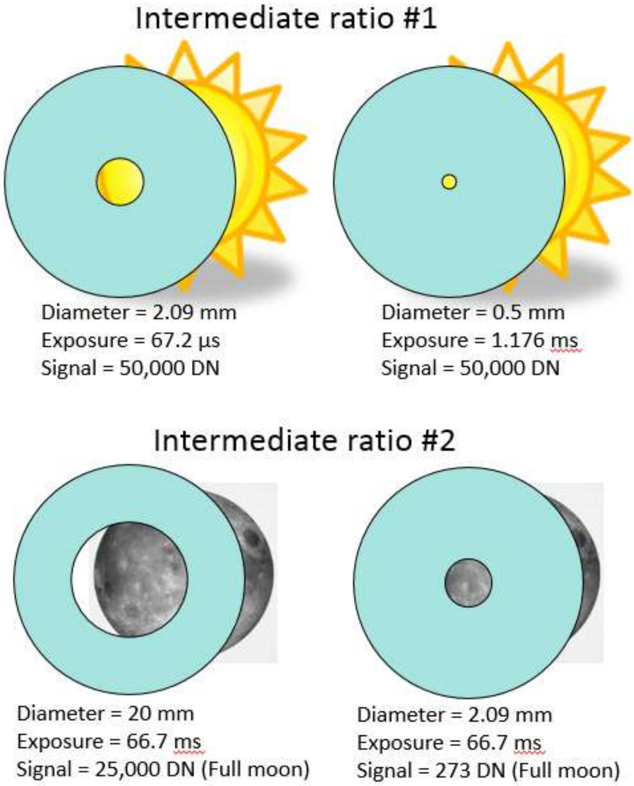

Figure 101. Aperture ratio measurement. The aperture ratio will be measured in two steps, between the small and intermediate aperture on the Sun, and between the intermediate aperture and large aperture on the Moon.

6.0 Uncertainty Budget

The validation of the measurement accuracy is generated through an analysis of the uncertainty contributions of each component of a radiometric measurement, including on-orbit and ground calibrations. The uncertainties fall into three different categories. First, there are a series of uncertainties that are associated with every image, including read noise and shot noise uncertainties. These are added to each data acquisition, regardless of the type of scan that was performed. Second, there are also uncertainties given by every single correction that is applied, directly from the algorithm flowcharts in Figure 1 – Figure 5. Every data pipeline that contains any specific algorithm, of which most are present in every pipeline, will also pick up the associated uncertainty, such as the uncertainty associated with the 2-row correction [algorithm 1B]. Third, there are systematic uncertainties specific to some of the scans themselves. This category has may be due to a specific correction present in one pipeline but not others, such as the application of the solar temporal variation, or it might be due to the method used to acquire the data such as the pointing accuracy in the flat field scans.

The naming convention helps keep all these uncertainties straight. Every uncertainty is given a short, but descriptor that appears at the beginning of the name. This descriptor may include the identifier "dark," which indicates that it comes from dark images. At the end of the name, the type of measurement that generated the uncertainty is added. This type can be: SSI, 0.5 mm FF, 20 mm FF, blank aperture, ground image, or lab measurement. The first four types are from on-orbit calibration scans of the same name. "Ground image" indicates that it is from a nadir science scan, which includes all Earth or lunar pointing measurements. "Lab measurement" indicates that it was an uncertainty that was measured during the characterization and calibration campaign in the lab during the build of the instrument. There are a total of 185 named uncertainties on the lists in the next sections.

6.1 Uncertainty List: Image Acquisition Contributors

To help with identifying all uncertainty contributors, three lists are presented here. All known uncertainty contributions from the first category, uncertainty due to acquiring images, is given in Table 1. Note that there are only five types of these uncertainties: read noise, shot noise, quantization noise, sensor after image uncertainty, and line driver settling time uncertainty. These five types are duplicated for every dark image, making a total of ten uncertainties of this type for each of the data types: ground image, SSI, 20 mm flat field, 0.5 mm flat field, blank aperture, and lab measurement, resulting in a total of 60 uncertainty contributors. The lab measurement category is included here for completeness, but these uncertainties are handled differently from the others, since there is not a specific data pipeline set up for them. They are introduced into the measurement primarily in the aperture ratio correction [algorithm 5B] in the SSI data pipeline.

Table 1. List of all Uncertainty Contributors Due to Acquiring Images (First Category)

Ground Image
Read Noise Ground Image
Shot Noise Ground Image
Quantization Noise Ground Image
Sensor After Image Uncertainty Ground Image
Line Driver Crosstalk Uncertainty Ground Image (also called line driver settling time)
Dark Read Noise Ground Image

Dark Shot Noise Ground Image
Dark Quantization Noise Ground Image
Dark Sensor After Image Uncertainty Ground Image
Dark Line Driver Settling Time Uncertainty Ground Image
Solar Spectral Irradiance
Read Noise SSI
Shot Noise SSI
Quantization Noise SSI
Sensor After Image Uncertainty SSI
Line Driver Settling Time Uncertainty SSI
Dark Read Noise SSI
Dark Shot Noise SSI
Dark Quantization Noise SSI
Dark Sensor After Image Uncertainty SSI
Dark Line Driver Settling Time Uncertainty SSI
Flat Field: Spectralon (20 mm)
Read Noise 20 mm FF
Shot Noise 20 mm FF
Quantization Noise 20 mm FF
Sensor After Image Uncertainty 20 mm FF
Line Driver Settling Time Uncertainty 20 mm FF
Dark Read Noise 20 mm FF
Dark Shot Noise 20 mm FF
Dark Quantization Noise 20 mm FF
Dark Sensor After Image Uncertainty 20 mm FF
Dark Line Driver Settling Time Uncertainty 20 mm FF

Flat Field: Small Aperture (0.5 mm)
Read Noise 0.5 mm FF
Shot Noise 0.5 mm FF
Quantization Noise 0.5 mm FF
Sensor After Image Uncertainty 0.5 mm FF
Line Driver Settling Time Uncertainty 0.5 mm FF
Dark Read Noise 0.5 mm FF
Dark Shot Noise 0.5 mm FF
Dark Quantization Noise 0.5 mm FF
Dark Sensor After Image Uncertainty 0.5 mm FF
Dark Line Driver Settling Time Uncertainty 0.5 mm FF
Blank Aperture
Read Noise Blank Aperture
Shot Noise Blank Aperture
Quantization Noise Blank Aperture
Sensor After Image Uncertainty Blank Aperture
Line Driver Settling Time Uncertainty Blank Aperture
Dark Read Noise Blank Aperture
Dark Shot Noise Blank Aperture
Dark Quantization Noise Blank Aperture
Dark Sensor After Image Uncertainty Blank Aperture
Dark Line Driver Settling Time Uncertainty Blank Aperture
Lab Measurement
Read Noise Lab Measurement
Shot Noise Lab Measurement
Quantization Noise Lab Measurement

Sensor After Image Uncertainty Lab Measurement
Line Driver Settling Time Uncertainty Lab Measurement
Dark Read Noise Lab Measurement
Dark Shot Noise Lab Measurement
Dark Quantization Noise Lab Measurement
Dark Sensor After Image Uncertainty Lab Measurement
Dark Line Driver Settling Time Uncertainty Lab Measurement

6.2 Uncertainty List: Pipeline Correction Algorithm Contributors

All known uncertainties from the second uncertainty contributor category are listed in Table 2. They are organized in a similar way as the previous list. These are the uncertainty contributors associated with every common box in the pipelines detailed in Figure 1 – Figure 5. The algorithm number is added to each uncertainty name to help provide clarity in where they originate in the pipelines. There are 9 contributors in this list that come from algorithms applied to the science or calibration data sets and then again to their respective dark images, and another 7 that are applied to the data sets after the dark images have been subtracted, and therefore are not additionally applied to the dark images. The first 10 algorithms are the same for each pipeline, and then there is some divergence between which pipeline uses different algorithms. This category adds 99 uncertainty contributors to the total list, not counting the non-fundamental uncertainties that are included. Non-fundamental uncertainties are contributors that only propagate other uncertainty contributors through a calculation, but do not add their own uncertainty.

Table 2. List of all Uncertainty Contributors Due to Applying Correction Algorithms (Second Category)

Ground Image
Bad Pixel Correction Uncertainty Ground Image [algorithm 1A]
Two Row Correction Uncertainty Ground Image [algorithm 1B]
True Dark Image Correction Uncertainty Ground Image [algorithm 1C]
Row-wise Dark Pedestal Shift Correction Uncertainty Ground Image [algorithm 1D]
Background Level Uncertainty Ground Image (Dark pedestal shift correction uncertainty) [algorithm 1E]
FPA Thermal Variation Uncertainty Ground Image [algorithm 2A]
FPA Linearity Uncertainty Ground Image [algorithm 2B]

FPE Thermal Variation Uncertainty Ground Image [algorithm 2C]
Blackbody Radiation Correction Uncertainty Ground Image [algorithm 3A]
Dark Bad Pixel Correction Uncertainty Ground Image [algorithm 1A]
Dark Two Row Correction Uncertainty Ground Image [algorithm 1B]
Dark True Dark Image Correction Uncertainty Ground Image [algorithm 1C]
Dark Row-wise Dark Pedestal Shift Correction Uncertainty Ground Image [algorithm 1D]
Dark Background Level Uncertainty Ground Image (Dark pedestal shift correction uncertainty) [algorithm 1E]
Dark FPA Thermal Variation Uncertainty Ground Image [algorithm 2A]
Dark FPA Linearity Uncertainty Ground Image [algorithm 2B]
Dark FPE Thermal Variation Uncertainty Ground Image [algorithm 2C]
Dark Blackbody Radiation Correction Uncertainty Ground Image [algorithm 3A]
Dark Subtraction Ground Image (not fundamental uncertainty contributor) [algorithm 3B]
Blank Aperture Subtraction Ground Image (not fundamental uncertainty contributor) [algorithm 3C]
Flat Field Correction Ground Image (not fundamental uncertainty contributor) [algorithm 4A]
Aperture Thermal Correction Uncertainty Ground Image [algorithm 2D]
F-Number Thermal Correction Uncertainty Ground Image [algorithm 2E]
Integration Time Ratio Uncertainty Ground Image [algorithm 5A] (Integration time zero offset uncertainty SSI)
Solar Spectral Irradiance
Bad Pixel Correction Uncertainty SSI [algorithm 1A]
Two Row Correction Uncertainty SSI [algorithm 1B]
True Dark Image Correction Uncertainty SSI [algorithm 1C]
Row-wise Dark Pedestal Shift Correction Uncertainty SSI [algorithm 1D]
Background Level Uncertainty SSI (Dark pedestal shift correction uncertainty) [algorithm 1E]
FPA Thermal Variation Uncertainty SSI [algorithm 2A]
FPA Linearity Uncertainty SSI [algorithm 2B]
FPE Thermal Variation Uncertainty SSI [algorithm 2C]

Blackbody Radiation Correction Uncertainty SSI [algorithm 3A]
Dark Bad Pixel Correction Uncertainty SSI [algorithm 1A]
Dark Two Row Correction Uncertainty SSI [algorithm 1B]
Dark True Dark Image Correction Uncertainty SSI [algorithm 1C]
Dark Row-wise Dark Pedestal Shift Correction Uncertainty SSI [algorithm 1D]
Dark Background Level Uncertainty SSI (Dark pedestal shift correction uncertainty) [algorithm 1E]
Dark FPA Thermal Variation Uncertainty SSI [algorithm 2A]
Dark FPA Linearity Uncertainty SSI [algorithm 2B]
Dark FPE Thermal Variation Uncertainty SSI [algorithm 2C]
Dark Blackbody Radiation Correction Uncertainty SSI [algorithm 3A]
Dark Subtraction SSI (not fundamental uncertainty contributor) [algorithm 3B]
Blank Aperture Subtraction SSI (not fundamental uncertainty contributor) [algorithm 3C]
Flat Field Correction SSI (not fundamental uncertainty contributor) [algorithm 4A]
Aperture Thermal Correction Uncertainty SSI [algorithm 2D]
F-Number Thermal Correction Uncertainty SSI [algorithm 2E]
Integration Time Ratio Uncertainty SSI [algorithm 5A] (Integration time zero offset uncertainty SSI)
Aperture Ratio Uncertainty SSI [algorithm 5B]
Flat Field: Spectralon (20 mm)
Bad Pixel Correction Uncertainty 20 mm FF [algorithm 1A]
Two Row Correction Uncertainty 20 mm FF [algorithm 1B]
True Dark Image Correction Uncertainty 20 mm FF [algorithm 1C]
Row-wise Dark Pedestal Shift Correction Uncertainty 20 mm FF [algorithm 1D]
Background Level Uncertainty 20 mm FF (Dark pedestal shift correction uncertainty) [algorithm 1E]
FPA Thermal Variation Uncertainty 20 mm FF [algorithm 2A]
FPA Linearity Uncertainty 20 mm FF [algorithm 2B]
FPE Thermal Variation Uncertainty 20 mm FF [algorithm 2C]

Blackbody Radiation Correction Uncertainty 20 mm FF [algorithm 3A]
Dark Bad Pixel Correction Uncertainty 20 mm FF [algorithm 1A]
Dark Two Row Correction Uncertainty 20 mm FF [algorithm 1B]
Dark True Dark Image Correction Uncertainty 20 mm FF [algorithm 1C]
Dark Row-wise Dark Pedestal Shift Correction Uncertainty 20 mm FF [algorithm 1D]
Dark Background Level Uncertainty 20 mm FF (Dark pedestal shift correction uncertainty) [algorithm 1E]
Dark FPA Thermal Variation Uncertainty 20 mm FF [algorithm 2A]
Dark FPA Linearity Uncertainty 20 mm FF [algorithm 2B]
Dark FPE Thermal Variation Uncertainty 20 mm FF [algorithm 2C]
Dark Blackbody Radiation Correction Uncertainty 20 mm FF [algorithm 3A]
Dark Subtraction 20 mm FF (not fundamental uncertainty contributor) [algorithm 3B]
Blank Aperture Subtraction 20 mm FF (not fundamental uncertainty contributor) [algorithm 3C]
Aperture Thermal Correction Uncertainty 20 mm FF [algorithm 2D]
F-Number Thermal Correction Uncertainty 20 mm FF [algorithm 2E]
Flat Field: Small Aperture (0.5 mm)
Bad Pixel Correction Uncertainty 0.5 mm FF [algorithm 1A]
Two Row Correction Uncertainty 0.5 mm FF [algorithm 1B]
True Dark Image Correction Uncertainty 0.5 mm FF [algorithm 1C]
Row-wise Dark Pedestal Shift Correction Uncertainty 0.5 mm FF [algorithm 1D]
Background Level Uncertainty 0.5 mm FF (Dark pedestal shift correction uncertainty) [algorithm 1E]
FPA Thermal Variation Uncertainty 0.5 mm FF [algorithm 2A]
FPA Linearity Uncertainty 0.5 mm FF [algorithm 2B]
FPE Thermal Variation Uncertainty 0.5 mm FF [algorithm 2C]
Blackbody Radiation Correction Uncertainty 0.5 mm FF [algorithm 3A]
Dark Bad Pixel Correction Uncertainty 0.5 mm FF [algorithm 1A]
Dark Two Row Correction Uncertainty 0.5 mm FF [algorithm 1B]

Dark True Dark Image Correction Uncertainty 0.5 mm FF [algorithm 1C]
Dark Row-wise Dark Pedestal Shift Correction Uncertainty 0.5 mm FF [algorithm 1D]
Dark Background Level Uncertainty 0.5 mm FF (Dark pedestal shift correction uncertainty) [algorithm 1E]
Dark FPA Thermal Variation Uncertainty 0.5 mm FF [algorithm 2A]
Dark FPA Linearity Uncertainty 0.5 mm FF [algorithm 2B]
Dark FPE Thermal Variation Uncertainty 0.5 mm FF [algorithm 2C]
Dark Blackbody Radiation Correction Uncertainty 0.5 mm FF [algorithm 3A]
Dark Subtraction 0.5 mm FF (not fundamental uncertainty contributor) [algorithm 3B]
Blank Aperture Subtraction 0.5 mm FF (not fundamental uncertainty contributor) [algorithm 3C]
Aperture Thermal Correction Uncertainty 0.5 mm FF [algorithm 2D]
F-Number Thermal Correction Uncertainty 0.5 mm FF [algorithm 2E]
Blank Aperture
Bad Pixel Correction Uncertainty Blank Aperture [algorithm 1A]
Two Row Correction Uncertainty Blank Aperture [algorithm 1B]
True Dark Image Correction Uncertainty Blank Aperture [algorithm 1C]
Row-wise Dark Pedestal Shift Correction Uncertainty Blank Aperture [algorithm 1D]
Background Level Uncertainty Blank Aperture (Dark pedestal shift correction uncertainty) [algorithm 1E]
FPA Thermal Variation Uncertainty Blank Aperture [algorithm 2A]
FPA Linearity Uncertainty Blank Aperture [algorithm 2B]
FPE Thermal Variation Uncertainty Blank Aperture [algorithm 2C]
Blackbody Radiation Correction Uncertainty Blank Aperture [algorithm 3A]
Dark Bad Pixel Correction Uncertainty Blank Aperture [algorithm 1A]
Dark Two Row Correction Uncertainty Blank Aperture [algorithm 1B]
Dark True Dark Image Correction Uncertainty Blank Aperture [algorithm 1C]
Dark Row-wise Dark Pedestal Shift Correction Uncertainty Blank Aperture [algorithm 1D]
Dark Background Level Uncertainty Blank Aperture (Dark pedestal shift correction uncertainty) [algorithm 1E]

Dark FPA Thermal Variation Uncertainty Blank Aperture [algorithm 2A]
Dark FPA Linearity Uncertainty Blank Aperture [algorithm 2B]
Dark FPE Thermal Variation Uncertainty Blank Aperture [algorithm 2C]
Dark Blackbody Radiation Correction Uncertainty Blank Aperture [algorithm 3A]
Dark Subtraction Blank Aperture (not fundamental uncertainty contributor) [algorithm 3B]

6.3 Uncertainty List: Scan Specific and Systematic Contributors

The final category of uncertainty contributors are the ones that are specific to individual scans. These include the final creation step of each of the calibration products, such as assembling a flat field, and the systematic uncertainties that only pertain to a single scan, such as polarization uncertainty in nadir science images. The list is organized in a similar way as the previous two lists, grouped by scan type. The ground image scan type is split into three separate categories: uncertainties that only apply to the reflectance data produce, uncertainties that only apply to the radiance data product, and uncertainties that apply to both data products. When the uncertainty is generated by a specific algorithm from the data pipelines, it is labeled with the algorithm number. There are an additional 26 uncertainties in this list, not counting the non-fundamental uncertainties.

Ground Image (Reflectance Data Product)
Solar Temporal Variation Uncertainty Ground Image [algorithm 6A]
SSI Ratio Uncertainty Ground Image [algorithm 6B]
Solar Zenith Angle Uncertainty [algorithm 6B]
Ground Image (Reflectance Data Product)
Unit Conversion Factor Generation Uncertainty Ground Image [algorithm 6C]
Ground Image (Both Data Products)
3-Pixel Binning Ground Image [algorithm 1F]
Wavelength Position Uncertainty Ground Image
Aperture Position Repeatability Ground Image
Polarization Uncertainty Ground Image
OSF Leakage Uncertainty Ground Image

PSF Uncertainty Ground Image
Camera Electronic Timing Uncertainty Ground Image
Scatter Uncertainty Ground Image
Solar Spectral Irradiance
Per Pixel Scan Rate Uncertainty SSI (previously called pointing uncertainty) [algorithm 7A]
Along slit Pixel FOV Uncertainty SSI [algorithm 7A]
Integration Along Columns (not a fundamental uncertainty contributor) [algorithm 7B]
Integration Across Scan Images (not a fundamental uncertainty contributor) [algorithm 7C]
Acquisition Period Uncertainty SSI [algorithm 7D]
Aperture Position Repeatability SSI
OSF Leakage Uncertainty SSI
Camera Electronic Timing Uncertainty SSI
Wavelength Position Uncertainty SSI
Flat Field: Spectralon (20 mm)
Spectral Distortion Correction Uncertainty 20 mm FF [algorithm 8B]
BTDF Correction Uncertainty 20 mm FF [algorithm 8B]
Creation of Flat Field (Not a fundamental uncertainty contributor) [algorithm 8B]
Glint Uncertainty 20 mm FF
Peak Alignment Uncertainty 20 mm FF [algorithm 8A]
Transmissive Diffuser Comparison Uncertainty
Pointing Uncertainty 20 mm FF
Flat Field: Small Aperture (0.5 mm)
Spectral Distortion Correction Uncertainty 0.5 mm FF [algorithm 8B]
Creation of Flat Field (Not a fundamental uncertainty contributor) [algorithm 8B]
Peak Alignment Uncertainty 0.5 mm FF [algorithm 8A]
Pointing Uncertainty 0.5 mm FF

Blank Aperture
Creation of Blank Aperture Image (Not a fundamental uncertainty contributor) [algorithm 9A]

6.4 Uncertainty Budget Plots

A version of the full uncertainty budget, with every known significant term included, is shown in Figure 102. There are many insignificant terms, especially in the dark uncertainties, which are not included. There are several features of this budget that are evident after a quick examination. The range of the shown budget is from 0 to 1 percent, with the CLARREO Pathfinder goal being less than 0.3% (3000 ppm), although there are some flyaway values right at the edges of the wavelength range. The budget is fixed to the CLARREO wavelength range, from 350 nm to 2300 nm. The budget has many terms that are highly sensitive to total amount of light present at a given wavelength. There is an uncertainty peak that appears at 850 nm because of the lower aluminum reflectivity and grating efficiency in this region (see Figure 34 and Figure 35.)

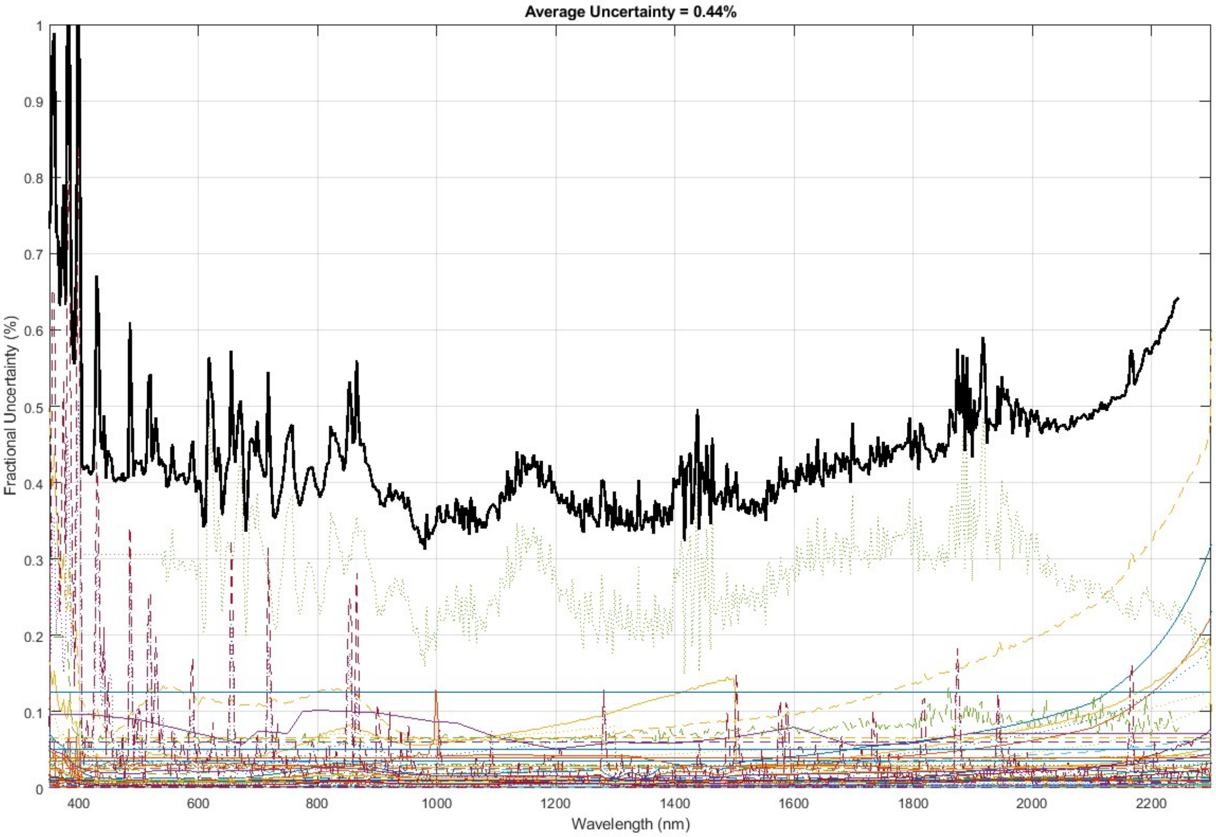

Figure 102. Uncertainty budget terms as a function of wavelength.

Since the imager will be viewing both solar and Earth ground scenes, it is necessary to make assumptions about the incoming spectra in order to generate an uncertainty budget. The budget will be different depending on the input scene. When looking at the sun, which is relatively constant, the radiance shown in Figure 103, blue line, is utilized. It should be noted that this spectrum is different from the normally-viewed solar irradiance (shown in Figure 70), because it has been scaled by the solid angle of the solar disk to be converted into radiance units. Earth scenes will always have spectral regions of nearly zero radiance due to water absorption bands in the atmosphere (evident in Figure 28) which cause a high non-instrument related uncertainty in those wavelength bands. As an attempt to represent the uncertainty of the instrument, rather than the dependence on the scene type, a perfect Lambertian surface with 30% reflectivity is assumed as the ground scene. The incident light source is taken to be the Sun. The resulting ground radiance is shown in Figure 103, red line. Note that the difference between the two radiances is approximately 5 orders of magnitude. It is evident, even on the logarithmic scale of Figure 103 that both the UV and IR portions of the input scenes are at lower radiance, which causes the overall increase in the error budget in these spectral regions.

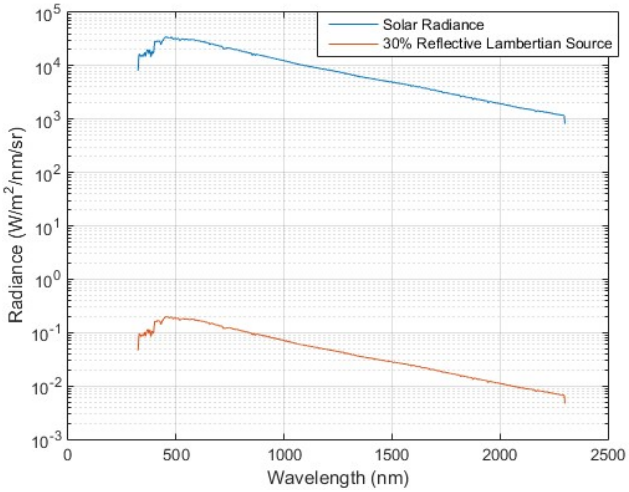

Figure 103. Uncertainty budget input radiance sources. The blue line is the solar radiance, and the red line is the simulated ground radiance.

6.5 Uncertainty Contributors: Image Acquisition

This section describes all the unique uncertainty contributors from the first category list above (section 6.1). These are the uncertainties that are generated with every image, and not associated with a specific algorithm or scan.

6.5.1 Read Noise

Read noise is the electronic noise associated with the readout of a sensor [6]. In a camera, there is read noise for every pixel, which is usually similar, but not necessarily the same as every other pixel. It is an independent noise source for every image. The read noise of each pixel is measured and combined independently to determine the read noise uncertainty contribution. The read noise of CLARREO HySICS will be measured on-orbit during commissioning. It is expected to be around 28 DN for all pixels.

The fractional uncertainty generated by a read noise of 28 DN is shown in eq. 56:

$$Unc._{Read\ noise\ single\ pixel} = \frac{28\ (DN)}{S_{Obj}(\lambda)} \qquad 56$$

An absolute uncertainty of 28 DN is applied to every pixel at the start of each pipeline.

Given a required ground resolution of 0.5 km per pixel, however, three pixels will be averaged together per spatial element of the ground scene. The averaging helps reduce this uncertainty by the square root of three, as shown in equation 57.

$$Unc._{Read\ noise\ ground\ image} = \frac{28\ (DN)}{\sqrt{3} \cdot S_{Obj}(\lambda)} \qquad 57$$

This random noise source can be reduced further through averaging an ensemble of pixels if lower resolution ground images are required. The uncertainty is reduced by the square root of the number of pixels averaged.

Read noise for various data sets is discussed in the sections below to give the reader an idea of how the uncertainty budget estimation was generated. The final uncertainty, however, uses equation 56 for every image acquired.

6.5.1.1 Dark Read Noise Ground Image Uncertainty

The dark read noise is nearly the same as described in the nominal scan. The average read noise per pixel is 28 DN, but 500 dark images will be used to generate the average dark image. In addition, since there are 3-pixels averaged for each spatial element, the dark read noise can be reduced by this factor as well. The result is given in equation 58. This tends to be a very small contributor due to the averaging.

$$Unc._{Dark\ Read\ noise\ ground\ image} = \frac{28\ (DN)}{\sqrt{3} \cdot \sqrt{500} \cdot S_{Obj}(\lambda)} \qquad 58$$

6.5.1.2 SSI Integrated Read Noise Uncertainty

In the SSI scan, pixels are summed to produce the integrated spectrum of the full solar disk. In a pure summation case, the independent uncertainties of the pixel used increases by the square root of the number of pixels. For the along-slit integration, the read noise contribution is the quadrature summation of the read noise in each pixel (assuming different read noise from each pixel):

$$RN_{col}(\lambda) = \sqrt{\sum_{pix} (\sigma_{Pixel\ Read\ Noise})^2} \qquad 59$$

where *pix* is the pixels to be integrated in a column. The result is the total amount of read noise at each wavelength (column) in each image.

In the across-slit (or images) direction, the summation is similar, but, for the same read noise in each image, can be reduced to:

$$\sigma_{SSI\ Read\ Noise} = \sqrt{\sum_{image} (RN_{col})^2} \qquad 60$$

where RN_{col} is the read noise of the column, and $image$ is the images in the integration.

The result is the total amount of read noise at each wavelength (column), which is scaled by the total power in the SSI integration at that wavelength to give fractional uncertainty:

$$Unc._{Read\ Noise}(\lambda) = \frac{\sigma_{SSI\ Read\ Noise}(\lambda)}{S_{Sun}(\lambda)} \qquad 61$$

where $S_{Sun}(\lambda)$ is defined in section 3.1.3.4. This uncertainty is shown in Figure 104, and represents the largest contributor to the solar spectral irradiance scan uncertainty. It should be noted that while the fractional shot noise uncertainty is decreased by a larger signal achieved by integrating multiple images, the read noise uncertainty increases by the square root of the number of images, and therefore generally becomes dominant when many images are summed.

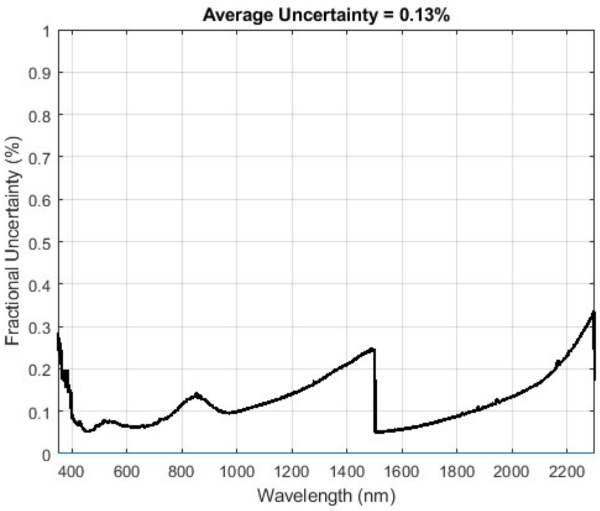

Figure 104. Fractional read noise uncertainty in SSI scan.

6.5.2 Shot Noise

Shot noise is the noise associated with detecting individual quanta of light, a photon, at discrete time instants [6]. The noise is a Poisson process, and can be applied equally to either the detection of photons incident on each pixel, or to the detection of the electrons (or holes) that the photon generates within the pixel. The number of electrons generated is known from the pixel gain, which was around 12 electrons/DN on the HySICS balloon FPA. The number of electrons is given by:

$$N_{electrons} = g_{pix} \cdot S_{pix} \qquad 62$$

where g is the pixel gain, and S_{pix} is the detected signal, in DN. As a Poisson process, the shot noise is the square root of the detected signal, and, in DN, is given by:

$$\sigma_{Pixel\ Shot\ Noise} = \frac{1}{g_{pix}} \sqrt{N_{electrons}} \qquad 63$$

It is important that shot noise is estimated from the actual signal present on the FPA, and not include the fixed offset of each ADC and pixel. The calculation is therefore performed following the true dark subtraction algorithm [algorithm 1C], which is intended to remove the undesired fixed pattern noise from the image to ensure a correct calculation of the shot noise.

6.5.2.1 Dark Shot Noise Ground Image Uncertainty

Despite the dark images having low signal, there is still signal present from dark current and blackbody radiation. This signal also generates shot noise.

As seen in section 6.5.1.1, the random uncertainty contributors from the dark images significantly benefit from using at least 500 averaged images to generate the dark image. In addition, with the 3-pixel averaging, the uncertainty can be reduced by another factor of $\sqrt{3}$, as shown in equation 64.

$$Unc._{Dark\ Shot\ noise\ ground\ image} = \frac{\sigma_{Pixel\ Dark\ shot\ noise}}{\sqrt{3} \cdot \sqrt{500} \cdot S_{Obj}(\lambda)} \qquad 64$$

where $\sigma_{Pixel\ Dark\ shot\ noise}$ contains the shot noise from both blackbody background and dark current.

6.5.2.2 SSI Integrated Shot Noise Uncertainty

In the integrated solar spectral irradiance case, the number of detected electrons is given by equation 62, where S_{pix} is the total integrated signal over all images in the scan within each wavelength bin. Shot noise in each image, and on each pixel, is an independent process, and can be summed in quadrature along each column to give the total shot noise at each wavelength:

$$\sigma_{Shot\ Noise}(\lambda) = \sqrt{\sum_{pix} (\sigma_{Pixel\ Shot\ Noise})^2} \qquad 65$$

where *pix* ranges from pixel 1 to pixel 480. The fractional uncertainty is given by scaling the above shot noise by the total detected signal:

$$Unc._{Shot\ Noise}\ (\lambda) = \frac{\sigma_{Shot\ Noise}(\lambda)}{S_{Sun}(\lambda)} \qquad 66$$

where $S_{Sun}(\lambda)$ is defined in section 0.

Although shot noise can often be a limiting uncertainty, the fractional contribution is significantly reduced in measurements with a large number of photons, as is the case when measuring the solar spectral irradiance. It is a nearly insignificant contribution to the total uncertainty budget.

6.5.3 Quantization Noise

Quantization noise is present in any signal that is digitized into discrete levels, as is the case in the HySICS 16-bit digitized camera signal. Signals reported by the camera are expected to have a uniform distribution within any one of the 2^{16} digitization levels. The quantization noise for a uniform distribution is given by equation 67 where LSB (least significant bit) is a single quantization level. Again, the fractional uncertainty is assumed to be the ratio of quantization noise and detected signal. It should be noted that, on average, the if read noise is around 8.3 DN, this noise source is approximately 0.29 DN, or 28.8 times lower than the read noise.

$$\sigma._{Quantization} = \frac{1}{\sqrt{12}}\ LSB \qquad 67$$

Quantization noise is an independent noise source, and which can be reduced by averaging to the square root of the number of values observed.

6.5.4 Sensor After Image Uncertainty

There has been evidence in previous programs that Teledyne detectors may have an after image due to a CTE mismatch between the HgCdTe substrate and the silicon ROIC. The mismatch causes the HgCdTe substrate to pull slightly away from the silicon, resulting in an increased amount of capacitance in the signal transfer. The increased capacitance slows the readout, causing some charge to be trapped, and then read out during the next frame acquisition. It is observed as an after image on the sensor. During the characterization and calibration campaign [2], the sensor after image was measured for various signal levels, and was found to always be lower than 120 ppm, which is set as the flat uncertainty on this contributor.

6.5.5 Line Driver Crosstalk Uncertainty

During testing, it was discovered that for very high gradient features, a crosstalk between FPE columns could be observed. The crosstalk is likely due to the line driver amplifiers not completely settling to their required voltage because high gradient features can force them to generate a very large voltage swing in a short amount of time. As a result, a pixel with high signal located to the right of a pixel with low signal can be slightly reduced.

This effect is very small, and does not turn on until there is at least 32767 DN difference between neighboring pixels. After this level, it has an estimated slope of 7.3 DN/655 DN additional difference between two neighboring pixels.

This uncertainty is calculated and stored as an absolute DN value per pixel, and dependent on the scene.

6.6 Uncertainty Contributors: Correction Algorithms

This section describes all the unique uncertainty contributors from the second category list above (section 6.2). These are the uncertainties that are generated with every image, and not associated with a specific algorithm or scan.

6.6.1 Bad Pixel Correction Uncertainty [algorithm 1A]

Uncertainty in the value of a bad pixel after it has been corrected by its neighbors is dependent on the uncertainty of all the pixels used in the calculation, and the associated covariance between those pixels. The covariance is likely to be different in the spectral and spatial dimensions as well. As such, covariance matrices will be studied from on-orbit data, and the uncertainty in corrected pixels will be determined during the first few months of data collection. Currently, this algorithm averages the uncertainties of the neighbors used in the correction. It is applied in the final step of each pipeline to allow for the uncertainties to be computed for the neighboring pixels.

The bad pixel correction algorithm is discussed in section 5.1.3.1.

6.6.2 Two-Row Correction Uncertainty [algorithm 1B]

The two-row correction is expected to mostly remove image-to-image variations in the scans, particularly caused by timing jitter between the two asynchronous clocks in the HISIE FPGA and FPA ROIC. It is important to identify and apply the uncertainty associated with image-to-image variations. Fortunately, this uncertainty is quite simple to measure, since it requires only a repeated measurement of a stable signal, which is obtained with every dark image acquisition.

The two-row correction uncertainty is defined as the standard deviation of the mean signal from the first 250 dark images in a data set. The mean signal of all pixels is used to eliminate the random noise sources in individual pixels. The residual timing jitter (and other noise sources, if present) that is not removed by the two-row correction of the pre-scan dark images shows up as an increased standard deviation in the images. It is stored as an absolute DN value for each image within a scan.

When summed, this uncertainty is taken as a dependent, systematic uncertainty for every pixel in any image, but assumed to be independent within other frames.

The two-row correction algorithm is discussed in section 5.1.3.2.

6.6.3 True Dark Image Correction Uncertainty [algorithm 1C]

True dark images, or the detector's fixed pattern noise, is subtracted from each image, including dark images. This is done to eliminate the signal offset before calculating shot noise, and applying the row-wise dark pedestal and full-frame dark pedestal corrections, which are dependent on true signal, and properly setting the zero-level before applying the linearity correction.

The true dark images are a pure offset for each pixel, measured during the cold target test [2], and will not change for the life of the mission. Since the true dark signal is removed from all images, it is re-inserted in the dark subtraction step, resulting in an image with no variation. As such, there is no uncertainty associated with the true dark subtraction.

The true dark image correction is discussed in section 5.1.3.3.

6.6.4 Row-wise Dark Pedestal Shift Correction Uncertainty [algorithm 1D]

The uncertainty associated with the row-wise dark pedestal correction was still being studied at the time of writing. However, a placeholder uncertainty computation has been created for the pipeline algorithms that is expected to have the form of the final uncertainty values.

The placeholder assumes that there is an uncertainty of 10% in the correction slope, and calculates the resulting uncertainty in the signal. This tends to be a small correction, which can only have a maximum of around 20 DN for a fully saturated row, so a 10% uncertainty in the slope leads to a correction uncertainty of 2 DN in the worse-case scenario.

This uncertainty is used as the same correction on every pixel within a row, which indicates it is dependent along every row, but independent down columns. Since there are no row-wise summations or averages that occur in any of the pipelines, this uncertainty can be treated as always independent.

The row-wise dark pedestal shift correction is discussed in section 5.1.3.4

6.6.5 Background Level Uncertainty (Dark pedestal shift correction uncertainty) [algorithm 1E]

The full-frame dark pedestal uncertainty was also still being studied at the time of writing. Like the row-wise version, a placeholder uncertainty computation has been created for the pipeline algorithms that is expected to have the form of the final uncertainty values.

The placeholder has three components to its uncertainty, expected to encompass the most likely types of uncertainty that might be generated from the algorithm. The first is a straight offset uncertainty, which would be the same for every pixel in an image. This value has been set to zero initially. The second is a fraction of the total power, where the fraction is set to 10% of the average correction slope for all pixels. The third is a fraction of the integration time, where the fraction has been set to zero initially.

These three terms are user definable, and will be set when the uncertainty contribution is better understood.

This correction applies to every pixel in an image, but with various, but probably not totally independent slopes. It is even more complicated across images, since the correction slope is always the same for any one pixel, and therefore are the same for all images, but the total image power is independent. The combination of these terms is quite complicated and still being studied. The maximum uncertainty assumption, which is that this uncertainty is dependent across all pixels and images, may be used out of simplicity.

The background level uncertainty algorithm is discussed in section 5.1.3.5.

6.6.6 FPA Thermal Variation Uncertainty [algorithm 2A]

The uncertainty associated with the FPA thermal correction is found empirically, by using the uncertainty in the FPA temperature (measured to be 0.014 °C over 12 hours). The correction value is determined three times: once for the measured temperature, and then for the measured temperature plus or minus the temperature uncertainty. The resulting values give a correction value plus or minus the correction uncertainty.

This method does not include the uncertainty in the FPA temperature correction curve fit. The curve fit has confidence intervals for each parameter, which are used in a monte carlo simulation to determine the total uncertainty from the fit. This value is summed in quadrature with the previously found correction uncertainty to determine the total uncertainty.

It is likely that the uncertainty from a monte carlo simulation is significantly overestimating the uncertainty, since it does not take into account that the correction curves are nearly linear over the small temperature ranges of concern. The true uncertainty should take into account that even if the correction fit is wrong, the relative fit is still much closer than the absolute uncertainty of any one value on the fit curve. This reduction in uncertainty has not been investigated or applied at the time of writing.

Since this algorithm operates with a correction that is nearly the same for every pixel, it is assumed to be dependent within an image, although that is likely an overestimation, and independent from image to image, as the temperature varies randomly.

The FPA thermal variation algorithm is discussed in section 5.1.3.6.

6.6.7 FPA Linearity Uncertainty [algorithm 2B]

The FPA linearity algorithm and uncertainties are discussed in section 5.1.3.7.

6.6.8 FPE Thermal Variation Uncertainty [algorithm 2C]

The FPE thermal variation uncertainty is approached in the same way as the FPA thermal variation uncertainty. Again, the temperature measurement uncertainty, measured at 0.004 °C, is used to calculate an upper and lower value from the correction. The result is used as an uncertainty in FPE correction.

Similarly to the FPA thermal correction, the absolute uncertainty calculation from the confidence intervals of the curve fit coefficients does not take into account that this is a relative correction, and significantly overestimates the uncertainty.

This uncertainty term is mostly dependent along columns, since the ADCs operate on even and odd columns, and is considered dependent over the whole image. It is mostly independent across images, since the temperature term fluctuates randomly.

The FPE thermal variation correction algorithm is discussed in section 5.1.3.8.

6.6.9 Blackbody Radiation Correction Uncertainty [algorithm 3A]

The blackbody radiation correction applies a slope map, dependent on the thermal change of the OSF, to every pixel. The uncertainty is generated by two sources: the uncertainty in the temperature measurement and the uncertainty in the correction slope map. The temperature measurement uncertainty is directly computed as the standard deviation of the OSF thermistor value when held at a constant temperature, and is set to 0.01 °C. The uncertainty in the slope map is intended to be calculated from on-orbit data, since the thermal gradients cannot be replicated in a laboratory environment, but is currently set to 10% of the slope value for laboratory measurements.

Like many of the thermal corrections, this one is considered dependent over any one image, but independent across images.

The blackbody radiation correction is discussed in section 5.1.3.9.

6.6.10 Dark Subtraction Uncertainty [algorithm 3B]

After all the uncertainty terms have been calculated and applied to the dark images, they are interpolated from the pre-scan dark images to the post-scan dark images. Using strict uncertainty propagation, the interpolated uncertainty would actually be reduced through the scan, due to averaging more images. While this is true for linear changes in the dark signal on each pixel, it is an underestimation if there are non-linear variations in the dark signal. To compensate for possible non-linear variation, the dark image uncertainty is assumed to remain linear, interpolated from one set of dark images to the other, rather than be reduced. The linearity of the dark signal over the duration of a nominal scan will be studied in on-orbit data. If it is found to be consistently linear, this uncertainty may be reduced after launch.

This uncertainty is a combination of the other fundamental uncertainties of the dark images, and represents a step in the uncertainty propagation chain, but will not be reported in the final list of uncertainties. If it were, it would be double-counting all the dark image uncertainty contributions.

The dark images and science images are independent, and can be directly summed in quadrature.

The dark subtraction algorithm is discussed in section 5.1.3.10.

6.6.11 Blank Aperture Subtraction Uncertainty [algorithm 3C]

Like the dark image subtraction algorithm, the blank aperture subtraction uses the total uncertainty computed in the blank aperture pipeline, rather than adding a new uncertainty contributor. This term is also required for uncertainty propagation, but, since it represents the summation of all the blank aperture uncertainties, it is left out of the final list of uncertainties.

The blank aperture and science images are independent, and can be directly summed in quadrature.

The blank aperture subtraction algorithm is detailed in section 5.1.3.11.

6.6.12 Flat Field Correction Uncertainty [algorithm 4A]

The uncertainty associated with applying the flat field correction to a data set is also merely a propagation through the calculation. The flat field correction map has its own uncertainties associated with it, computed within its pipeline, and it is multiplied by the science data. No new uncertainty contributor is produced.

The two scans are independent, and their fractional uncertainties are summed in quadrature. In this computation, since it is a multiplication step, fractional uncertainties are used, rather than the absolute DNs that are used in the dark image and blank aperture subtraction steps.

The flat field correction algorithm is described in section 5.1.3.12.

6.6.13 Aperture Thermal Correction Uncertainty [algorithm 2D]

The aperture thermal correction, being a simple multiplication of two factors, the temperature and the aluminum CTE, is merely the propagation of the uncertainties in those values. The temperature uncertainty is estimated at 0.02 °C, and the aluminum CTE uncertainty is set to 10% of the CTE. A search for CTE of aluminum reveals that there are reported numbers of up to a 5% variation, depending on the type of aluminum used.

These fractional uncertainties are summed in quadrature to provide the total aperture thermal correction uncertainty.

This uncertainty simultaneously applies to the whole image, and is propagated as a multiplicative dependent uncertainty.

The aperture thermal correction is discussed in section 5.1.3.13.

6.6.14 F-Number Thermal Correction Uncertainty [algorithm 2E]

The F-number thermal correction uncertainty is nearly identical to the aperture thermal correction uncertainty. There are two individual contributors that are multiplied together: the F-number vs temperature slope, and the delta temperature. The uncertainties are similarly propagated by summing their fractional values in quadrature. The F-number vs temperature slope uncertainty is set to 20% of the slope value, and the temperature uncertainty has been measured at 0.04 °C.

This uncertainty simultaneously applies to the whole image, and is propagated as a multiplicative dependent uncertainty.

The f-number thermal correction is discussed in section 5.1.3.14.

6.6.15 Integration Time Ratio Uncertainty [algorithm 5A]

The integration time associated with a particular scan is an integer number of detector readout row times (RT). There is no uncertainty associated with choosing the integer value. The conversion from RT to seconds, despite having some associated uncertainty, is cancelled out of the integration time ratio. The only uncertainty in the integration time ratio calculation comes from the uncertainty in the 0 RT integration time offset. The 0 RT value has been measured in the lab to actually be 0.965 RT, with an uncertainty of 0.001 RT.

This uncertainty is merely propagated through the integration time ratio algorithm. As might be expected, it is a larger fractional uncertainty for shorter integration times, and a smaller fractional uncertainty for longer integration times.

The factor is a multiplier for all images of a scan, and is dependent for all pixels.

The integration time ratio algorithm is discussed in section 5.1.3.15.

6.6.16 Aperture Ratio Uncertainty [algorithm 5B]

The aperture ratio application only appears in the SSI pipeline. The aperture ratio, as described in section 5.2.1.2, is purely a measurement made in the lab during the calibration campaign. It ultimately represents a propagation of all the uncertainties associated with the measurement of the aperture ratio into the SSI data pipeline, and from there, into the reflectance and radiance data pipeline.

The measurement of the aperture ratio, and all the associated uncertainties is described in [22], the characterization and calibration report.

The aperture ratio is implemented as a single vector used to scale the SSI scan (also a single vector after the integration steps), and can be propagated using a quadrature sum of fractional uncertainties into the SSI calculation. The difference between this uncertainty and the other uncertainties that propagate from one pipeline to another, such as the flat field uncertainty, is that the full aperture ratio uncertainty will be the same for all data sets, since it was measured in a laboratory, not on-orbit. All of its individual components, instead of being separated into fundamental uncertainties like the other propagation steps, are kept as a single, total uncertainty. This choice facilitates pipeline design, since a single uncertainty can be applied, rather than computing the exact same uncertainty from laboratory measurement data in a separate pipeline.

6.6.16.1 Aperture Ratio Attenuation Uncertainty Contributors

Despite being summed into a single uncertainty to be propagated into the SSI pipeline, there are a handful of significant uncertainty contributors that comprise it which are described here.

The second type of attenuation used to view the solar signal, as described in section 5.2, is changing the size of the aperture, from the Earth-viewing 20 mm aperture, to the solar-viewing 0.5 mm aperture. Ideally, if the optical system behaved the same way for both apertures, the attenuation factor would be a pure ratio of the areas of the two apertures, which is a factor of 1600, or 3.2 orders of magnitude. However, the optical system does not treat both apertures the same, and, in particular, the efficiency of the grating depends on how many grating rulings are illuminated, which is different for the two apertures, and on the wavelength of light. As a result, the aperture ratio must be measured within the full optical system.

The aperture ratio measurement is a relative measurement made by swapping from the Earth to the solar viewing aperture while viewing a stable light source. The ratio between the detected power levels on each individual pixel is equivalent to the aperture ratio. Since the light is dispersed spectrally, the measurement conveniently provides a wavelength dependence as well, provided the light source covers the full CLARREO Pathfinder wavelength range. When viewing the light source with the larger 20 mm aperture, the signal is generally quite large, and the integration time must be decreased to compensate. Likewise, when viewing with the 0.5 mm aperture, the integration time must be increased to compensate. The integration time has an attenuation factor of around 2.8 orders of magnitude, which is still not high enough to completely compensate for the aperture ratio attenuation factor. The remaining 0.4 orders of magnitude are accounted for by the dynamic range of the detector, which is 16-bits.

Using the integration time to compensate for the aperture ratio attenuation rather than varying the light source power is significantly easier but requires precise knowledge of the integration time linearity. It is for this reason that the integration time uncertainties are included twice in the uncertainty budget.

Uncertainties associated with the relative measurement include the common random uncertainties, such as read noise, shot noise, dark versions of each, and quantization noise. They also include diffraction uncertainty from both the apertures, and background level uncertainty, as is common in the other HySICS measurements. In addition, there are laboratory setup uncertainties, including random variations in the light source, and a catch-all measurement uncertainty determined by repeating the measurement multiple times to observe variation in the aperture ratio. All of these uncertainties are repeated twice, once for the 20 mm aperture measurement, and once for the 0.5 mm aperture measurement. The last two uncertainties, the dark image offset and the short exposure uncertainty, are place-holders that were discovered on the HySICS balloon instrument, but expected to be better understood on CLARREO Pathfinder. The full budget is shown in Figure 105.

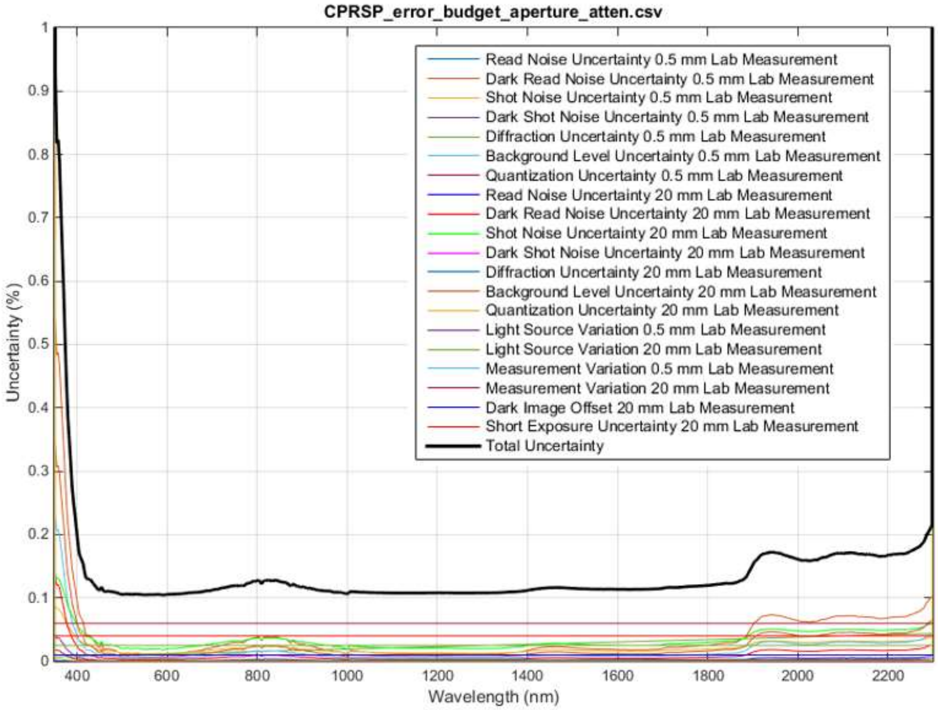

Figure 105. Aperture ratio attenuation uncertainty budget.

To determine the fractional uncertainty of each of these contributors, it is necessary to assume a light source spectral irradiance. In the HySICS balloon flight, two separate light sources were used, an FEL turned to a low power level, and a white LED. Together, these sources covered most, but not all of the wavelength range. For CLARREO Pathfinder, a Labsphere light source with plasma lamps to cover the UV/VIS range, and tungsten lamps with blackbody output to cover the IR portion. These sources will be input into an 8-12 inch integration sphere. A high light field uniformity is required if the apertures are merely swapped back and forth. Any non-uniformity in the light field will be compensated by dithering the field of view of the 0.5 mm aperture over the full 20 mm aperture field of view and averaging the result. The more uniform the field to begin with, the less dithering is required for an accurate ratio, hence the integration sphere. The assumed source spectral irradiance is shown in Figure 106. It should be noted that we are still in talks with Labsphere to generate this spectrum, so the uncertainty results based on it may have minor variations from this analysis. It will be updated when we have more information.

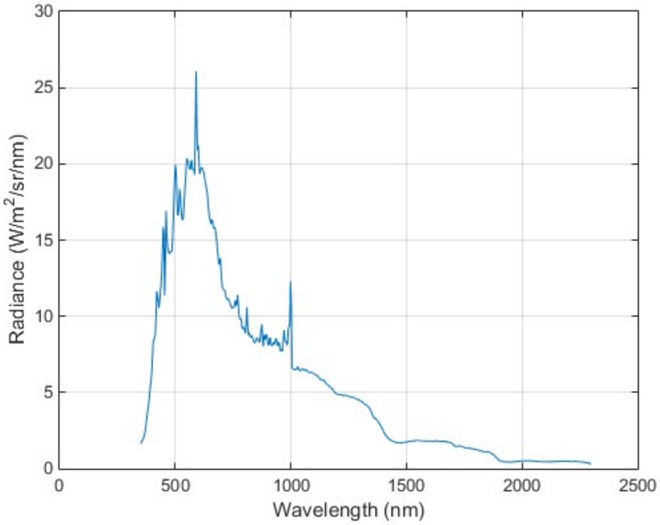

Figure 106. Assumed aperture ratio measurement light source spectrum.

6.6.16.1.1 Read Noise Uncertainty 0.5 mm and 20 mm Lab Measurement

The read noise uncertainty for both the 0.5 mm and 20 mm aperture ratio laboratory measurement is found in the same way as described in other read noise sections (e.g. section 6.5.1.) The benefit of making the measurement in a laboratory is that a high number of images can be averaged together to reduce the random uncertainties, such as read noise. In this case, 5000 images are assumed to be used. 5000 images is the equivalent of 5.5 minutes of data acquisition. The read noise is given by equation 68, where $S_{Source}(\lambda)$ is the detected signal from the laboratory light source, in DN. Note that the detected signal will be different for the 0.5 mm and 20 mm aperture measurements.

$$Unc._{Read\ noise\ Lab\ Measurement} = \frac{8.3\ (DN)}{\sqrt{5000} \cdot S_{Source}(\lambda)} \qquad 68$$

6.6.16.1.2 Dark Read Noise Uncertainty 0.5 mm and 20 mm Lab Measurement

The dark read noise uncertainty for a laboratory measurement is also the same as for other dark read noise (e.g. section 6.5.1.1.) Again, it can be significantly reduced through averaging, and 5000 images will be assumed here as well. The dark read noise uncertainty is the same as the read noise uncertainty, given by equation 69.

$$Unc._{Dark\ read\ noise\ Lab\ Measurement} = \frac{8.3\ (DN)}{\sqrt{5000} \cdot S_{Source}(\lambda)} \qquad 69$$

6.6.16.1.3 Shot Noise Uncertainty 0.5 mm and 20 mm Lab Measurement

As described in section 6.5.2.2, the shot noise is dependent on the signal level. Again, as a random noise source, it is reduced by the number of averaged images, which will be 5000, as described in section 6.6.16.1.2. The uncertainty is given by equation 70.

$$Unc._{Shot\ noise\ Lab\ Measurement} = \frac{\sigma_{Pixel\ shot\ noise}}{\sqrt{5000} \cdot S_{Source}(\lambda)} \tag{70}$$

6.6.16.1.4 Dark Shot Noise Uncertainty 0.5 mm and 20 mm Lab Measurement

The dark shot noise consists of shot noise from background blackbody radiation and from the dark current, as described in section 6.5.2.1. It is given by equation 71, and reduced by the number of dark images averaged.

$$Unc._{Dark\ Shot\ noise\ Lab\ Measurement} = \frac{\sigma_{Pixel\ Dark\ shot\ noise}}{\sqrt{5000} \cdot S_{Source}(\lambda)} \tag{71}$$

6.6.16.1.5 Quantization Uncertainty 0.5 mm and 20 mm Lab Measurement

The quantization uncertainty is described in section 6.5.3. Again, 5000 images are assumed to be averaged. The uncertainty is given by equation 72.

$$Unc._{Quantization\ Lab\ Measurement} = \frac{\left(\frac{1}{\sqrt{12}} \cdot LSB\right)}{\sqrt{5000} \cdot S_{Source}(\lambda)} \tag{72}$$

6.6.16.1.6 Background Level Uncertainty 0.5 mm and 20 mm Lab Measurement

The background level uncertainty is described in section 5.1.3.5.

6.6.16.1.7 Light Source Variation 0.5 mm and 20 mm Lab Measurement

Since the light source is expected to be constant throughout the aperture ratio measurement, any light source variation causes an error in the ratio. On the HySICS balloon measurements, the short-term (6 minute) light source variation was on the order of 20 ppm, and the long term (overnight) variation was a bit less than 100 ppm. As we will be acquiring a new light source for CLARREO, these measurements are not valid, and a 0.1% uncertainty placeholder will be used. The source level will be tracked throughout the experiment, and used to correct the light source variation over long time periods. It should be noted, however, that over short term periods, this variation will likely be random, and can benefit from multiple measurements. It is expected that through some amount of averaging, it can be driven down to 250 ppm.

6.6.16.1.8 Measurement Variation 0.5 mm and 20 mm Lab Measurement

The aperture ratio measurement will be performed multiple times in an effort to gather enough statistical information to know if the amount of variation is expected given the uncertainties described here. If the variation is higher than expected, it will be used as another uncertainty contribution after the known variations have been mathematically removed. This uncertainty serves as a catch-all for any unknown, random variations. As a placeholder, it is set at 600 ppm, which was the amount of measurement variation observed during the HySICS balloon instrument testing.

6.6.16.1.9 Dark Image Offset 20 mm Lab Measurement

During the HySICS balloon testing, a slight change in the dark offset was observed for each scan, defined as the continuous acquisition of a prescribed number of images. If the instrument made a scan to acquire the data, and then a second scan to acquire the associated dark images, there was an uncertainty due to this offset. It was removed by forcing the instrument to take both portions of the acquisition on the same scan, but not before taking some of the lab-based data which has some associated uncertainty for the 20 mm measurement. CLARREO Pathfinder will run if the mode to acquire light and dark images during the same scan if it is necessary. It should be nearly eliminated for CLARREO Pathfinder, and is only assigned a 0.01% uncertainty as a placeholder.

6.6.16.1.10 Short Exposure Uncertainty 20 mm Lab Measurement

There is often some amount of measurement uncertainty associated with acquiring data at very short integration times. In HySICS, because of the high light level from the FEL, the 20 mm aperture ratio measurement was required to be at 2 row times (33.6 μs) or 3 row times (50.4 μs.) Although it was never characterized, it appeared that there was a previously unknown linearity error visible up to 8 row times (134 μs) when analyzing this data. It is unknown if the CLARREO Pathfinder camera will have this uncertainty associated with short exposure times, but it will be studied now that we are aware of the possibility. In addition, for this test and the expected light level of the Labsphere source, the shortest exposure time will be well out of this range, at 100 row times (1.68 ms.) As a placeholder, the uncertainty assigned to it is 400 ppm.

6.7 Uncertainty Contributors: Scan Specific and Systematic

The third category of uncertainties mostly contains uncertainty computations that are applied to a single pipeline, rather than algorithms that can be repeated for multiple pipelines. This section describes all the uncertainty contributors from the third category list above (section 6.3).

6.7.1 Solar Temporal Variation Uncertainty [algorithm 6A]

The solar temporal variation, described in section 5.1.3.16, is a ratio of two TSIS SIM data sets that are smoothed through a convolution with the HySICS ILS. The uncertainty associated with it is not technically a HySICS instrument uncertainty, but is included in the HySICS uncertainty budget for completeness.

For the nominal case, the temporal variation measurement is a relative measurement made with TSIS SIM. It is assigned a 100 ppm fractional uncertainty, and will be further studied in discussions with the TSIS SIM team.

6.7.2 SSI Ratio Uncertainty [algorithm 6B]

There are two sources of uncertainty that appear in the SSI ratio (section 5.1.3.17), the uncertainty propagated from the SSI pipeline, and additional uncertainty picked up from interpolating the SSI to the nadir science data wavelength grid. The propagation of the SSI uncertainty to the ratio calculation is not a fundamental uncertainty source, but the interpolation step is. The uncertainties in the SSI interpolation are dependent on the covariance of the SSI data points, and are being further studied. In the likely scenario where the SSI scan and nadir scans do not have appreciable wavelength scale shift because the instrument temperature does not drift, the interpolation uncertainty is reduced and nearly eliminated.

These two sources of uncertainty are summed in quadrature with the temporal variation uncertainty from the previous section.

6.7.3 Solar Zenith Angle Uncertainty [algorithm 6B]

As described in the reflectance equation, 5, there is a reduction in power at the measurement location dependent on the solar zenith angle. Uncertainty in the angle results in uncertainty in the reflectance.

The solar zenith angle is calculated during the open-loop geolocation algorithm [181253]. The accuracy of the solar zenith angle is directly related to the accuracy of the geolocation, set to 400 m (1-sigma) as of the time of writing. This indicates that the ground point has a radial Gaussian distribution around the geolocated position with a standard deviation of 400 m, which, due to the curvature of the Earth over 400 m, causes a small error in the solar zenith angle.

The reflectance uncertainty on the solar zenith angle works out to 0.077 ppm when the Sun is directly overhead. This is a small enough term that it is included here for completeness but not added to the uncertainty budget.

6.7.4 Unit Conversion Factor Generation Uncertainty [algorithm 6C]

When generating the nadir science radiance data product (section 5.1.3.18), there are several sources of uncertainty. The two primary sources are the uncertainty produced in the “cross convolution” step used to compare the SIM SSI and the HySICS SSI, shown in Figure 74, and the TSIS SIM SSI uncertainty. The less significant sources of uncertainty are the ILS shape uncertainty, and the interpolation of the unit conversion factor to the nadir science data wavelength grid.

The cross convolution error, which is directly taken to be uncertainty, is outlined in section 5.2.1.5.

The TSIS SIM SSI uncertainty varies across the spectrum, and is less than 0.2% over most of the spectral range. This is a large uncertainty contribution that is present for the radiance data product that is not present for the reflectance data product. It is due to this term that, whenever possible, the reader should use the reflectance data product.

The ILS shape uncertainty, investigated through simulations of varying the ILS shape, have shown that the unit conversion factor is relatively insensitive to the shape of the ILS changing. This is primarily due to the fact that the SIM ILS is significantly wider than the HySICS ILS over the majority of the spectral range, and further smoothing through convolution with the HySICS ILS does not appreciably change the spectrum. Simulations show that even up to a 50% increase in the HySICS ILS width does not add a significant amount of error, shown in Figure 107. This uncertainty is being ignored while ILS measurement data uncertainty is studied.

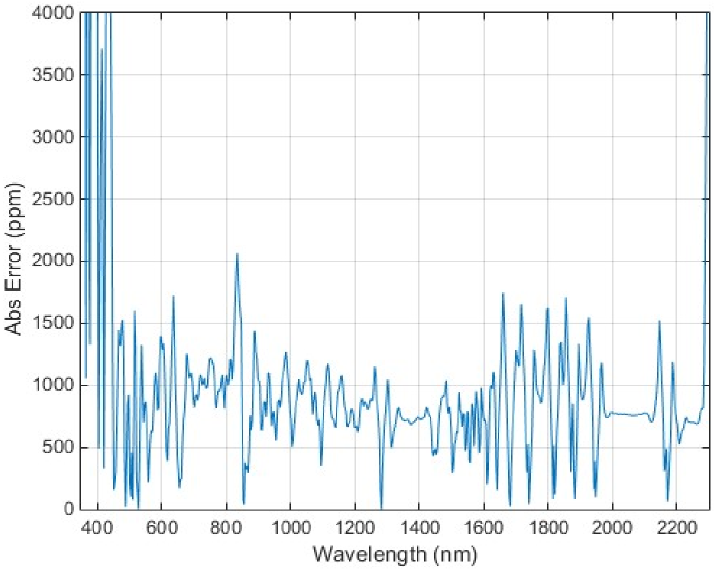

Figure 107. Error in the unit conversion factor due to an error of 50% larger ILS width. This error is less than 0.15% (1500 ppm) over most of the spectral range.

The final source of additional error is from an interpolation of the unit conversion factor to the nadir science data wavelength grid. Unlike for the reflectance scan, this interpolation is of a smooth, and slowly varying function, which has very low error in the interpolation. This factor will be ignored unless the unit conversion factor, measured on-orbit, has unexpected high spectral frequency components.

6.7.4.1 External SSI Uncertainty

It should be noted that since the CPRSP SSI measurement is directly compared to an external SSI, such as the TSIS SIM SSI, all uncertainties in the external measurement must be included in the total uncertainty budget. For TSIS SIM, this uncertainty is well documented, as in the TSIS SIM ATBD, [5]. The baseline TSIS SIM uncertainty is not included in the CLARREO Pathfinder uncertainty budget because it is independent of the CLARREO mission.

6.7.5 3-Pixel Binning [algorithm 1F]

Both HySICS data sets, reflectance and radiance, are 3-pixel binned (section 5.1.3.19) to reduce data volume and uncertainties.

In an averaging step, independent uncertainties are reduced by the square root of the number of pixels used. The additive dependent uncertainties are averaged, and the multiplicative dependent fractional uncertainties are averaged, meaning that they aren't reduced, but also don't increase.

This algorithm only uses previously defined uncertainties, and does not generate any new ones.

6.7.6 Wavelength Position Uncertainty

The wavelength positioning uncertainty is dependent on the amount of uncertainty in the wavelength scale location coupled with the measured ground signal, which is determined via the Pen-ray measurement, discussed in section 5.2.3. If the measured signal has a high spectral gradient, small errors in the wavelength position can cause high uncertainties in the resulting signal measurement.

This is one of the few algorithms in this section that can be reused, once for the nadir science data scans, and once for the SSI scans. In both cases, the spectral gradient in the images is calculated, and multiplied by the wavelength scale uncertainty at each wavelength bin. The result is the wavelength position uncertainty.

6.7.7 Aperture Position Repeatability (Large and Small Apertures)

The instrument aperture is on a tightly controlled, motorized wheel. It is expected to maintain its position with an uncertainty of 0.0003 degrees. However, the instrument does not have the same throughput if the aperture is moved. To estimate the signal uncertainty due to uncertainty in the aperture position, a measurement of a uniform, constant light field was made at different aperture positions.

For the large aperture, the throughput versus aperture position is shown in Figure 108, and for the small aperture, it is shown in Figure 109.

The gradient at zero degrees from nominal is 1.3%/deg, and 3.3%/deg for the large and small apertures respectively. The resulting uncertainty from a 0.0003 degree motion of the aperture wheel is 4 ppm and 10 ppm respectively.

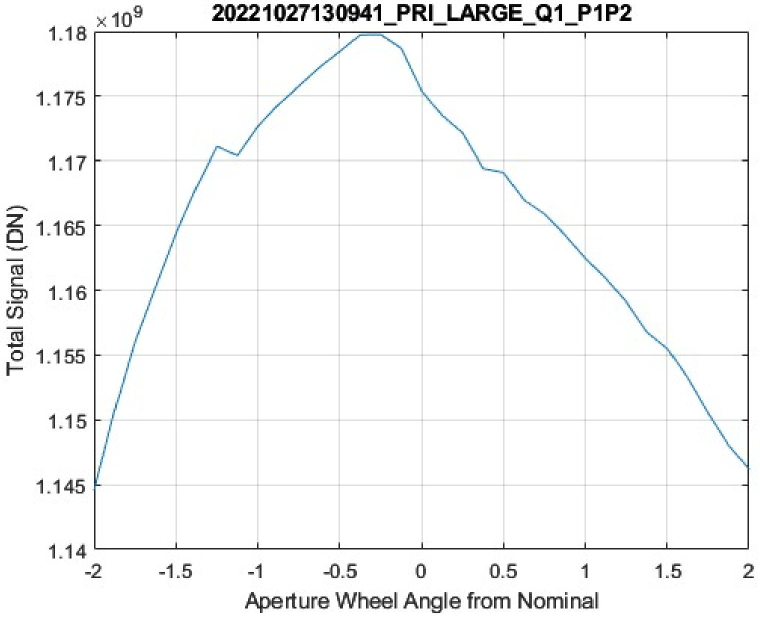

Figure 108. Large aperture throughput versus aperture position deviation from nominal angle.

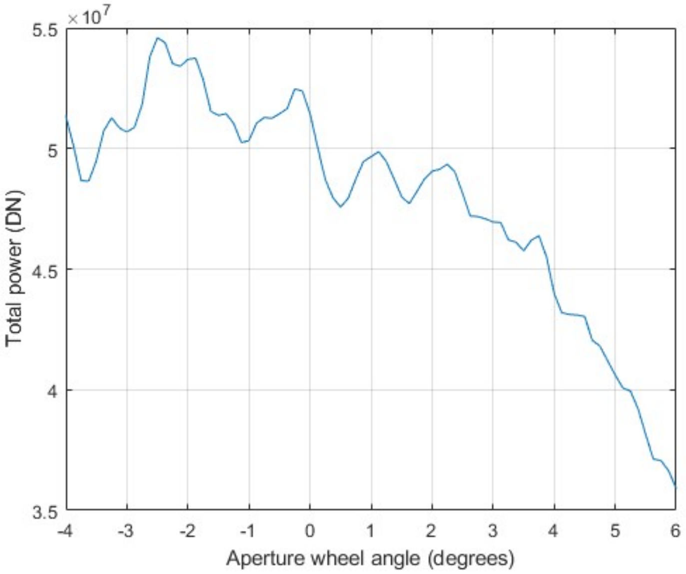

Figure 109. Small aperture throughput versus aperture position deviation from nominal angle.

6.7.8 Polarization Uncertainty

The HySICS instrument polarization is shown in Figure 110. This is a ground measurement that cannot be verified on-orbit, and is not expected to change through the entire mission. This instrument polarization interacts with the scene polarization to produce an error in the measurement. The scene polarization used in the uncertainty budget is a simple line, with 20% polarization at 350 nm, and dropping to 0% polarization at 2300 nm. The scene error is merely the multiplication of these two arrays, shown in Figure 111. Since there is no measurement of the scene polarization while HySICS is scanning the Earth, the nominal error is used as the polarization uncertainty for every scene.

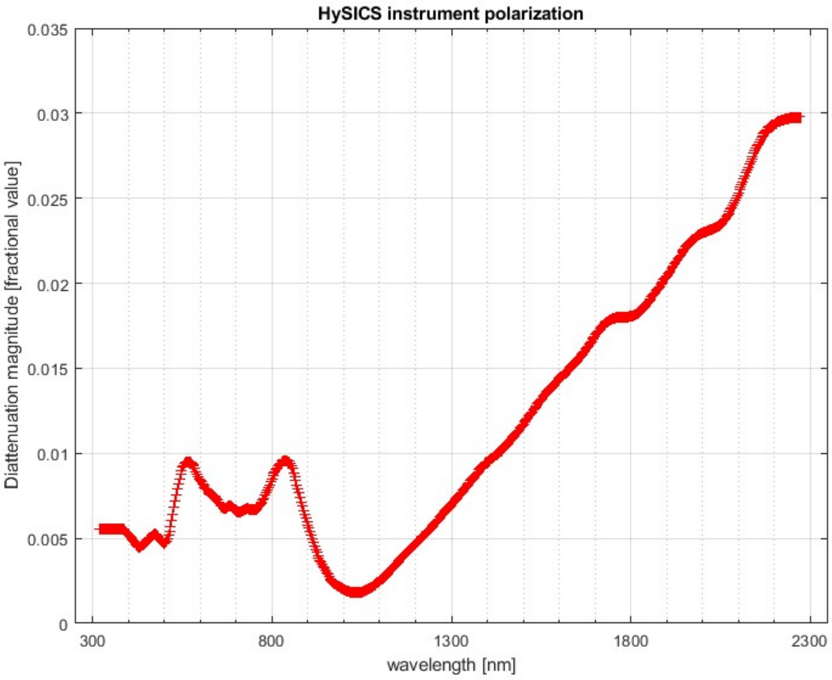

Figure 110. HySICS Instrument Diattenuation.

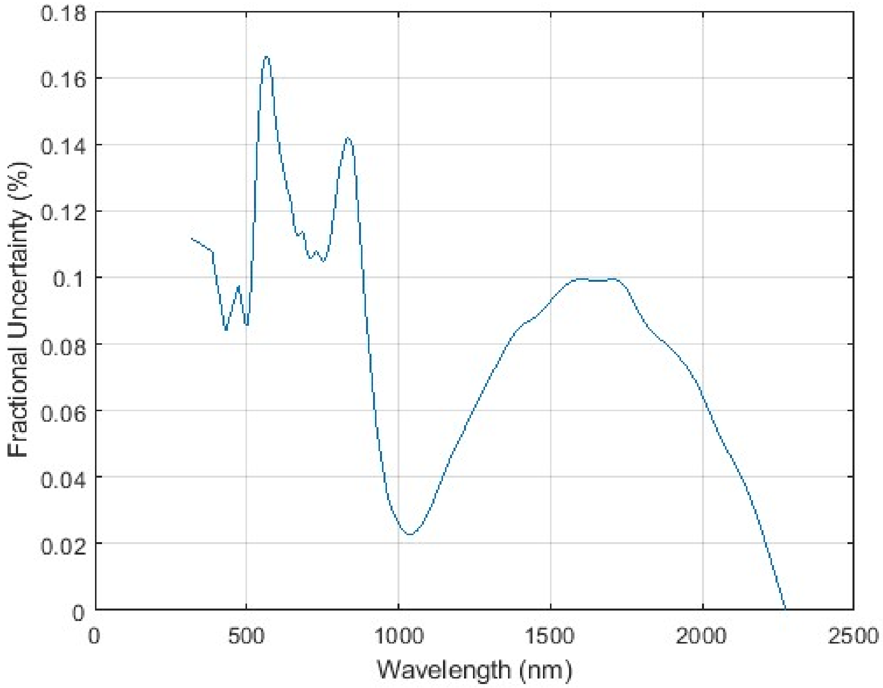

Figure 111. Nominal scene error due to polarization sensitivity.

6.7.9 OSF Leakage SSI and Ground Measurement Uncertainty

The order sorting filter is made from three separate interference filters, paneled together on the vacuum window in front of the detector array, as shown in Figure 112. Like all interference filters, there is a small amount of unwanted leakage light that is transmitted. Using the transmission versus wavelength plots of the order sorting filter from the HySICS balloon flight, shown in Figure 113, the amount of second-order leakage light can be predicted. The fractional uncertainty is the ratio of this leakage light to the expected signal. If necessary, it may be possible to measure this leakage light and digitally remove the leakage during post processing. The second order light from the grating, however, has twice the dispersion of the first order, meaning that some interpolation between every other wavelength bin would be necessary, causing some error. The OSF leakage uncertainty assumes that all the leakage light is an error source in both the SSI measurement and the ground measurement.

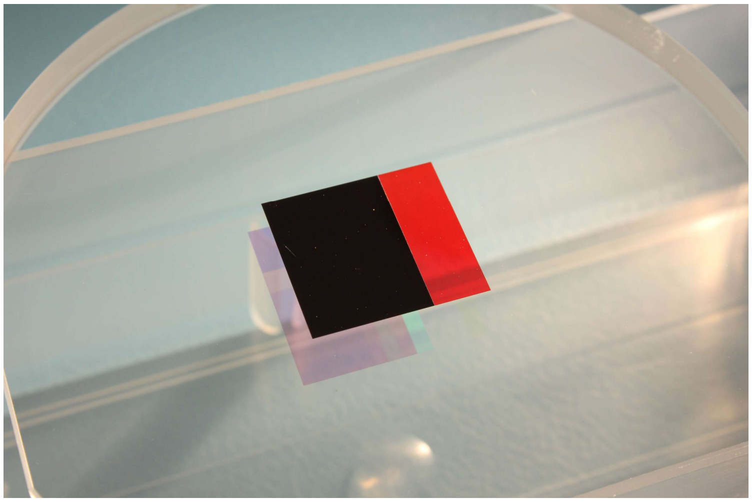

Figure 112. HySICS balloon instrument order sorting filter. The filter contains three regions, one that is nearly transparent (clear, on the right), one that blocks light below 650 nm (red, in the middle), and one that blocks light below 1200 nm (black, on the left).

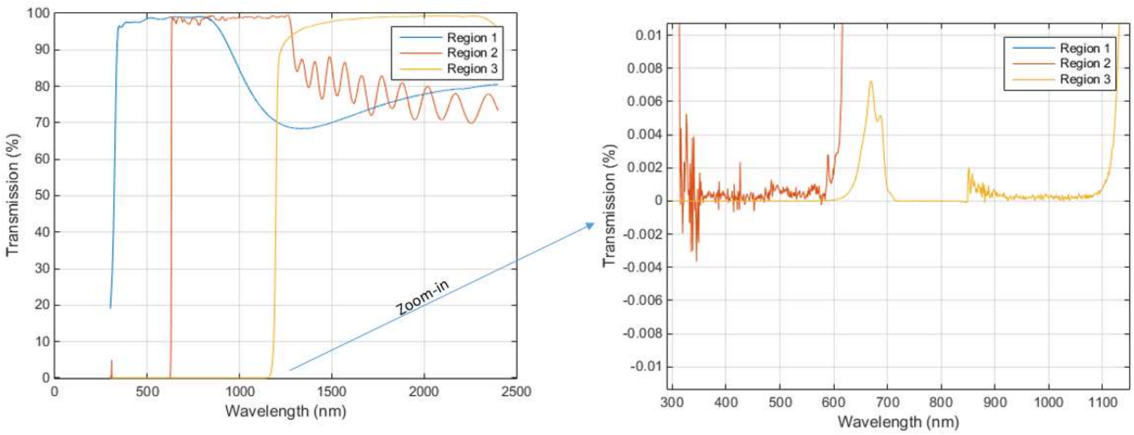

Figure 113. Order sorting filter transmission versus wavelength plots.

6.7.10 Point Spread Function Uncertainty

The optical point spread function (PSF) is a measurement of how an instrument “sees” a point source at infinity. It is an optical impulse function, and is uses as an indication of the distortion of the instrument. For HySICS, the point spread function at various wavelengths and field angles is shown in Figure 114.

The point spread function can be convolved with the measured scene to estimate the field distortion. The convolution results in a blurring of the image, as shown in Figure 115. The blurring does not attenuate or vignette power, but rearranges it, and features with high spatial gradients become smoother.

Error caused by the point spread function blurring the image is estimated based on the size of the region to be measured. For HySICS, a 15 x 15 km square is used as the measurement region. The error is found by a comparison of the total power in a high-resolution scene with and without the PSF convolution. For a nominal scene, the HySICS PSF error is shown in Figure 116. This PSF error map is directly used as the PSF fractional uncertainty in all images. Work to repeat the error analysis on many different ground scenes will continue in the future.

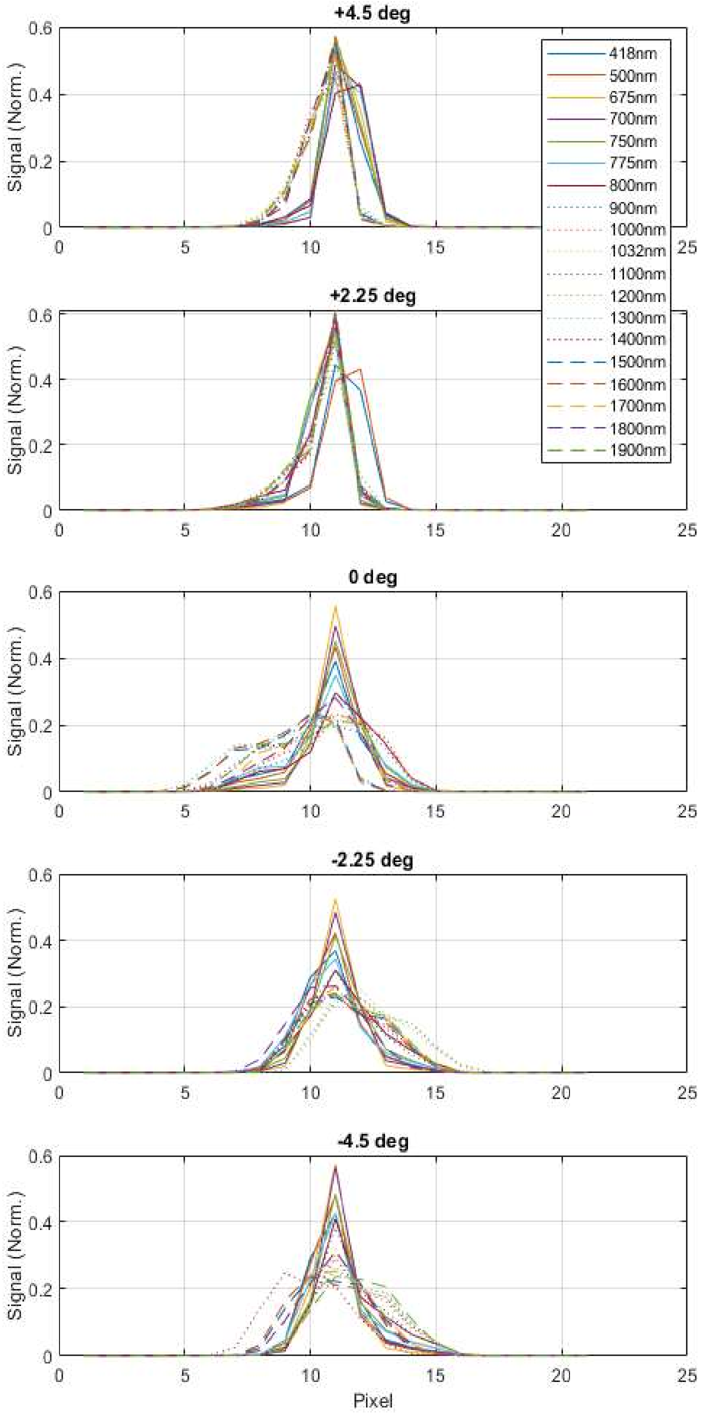

Figure 114. HySICS point spread function at various wavelengths (in color) and field angles (plots from top to bottom).

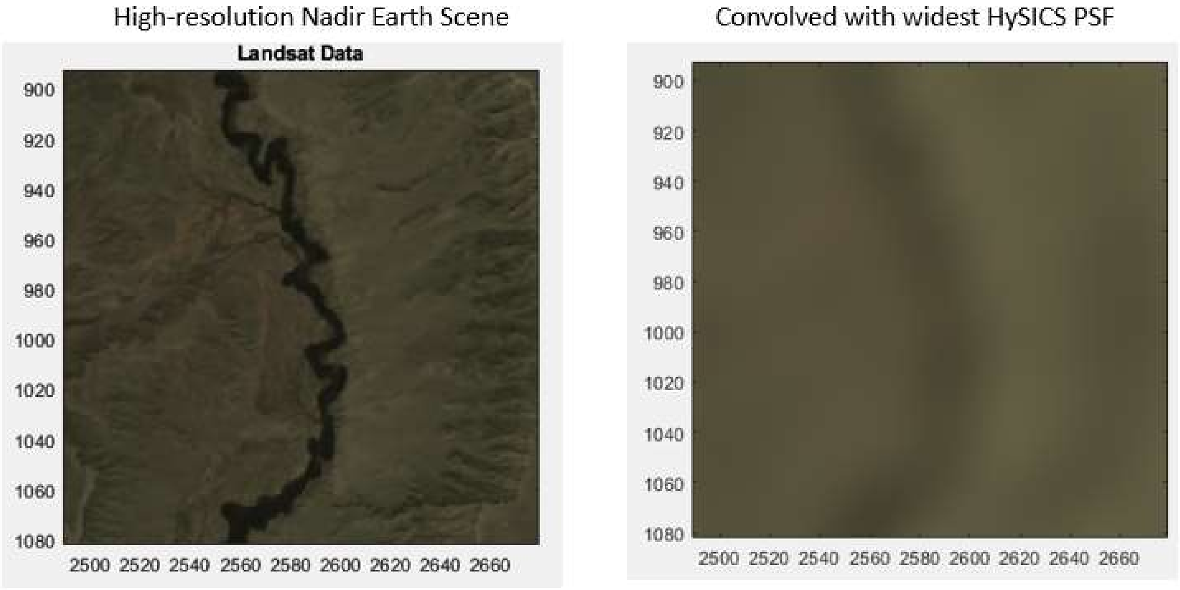

Figure 115. Left: High resolution scene obtained from Landsat data. Right: scene convolved with widest PSF to show blurring.

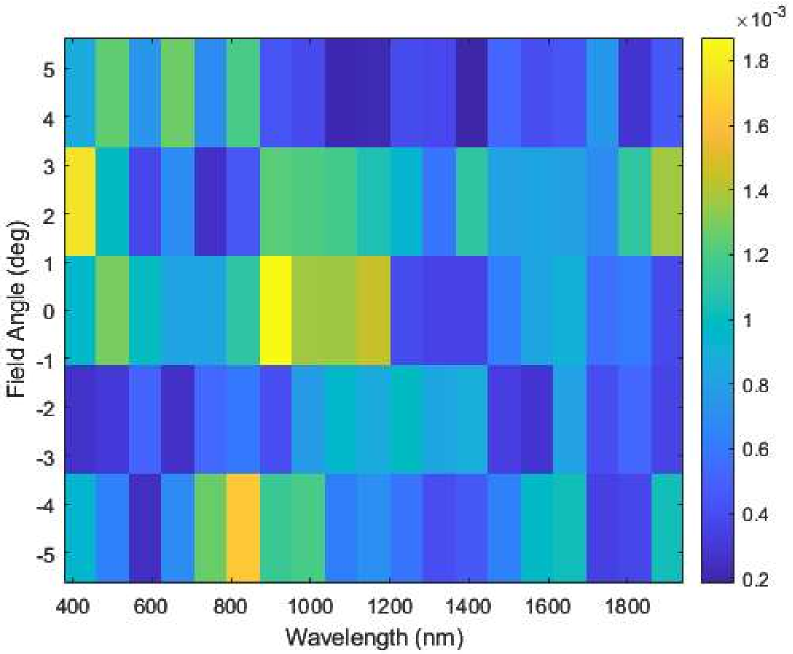

Figure 116. HySICS PSF fractional error in a nominal Earth scene.

6.7.11 Camera Electronic Timing Uncertainty

The camera electronic uncertainty is measured using a high precision oscilloscope. The start and stop edge signals can be read out from the FPE, and the timing difference between them represents the full integration time. For the HySICS camera, the integration time is specified as an integer number of row readout times, where a single row time is 122.85 µs, and the number of row times can go up to 538, or 66.211 ms (including the zero offset). The full timing measurement of the HySICS balloon camera is shown in Figure 117, where the horizontal axis is given in row times, from 1 to 2047. The data is fit to a line, and the residual, given in ppm of the full range, is plotted in Figure 118. The electronic linearity of the camera is better than 1.6 ppm across its full range. The CLARREO HySICS camera performs similarly. This level is easily good enough to rely on it as a standard to determine gain uncertainty, and used to precisely vary the amount of light to be detected the sensor. The electronic linearity uncertainty is counted twice, once for the nadir science scans, and once for the SSI scan, although it is so low that it is inconsequential in the full uncertainty budget.

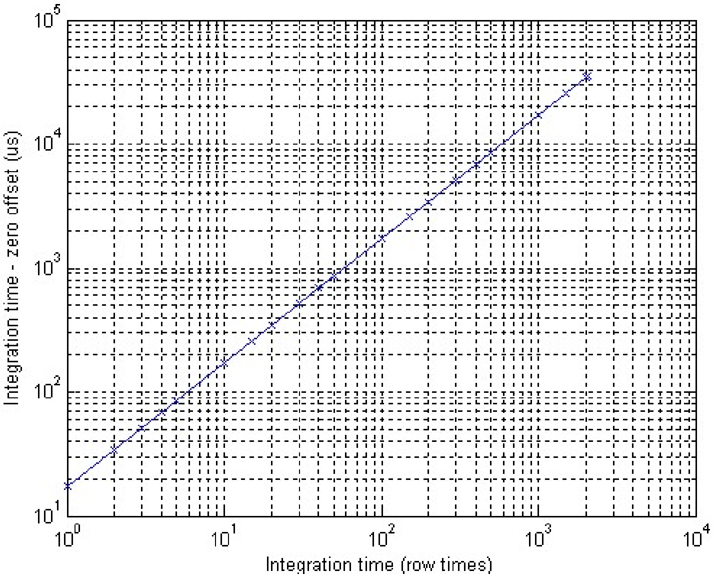

Figure 117. Electronic linearity measurement. The horizontal axis is in row times, and integer number of 16.8 us, and the vertical axis is the measured integration time.

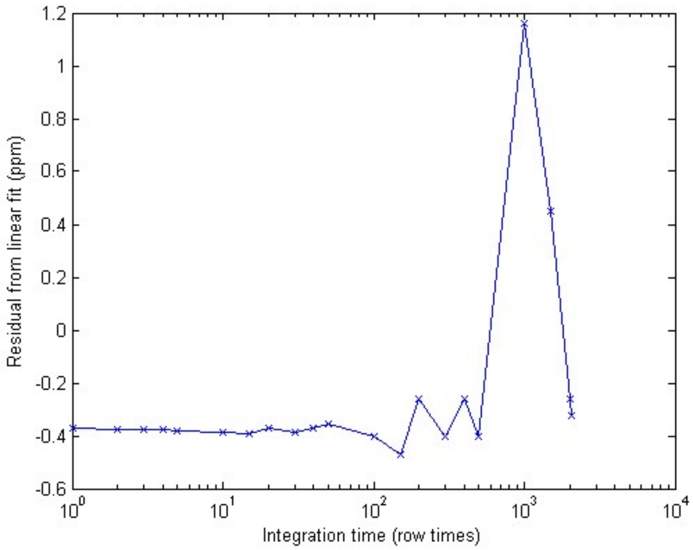

Figure 118. Electronic timing linear residual. The electronic timing of the HySICS balloon camera is better than 1.6 ppm across its full integration time range.

6.7.12 Scatter Uncertainty

The instrument scatter was measured during the calibration and characterization campaign over multiple tests, including with bright monochromatic light sources that were varied across the full spectral range, and similar diffuse and broadband light sources. The data set has been mined to identify the most consequential scatter sources. The maps of the two most significant scatter sources are shown in Figure 119 and Figure 120. As of the time of writing, these error maps are directly used as uncertainties. In the future, they will be investigated to determine if they can be converted to scatter slope maps that can be multiplied with the image to attempt to estimate a per-image scatter.

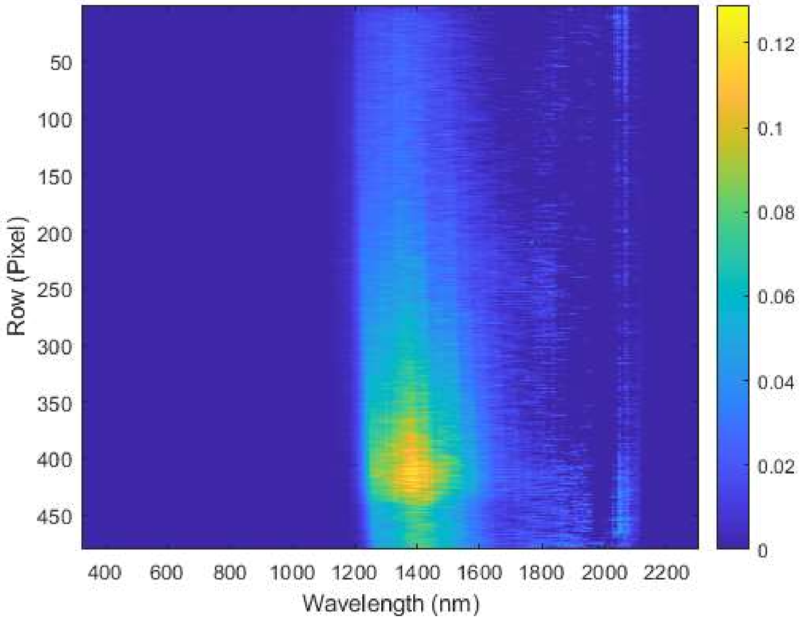

Figure 119. "Sidecar scatter" error map, in percentage.

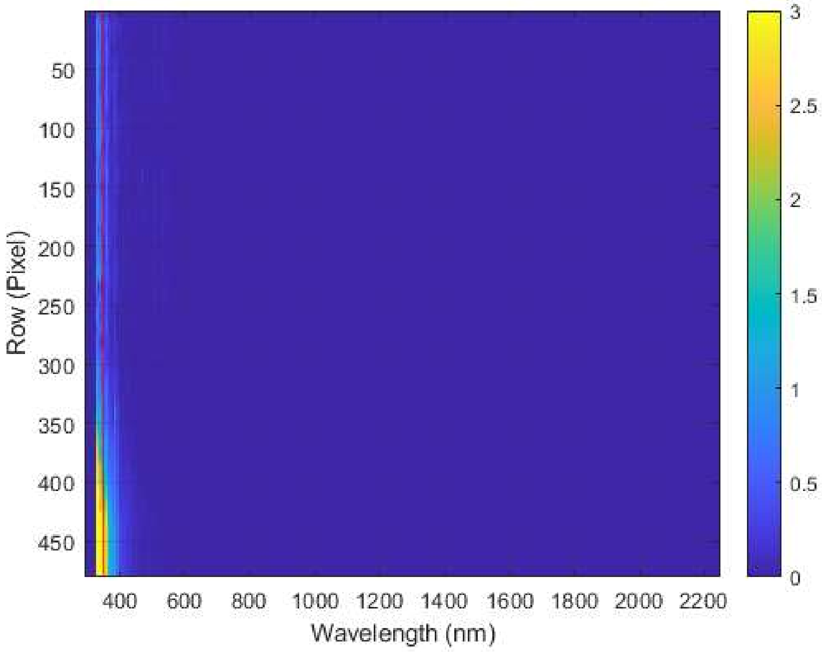

Figure 120. "UV Edge Scatter" error map, in percentage.

6.7.13 Per Pixel Scan Rate Uncertainty (previously called pointing uncertainty) [algorithm 7A]

Since the SSI integration relies on knowledge of the pointing to provide the per-pixel scan rates, an uncertainty in the pointing knowledge is required. This uncertainty is being studied by the HPS team. As a placeholder, the uncertainty is specified as 500 ppm of the scan rate.

6.7.14 Along slit Pixel FOV Uncertainty [algorithm 7A]

The second scaling factor necessary for the SSI integration is the along-slit per-pixel FOV. This FOV was measured in the lab, and shown in Figure 121. There are two glitches in this data set that have not been removed in this plot, but are understood and can be ignored at approximately row 65 and row 350. The FOV uncertainty is approximately 3 urad without averaging or curve fitting. These techniques will be applied to further reduce the uncertainty. Since this data is from a measurement on the ground, it is not expected to change throughout the mission. It is saved as a vector, and propagated into the uncertainty as a fraction of the pixel FOV size.

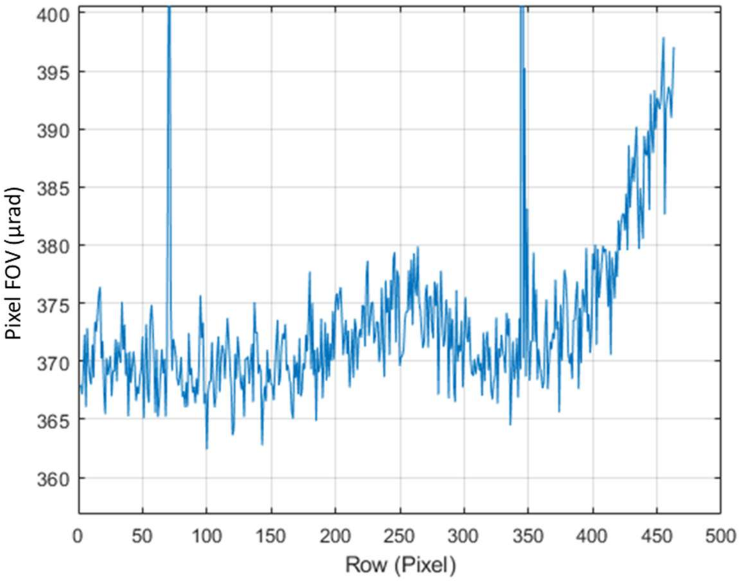

Figure 121. Along-slit per-pixel field of view.

6.7.15 Integration Along or Across Columns [algorithm 7B and 7C]

To perform the SSI integration, pixels are summed down columns (section 5.2.1.1.2) and across images (section 5.2.1.1.3). This summation does not generate any new uncertainties, but it does require a propagation of uncertainty step. Like the other similar steps, the resulting uncertainty is necessary for further uncertainty study, but it is not saved in the uncertainty list.

In the summation, independent uncertainty contributors are summed in quadrature, and additive dependent ones are just summed. Multiplicative dependent contributors are summed in fractional form.

6.7.16 Acquisition Period Uncertainty [algorithm 7D]

The final scaling factor required for the SSI integration is the acquisition period of the images. Together with the scan rate, it can be used to determine per-image scan motion of each pixel. If this factor is used, it will take the place of both the acquisition period and the scan rate scaling factors.

The acquisition period is determined by the FPGA signal to the FPA. The timing oscillator driving the FPGA has an uncertainty of 10 ppm, which is directly used in the uncertainty propagation for this step.

6.7.17 Spectral Distortion Correction Uncertainty [algorithm 8B]

The spectral distortion correction, described in section 5.2.2.4, uses wavelength data to estimate the wavelength scale distortion on the FPA. The distortion is given as a surface polynomial, as shown in Figure 80. To estimate the uncertainty in the fit, a monte carlo simulation, is used to perturbe the surface polynomial given the confidence intervals of all the coefficients. This generates hundreds of new surface polynomials that are also used to attempt a distortion correction. The standard deviation of each pixel in the corrected images is used as the uncertainty in the distortion correction.

As stated in section 6.7.1, the uncertainties associated with interpolating a solar spectrum are still being studied, but will be incorporated into to this uncertainty in the future.

6.7.18 BTDF Correction Uncertainty [algorithm 8B]

As described in section 5.2.2.2, the relative BTDF of the transmissive diffuser must be known to correct for it in the large aperture flat field. The transmissive diffuser BTDF was measured, and is shown in Figure 81. The uncertainty measured from multiple BTDF measurements is 106 ppm.

6.7.19 Creation of Flat Field [algorithm 8B]

The flat fields are created as described in section 5.2.2.3. There are several steps required to propagate per-pixel uncertainties through this process. While the signal on each pixel has a known uncertainty value, the normalization factor, or dividing by the mean of a column, requires finding the average of many pixels in a column. The uncertainties are propagated through this averaging step in a similar way as they are for the 3-pixel binning algorithm.

Independent uncertainties are reduced by the square root of the number of pixels used. The additive dependent uncertainties are averaged, and the multiplicative dependent fractional uncertainties are averaged, meaning that they aren’t reduced, but also don’t increase.

This algorithm only uses previously defined uncertainties, and does not generate any new ones.

6.7.20 Glint Uncertainty

In order for the Spectralon flat field to be accurate, the light incident on the diffuser must be constant throughout the whole scan. While this is not in question from the Sun light, glint sources, such as reflections off the instrument, off the ISS structure, or even reflected light from the Earth, which could change over the course of a single scan, can cause error in the flat field estimation. Simulations of the ISS structure glint are on-going, but expected to be small. As a placeholder, their uncertainty contribution is set at 0.1% of the total light, and is the dominant uncertainty term in the Spectralon flat field scan, and one of the dominant contributors in the overall uncertainty budget.

Perhaps the largest glint source is Earthshine, defined as light reflecting off the Earth and incident on the Spectralon diffuser. A full analysis of the worst-case scenario has shown that the expected Earthshine variation during the course of the scan can be as high as 600 ppm of the total light given a large transition on the Earth (such as snow to water across the full field of view) with a pitch angle of 86.5 degrees below the solar disk. While possible, this scenario is unlikely, and the Earthshine error is generally nonexistent.

6.7.21 Peak Alignment Uncertainty [algorithm 8A]

Since the flat field scan moves the solar peak in the spatial direction along the sensor, it is possible to use only the image information to determine its pixel location, which is required for an accurate flat field calibration. In the original flat field analysis from the HySICS balloon flight, the measured solar peak as it crossed each pixel was used to determine the peak alignment. The solar peak, as measured by every pixel, is shown in Figure 78. The solar peak location, when only the image data is used, is difficult to determine at sub-scan rate levels due to shot noise and read noise. However, the ability to align these peaks is greatly improved given the 5 arcsec pointing knowledge that CLARREO Pathfinder is expected to have access to via the fine sun sensor. At the expected scan rate of 18.75 arcsec/image (4 images per pixel of a stationary solar location,) a 5 arcsec knowledge error in the solar peak location corresponds to just over a quarter of an image (0.267 images), and equates to a maximum of 100 ppm of error in the signal level if 5 images are used at the top of the solar peak.

Since the Spectralon flat field will also be a scan over the solar disk, it is again necessary to line up each solar peak as it crosses over an individual pixel on the camera. Because the solar peak is being diffused by a nearly Lambertian diffuser, it will be extremely wide compared to the solar disk. As a result of the wide peak, the sensitivity to peak alignment is significantly diminished compared to that of the solar flat field, and its associated uncertainty is nearly negligible. It is so small as to be difficult to estimate, but is likely less than 1 ppm for 5 arcsec knowledge of the pointing. As a conservative placeholder, 100 ppm is used in the uncertainty budget. There is very little effect on the total uncertainty between 1 ppm and 100 ppm for this term.

6.7.22 Transmissive Diffuser Comparison Uncertainty

During the characterization and calibration campaign, it was attempted to verify that the transmissive diffuser aperture created the same flat field as the large aperture, which cannot use the Sun for a flat field measurement. The two flat fields, one with just the bare aperture and one with the transmissive diffuser, are shown in Figure 122.

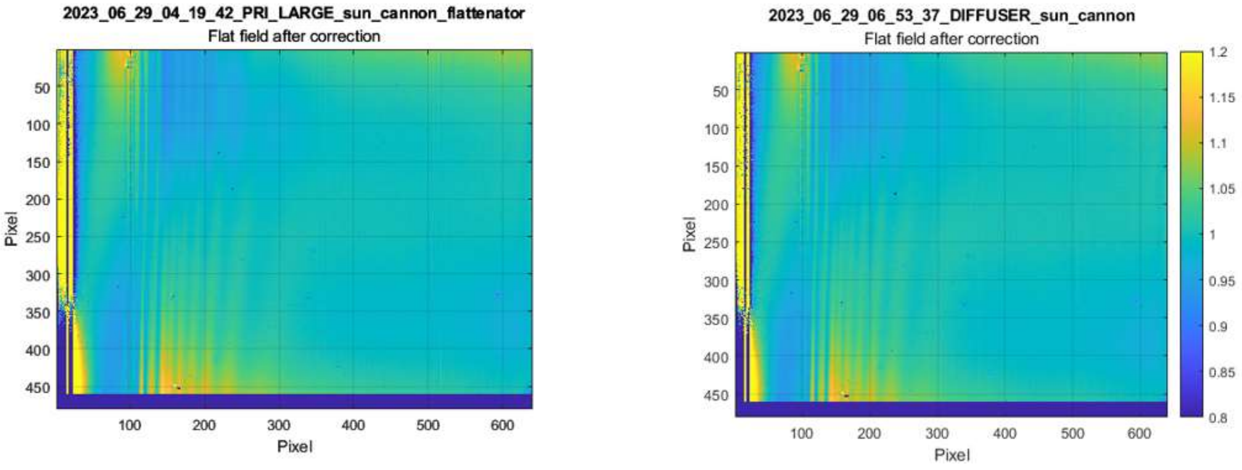
2023_06_29_04_19_42_PRI_LARGE_sun_cannon_flattenator
Flat field after correction

2023_06_29_06_53_37_DIFFUSER_sun_cannon
Flat field after correction

Figure 122. Flat field comparison test. Image on the left was generated without a diffuser, and the image on the right was generated with a diffuser.

By eye, these flat fields are extremely similar. The difference image is shown in Figure 123.

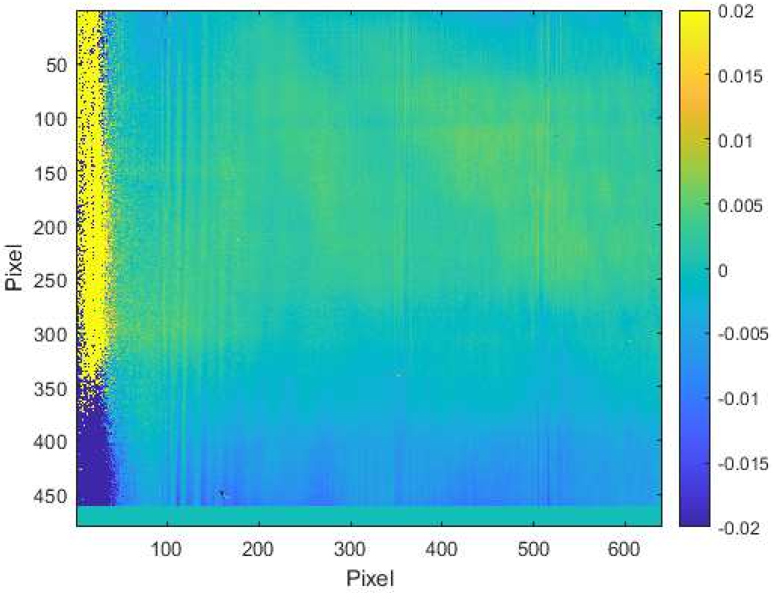

Figure 123. Difference image of the two comparison flat fields. Values are fractional.

The standard deviation of the lit portion of this image is 0.28%, which is used as the comparison uncertainty between the large aperture and transmissive diffuser flat fields. It is likely this value is significantly overestimating the uncertainty, since the comparison between the two scans is so difficult. Future data analysis work will be done to attempt to reduce this uncertainty.

6.7.23 Pointing Uncertainty

Since the solar spectral irradiance scan is assembled and integrated over many overlapping images, as discussed in section 5.2.1, uncertainty in the oversampling factor leads to an uncertainty in the unit conversion factor. The oversampling factor is generated via two parameters, the pointing of the instrument with respect to the center of the solar disk, and the width of the slit. In essence, if the slit is slightly larger than assumed, there will be slightly too much power measured during the SSI. However, during a ground scene measurement, the slit will still be slightly larger than assumed, making the calibration valid.

The pointing error, or jitter, in the measurement is apparent in the FSS (fine sun sensor) data, as seen in Figure 61. The measurement uncertainty is due to the power gradient during the scan, as shown in Figure 124. The higher the gradient, (e.g. right at the edge of a solar measurement) the more total error generated by pointing uncertainty.

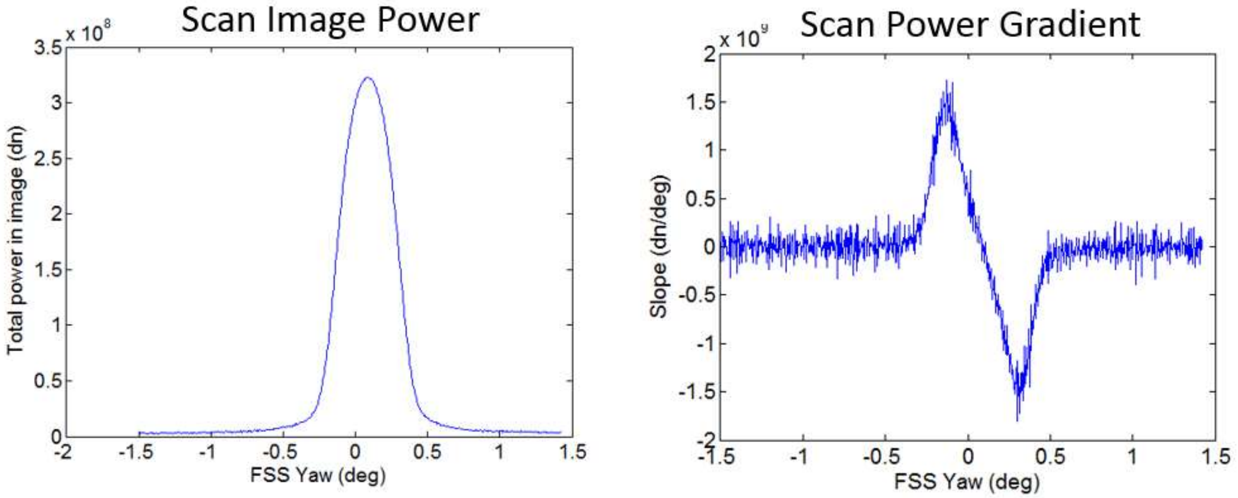

Figure 124. Total power during an SSI scan, in DN, and gradient versus pointing position.

The total uncertainty in each image of the scan is determined by the scan power gradient multiplied by the pointing uncertainty. The resulting values are added in quadrature from each image of the scan, giving a total uncertainty for the measurement. This uncertainty is then applied equally across the full spectral range.

During the HySICS balloon flight, the FSS uncertainty was 1.06 arcsec, and the full scan uncertainty was 0.011%.

6.7.24 Creation of Blank Aperture Image [algorithm 9A]

The blank aperture image is created by averaging a scan of blank aperture images (section 5.2.4). This averaging step does not generate any new uncertainties, but it propagates the per-pixel uncertainties through averaging multiple images. Independent uncertainties are reduced by the square root of the number of pixels used. The additive dependent uncertainties are averaged, and the multiplicative dependent fractional uncertainties are averaged.

Appendix A - Diffraction Calculation

The lost light, outside the collection window, can be determined by starting with the diffraction equation for an infinite half-plane [10]:

$$I(r,\theta) = I_0 \frac{\lambda}{16\pi^2 r sin^2(\phi/2)} \qquad 73$$

with the variables defined by the geometry shown in Figure 125. The incident intensity is given by I_0. θ and ϕ both represent the diffraction angle, and are related by $\theta - \phi = \frac{3\pi}{2}$. λ is the wavelength dependency, and r is the distance from the edge to the measurement point.

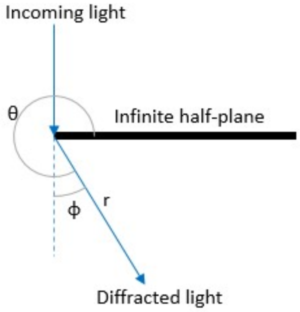

Figure 125. Geometry for diffraction from infinite half-plane.

The equation can be converted to represent the total fraction of diffracted light that misses a collection window [14]:

$$\frac{I(\phi_{Min,1},\pi)}{I_{Total}} + \frac{I(\phi_{Min,2},\pi)}{I_{Total}} = \frac{\lambda}{4\pi^2 R}\left[\frac{1}{tan(\phi_{Min,1}/2)} + \frac{1}{tan(\phi_{Min,2}/2)}\right] \qquad 74$$

given the geometry in Figure 126. In this equation, $\frac{I(\phi_{Min,1},\pi)}{I_{Total}}$ and $\frac{I(\phi_{Min,2},\pi)}{I_{Total}}$ represent the fraction of diffracted light between the top and bottom edge of the collection window, given by the angles $\phi_{Min,1}$ and $\phi_{Min,2}$, and the input aperture plane, given by an angle of π. The radius of the input aperture is given by R, and the radius of the collection window is given by r_d. Light is always diffracted into the plane perpendicular to the tangent of the input aperture edge. The total fraction of lost light is found by integrating the above equation around the circumference of the input aperture.

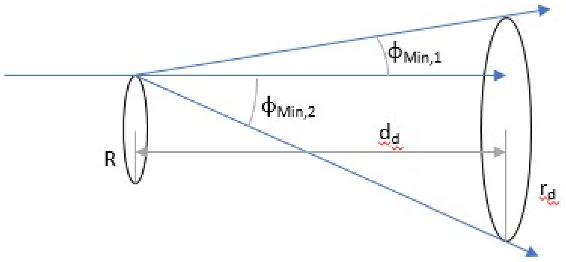

Figure 126. Geometry for calculating the total fraction of light that falls outside a collection window.

Although the collection window in the derivation of the lost light equation is circular, it can be any shape, as long as the minimum acceptance angles angles, $\phi_{Min,1}$ and $\phi_{Min,2}$, can be determined. A rectangular collection window, similar to the collection window from a HySICS solar irradiance scan, is shown in Figure 127. Finally, since the 4MA telescope is located directly behind the entrance aperture, the collection window acceptance angles, $\phi_{Min,1}$ and $\phi_{Min,2}$, are found using the 4MA Zemax simulation. Figure 128 shows one edge angle, $\phi_{Min,1}$, for the 0.5 mm input aperture given the HySICS balloon collection window, defined by the slit size, 14.4 mm x 28.297 µm, and a linear, cross-slit scan from -1.5 degrees to +1.5 degrees. After integrating around the input aperture, and repeating for all wavelengths, the total lost power fraction for this scan is shown in Figure 129.

The uncertainty in the lost light from given in a diffraction calculation is 1.8% of the amount of lost light, a level set by NIST. The lost light from diffraction is added to the detected light from the solar irradiance scan to account for the total spectral irradiance, as shown in Figure 130, which represents the total amount of light entering the instrument aperture.

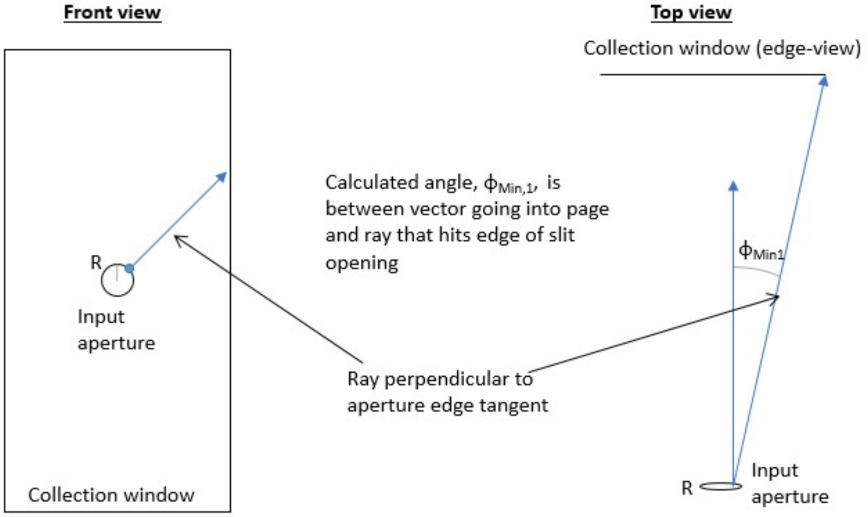

Figure 127. Diffraction geometry for a rectangular collection window, similar to HySICS. The left figure shown the diffraction if the input light is moving into the page, and diffracts off the edge of the input aperture. From the top view, on the right, the $\phi_{Min,1}$ angle between the incoming ray and the diffracted ray is visible.

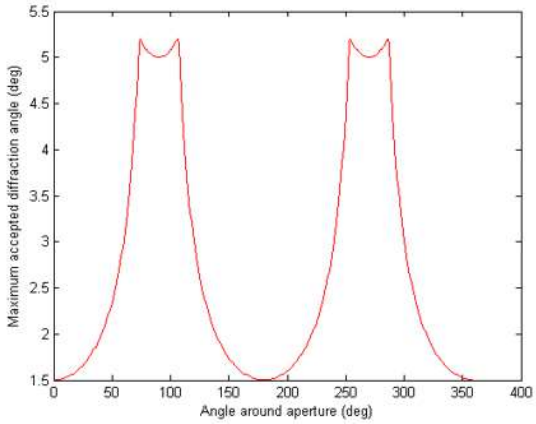

Figure 128. Minimum acceptance angle all the way around the aperture, given the HySICS 4MA, slit, and scan geometry. The acceptance angle is periodic, with the minimum values of 1.5 degrees (defined by the scan extents), and the maximum value of just over 5 degrees located at the corners of the collection window.

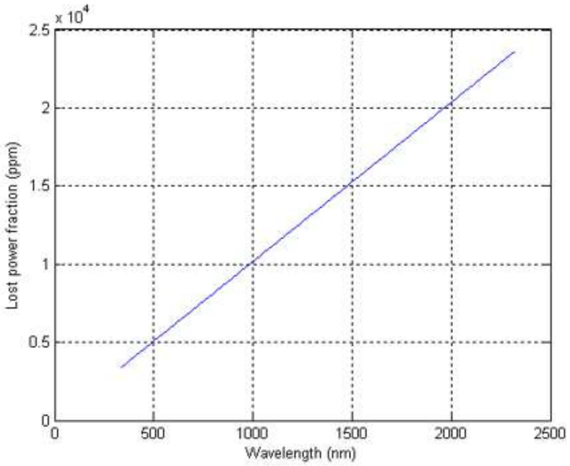

Figure 129. Lost power due to diffraction over the entire wavelength range. This plot shows that at 1000 nm, approximately 10,000 ppm (1%) of the light is lost to diffraction.

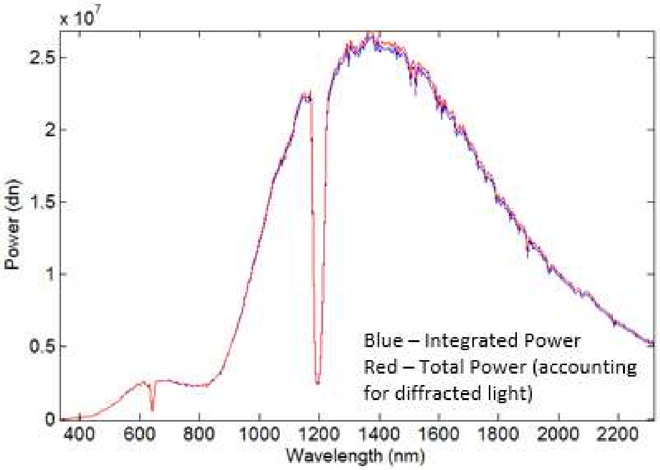

Figure 130. Total integrated light in HySICS balloon solar spectral irradiance scan, including correction for lost diffracted power. This is the un-calibrated total measured light from the sun.

Appendix B -

In the flat field testing we discovered an unexpected and not fully understood behavior in the FPA, which has been dubbed the 'cursed row' phenomena. The flat field test worked by illuminating the FPA with a light pattern, which was walked from the bottom of the FPA to the top in steps of 1 row. A few images from one scan are shown in Figure 131.

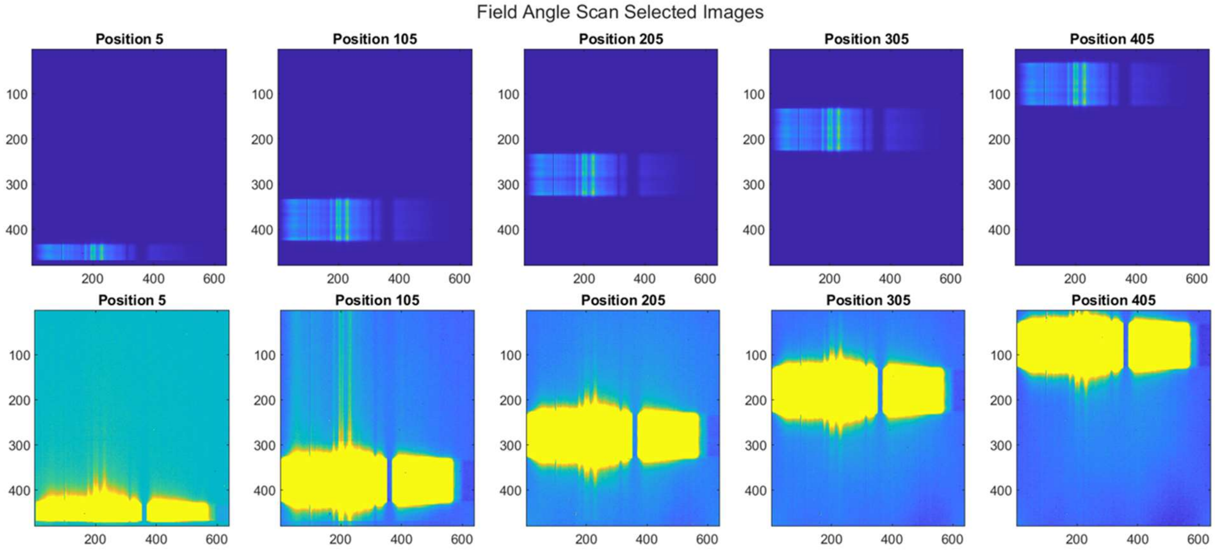

Figure 131. A set of images from a flat field scan with color scales showing the full range (top) and low level structure (bottom).

While the exact dynamics of the cursed are not fully understood, the general manifestation is known and easy to recognize. Specifically, there is a row (the 'cursed row') on the FPA, that, when illuminated, leads to whatever light pattern is on that row being written over the entire FPA at a low level. This can be seen in the above images, in the image for Position 105 on the bottom row, where you can see vertical streaks extending over the whole range of the FPA, that are not present in the images for the other positions.

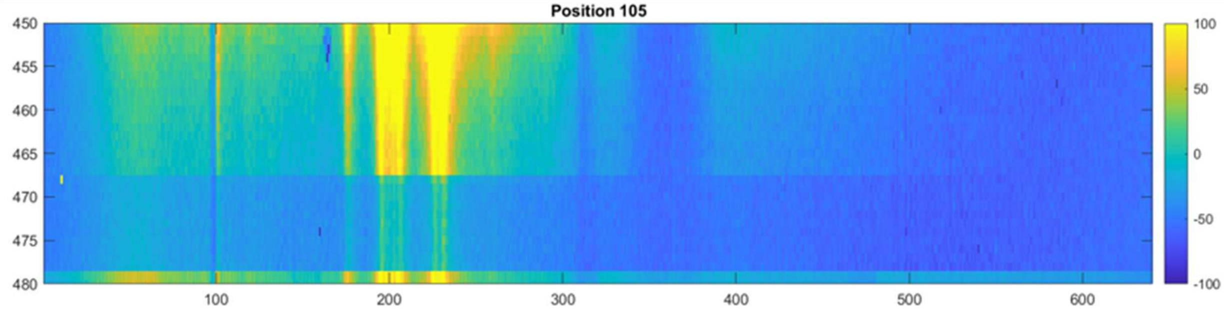

Figure 132. The bottom of the FPA in Position 105 from Figure 131. The hard edge in the light pattern at row 467 is from the slit – below this row no light can reach the FPA. The streaks can be observed to extend into this dark region, and even into the two extra rows at the bottom of the image, which are not sensitive to light.

Additionally, if we zoom in on the bottom few rows of the detector, we can see that this effects is magnified in the two extra rows, as shown in Figure 132. In the instrument, the slit provides a hard edge blocking light from rows below row 467. You can see the streaks extend below this edge, and in particular, in rows 479 and 480, the extra rows, the streaks are magnified. As these rows are not sensitive to light, is how we originally determined this was not an optical phenomena.

The exact row for which this phenomena occurs is determined by the integration time setting for our operation, and we specifically expect it to be present for any integration time setting between 55 and 536 row times.

There are additional complications in the phenomena beyond having whatever light pattern is in the cursed row being written over the FPA. There is evidence that a range of rows directly above the cursed row, of unknown width, also have an effect when illuminated. This can be seen in Figure 133. In particular, the top left plot shows the mean signal in the full FPA over a full scan.

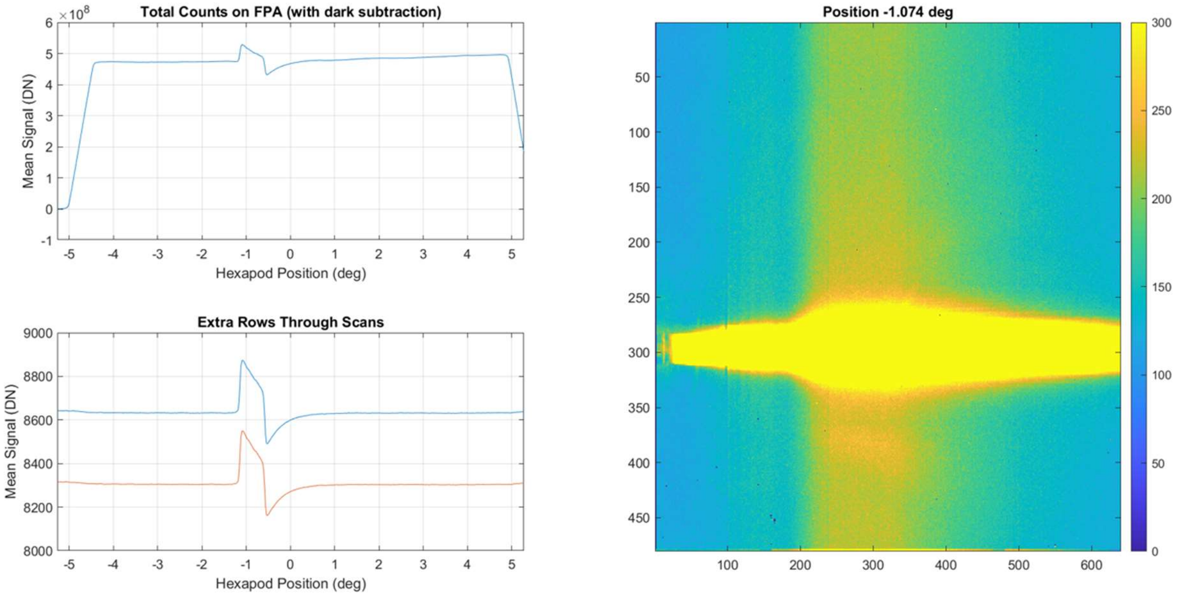

Figure 133. The mean signal in the FPA as a function of scan position for a flat field scan (top left), and the mean signal in the extra rows (bottom left). The power initially rises as the light walks onto the detector, then is level as it walks up, until it reaches the cursed row, where it jumps suddenly. The dip following the jump indicate that illuminating the rows above the cursed row lead to a depression of the signal. On the right is an image where the light first walks onto the cursed row, showing the characteristic vertical streaking.

Initially the power rises as the light walks onto the FPA. Once the patterns is on the FPA, the power is constant as it walks up, until it first reaches the cursed row. At this point, the signal suddenly jumps. As the light pattern continues to walk up, the signal is observed to drop, and when the light pattern walks off the cursed row, the signal drops down below baseline. This indicates the effect of the rows directly above the cursed row – when illuminated, they cause a low level depression in the signal over the full FPA.

Because the full dynamics of the cursed row are not understood, and we are largely able to avoid it with a proper choice of integration time, we have not attempted an exact correction. In some tests however, it is unavoidable. In particular, for the tests taken in the cold target test campaign for the LED data, it is present in all the data taken between integration times 55 and 537. This is important for the linearity and full frame dark pedestal correction characterization.

To deal with the cursed row in these data sets, we decided to build a simple correction that corrects for the net effect of the cursed row. In Figure 134, we see a sample linearity curve as described in section 5.1.3.7.

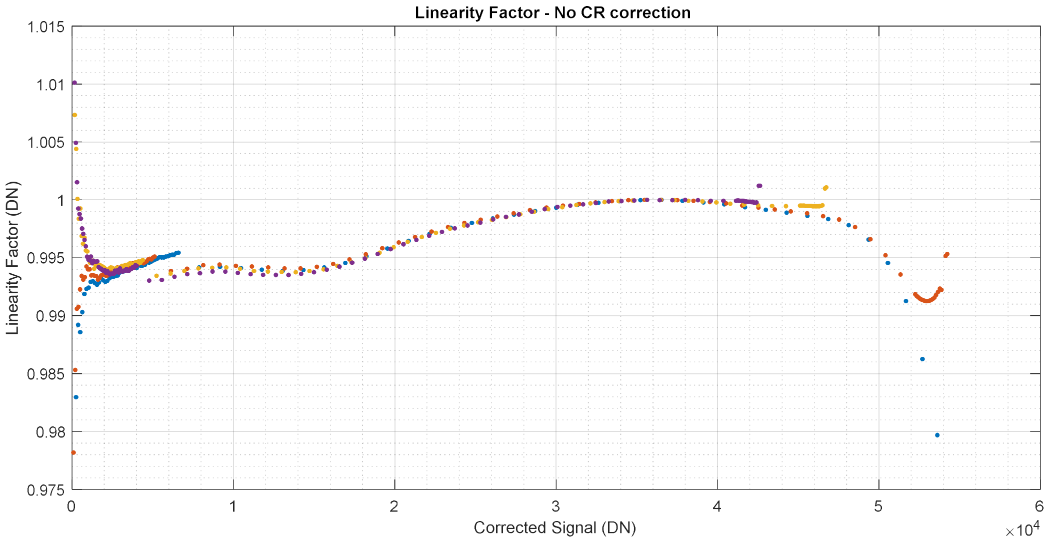

Figure 134. Linearity curves for the warm target data sets as described in Section 5.1.3.7. The net effect of the cursed row is the jumps in the data around 5000 DN, and then in the final two points of the purple, yellow, and red curves.

The cursed row is responsible for the jumps in the curves present around ~5000 DN and in final two points of the purple, yellow, and red curves. To correct for this, the magnitude of these jumps is first characterized – this shows the net effect of the cursed row phenomena. This effect is modeled as

$$l_f = \frac{1}{l_{f_{max}}} \frac{1}{int + z_0} sig(1 + \alpha_{cr}) \tag{75}$$

Here, sig is the signal absent any cursed row effect, l_f is the linearity factor, l_{fm} is the normalization constant, *int* is the integration time setting, z_0 is the true integration time offset, and α_{cr} characterizes the effect of the cursed row. By extrapolating the previous trend in the linearity curves, we characterize the magnitude of the jump for the final two data points in the purple and yellow data sets. This difference, Δl_f, is then use to give the α_{cr}

$$\alpha_{cr} = \Delta l_f \frac{l_{f_{max}}(int + z_0)}{sig} \tag{76}$$

To correct for the cursed row effect, the signal for any data taken at an integration time between 55 and 537 is adjusted by this factor. The results can be seen in Figure 135, where the jumps due to the cursed row have largely vanished.

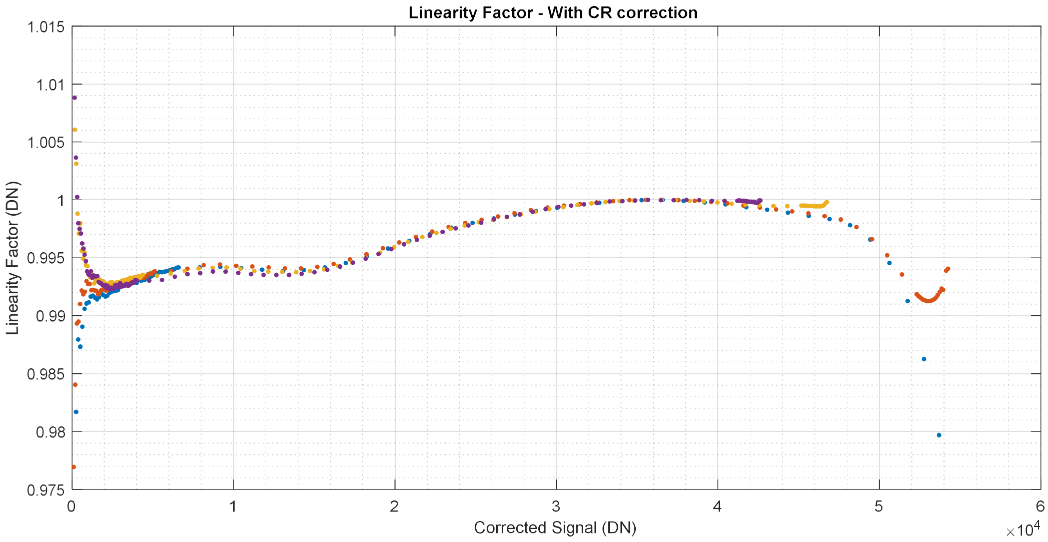

Figure 135. The linearity factors after correcting for the cursed row effect. The jumps are largely gone.

A quick implementation of the cursed row correction is given here.

Step	Description
1	Load the cursed row proportionality constant, α_{cr}
2	Loop through each image
3	If the integration time is between 55 and 536 (inclusive), sum the image from rows 1 – 478 and columns 3 - 640
4	Multiply the sum by the proportionality constant, α_{cr}
5	Subtract the product from the image.